The influence of turbulence on aggregation of small particles in agitated vessels

Please check the document version of this publication:

• A submitted manuscript is the version of the article upon submission and before peer-review. There can be important differences between the submitted version and the official published version of record. People interested in the research are advised to contact the author for the final version of the publication, or visit the DOI to the publisher's website.
• The final author version and the galley proof are versions of the publication after peer review.
• The final published version features the final layout of the paper including the volume, issue and page numbers.

[Link to publication](#)

Download date: 09. Feb. 2020

THE INFLUENCE OF TURBULENCE

ON AGGREGATION OF SMALL PARTICLES

IN AGITATED VESSELS

K.A. KUSTERS

THE INFLUENCE OF TURBULENCE

ON AGGREGATION OF SMALL PARTICLES

IN AGITATED VESSELS

Proefschrift

Voor mijn ouders

DANKWOORD

SUMMARY

The critical stage in the synthesis of solids in liquids is often the formation of aggregates. The properties of the product are dependent on the morphology and especially the size of the aggregates. If the solid particles stick together by the action of Van der Waals attraction, the aggregation process is called coagulation.

In this thesis the influence of the hydrodynamics in baffled turbine agitated vessels on the turbulent coagulation of small solid particles is studied, with special focus on the dependence of the aggregate size on stirrer speed, on concentration of solids, destabilizer concentration and vessel size.

The final aggregate size obtained in a batch coagulation experiment, proved to be the result of a dynamic equilibrium between growth in zones of low turbulent shear stress and break-up of aggregates in zones of high shear stress. Important parameters in the coagulation process are the local strain rate, the hydrodynamical shear stress acting on the aggregates and the residence times of the aggregates in zones of different strain rate and shear stress. The strain rate controls the frequency of collisions between the particles. The shear stress determines the local maximum size of the aggregates. In the viscous subrange of turbulence both strain rate and shear stress are proportional to the square root of the local turbulent energy dissipation rate per unit mass. This is relevant for aggregates smaller than the Kolmogorov microscale. The residence time in the zones of low shear stress represents the time during which the aggregates are able to grow. If break-up is assumed to proceed almost instantaneously, the break-up frequency is given as the number per unit time the aggregates enter the high shear zones.

The residence times of the aggregates in the zones of different strain rate and shear stress plus the break-up frequencies were, for various aggregate sizes, computed from a particle tracking simulation program. The particle tracking program predicts the movement of a dispersed phase particle in the agitated vessel. This program requires exact knowledge of the flow field in the vessel i.e., mean and fluctuating velocities, integral length scale and local energy dissipation rate in every point of the vessel. To obtain the required information, laser Doppler velocimeter measurements have been

performed in vessels similar to the ones in which the coagulation experiments were carried out. Interpolation between the measured points was done with mathematical models based on mass balances and empirical correlations, describing the flow pattern and the shear field in the stirred vessel.

The particle tracking showed that the residence time weighted strain rate differs significantly from the strain rate calculated from the mean energy dissipation rate in the vessel. Application of the latter one in the computation of the collision frequencies would lead to substantial errors.

The effects of hydrodynamic and interparticle interactions during collision can be incorporated into coagulation-rate equations by defining collision efficiencies. Starting from the theoretical analysis concerning the streamlines in and around porous particles as presented in the literature, approximate values for the collision efficiencies of aggregates were computed. These values proved to be much greater than the collision efficiencies for solid spheres.

An increase of porosity with aggregate size was observed experimentally which explains the exponential type of growth of aggregates in the coagulation experiments. The increase of porosity with aggregate size could be well described by a fractal law, which assigns a fractal dimensionality to the floc structure.

Based upon the particle tracking results, the calculated collision efficiencies for porous aggregates and the information about the floc structure, a coagulation model was developed to describe the dynamic behaviour of the particulate system in a turbine agitated vessel. The model solves the population balances and predicts the evolution of the aggregate size in a batch experiment as a function of impeller speed, of solids concentration and destabilizer concentration.

The dependency of the coagulation rate on the average strain rate which is controlled by the stirrer speed, was found experimentally to be almost linear. The growth rate increases proportionally with solids concentration. Both findings are in agreement with predictions by the coagulation model.

The final aggregate size which is determined by a dynamic equilibrium of growth and breakup, increases with solids concentration since the growth rate is enhanced with respect to the breakup rate. Increase of the stirrer speed increases the shear stress acting on the aggregates and decreases the final aggregate size according to a power law, with the exponent depending on the fractal dimensionality of the flocs. Comparison of simulation results with the experimental findings showed that the coagulation model predicts quantitatively the final aggregate size as a function of solids concentration and impeller speed. The variation of floc size with destabilizer concentration could be well described with the DLVO (Deryaguin, Landau, Verwey and Overbeek) theory incorporated in the coagulation model.

The course of coagulation proved to be hardly affected by the scale of operation at equal values of the average rate of energy dissipation. Laser Doppler measurements revealed a dependence of the energy dissipation rate distribution on vessel size. The energy dissipation rate at the impeller blade tip was found to decrease with scale-up, whereas the energy dissipation rate in the bulk of the vessel was found to do the opposite. The net effect of these changes is presumably too small to influence the coagulation process significantly.

SAMENVATTING

Bij de bereiding van vaste stoffen vanuit de vloeistoffase worden vaak clusters van deeltjes ofwel aggregaten gevormd. De eigenschappen van het product zijn afhankelijk van de morfologie en vooral van de grootte van de gevormde aggregaten. Het aggregatie-proces wordt aangeduid met de term coagulatie als de bindingskrachten tussen de deeltjes een gevolg zijn van Van der Waals aantrekking.

In dit proefschrift is een studie vastgelegd naar de invloed van de hydrodynamica in geroerde vaten op de turbulente coagulatie van kleine vaste deeltjes. Deze studie beschrijft de invloed van roerdertoerental, vaste stof-concentratie, concentratie van destabilisator en van vatdiameter op de grootte van de gevormde aggregaten.

De eindgrootte van de aggregaten verkregen in een ladingsgewijs coagulatie-experiment, blijkt bepaald te worden door het dynamisch evenwicht tussen groei en afbraak van de aggregaten in zones met respectievelijk een lage en een hoge turbulente afschuifspanning. Belangrijke parameters ter beschrijving van het coagulatie-proces zijn de locale reksnelheid, de locale hydrodynamische afschuifspanning die op de aggregaten werkt en de verblijftijden van de aggregaten in de zones met een verschillende reksnelheid en afschuifspanning. De reksnelheid bepaalt de frequentie van botsingen tussen de deeltjes. De afschuifspanning bepaalt de locale maximale aggregaatgrootte. In het visceuze wervelregime van turbulentie zijn zowel reksnelheid en afschuifspanning evenredig met de wortel uit de locale energie dissipatie per massa-eenheid van suspensie. Deze reksnelheid en afschuifspanning zijn relevant voor de vorming van aggregaten kleiner dan de Kolmogorov microlengteschaal. Gedurende de verblijftijd in zones met lage afschuifspanning kunnen de aggregaten uitgroeien. De opbreekfrequentie is gelijk aan de frequentie waarmee de aggregaten de zones met hoge afschuifspanning passeren.

De verblijftijden van de aggregaten in zones met hoge en lage afschuifspanning, en de opbreekfrequenties zijn berekend met behulp van een computerprogramma dat de beweging van een deeltje door een geroerd vat simuleert. Dit programma maakt gebruik van gegevens betreffende het

stromingsveld in het geroerde vat, die verkregen zijn met behulp van laser Doppler snelheidsmetingen. Gemiddelde snelheden, snelheidsfluctuaties, integrale lengteschalen en energiedissipaties zijn bepaald voor diverse locaties in het geroerde vat. Tussen de gemeten punten is met behulp van massa balansen en empirische correlaties geïnterpoleerd teneinde het stromingspatroon en het turbulente afschuifveld in het gehele vat vast te leggen.

De frequentie van botsingen tussen deeltjes wordt berekend met de verblijftijdsgemiddelde reksnelheid. Deze botsingsfrequentie wordt vervolgens gecorrigeerd met een botsingsefficiency die de invloed van de aantrekkende krachten en de hydrodynamische interactie tussen de deeltjes in rekening brengt. Uitgaande van een in de literatuur gegeven theoretische analyse betreffende stroomlijnen in en om poreuze aggregaten zijn efficiencies van botsingen tussen aggregaten afgeschat. Deze bleken veel groter te zijn dan de botsingsefficiencies voor massieve deeltjes.

Experimenteel is een toename van porositeit met aggregaatgrootte vastgesteld. Deze toename verklaart de versnelde groei van de aggregaten zoals waargenomen bij de coagulatie experimenten. Het porositeitsverloop met de aggregaatgrootte kan goed beschreven worden door aan de vlokstruktuur een fractale dimensie toe te kennen.

Ter beschrijving van het dynamisch gedrag van het coagulerende systeem in het geroerde vat is een coagulatiemodel opgesteld. Het model gaat uit van de resultaten van het genoemde simulatieprogramma, de berekende botsingsefficiencies voor poreuze aggregaten en van de informatie omtrent de structuur van de gevormde aggregaten. Met het coagulatiemodel worden de populatie balansen over de verschillende aggregaatgroottes simultaan opgelost en wordt het verloop van de aggregaatgrootte in de tijd berekend voor een ladingsgewijs coagulatie-experiment als functie van roerdertoerental, vaste stof-concentratie en concentratie van destabilisator.

Experimenteel is vastgesteld dat de coagulatiesnelheid vrijwel evenredig toeneemt met de gemiddelde reksnelheid in het roervat welke bepaald wordt door het toerental van de roerder. Tevens is gevonden dat de groeisnelheid evenredig toeneemt met de vaste stof-concentratie. Deze resultaten zijn in overeenstemming met de modelberekeningen.

De eindgrootte van de aggregaten neemt toe met de vaste stof-concentratie omdat hierbij de groeisnelheid van de aggregaten wordt vergroot terwijl de opbreeksnelheid constant blijft. Verhoging van het toerental van de roerder vergroot de afschuifspanning die op de aggregaten werkt en verlaagt de eindgrootte van de aggregaten volgens een machtwet waarvan de exponent afhangt van de fractale dimensie van de aggregaten. Uit de vergelijking van de resultaten van het coagulatie model met de experimentele resultaten blijkt dat met het coagulatiemodel kwantitatieve voorspellingen van de eindgrootte van de aggregaten als functie van vaste stof-concentratie en roerdertoerental gedaan kunnen worden. De variatie van de aggregaatgrootte met de destabilisator-concentratie kan goed beschreven worden indien de DLVO-theorie (Deryaguin, Landau, Verwey en Overbeek-theorie) opgenomen wordt in het coagulatie model.

De eindgrootte van de aggregaten blijkt niet afhankelijk te zijn van de grootte van het vat bij constante energietoevoer per eenheid van massa van de suspensie. Laser Doppler snelheidsmetingen toonden aan dat de energiedissipatie bij de roerdertip afneemt bij schaalvergroting, terwijl de energiedissipatie verdeling in de bulk van het vat toeneemt. Het netto effect van deze veranderingen is waarschijnlijk te klein om het coagulatie proces merkbaar te beinvloeden.

CONTENTS

CHAPTER I
INTRODUCTION

1.1. OBJECTIVES

Many solid products from the chemical industries are produced by precipitation from reactive solutions. Typical examples of these products are ceramics, catalysts, fine chemicals, pharmaceuticals, non-ferrous oxides and halides, etc. Precipitation involves a sequence of steps, ranging in size scale from the molecular to the macroscopic and comprising chemical reaction, nucleation, crystal growth and aggregation processes. The latter process wherein the particles stick together to form flocs, is thought to be highly decisive for the final size distribution and morphology of the solids, that determine the properties of both suspension and dried product. In particular, an understanding of the aggregation mechanism is of primary importance with regard to the behaviour, handling and treatment of suspension and product.

Apart from being part of precipitation processes, particle aggregation is used for systematic size enlargement of particles for example in polymerization processes and water purification and waste-water treatment processes. The solid particles that are to be separated from the liquid phase, are in the low or sub-micron range and they either remain in suspension or settle too slowly for economic sedimentation. Furthermore they are difficult to filter. Usually appreciable separation rates cannot be achieved unless individual primary particles are aggregated into larger units. Because Brownian (perikinetic) aggregation is usually insufficiently rapid for economic reasons, shear (orthokinetic) aggregation is generally employed in a stirred tank, where suspension and aggregation-promoting agent (destabilizer) are mixed.

The stirred tank is also frequently used as chemical reactor in precipitation processes where the different reactants are to be brought into contact. In stirred tanks in which turbulent conditions normally prevail, the flow patterns are complex and the shear field is far from uniform, thereby complicating adequate tests of theoretical predictions to be made. However, results from experimental studies in ideal systems with a nearly uniform shear

rate throughout the suspension like in a Couette type apparatus, are generally not directly applicable to a stirred tank. One reason for this may be the size and morphology of the aggregates being dependent upon the flow field in which they are produced.

In this study therefore the stirred tank has been selected for the purpose of practical application. The objective of this work is to gain insight into the effects of operating variables and the scale of operation on the final size distribution and morphology of the aggregates.

The present thesis follows up on earlier research conducted on aggregation in stirred tanks (De Boer 1987) and comprises the investigation of both aggregation and hydrodynamics in stirred tanks. The emphasis hereby lies on linking the heterogeneous turbulent shear field to the aggregation processes in stirred tanks.

1.2. PREVIEW

A review on theories concerning aggregation in turbulent flows is presented in chapter 2. Aggregation mechanisms are discussed and expressions relating the characteristics of a stationary homogeneous turbulent flow field to the kinetics of the aggregation process are presented together with their range of application. Subsequently the process of limited growth is addressed. The limited growth is shown to be most likely caused by the process of aggregate breakup. In order to model the aggregation process, a breakup criterion that describes the dependence of aggregate size on the turbulent energy dissipation rate, has to be formulated. The breakup criterion results from equating the stresses causing deaggregation to the mechanical aggregate strength. The mechanisms for breakup of aggregates are identified and their relative importance in determining the final aggregate size is evaluated. The mechanical strength depends on the structure of the aggregates. Models that are used to describe the cluster structure are reviewed. They are shown to give rise to different breakup criteria. Finally breakup kinetics in homogeneous turbulent flow are discussed.

Chapter 3 is concerned with the hydrodynamics in the stirred vessels wherein the aggregation process is studied. The measurement technique that has been used to characterize the turbulent flow field is discussed. The results show that the distribution of the turbulent energy dissipation rate is far from uniform in the stirred tanks. Furthermore measurements in geometrical similar vessels of three different sizes show that the distribution of energy dissipation rate is to some extent dependent on scale.

In chapter 4 the influence of the heterogeneity in the energy dissipation rate has been incorporated in modelling the aggregation process. The aggregation theories, as presented in chapter 2, are based on the assumption of homogeneous turbulence. In modelling the aggregation in the heterogeneous turbulent flow field in stirred tanks, these theories are only to be applied to local values of the energy dissipation rate.

Chapter 5 is dedicated to the growth of aggregates in stirred tanks. First the selection and preparation of the model suspension is described. Secondly a short discussion is devoted to the experimental technique used to characterize the size and porosity of the formed flocs in the aggregation experiments. Subsequently, the effect of the heterogeneous shear field on the initial stages of aggregation, where primary particles cluster into doublets, is examined. Existing theories about the collision efficiencies for encounters between mono sized spherical particles are evaluated. Finally, the kinetics of the following stages of the aggregation process are considered. The aggregates proved to be highly porous with their porosity increasing with the aggregate size. The implications of this increase of porosity with size on the kinetics of the aggregation process are discussed. With values derived for the collision efficiencies for encounters between porous particles the aggregate growth could be adequately described.

Chapter 6 is concerned with the final stages of aggregation. The dynamic equilibrium between growth and breakup of the aggregates that determines the final aggregate size, is shown not to be dependent on the initial conditions of the batch experiments. Knowledge of the size and porosity of the aggregates enabled us to define a breakup criterion that is needed in the description of

the dynamic behaviour of the particulate system. With this breakup criterion and with the results of chapter 4, the aggregation process is modelled. The evolution of the aggregate size as a function of impeller speed, solids concentration and destabilizer as predicted by the model is compared to experimental findings. Finally, the effects of up scaling are examined.

Chapter 7 combines the conclusions from the previous chapters into one uniform description of the aggregation process in stirred tanks. Furthermore the application of the presented model to describe the aggregation process in stirred tanks to experimental conditions other than those tested in this work and to particulate systems with different physical properties is discussed. Also suggestions for future areas of research are presented.

CHAPTER II
AGGREGATION THEORY

2.1. INTRODUCTION

Aggregation results when two or more particles collide and adhere. Except for very dense suspensions, simultaneous encounters between three or more particles can be ignored. In order that two particles aggregate, they must first be brought into close proximity by a transport mechanism. The transport mechanism gives rise to what is referred to as a "collision". The various transport mechanisms are presented in section 2.2. Whether or not the particles remain attached to each other after a collision is dependent on the net interparticle forces being attractive or repulsive. If the particles in the suspension tend to stick together upon approach, the suspension is said to be unstable. The theory concerning the stability of colloidal suspensions is treated in section 2.3.

In this research we confined ourselves to the aggregation in turbulent flows. Section 2.4 deals with those aspects of turbulence that are most relevant to the aggregation process. In the following sections several models for the prediction of collision frequencies are reported. These aggregation models do not set an upper limit to the growth of the aggregates, as has been observed experimentally. Theoretical aspects on the maximum aggregate size and its causes are therefore included in the final sections of this chapter.

2.2. TRANSPORT MECHANISMS

The mechanisms that can cause relative motion of the particles in the fluid are:
1. Brownian motion causing "perikinetic aggregation".
3. Motion of the particles with the fluid flow: spatial velocity variations in the fluid give particles different velocities and thus cause collisions. This type of aggregation is referred to as "orthokinetic aggregation".
4. Motion of the particles relative to the fluid flow due to the inertia of the particles

5. Motion of the particles relative to the fluid flow due to gravity

6. Brownian and fluid motion near the interface between the suspending medium and the surroundings (Heller and Peters, 1970). At the interface the colloidal particles aggregate due to their Brownian motion. If the colloidal particles adsorb preferentially at the interface, the suspension is locally concentrated and interfacial perikinetic aggregation proceeds at a higher speed than the Brownian aggregation in the bulk of the suspending medium. Surface renewal is accomplished by the fluid motion near the interface. Whether the interfacial Brownian aggregation or the surface renewal is rate controlling depends on their relative magnitudes.

If the particles are sub micron in size, Brownian motion is appreciable. However, as the particles grow larger, Brownian coagulation becomes less important and the other aggregation mechanisms take over. If particles are not preferentially adsorbed at the interface and/or the ratio of the surface to the volume of the suspension is small, the surface aggregation is also negligible.

2.3. COLLOIDAL STABILITY

Whether or not the particles stick together when they are brought into close range depends on the colloidal stability of the suspension. Colloid stability is governed by electrostatic and/or steric repulsion.

The electrostatic repulsion results from the surface charge the particles usually attain from dissociation of ionic surface groups or adsorption of ions from the suspending medium. Ions of opposite charge (counter ions) to that of the surface charge of the particles are attracted toward the surface while ions of like charge (co ions) are repelled from the surface. This attraction and repulsion, when combined with the random thermal motion of the ions, leads to the formation of an diffuse electric double layer. The thickness of the double layer is given by the Debye length $(1/\kappa)$:

$$\kappa = \left[\frac{e^2 \sum_i n_i z_i^2}{\varepsilon_r \varepsilon_0 k_B T} \right]^{1/2} \tag{2-1}$$

where n_i is the number of ions i per m^3 in the bulk of the suspension, e the elementary charge, z_i the valency of ion i, k_B is Boltzmann's constant, T is

the absolute temperature, ε_r is the relative dielectric constant of the suspending medium and ε_0 is the permittivity of vacuum.

Eq.(2-1) reduces in the case of a symmetrical electrolyte to

$$\kappa = \left[\frac{2 e^2 n z^2}{\varepsilon_r \varepsilon_0 k_B T} \right]^{1/2} \tag{2-2}$$

where n is the number of symmetrical electrolyte molecules per m^3 suspension. Due to the surface charge, the particles acquire a surface potential. This potential is the result of the charge density difference between the particle surface and the bulk of the fluid. Consequently, when two particles of the same charge approach each other, a repulsive force develops, owing to the potential energy interactions.

The energy of interaction of two charged equal sized spherical particles can be mathematically quantified using the Derjaguin, Landau, Verwey, Overbeek (DLVO) theory (Verwey and Overbeek 1948) if interaction between the particles occurs at constant surface potential. For low surface potential ψ_0 (< 25 mV), the potential energy of repulsion between two particles is (Lyklema 1968):

$$V_R = 2\pi \varepsilon_r \varepsilon_0 a_1 \psi_0^2 \ln(1 + \exp(-\kappa H)) \tag{2-3}$$

if H is the distance of separation between the two sphere surfaces (H = r - 2a$_1$ if r is the distance between the centres of the particles and a$_1$ the radius of the primary spherical particles).

A useful expression that is applied to somewhat higher potentials is:

$$V_R = \frac{64\pi n k_B T a_1}{\kappa^2} \gamma^2 \exp(-\kappa H) \tag{2-4}$$

where $\gamma = \tanh(ze\psi_0 / 4k_B T)$

For spherical particles with a high potential no analytical expression is available but a graphical representation is given in Verwey and Overbeek, 1948.

Eq.(2-3) and (2-4) are derived by treating the ions as point sources of charge. However, the ions in the solution (whether bare or hydrated) have a finite size and so are not able to get closer than a certain distance from the particle's surface. Therefore a charge-free region exists near the surface, which must be treated differently from the rest of the double layer. One way of handling this is to separate this charge-free zone from the diffuse double

layer by a hypothetical boundary as the Stern surface. The Stern surface is situated a distance δ from the actual surface. Outside the Stern surface, the double layer can still be described by eq.(2-3) and (2-4). The only modification of the analysis of the diffuse double layer required by the introduction of the Stern surface is that the potential at the Stern plane ψ_δ replaces ψ_0 as the inner boundary of the diffuse layer. The nearest practical approximation to ψ_δ is the electrokinetic or zeta potential ζ, the potential at the slipping plane which can be determined by electrophoresis.

Overbeek (1977) pointed out that the condition of constant charge is probably a better approximation than that of constant potential during interaction for most colloidal systems. Frens and Overbeek (1972) described a method of deriving the interaction energy at constant charge V_R^σ when that at constant potential V_R^ψ is given. For low ψ_δ (< 25 mV) the repulsion energy for constant surface charge on the approaching particles V_R^σ is given by:

$$V_R^\sigma = V_R^\psi - 2\pi \, \varepsilon_r \varepsilon_0 \, a_1 \, \psi_\delta^2 \, \ln(1 - \exp(-2\kappa H)) = - 2\pi \, \varepsilon_r \varepsilon_0 \, a_1 \, \psi_\delta^2 \, \ln(1 - \exp(-\kappa H))$$

(Wiese and Healy 1970)   (2-5)

Frens and Overbeek (1972) showed that for $\kappa H > 1$ the differences between V_R^σ and V_R^ψ become negligible small. For low ψ_δ this follows directly from comparing eq.(2-5) with eq.(2-3). As the repulsion is mainly governed by the outer part of the electrical double layer, the results of the DLVO theory are therefore not very different from the "constant charge" case.

In addition to a repulsion energy, also an energy of attraction V_A is developed between two interacting colloidal particles. This attraction is a consequence of van der Waals forces. The van der Waals attraction is of molecular origin and is presented for small separations between two spherical particles by:

$$V_A = - \frac{A_{1(2)} \, a_1}{12 \, H}$$

(2-6)

where $A_{1(2)}$ is the Hamaker constant describing the attraction between two particles 1 in a medium 2.

The summation of attractive and repulsive potential energies provides the net energy of interaction, which is shown for a stable colloid in figure 2.1. where the net interaction energy is plotted against the separation distance of two colloidal particles. A positive interaction energy at a certain separation

distance indicates that the repulsive forces are predominant, whereas a negative potential indicates that attractive forces are predominant. The potential energy maximum hinders the colliding particles to stick together into the primary minimum. The primary minimum corresponds to the minimum in the energy curve at the left hand side of the energy barrier. The secondary minimum which is also indicated in fig. 2.1 is for most cases not sufficiently deep to withstand redispersion of the particles by their Brownian motion or turbulent motion.
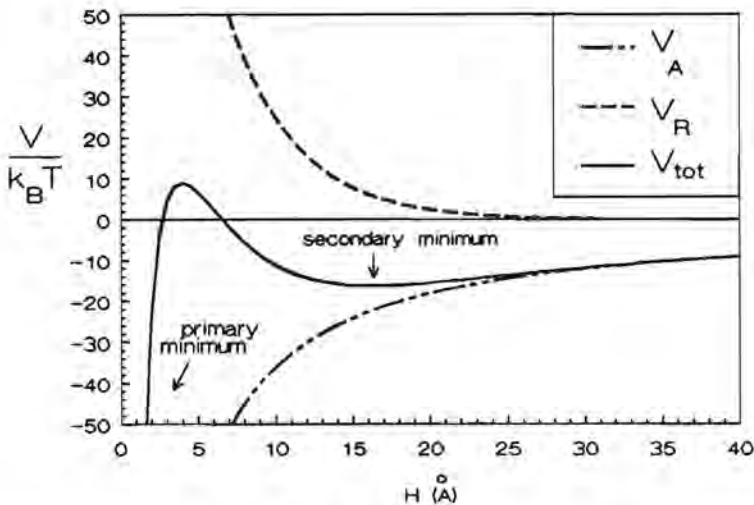
Figure 2.1. The net energy of interaction between two spherical particles, as a function of interparticle distance H.

The suspension can be destabilized by increasing the ionic strength of the suspending medium by adding salt or acid. In this way the electrostatic repulsion caused by the double layers around the charged particles is lowered and the energy maximum is lowered, thus enhancing the possibility of the particles to stick together by the action of Van der Waals attraction. The aggregation process of particles sticking together due to compression of the double layer by salt or acid is called coagulation.

Another way of destabilizing a suspension is by adding small amounts of long-chain polymer. The polymer absorbs onto the surface of the primary

particles and the polymer chains overlap the double layer. Bridges of polymer perform the linking between the particles. This aggregation process is called flocculation* (Tomi and Bagster 1978).

On the contrary adding large amounts of long-chain polymer stabilizes the colloidal system. The surface of the particles is now covered with polymer chains to such an extent that mutual approach is impossible due to steric hindrance. This hindrance results in steric stabilization of the suspension. Again a potential energy barrier needs to be overcome if the particles are to aggregate.

As we are primarily interested in aggregation as it occurs in precipitation and crystallization processes, we confined our study to the coagulation of particles.

2.4. COAGULATION KINETICS IN TURBULENT FLOW

2.4.1. INTRODUCTION

Aggregation mechanisms depend on the hydrodynamic regime in stirred tanks, that is mainly turbulent when low viscous Newtonian liquids are used. The turbulent flow consists of a continuum of eddies ranging in size from the dimensions of the turbulence generating device, i.e. the mechanical agitator, to the Kolmogorov micro scale, a term which will be defined later. Eddies of a scale approximating the size of the particles control the aggregation process. The eddy sizes in a turbulent flow can be separated into three groups:
1. energy containing eddies,
2. viscous subrange,
3. inertial subrange.

In section 2.4.2 these different eddy scales will be reviewed. In the sections 2.4.3 and 2.4.5 different kinetic equations are presented to describe aggregation processes within these different eddy size subranges. These kinetic expressions are based on the assumption of stationary homogeneous isotropic turbulence in which local statistical quantities (for example mean velocity and energy dissipation rates) are independent of position and

---

* *It should be noted that the term flocculation is also used to distinguish coagulation in the secondary minimum from coagulation in the primary minimum.*

direction. This is an idealized picture of the turbulent flow field in a stirred tank, as will become clear from the hydrodynamic study presented in chapter 3. The assumption of stationary homogeneous isotropic turbulence however leads to convenient expressions for the aggregation kinetics within the different eddy size subranges.

2.4.2. SCALES OF TURBULENCE

One of the characteristics of turbulent fluid motion is its randomness, both in space and time. The most useful approach to deal with turbulence is a statistical one, in which the instantaneous Cartesian fluid velocity components (U_1, U_2, U_3) at a point are represented by a mean and a fluctuating part $(\bar{U}_1 + u_1', \bar{U}_2 + u_2', \bar{U}_3 + u_3')$, the so-called Reynolds decomposition. The mean flow $\bar{U}_i$ is a time average:

$$\bar{U}_i = \lim_{t \to \infty} \frac{1}{t} \int_{t_0}^{t_0 + t} U_i \, dt' \tag{2-7}$$

In a homogeneous flow, the time average $\bar{U}_i$ is independent of position and resembles the spatial average of U_i.

The mean value of the velocity fluctuations is zero by definition, whereas the root-mean-square (rms) velocity fluctuation (u_i) represents the spread of the velocity distribution:

$$u_i^2 = \overline{(u_i')^2} = \lim_{t \to \infty} \frac{1}{t} \int_{t_0}^{t_0 + t} u_i'^2 \, dt' \tag{2-8}$$

The turbulent kinetic energy k per unit mass contains the contributions from the three directions in space:

$$k = \frac{1}{2} (u_1^2 + u_2^2 + u_3^2) = \frac{3}{2} u^2 \tag{2-9}$$

If the turbulent flow is isotropic, there is no preference for any specific direction and $u_1 = u_2 = u_3 = u$. Even if the large-scale structure of the actual turbulence is anisotropic, the rms fluctuating velocity averaged over the 3 directions in space, i.e., u as defined by eq.(2-9) can still be used as

a first approximation for the intensity of the turbulence fluctuations.

Another quantity of importance is the two point velocity correlation function. Consider, for example, the velocities u_i' and u_j' in the x_i and x_j direction respectively. If r_k denotes the displacement in the x_k direction, the two-point correlation function is defined as:

$$R_{ij}(r_k) = \frac{\overline{u_i'(x)\, u_j'(x+r_k)}}{u_i \, u_j} \tag{2-10}$$

If $i = j = k$, this function is called the longitudinal velocity correlation $f(r)$. The lateral velocity correlation function $g(r)$ represents the two point correlation function of the velocity fluctuations normal to the vector separation r, i.e. $i = j$ and $k \neq i$.
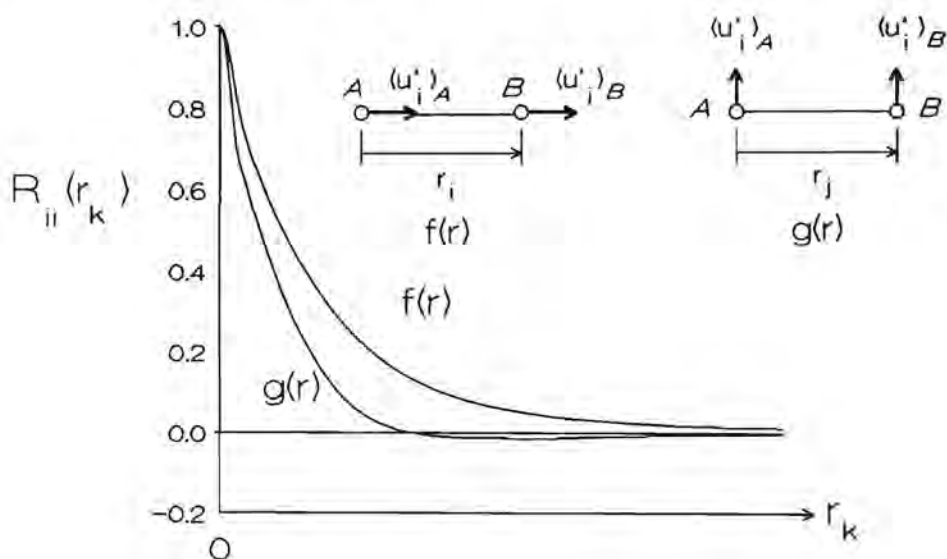
Figure 2.2. Longitudinal and lateral velocity correlations.

If $R_{ij}(r_k) = \pm 1$, the correlation is said to be perfect. If $R_{ij}(r_k) = 0$, u_i' and u_j' are uncorrelated. If the two points in the fluid are close together, the velocities of the turbulent fluid at these points are closely related. As $r_k \to 0$, the two points coincide and $R_{ij}(0) = 1$. As r_k gets large, the velocities become independent from each other so $R_{ij} \to 0$.

The turbulence eddies may be considered for present purposes as components of the fluid motion which are characterized by different velocities $\Delta u(r)$ and by the distances over which these velocities change significantly (the scale of eddy motion). The eddy velocity $\Delta u(r)$ is given by the rms velocity difference of the fluid flow over the corresponding eddy scale r:

$$\Delta u(r) = \left[\overline{\{u_i'(x) - u_i'(x+r_i)\}^2} \right]^{1/2} = u_i \left[2 \{ 1 - f(r) \} \right]^{1/2} \qquad (2\text{-}11)$$

Expressions for the rms velocity difference $\Delta u(r)$ in subsequently the macro, viscous and inertial subrange of eddy sizes are presented in the following sections. These expressions are then used in formulating kinetic equations for collision rates in the different eddy size regimes.

Energy containing eddies

The energy containing eddies in a stirred vessel are generated by the impeller and their length scale L, sometimes referred to as the Eulerian* macro scale of the turbulent flow, is expected to be roughly the same order as the size of the impeller blades. The velocity correlation is lost over the size of these large scale eddies, i.e. $f(L) = 0$ and the velocity scale of the energy containing eddies is therefore equal to $\sqrt{2}$ times the rms velocity u.

The impeller provides these large scale eddies with a certain amount of turbulent kinetic energy per unit mass k. For the energy containing eddies, the Reynolds number that corresponds to the eddy scale $Re_L = \Delta u(L) L/\nu \cong uL/\nu$, is very large. Therefore in fluid motion with a scale $r \cong L$, viscous forces actually have no effect. The large scale eddies lose a negligible fraction of their energy to direct viscous dissipation. They, however, produce smaller eddies, for which the Reynolds number rapidly decreases with decreasing r. At a certain value of $r = \eta$ the Reynolds number for the corresponding motion Re_η is approximately unity. This means that in the region of η viscous forces begin to have a noticeable effect on the motion of the fluid. Eddy motion of scale η is accompanied by dissipation of energy. This energy is continually withdrawn by the small scale motion from the large scale motion, so that one

* *The adjective "Eulerian" is used whenever correlations in a fixed frame of reference are considered, as for example with the two point correlation or with a time correlation in one fixed point. In contrast the adjective "Lagrangian" refers to moving points ("fluid particles").*

may visualize the existence of a continuous transfer of energy from large scale eddies to eddies progressively smaller in scale, until in eddies with scale on the order of η, it is converted into heat. Thus although turbulent motion occurs only at relatively high Reynolds numbers Re_L, it is accompanied by considerable dissipation of energy. The rate of energy transfer to the small-scale eddies is thought to be proportional to the amount of kinetic energy $k \sim u^2$ divided by the time scale of the large eddies $L/\Delta u(L) \approx L/u$. This energy is dissipated at a rate ε, which should be equal to the supply rate. Hence (Taylor 1935)

$$\varepsilon \sim \frac{u^3}{L} \tag{2-12}$$

which states that viscous dissipation of energy can be estimated from the large scale dynamics, which do not involve viscosity.

Eq. (2-12) provides an estimate for the rms velocity fluctuations in the flow field, if ε and L are known:

$$\Delta u(r) = (2)^{1/2} u \sim (2)^{1/2} (\varepsilon L)^{1/3} \tag{2-13}$$

Viscous subrange

As mentioned earlier, dissipation of turbulent energy by viscous effects increases as the size of the eddy decreases, up to a maximum for the smallest eddies. The parameters determining the smallest scale of motion are the dissipation rate per unit mass ε and the kinematic viscosity ν. With these parameters, one can form length, time and velocity scales as follows:

$$\eta = (\nu^3/\varepsilon)^{1/4} \tag{2-14}$$
$$\tau_K = (\nu/\varepsilon)^{1/2} \tag{2-15}$$
$$v_K = (\nu\varepsilon)^{1/4} \tag{2-16}$$

These scales are referred to as the Kolmogorov micro scales of length, time and velocity. The Reynolds number formed with η and v_K is equal to one:

$$\eta v_K / \nu = 1 \tag{2-17}$$

which illustrates that the small-scale motion is strongly affected by viscosity. Within the smallest eddies there is approximately uniform strain. The rms strain rate s_{ii} is:

$$s_{ii} = [\overline{(\partial u_i/\partial x_i)^2}]^{1/2} \cong \frac{v_K}{\eta} = (\varepsilon/\nu)^{1/2}. \tag{2-18}$$

The rms velocity difference between two points within the smallest eddies is therefore equal to:

$$\Delta u(r) = s_{ij} \, r \cong (\varepsilon/\nu)^{1/2} \, r \tag{2-19}$$

A quantitative estimate was made by Taylor (1935) by assuming isotropic turbulence:

$$\Delta u(r) = (1/15)^{1/2} \, (\varepsilon/\nu)^{1/2} \, r \tag{2-20}$$

Although the large-scale motion in a turbulent flow is always anisotropic, the above equation can be used provided the Reynolds number Re_L is large enough. In that case the small eddies have very small time scales compared to the time scale of the large scale energy containing eddies. The time scale of the small eddies is given by eq.(2-15) whereas the time scale of the large scale eddies may be approximated by $L/\Delta u(L)$. The ratio of these time scales is with the use of eq. (2-13) and $Re_L = \Delta u \, L/\nu$ given by:

$$\frac{\tau_K}{(L/\Delta u)} = \frac{(\nu/\varepsilon)^{1/2}}{(L/\Delta u)} \sim \frac{(\nu L /(\Delta u^3))^{1/2}}{(L/\Delta u)} = Re_L^{-1/2} \tag{2-21}$$

which approaches zero as $Re_L \to \infty$.

This suggests that there is very little interaction between the small scale fluctuations and the large scale motion. The small-scale structure tends to be independent of any orientation effects introduced by the mean flow, so that all properties relating to the small eddies may be expected to be isotropic on the average. This local isotropy ensures the validity of eq.(2-20).

Inertial subrange

The inertial subrange is the range of eddies intermediate in size between the large-scale eddies of the system and Kolmogorov's micro scale. Kolmogorov (1941) has postulated that the fluid motion in this range is independent of both viscosity and the large scale structure of turbulence for large Reynolds numbers. These eddies of intermediate size merely transfer the kinetic energy of the large scale eddies to the small scale eddies and are therefore only governed by the energy transfer rate, i.e., ε. From dimensional reasoning it follows that:

$$\Delta u(r) = C \, (\varepsilon r)^{1/3} \tag{2-22}$$

Experimental data indicate that $C \cong 1.37$ approximately (Rotta 1972).

Table 2.1 summarizes the various eddy subranges and the corresponding spectral laws for the differential velocity fluctuations.

The overlap between the viscous and inertial subrange, which is referred to as the transition subrange, has been numerically evaluated by Obuchov and Jaglom (1958), and can be approximated by (Liepe 1988):

$$\Delta u(r) = .47 \; \varepsilon^{5/12} \; r^{2/3} \; / \; \nu^{1/4} \tag{2-23}$$

This expression is also included in table 2.1.

Table 2.1. Eddy subranges with corresponding expressions for the differential velocity fluctuations

subrange	eddy size r	$\Delta u(r)$
viscous	$6\eta \;\; < r$	$(1/15)^{1/2} \; (\varepsilon/\nu)^{1/2} \; r$
transition	$6\eta \;\; \leq r < 25\eta$	$.47 \; \varepsilon^{5/12} \; r^{2/3} \; / \; \nu^{1/4}$
inertial	$25\eta \;\; \leq r < L \, / \, 2$	$1.37 \; (\varepsilon r)^{1/3}$
macro	$L \, / \, 2 \leq r \sim L$	$(2)^{1/2} \; (\varepsilon L)^{1/3}$

In fig. 2.3 $\Delta u(r)/(\varepsilon \nu)^{1/4}$ is plotted versus the distance between the two points of interest relative to the Kolmogorov micro scale for three values of Re_L. From fig. 2.3 it follows that it is acceptable to leave out the expression for the transition region and to use expression (2-20) for values of r up to $10 \cdot \eta$. Beyond that value expression (2-22) is approximately applicable.

Fig. 2.3 shows that only for large Reynolds numbers $Re_L > \sim 5000$, there exists an inertial subrange of eddies for which both viscous dissipation and the large scale structure of the turbulence are unimportant. The large Reynolds numbers that are necessary for the existence of an inertial subrange, make such a regime doubtful in practice. Nevertheless the assumption is sometimes made in order to derive convenient analytical equations to describe to the behaviour of particles comparable in size with eddies between the viscous and macro subranges.
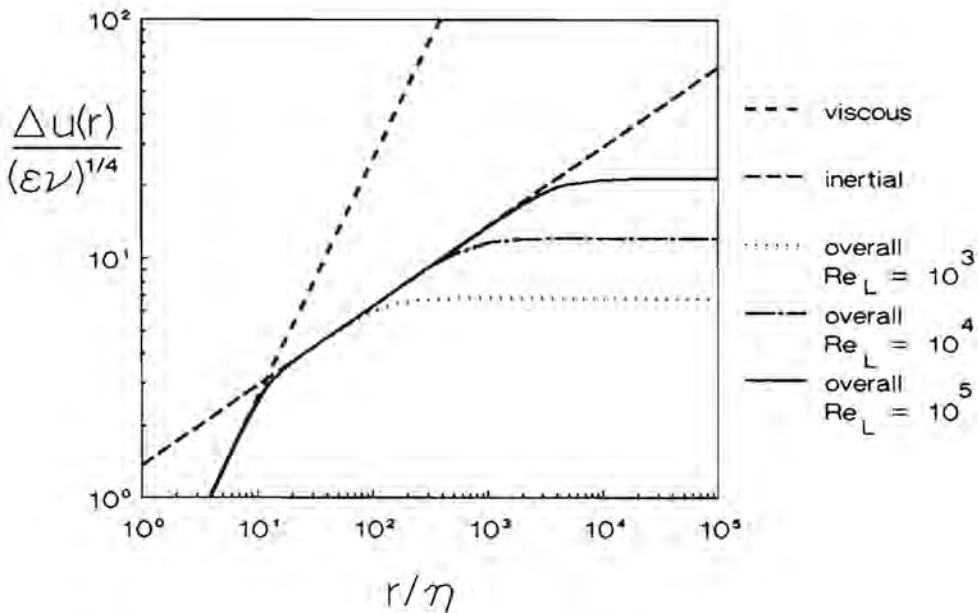
Figure 2-3. rms velocity difference between two points in the fluid versus the distance of separation

The rms velocity difference $\Delta u(r)$ denotes the spatial velocity variation in the fluid that gives rise to different particle velocities and hence induces collisions between the particles. The various expressions for $\Delta u(r)$ are very useful in formulating equations for orthokinetic collision frequencies in the different eddy size regimes, as will be shown in the next section.

2.4.3. PARTICLE ENCOUNTERS IN TURBULENT FLOW

There are two ways in which turbulence causes collisions between neighbouring particles. Firstly, there are the spatial variations of turbulent velocity, which bring the particles in contact. Secondly, each particle is moving relative to the fluid surrounding it, owing to the inertia of a particle being different from that of an equal volume of fluid. First the collisions induced by the fluid flow are considered. Later on the effects of inertia of the particles are taken into account.

Orthokinetic turbulent coagulation

In this section we follow the approach of Saffman and Turner (1956) to compute the collision frequency between particles with radii a_i and a_j that are assumed to move with the fluid. Particle i is taken as the reference particle whose center is at the origin of the radius R of the collision envelope. The collision radius R is taken as the sum of the two radii a_i and a_j.

If the distortion of the flow field due to the presence of the particles and the interparticle forces are neglected, the collision rate per unit volume J^0_{ij} is given by the number of particles j flowing into the collision sphere multiplied by the number concentration of particles i:

$$J^0_{ij} = -n_i n_j \int_{\Delta u'(R)<0} \overline{\Delta u'(R)} \ dS \qquad (2\text{-}24)$$

where n_i = number concentration of particles of size a_j

$\Delta u'(R)$ = the momentary radial component of the relative fluctuating fluid velocity between two points separated by a distance $r = R$

S = the surface of the collision sphere with radius R.

The surface integral is confined to inward directed fluid flow ($\Delta u'(R) < 0$) through the collision sphere surface at $r = R$. To evaluate the integral, we note that the continuity of the fluid demands the inward and outward flow to be equal:

$$\int_{\Delta u'(R)<0} \Delta u'(R) \ dS + \int_{\Delta u'(R)>0} \Delta u'(R) \ dS = 0 \qquad (2\text{-}25)$$

Hence, the integral in eq.(1-24) becomes:

$$\int_{\Delta u'(R)<0} \overline{\Delta u'(R)} \ dS = 1/2 \int_{r=R} \overline{|\Delta u'(r)|} \ dS = 1/2 \int_{r=R} \overline{|\Delta u'(r)|} \ dS \qquad (2\text{-}26)$$

where the averaging is performed over all particles i in the homogeneous turbulent flow field.

In the case of isotropic turbulent flow the third integral in eq.(2-26) is

$$1/2 \int_{r=R} \overline{|\Delta u'(R)|} \ dS = 2\pi \ (a_i + a_j)^2 \ \overline{|\Delta u'(R)|} \qquad (2\text{-}27)$$

If the relative velocity $\Delta u'(R)$ is assumed to be Gaussian distributed (Townsend 1947, Kuboi et al. 1972), it follows that

$$\overline{|\Delta u'(R)|} = \left[\frac{2}{\pi}\right]^{1/2} \Delta u(R) \tag{2-28}$$

Combining equations (2-28), (2-27), (2-26) and (2-24) gives the collision rate,

$$J^0_{ij} = (8\pi)^{1/2} (a_i + a_j)^2 n_i n_j \Delta u(a_i + a_j) \tag{2-29}$$

Substituting the relations for $\Delta u(r)$ from table 2.1 with $r = R$ in eq.(2-29) gives the collision frequencies per unit volume corresponding to the various eddy size subranges. These collision rate expressions are tabulated in table 2.2.

Table 2.2. Eddy subranges with corresponding expressions for the orthokinetic collision frequency

subrange	eddy size r	$J^0_{ij} / n_i n_j$
viscous	$6\eta < r$	$1.29 \, (\varepsilon/\nu)^{1/2} \, (a_i + a_j)^3$
transition	$6\eta \le r < 25\eta$	$2.36 \, \varepsilon^{5/12}/ \nu^{1/4} \, (a_i + a_j)^{8/3}$
inertial	$25\eta \le r < L / 2$	$6.87 \, \varepsilon^{1/3} \, (a_i + a_j)^{7/3}$
macro	$L / 2 \le r \sim L$	$7.09 \, (\varepsilon L)^{1/3} \, (a_i + a_j)^2$

Camp and Stein (1943) obtained a result for the viscous subrange similar to the above mentioned more rigorous equation derived by Saffman and Turner(1956) by substitution of $(\varepsilon/\nu)^{1/2}$ for the shear rate γ in the so-called Von Smoluchowski equation. The Von Smoluchowski (1917) expression for the collision frequency per unit volume of two particles with radii a_i and a_j was derived for coagulation in simple shear flow for which the undisturbed velocity of fluid is given by $U = (\overline{U}_1, 0, 0)$ with $\overline{U}_1 = \gamma y$ and is given by:

$$J^S_{ij} = 4/3 \, (a_i + a_j)^3 \, \gamma \, n_i n_j \tag{2-30}$$

Substituting $\gamma = (\epsilon/\nu)^{1/2}$ into eq.(2-31) gives an equation for the orthokinetic coagulation in the smallest eddies with the numerical constant $4/3 = 1.33$ instead of 1.29 of Saffman and Turner's more rigorous solution.

Additional inertial effects in particle encounters

We also have to consider the collisions brought about by the inertia of the particles. The fluid velocity difference $\Delta u(R)$ is now replaced by the rms difference between the velocities of the two colliding particles $\Delta w(R)$ in eq.(2-30) (Williams and Crane, 1983):

$$J^0_{ij} = (8\pi)^{1/2} R^2 n_i n_j \Delta w(R) \qquad (2\text{-}31)$$

$\Delta w(R)$ comprises the difference between the particle velocities due to the spatial fluid velocity variation over the distance $R = a_i + a_j$ as well as the difference due to the inertia of the particles.

In order to derive eq.(2-31) isotropy is assumed in the relative velocity of the particles. This implies that the acceleration of the particles by gravity, which solely influences the motion in vertical direction, is negligible with respect to the acceleration of the particles by the isotropic fluid flow. This assumption will be shown to be valid for the usual experimental conditions in a stirred tank.

In the following paragraphs expressions for $\Delta w(R)$ are derived for subsequently the viscous and macro subrange.

Inertial effects in the viscous subrange

In the viscous subrange the rms velocity difference $\Delta w(R)$ is given by (Saffman and Turner (1956)):

$$\Delta w(R) = \left[\overline{(q_i - q_j)^2/ 3 + \Delta u(R)^2} \right]^{1/2} \qquad (2\text{-}32)$$

where q_i = the relative velocity vector between particle i and its surrounding fluid.

This equation is valid since $\Delta u(R)$ is statistically independent of q_i and q_j.

To calculate the variance of $q_i - q_j$, we need to know the correlation

coefficient C_{ij} between q_i and q_j and the mean square velocities $\overline{q_i^2}$ and $\overline{q_j^2}$ of particle i and j respectively:

$$\overline{(q_i - q_j)^2} = \overline{q_i^2} - 2\overline{q_iq_j} + \overline{q_j^2} = \overline{q_i^2} - 2 C_{ij}\left[\overline{q_i^2}\ \overline{q_j^2}\right]^{1/2} + \overline{q_j^2} \qquad (2\text{-}33)$$

C_{ij} is equal to unity since the particles experience the same value of fluid acceleration within the smallest eddies.

To calculate the mean square velocity $\overline{q_i^2}$, we have to solve the equation of motion of a particle as presented by Tchen(1947). Omitting the Basset "history" term, this equation is given by:

$$\frac{dq}{dt} + \frac{q}{\tau_p} = \left[\frac{2(\rho_p - \rho)}{2\rho_p + \rho}\right]\left[\frac{du}{dt} + g\right] \qquad (2\text{-}34)$$

where τ_p = the relaxation time of the particle = $(2\rho_p + \rho)\ a^2/(9\mu)$ for small particles obeying Stokes' law, i.e. the particle Reynolds number

$$Re_p = |\ U - U_p|_{rms}\ d_p\ /\ v \leq 1,$$

g = the accelereration vector due to gravity

The relaxation time is the time associated with the response of the particle to the applied fluid drag. It can be defined as the time of the particle to slow down to U_0 / exp(1.0) if the particle is projected into a still fluid at velocity U_0.

In order to evaluate the relative magnitude of the two terms on the right hand side of eq.(2-34) we have to consider the ratio between the relaxation time τ_p of the particles and the time scale τ_K of the smallest eddies, that is given by eq.(2-15). The ratio of these two time scales is:

$$\frac{\tau_P}{\tau_K} = \frac{2\rho_p + \rho}{36\rho}\left[\frac{2\ a}{\eta}\right]^2 \qquad (2\text{-}35)$$

For solid particles ρ_p ranges mainly from 1000 to 4000 kgm^{-3}. The density of liquids differs in most cases not much from the density of water, i.e. 1000 kgm^{-3}. Substituting these values for the densities of solid and liquid in eq.(2-35) it can be easily seen that the relaxation time is smaller than the Kolmogorov time scale in liquid suspensions if the particles are smaller than the Kolmogorov micro scale. It should be noted that this is not the case with gaseous systems.

With τ_p small compared with the time scale of the smallest eddies the first term on the left-hand side of eq.(2-34) can be neglected. Hence we obtain for the mean square velocity difference between particle and fluid:

$$\overline{q^2} = \tau_p^2 \left[\frac{2(\rho_p - \rho)}{2\rho_p + \rho} \right]^2 \left[\overline{(\frac{d\mathbf{u}}{dt})^2 + \mathbf{g}^2} \right] \tag{2-36}$$

Because the particles follow the fluid flow almost completely,

$$\overline{(\frac{d\mathbf{u}}{dt})^2} = \overline{(\frac{D\mathbf{u}}{Dt})^2} = 3 \overline{(\frac{D\mathbf{u'}}{Dt})^2} \tag{2-37}$$

where $\overline{(\frac{D\mathbf{u'}}{Dt})^2}$ denotes the mean square acceleration of a fluid particle, that is given by (Hinze 1975a):

$$\overline{(\frac{D\mathbf{u'}}{Dt})^2} = 1.16 \ \varepsilon^{3/2} \ \nu^{-1/2} \tag{2-38}$$

With e.g. $\varepsilon \sim 1$ W/kg in a stirred tank and $\nu \sim 10^{-6}$ m^{2}s^{-1} for aqueous suspensions $3\overline{(\frac{D\mathbf{u'}}{Dt})^2}$ becomes $\sim 3 \ 10^3$ m^{2}s^{-1} and this is much larger than the acceleration due to gravity. The acceleration due to gravity can therefore be neglected. This validates our previous assumption of isotropy in the relative velocity between the particles in the derivation of eq.(2-32).

Combining equations (2-38), (2-37), (2-36), (2-33) and (2-32) yields the following expression for the collision rate in the viscous subrange which comprises both the collisions due to the inertia of the particles (first term between brackets) and the collisions brought about by the fluid flow (second term between brackets):

$$J^0_{ij} = (8\pi)^{1/2} \ R^2 \ n_i n_j \left[1.16 \left[\frac{2(\rho_p - \rho)}{2\rho_p + \rho} \right]^2 (\tau_{pi} - \tau_{pj})^2 \ \nu^{-1/2} \ \varepsilon^{3/2} \right.$$

$$\left. + \frac{1}{15} \ R^2 \ \frac{\varepsilon}{\nu} \right]^{1/2} \tag{2-39}$$

In deriving this equation we assumed the densities of the two colliding particles to be equal, i.e. $\rho_{pi} = \rho_{pj} = \rho_p$. With collisions between aggregates of different sizes this may not be the case because of variations in porosity, but the assumption of equal particle densities enables us to evaluate the relative importance of the collisions brought about by the different inertia of the particles and those brought about by the fluid flow more easily.

The first term between the brackets on the right-hand side of eq.(2-39) is zero when τ_{pi} and τ_{pj} are zero or equal, or when $\rho_p = \rho$. The ratio of the first term to the second in eq. (2-39) is:

$$10.4 \left[\frac{2(\rho_p - \rho)}{2\rho_p + \rho} \right]^2 (\nu\varepsilon)^{1/2} (\tau_{pi} - \tau_{pj})^2 / R^2 =$$

$$0.516 \left[\frac{2(\rho_p - \rho)}{2\rho_p + \rho} \right]^2 (\varepsilon/\mu^3\rho)^{1/2} a_i^2 (1 - \lambda^2) \tag{2-40}$$

where $\lambda = a_j / a_i$ and $a_i \geq a_j$.
With $\lambda = 0$, this ratio is equal to and larger than unity if:

$$2a_i / \eta \geq 2.16 \left(\frac{\rho}{\rho_p - \rho} \right) \tag{2-41}$$

Hence we can conclude that with liquid suspensions, the particles have to be at least of the size of the Kolmogorov micro scale η, for the collisions due to the inertia to become important relative to those caused by differences in the velocities in the fluid flow. In liquid suspensions the collision rate between particles that are smaller than the Kolmogorov micro scale, can therefore be obtained from the equation that only takes into account the collisions brought about by the fluid flow.

Inertial effects in macro subrange

If the particles become of the size of the large-scale eddies, the colliding particles may be assigned independent random velocities since they acquire momentum from different independently moving eddies (Abrahamson 1975). If isotropy is assumed on the scale of the collision process, the particle velocities also have independent directions. Based upon these assumptions and in the absence of gravitational and centrifugal accelerations, the relative velocity between the colliding particles $\Delta w(R)$ is given by the vector summation of the independent particle fluctuating velocities w_i and w_j, i.e., $\Delta w(R) = \sqrt{(w_i^2 + w_j^2)}$ and eq.(2-32) reduces to:

$$J_{ij}^0 = (8\pi)^{1/2} R^2 n_i n_j \sqrt{(w_i^2 + w_j^2)} \tag{2-42}$$

The particle fluctuating velocity can be obtained by solving the Tchen equation (2-34) for the case that the relaxation time of the particles is larger than the time scale of the smallest eddies. Now, the first term on the left-hand side of eq.(2-34) cannot be ignored. Levins and Glastonbury (1972) solved this equation by assuming an exponential form for the Lagrangian "fluid particle" autocorrelation $R_L(\tau)$, i.e.,

$$R_L(\tau) = \exp(- \tau / T_L) \tag{2-43}$$

This exponential function does also include the inertial subrange as has been shown by Hinze (1975b). The Lagrangian time scale T_L is related to the Eulerian longitudinal integral length scale:

$$T_L = L_L / u = \beta L_f / u \tag{2-44}$$

where L_L = Lagrangian length scale

L_f = Eulerian longitudinal length scale = $\int_0^\infty f(r) \, dr$, where $f(r)$ is the longitudinal velocity correlation function.

According to Hinze (1975c): $\beta \cong 0.4$

Furthermore Tennekes and Lumley (1989) showed that in isotropic homogeneous turbulence, $L_f = L/2$. Hence,

$$T_L = 0.2 \, L / u \tag{2-45}$$

If an exponential function for the Lagrangian correlation is assumed, then the particle fluctuating velocity w and the relative velocity q between particle and fluid flow are given by:

$$\frac{w^2}{u^2} = \frac{a \, T_L + b^2}{a \, T_L + 1} \tag{2-46}$$

and,

$$\frac{q^2}{u^2} = \frac{(1 - b)^2}{a \, T_L + 1} \tag{2-47}$$

where $a = \dfrac{3\rho \, C_D \mid U - U_p \mid_{rms}}{4 \, (2\rho_p + \rho) \, a}$ (Schwartzberg and Treybal 1968)

q = rms velocity difference between fluid and particle

C_D = turbulent drag coefficient

$b = (3\rho \, /(2\rho_p + \rho))$

T_L = Lagrangian time scale

The rms fluid fluctuating velocity u is approximately equal to $(\varepsilon L)^{1/3}$ (see eq.(2-12) in section 2.4.2).

The parameter a reduces to $1/\tau_p$ if Stokes' law is applicable, i.e. the particle Reynolds number $Re_p = |\ U - U_p|_{rms}\ d_p\ /\ v \leq 1$. For Stokes' law to be applicable with particles of the size of the large scale eddies, the density difference between the particles and the liquid has to be sufficiently small. This may be the case for highly porous aggregates. With parameter a equal to $1/\tau_p$ eq.(2-46) becomes an explicit formula relating the particle fluctuating velocity directly to the rms velocity fluctuation of the fluid if the Lagrangian integral time scale is known. Substitution of eq.(2-46) into eq.(2-42) renders the collision frequency for particles in the macro subrange of turbulence. It should, however, be noted that the equations (2-46) and (2-47) are only approximate for particle densities of the order of the fluid density. This is because eq.(2-34) is obtained by omitting the Basset term from the equation of motion of a particle in fluid flow. With the particle density close to that of the fluid this is only valid when the particle closely follows the fluid flow (Hjelmfelt and Mokros 1966), i.e. when the particles are smaller than the Kolmogorov micro scale. Collision frequency expressions of large particles in liquid suspensions derived by substitution of eq.(2-46) in eq.(2-42) should therefore only be used as first approximations.

According to Kuboi et al.(1974), the particle fluctuating velocity w should also be corrected for the fact that the particles can only respond to eddies equal or larger than their diameter. When one considers the motion of a particle, the contribution of eddies less than its size has to be omitted and the effective turbulent fluid velocity u(d) is given by:

$$u^2(d) = \frac{2}{3} \int_0^{k_d} E(k)\ dk \tag{2-48}$$

where E(k) is the three dimensional wave number power spectrum (Tennekes and Lumley 1972) and k_d represents the wave number corresponding to eddy size d. If we approximate in analogy with Tennekes and Lumley (1972) E(k) by $1.5 \cdot u^2\ L \cdot (kL)^{-5/3}$ between a wave number $k_0 L = \left(\frac{3}{2}\right)^{3/2}$ and a wavenumber $k\eta = 1$, and put E(k) equal to zero outside that range, u(d) is given by:

$$u^2(d) = u\ (1 - (k_d\ L)^{-2/3})^{1/2} \cong u\ (1 - (d\ /\ L)^{2/3})^{1/2} \tag{2-49}$$

From the experimental data presented by Kuboi et al. (1974) we may conclude that replacement of u in eq.(2-46) by u(d) as given by eq.(2-49) yields a reasonable estimate of this so-called filtering effect.

Inertial subrange

For the intermediate case where the approach velocities of the particles are neither well correlated nor completely independent, we can start again from eqs. (2-33) and (2-34) wherein the relative velocities q_i and q_j are now obtained from eq.(2-48). The problem is however to estimate the correlation coefficient C_{ij} between q_i and q_j. An expression for C_{ij} has been presented by Williams and Crane (1983) for particles in turbulent gas flows but at present no analytic expression for C_{ij} for particles in liquid turbulent suspensions is available.

For almost neutrally buoyant particles however it has been found that the collision frequency may be computed from the orthokinetic expression for the inertial subrange (Kuboi et al. 1972).

Conclusions

In liquid suspensions the inertia of the particles hardly contribute to additional collisions in the viscous subrange of turbulence. Hence the collision rate may be estimated by:

$$J^0_{ij} = 1.294 \ (\varepsilon/\nu)^{1/2} \ (a_i + a_j)^3 \ n_i \ n_j \tag{2-50}$$

In the inertial subrange the collision rate for almost neutrally buoyant particles ($\rho_p \cong \rho$) may be approximated by the orthokinetic equation:

$$J^0_{ij} = 6.87 \ \varepsilon^{1/3} \ (a_i + a_j)^{7/3} n_i n_j \tag{2-51}$$

In the macro subrange the collision frequency reduces to:

$$J^0_{ij} = 5.01 \ (a_i + a_j)^2 \ n_i \ n_j \ \sqrt{(w_i^2 + w_j^2)} \tag{2-52}$$

where w_i for a neutrally buoyant particle may be estimated by eq.(2-49):
$w_i = u(d_i) \cong (\varepsilon L)^{1/3} \ (\ 1 - (\ d_i \ / \ L \ )^{2/3} \ )^{1/2}$

2.4.4. HYDRODYNAMIC INTERACTION IN TURBULENT ENCOUNTERS OF SMALL PARTICLES

In the previous analyses it was assumed that the trajectories of the colliding particles are not modified by the interparticle forces. This is probably true for collisions in which the effect of the inertia of particles is predominant, but it is unlikely to be the case for the collisions between smaller particles which follow the fluid flow. For suspended particles in water the interparticle forces include the attractive Van der Waals force, the repulsive double layer force and a repulsive hydrodynamic force. The latter arises mainly from the distortion of the fluid flow due to the presence of the particles. When the particles come close together they will not pursue their approach along rectilinear paths as was assumed in the previous sections. In addition to the preceding effect particle j does not follow the curvilinear streamlines around reference particle i because of the pressure built up in the liquid film that is being expelled upon mutual approach. The hydrodynamic interaction tends to inhibit encounters between particle pairs. The orthokinetic collision efficiency (also called the coagulation efficiency), which is defined as the ratio of the true collision frequency and the one calculated when disregarding the interparticle forces is then less than unity. On the other hand, in the case of complete destabilization, with concentration of destabilizer above the critical coagulation concentration, the summation of the electrostatic repulsion and Van der Waals forces results in attraction, so the resulting force will enhance the collision efficiency.

At present no rigorous analysis accounting for hydrodynamic interactions between particles in turbulent orthokinetic encounters has been carried out. However, since the collisions between small particles in the smallest eddies can be considered as collisions in a simple shear flow, multiplying equation (2-50) by the collision efficiency computed for simple shear with $\gamma = (\varepsilon/\nu)^{1/2}$ suggests a first approximation for the turbulent situation.

The collision efficiencies for spherical particles in simple shear flow can be derived from calculations of the relative particle trajectories. Both Adler (1981) and Higashitani (1982) presented computations of the collision frequency in simple shear flow as a function of the shear rate in the form of the parameter $N_s = 6\pi\mu (a_i + a_j)^3 \gamma / A_{1(2)}$ and the ratio of particle sizes

$\lambda = a_j / a_i$. In the absence of double layer forces the orthokinetic efficiency was found to decrease with increase of N_s. Furthermore coagulation between equally sized particles (homocoagulation) turned out to be more favourable than coagulation between unequal particle sizes (heterocoagulation).

The collision efficiencies computed by Adler and Higashitani are applicable to encounters between solid rigid spheres, i.e., to the formation of doublets in the early stages of coagulation. The hydrodynamic interactions between the porous multiplets which are formed in the coagulation process will be far less pronounced than for solid rigid spheres, if the fluid flow is able to penetrate the aggregates. On the other hand the Van der Waals attraction force between porous aggregates is smaller than between solid rigid spheres. The only attractive interaction between two porous flocs which needs to be considered is that between the two nearest primary particles since the other particles in the two flocs are separated by too large a distance for the interaction forces to be effective (Firth and Hunter 1976).

The complex nature of the interaction between porous aggregates probably invalidates the use of the collision efficiencies as computed by Adler and Higashitani to describe the coagulation at the multiplet level.

2.5 DISRUPTION OF AGGREGATES

2.5.1. INTRODUCTION

In a coagulation process the aggregates do not grow indefinitely. Since the establishment of a maximum size for aggregates has been observed experimentally, information on the maximum size and its causes are required for modelling aggregation processes.

Possible causes for a maximum aggregate size are:

1) aggregate break-up

2) the orthokinetic collision efficiency becoming zero.

The latter mechanism has been proposed by Brakalov (1987). If the aggregates are impenetrable, their collision efficiency drops off rapidly with increase of aggregate size due to hydrodynamic interaction. Finally, a size is reached at which the aggregates can not form any stable doublets, the collision efficiency becomes zero and the aggregates stop to grow. For the aggregates to be completely impenetrable, however, they have to be very closely packed. Such structures are not likely to be formed in the aggregation process as will be shown in chapter 5. In agglomeration* processes wherein the interstices between the primary particles in the flocs are filled up by crystal growth, this mechanism could play an important part in determining the final size of the agglomerates.

Because no concentration dependency of the break-up rate was observed for either aggregates smaller (De Boer 1987) or larger than the Kolmogorov micro scale (Glasgow and Luecke 1980), a deaggregation mechanism due to collisions between the aggregates is omitted. The break-up of aggregates is expected to be brought about by hydrodynamic stresses acting on the particles. In the next section the various hydrodynamic stresses are discussed. Their relative importance in determining the final aggregate size of the coagulation process will be evaluated for the different eddy size subranges in homogeneous isotropic turbulent flow.

---

* *The term agglomeration is used whenever aggregation and crystal growth occur simultaneously. In that case the physical bonds between the primary particles in the aggregates are replaced by crystalline bridges.*

2.5.2 HYDRODYNAMIC STRESSES

The turbulent hydrodynamic stresses can be divided into two groups:

1) The bulk stresses that are induced within the aggregate structure by instantaneous turbulent velocity differences across the aggregate. These stresses result in aggregate deformation and ultimately in floc splitting (Thomas 1964).

2) the surface shearing stresses that arise from the turbulent fluid drag on the aggregates. The fluid drag acts on the floc surface and gives rise to surface erosion of the floc (Parker 1972).

ad 1)

The fluctuating fluid velocities on opposite sides of the floc result in shear stresses in the viscous subrange and in normal pressure stresses in both inertial and macro subrange of turbulence. The shear stresses relate to the fluctuating velocities acting parallel to the surface of the floc whereas the normal pressure stresses relate to the fluctuating velocities normal to the floc surface. See fig. 2.4.
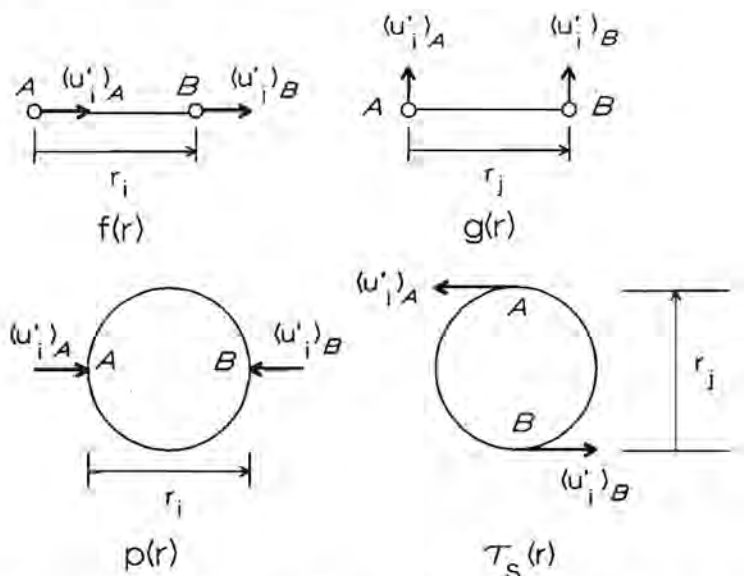
Figure 2.4. Shear and pressure stresses due to fluctuating velocities on opposite sides of the floc.

The shear stress τ_s acting upon the floc is of the order of the shear stress in the fluid:

$$\tau_s \sim \mu \ s_{ij} = \Delta v(d_p)/d_p \tag{2-53}$$

where s_{ij} = shear rate in turbulent flow

     d_p = floc diameter = $2a_p$

     $\Delta v(r)$ = rms difference in velocities normal to the separation vector r

                between two points that are a distance $|r| = r$ apart.

The rms velocity difference $\Delta v(r)$ in eq.(2-53) is given by:

$$\Delta v(r) = \left[\ 2 \ u^2 \ (\ 1 - g(r)) \ \right]^{1/2} \tag{2-54}$$

where $g(r)$ = the lateral or transverse velocity correlation function.

In isotropic turbulence $g(r)$ is related to $f(r)$ (Hinze, 1975d):

$$g(r) = f(r) + \frac{r}{2} \frac{\partial f(r)}{\partial r} \tag{2-55}$$

Combining (2-55), (2-11) and (2-54) gives:

$$\Delta v(r) = \left[\ \Delta u(r) \ \left[\ \Delta u(r) + r \ \frac{\partial(\Delta u(r))}{\partial r} \ \right) \ \right]^{1/2} \tag{2-56}$$

where $\Delta u(r)$ can be obtained from table 2.1.

For the viscous subrange application of (2-56) results in:

$$\Delta v(r) = \Delta u(r) \ \sqrt{2} = (2\varepsilon/15v)^{1/2} \ r \qquad \text{for } r \leq \eta \tag{2-57}$$

Hence, the shear stress τ_s in the viscous subrange may be expressed as:

$$\boxed{\tau_s = \mu \ \sqrt{(\ 2\varepsilon \ / \ 15v)} = \sqrt{(2 \ \rho \ \mu \ \varepsilon \ /15)} \tag{2-58}}$$

The normal pressure stresses p are estimated by (Tomi and Bagster 1978):

$$p \sim \rho \ (\Delta u(d_p))^2 \tag{2-59}$$

Substitution of the expressions for $\Delta u(r)$ from table 2.1 in eq.(2-59) yields for the rms normal pressure stresses in the inertial and macro subranges respectively the following equations:

$$\boxed{p = \rho \ 1.88 \ (\varepsilon d)^{2/3} \tag{2-60}}$$

$$\boxed{p = 2 \ \rho \ (\varepsilon L)^{2/3} \tag{2-61}}$$

ad 2)

Estimates for the surface shearing stresses σ_s that result from the difference in particle and fluid velocity are obtained by dividing the turbulent fluid drag force by the surface area of the floc. Thus these shearing stresses are expressed as:

$$\sigma_s = 6\pi \mu a_F |q| / 4\pi a_F^2 = 3\sqrt{3} \mu q / 2a_F \qquad (2\text{-}62)$$

where Stokes' law is applicable. In deriving eq.(2-62) isotropy is assumed in the velocity components relative to the fluid velocity vector, so the mean square relative particle velocity q^2 in each direction is equal to one third of the squared amplitude of the relative velocity vector q.

In the viscous subrange of turbulence the particle velocity relative to the fluid flow is given by:

$$q = 1.08 \, \tau_p \left[\frac{2(\rho_p - \rho)}{2\rho_p + \rho} \right] v^{-1/4} \, \varepsilon^{3/4} \qquad (2\text{-}63)$$

with $\tau_p = (2\rho_p + \rho) a^2 / 9\mu$

Substitution of eq.(2-63) in eq.(2-62) yields for the shearing stress:

$$\sigma_s = 0.624 \, (\rho_p - \rho) \, v^{-1/4} \, \varepsilon^{3/4} \, a_F \qquad (2\text{-}64)$$

For aggregates in the inertial subrange of turbulence, the particle velocity relative to the fluid is given by eq.(2-47). When $\tau_p \gg T_L$, eq.(2-47) reduces to:

$$q = (1 - b) \, u = \left[\frac{2(\rho_p - \rho)}{2\rho_p + \rho} \right] (\varepsilon L)^{1/3} \qquad (2\text{-}65)$$

This is the maximum relative velocity the aggregates can attain.

Substituting eq.(2-65) in eq.(2-62) gives the expression for the maximum shear stress due to fluid drag in the inertial subrange of turbulence, provided Stokes law is applicable:

$$\sigma_s = 3\sqrt{3} \mu q / 2a_F = 2.60 \, \mu \left[\frac{2(\rho_p - \rho)}{2\rho_p + \rho} \right] (\varepsilon L)^{1/3} \, a_F^{-1} \qquad (2\text{-}66)$$

For Stokes' law to be applicable, the density difference between the aggregates and fluid should be small. With high values of porosity within the aggregates this requirement is satisfied.

In the following sections we evaluate whether the surface shearing stresses or the bulk stresses are responsible for aggregate break-up. Break-up criteria are formulated for the viscous and inertial subranges.

In the viscous subrange the ratio of the surface shearing stress σ_s due to fluid drag (eq. (2-64)) to the shear stress τ_s due to fluid velocity differences across the aggregate size (eq. 2-58) amounts to:

$$\frac{\sigma_s}{\tau_s} = 0.854 \left[\frac{\rho_p - \rho}{\rho} \right] \left[\frac{2a_F}{\eta} \right] \tag{2-67}$$

This ratio is always smaller than unity in liquid suspensions. So provided the surface yield strength does not differ much from the tensile strength of the cluster matrix, the rupture criterion in the viscous subrange may be expressed as:

$$\tau_s \geq S \tag{2-68}$$

where S denotes the floc yield strength.

So we conclude that the aggregate size in the viscous subrange of turbulence is governed by the equality of the hydrodynamic shear stress τ_s to the counteracting binding aggregate stress S.

In the inertial subrange we may compare the maximum surface shearing stress from eq.(2-66) to the pressure stress given by eq. (2-60). The ratio of these stresses is equal to:

$$\frac{\sigma_s}{p} = 2.77 \left[\frac{2(\rho_p - \rho)}{2\rho_p + \rho} \right] \left(\frac{L}{\eta} \right)^{1/3} \left(\frac{\eta}{2a_F} \right)^{5/3} \tag{2-69}$$

With the use of eq.(2-13) and eq.(2-14) the ratio of the integral length scale and the Kolmogorov micro scale may be expressed as a function of the Reynolds number that corresponds to the large scale eddies Re_L ($= \Delta u(L) \cdot L / \nu$):

$$\left(\frac{L}{\eta} \right) = (u \, L / \nu)^{3/4} = 2^{-3/8} \, (Re_L)^{3/4} \tag{2-70}$$

Substituting eq.(2-70) in (2-69) yields:

$$\frac{\sigma_s}{p} = 2.14 \left[\frac{2(\rho_p - \rho)}{2\rho_p + \rho} \right] \left(\frac{\eta}{2a_F} \right)^{5/3} (Re_L)^{1/4} \tag{2-71}$$

It can be readily shown that even at large Reynolds numbers Re_L (≥ 1000) σ_s/p does not become larger than unity for aggregates in the inertial subrange, i.e. $2a_F > 25 \eta$. So if the surface shear strength is not significantly less than the compressive strength of the cluster matrix, break-up of aggregates with sizes in the inertial subrange will occur whenever the pressure stress exceeds the compressive bulk strength, i.e. :

$$p \geq S \tag{2-72}$$

Information about the size dependency of the floc strength is required in order to translate the break-up criteria (2-68) and (2-72) into relations linking the maximum aggregate size to the turbulent energy dissipation rate. This information is given in the next section.

2.6. FLOC STRENGTH

Expressions relating floc size to its yield strength S are to be substituted in the break-up criteria that were defined in the previous section in order to derive the dependence of aggregate size on the energy dissipation rate in the turbulent flow.

The strength of the cluster matrix is equal to the bonding force between the primary particles in the floc times the number of bonds per m^2 that have to be broken in the fracture area. The bonding force is due to the Van der Waals attraction between the primary particles. In the next section an expression for the bonding force between particles in contact is presented. The number of bonds per unit fracture area is determined by the packing of the primary particles in the floc. It will be shown in section 2.6.1 that flocs are generally nonuniform in composition resulting in a floc strength decreasing with aggregate size.

2.6.1 BONDING FORCE

The bonding force between two spherical primary particles is obtained by differentiating the net interaction energy given by $V_A + V_R$ to the separation distance H. If the repulsive forces are negligible ($V_R \ll V_A$), the bonding force is given by dV_A / dH :

$$F = \frac{A\, a_i}{12\, H^2} \qquad\qquad (2\text{-}73)$$

If the particles are able to make solid contact, i.e., H = 0, the attractive force would become infinitely large. In that case it would be impossible to disrupt the flocs, which is in contradiction with experimental observations (Frens and Overbeek 1972). There is a certain distance of closest approach for two particles due to strong repulsive forces that act only over a short distance. Not only is it impossible that the surface atoms of the particles interpenetrate due to Born repulsion, but it is also highly improbable that a collision brings two particles closer together than twice the distance δ between a particle surface and the Stern plane of the electrical double layer, because of the structural repulsion of the absorbed solvent layer (Firth and Hunter 1976b).

This short range repulsion modifies the attractive force expression near the distance of closest approach H_0 and eq.(2-73) is then longer applicable. The form of the attractive force close to H_0 follows from rheological measurements performed on volume filling colloidal networks that are formed by coagulation of concentrated suspensions. These measurements (Van den Tempel 1961, Firth and Hunter 1976a, Buscall 1982, Sonntag and Russel 1987b) clearly demonstrate the linearly elastic behaviour of the networks at small deformations prior to rupture. Linear elasticity implies that the tensile stress rises linearly with increase of the relative extension:

$$S = E\, e \qquad\qquad (2\text{-}74)$$

This extension of the network is related to the increase of interparticle distance by (Van den Tempel 1961):

$$e = \frac{H - H_0}{2\, a_i} \qquad\qquad (2\text{-}75)$$

where H = the separation distance after stretching

Measurements on colloidal networks are usually carried out in simple shear flow in order to avoid liquid movement with respect to the solid framework. The shear γ that corresponds to the relative elongation in simple shear flow is:

$$\gamma = 2\ e = \frac{H - H_0}{a_1} \tag{2-76}$$

The initial elastic bulk (E), shear (G) and compressive (K) moduli are respectively (Van den Tempel 1961):

$$E = \left[\frac{dS}{de} \right]_{H_0} = \left[\frac{dS}{dH} \right]_{H_0} \frac{dH}{de} = 2\ a_1 \left[\frac{dS}{dH} \right]_{H_0} \tag{2-77}$$

$$G = \frac{E}{2(1 + v_p)} \tag{2-78}$$

$$K = \frac{E}{3(1 - 2v_p)} \tag{2-79}$$

where v_p = Poisson's ratio $\approx 1/4$ (Buscall 1982)

The dependence of the tensile stress on the separation distance is solely expressed in the interparticle attractive force F. Hence the linear elasticity implies that the attractive force close to H_0 is given by:

$$F = Z\ (H - H_0) \tag{2-80}$$

The force rises linearly with the separation distance to a maximum value at the critical strain where rupture takes place. Firth and Hunter (1976b) proposed to match eq.(2-73) and (2-80) at this critical separation distance H_1 for both value and slope, demanding continuity in both floc stress and moduli. In that case the following expressions for the constants Z and H_1 are derived:

$$Z = \frac{A\ a_1}{6\ H_1^3} \tag{2-81}$$

$$H_1 = 2\ H_0 \tag{2-82}$$

Hence, in the absence of electrostatic repulsion the bonding force which corresponds with the critical floc stress, i.e., the floc strength is given by:

$$F = \frac{A\ a_1}{12\ H_1^2} = \frac{A\ a_1}{48\ H_0^2} \tag{2-83}$$

where H_0 is approximately twice the distance δ between particle and Stern

surface. The distance δ varies from about one bare ion radius (say 0.1 nm) up to one hydrated ion radius ($\sim$ 0.5 nm), resulting in values for H_1 between 0.4 and 2 nm.

2.6.2 FLOC STRUCTURE

The simplest model for cluster structure, which pictures the aggregate as having a uniform structure and cohesive strength, was proposed by Rumpf (1962). He derived the following expression for the tensile strength of a homogeneous assembly of equal sized spherical particles at solids volume fraction φ:

$$S = \frac{9}{8} k_c \; \varphi \; F \; / \; 4\pi a_1^2 \qquad\qquad (2\text{-}84)$$

where k_c = average number of links per primary particle in the fracture area that have to be broken in order to disrupt the aggregate.

   F = bonding force between two primary particles

   a_1 = radius of primary particle

In a homogeneous structure the parameter k_c is identical to the mean coordination number, i.e., average number of points of contact between one primary spherical particle and its neighbours. This coordination number k depends on the solids volume fraction φ.

For a homogeneous packing the expression:

$$k_c \cong 14.64 \; \varphi^{1.2} \qquad\qquad (2\text{-}85)$$

may be used (see fig. 2.5).

Since the floc strength as defined by eq.(2-84) is independent of the aggregate size for aggregates of uniform structure, the rupture criterion (2-68) predicts that at a critical intensity of turbulence ε_b, when the induced shear stress exceeds the yield stress of the structure, all aggregates within the viscous subrange are ruptured. In general, this behaviour is not observed in practice.

This difference between theory and experimental observation can be explained by acknowledging that the strength of aggregates decreases with increasing size, with the result that the assumption of uniform structure (and hence strength) for all sizes never holds in practice and that for each aggregate size there exists a critical value of τ_s which causes break-up.
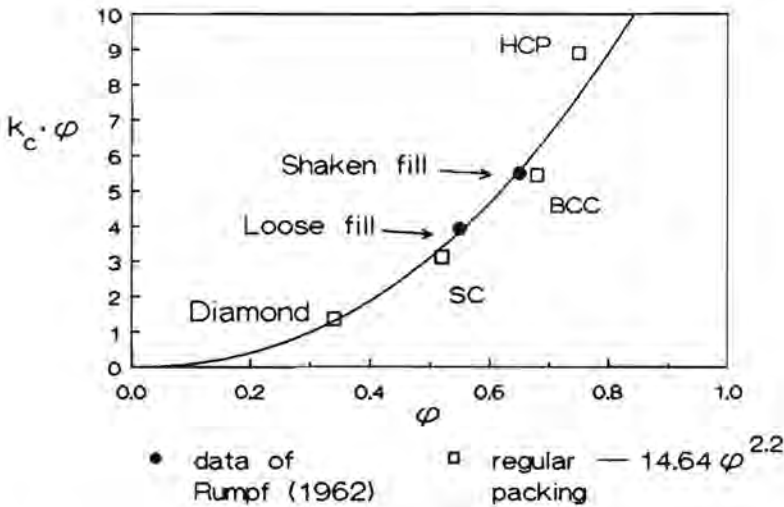
Figure 2.5. Coordination number k_c in uniformly packed structure as a function
of solids density φ. The different structures plotted in the
figure are: HCP = hexagonal close packed, BCC = body centered
close packed, SC = simple cubic packed, Diamond = diamond
structure, Loose and Shaken Fill correspond to data points
presented by Rumpf (1962) for loose and jarred packings of lead
spheres of uniform size.

Qualitatively the weaker structures of larger flocs are due to their being
built up of smaller more dense aggregates which have collided and remained
linked at their points of contact, resulting in a more porous arrangement of
lower overall density and hence weaker structure. The smaller aggregates are
formed by grouping of even smaller more densely packed aggregates. This
process repeats itself down to the primary particle level resulting in a
so-called multilevel floc structure (François and Van Haute 1985).

In recent years it has been shown that a convenient way of describing this
non-homogeneous aggregate structure is in terms of self similar fractal
geometry (Meakin 1988). Self similar fractal structures are invariant to a
change of length scale, so they look the same under different magnifications.
In reality, there is no exact self similarity with individual colloidal

aggregates, i.e., they cannot be mapped exactly onto itself after dilation or contraction due to the randomness of the structure. However, colloidal structures display normally an average or statistical self-similarity which validates the use of the fractal description.

The structure of the fractal aggregates is characterized by the so-called fractal dimensionality. The fractal dimensionality is a measure of how particles fill the space of an aggregate. The dependency of the total number of primary particles i in the aggregate on the floc radius a_i is given by:

$$i = j \, (a_i / a_j)^D \tag{2-86}$$

where D has a value between 1 and 3 and a_j denotes the radius of the aggregate consisting of j primary particles with $j \leq i$. The radius a_j marks the onset of the fractal geometrical scaling relationship (2-87). It should be noted that $j > 2$ because a doublet of two primary particles is uniquely defined and cannot be characterized by different values of D. Frequently eq.(2-86) is rewritten as:

$$i = c \, (a_i / a_1)^D \tag{2-87}$$

where a_1 denotes the primary particle size and c is given by:

$$c = \varphi_j \, (a_j / a_1)^{3-D} \tag{2-88}$$

with φ_j denoting the volume fraction of solids within the floc consisting of j primary particles.

If flocs are uniformly porous, the exponent in eq.(2-88) would be equal to the Euclidean dimension of space, i.e., 3. A smaller exponent means that the density of particles within the floc decreases away from its center. In that case the average solids density φ of the floc varies with floc radius a_F according to:

$$\varphi = c \, (a_F / a_1)^{D-3} \tag{2-89}$$

The variation in volume fraction φ with the radial position r within the floc is given by:

$$\varphi(r) = c \, D/3 \, (r / a_1)^{D-3} = \varphi_0 \, (r / a_1)^{D-3} \tag{2-90}$$

The parameter k_c from eq.(2-84) is probably smaller than in the case of a homogeneous structure and its dependency on floc density is expected to be stronger. The variation of parameter k_c with floc density is assumed to be given by:

$$k_c = B \, \varphi^{n-1} \tag{2-91}$$

where n and B are constants.

Combining eq.(2-91), (2-89) and (2-84) yields:

$$S = \frac{9}{8} \, \text{B} \; \varphi^n \, F \, / \, 4\pi a_1^2 = \frac{9}{8} \, \text{B} \; c^n \, (a_F \, / \, a_1)^{n(D-3)} \, F \, / \, 4\pi a_1^2 \qquad (2\text{-}92)$$

This power law dependence of floc strength on floc density is equivalent to the one as adopted by Sonntag and Russel (1987a). They defined the floc strength as a function of the radial position within the floc:

$$S(r) = S_0 \, (r \, / \, a_1)^{D-3} = S_0 \, \big[\, \frac{\varphi(r)}{\varphi_0} \, \big]^n \qquad (2\text{-}93)$$

Sonntag and Russel (1987a) showed that the rupture of the floc occurs at an almost constant relative radial position within the floc, which means that $r \sim a_F$. With use of this proportionality it follows from comparison of eq.(2-93) and (2-92) that $S_0 \sim F \, / \, a_1^2$.

The power law dependency of floc strength on φ originates from experiments where the shear modulus of coagulated networks was determined as a function of solids volume fraction (Sonntag and Russel 1987b). For a volume-filling network formed by Brownian coagulation of aqueous polystyrene particles they found $G \sim \varphi^n$ with $n = 2.5$. Since the shear modulus is related to the floc strength through eqs.(2-78) and (2-77) it follows that the floc strength should display a similar dependency on floc density φ.

2.7 BREAK-UP CRITERIA

The force balance between aggregate strength and induced stresses describes the effect of agitation on the aggregate size. Balances are treated for the viscous and inertial subrange in the following sections.

2.7.1 BREAK-UP CRITERION IN VISCOUS SUBRANGE OF TURBULENCE

Equating the floc strength to the shear stress acting on the floc gives a relationship between the maximum aggregate size a_F and the shear rate s_{ij}:

$$a_F \sim a_1 \, (\tau_s \, / \, S_0)^{\frac{1}{n(D-3)}} = a_1 \, (\mu \, s_{ij} \, / \, S_0)^{\frac{1}{n(D-3)}} \qquad (2\text{-}94)$$

This break-up criterion was presented by Sonntag and Russel (1987a) in a somewhat different format for an isolated floc in simple shear flow. They presented the following relationship between the dimensionless aggregate size ξ and the shear rate:

$$\xi = a_F / \sqrt{k_p} \sim (s_{ij})^{(D-1)/2n(D-3)} \tag{2-95}$$

where k_p is the floc permeability.

For a porous assemblage of identical spheres, however, they showed that the permeability k_p is proportional to $a_F^{(3-D)}$. Substitution of this proportionality in (2-95) yields the same dependency of floc size on shear rate as expressed by eq.(2-94).

Substituting $s_{ij} = \sqrt{(2\varepsilon/(15v))}$ and the proportionality $S_0 \sim F / a_1^2$ in eq.(2-94) yields:

$$a_F \sim a_1 \left[(\rho \mu \varepsilon)^{1/2} / S_0 \right]^{\dfrac{1}{n(D-3)}} \sim a_1 \left[(\rho \mu)^{1/2} a_1^2 / F \right]^{\dfrac{1}{n(D-3)}} \varepsilon^{\dfrac{1}{2n(D-3)}} \tag{2-96}$$

So, if a fractal description of the floc structure is assumed to be valid and a power law dependence of the floc strength on solids volume concentration is used, then the aggregate size in the viscous subrange of turbulence is expected to vary with the energy dissipation rate according to a power law with exponent $1 / 2n(D-3)$.

2.7.2 BREAK-UP CRITERION IN INERTIAL SUBRANGE OF TURBULENCE

As the compressive modulus is found to be almost equal to the shear modulus (Buscall 1982), the compressive strength is expected to have a similar dependency on floc size as the tensile or shear strength. Equating (2-92) to the fluid pressure stress in the inertial subrange yields the following variation of floc size with energy dissipation rate:

$$a_F \sim (\varepsilon)^{\dfrac{2}{3n(D-3) - 2}} \tag{2-97}$$

2.7.3. DISCUSSION ON BREAK-UP CRITERIA

To compute the power law coefficients of the break-up criteria, values of the constant n and of the fractal dimensionality D for flocs formed in turbulent flows are required. Although there is a lot of literature around on the fractal structures of aggregates, it should be noted that most publications deal exclusively with the case of aggregates formed by Brownian motion or by laminar flow. With Brownian coagulation the fractal dimensionality is approximately 1.7 (Meakin 1988). Experiments conducted by Sonntag and Russel (1986) wherein flocs of polystyrene particles grown by Brownian coagulation were sheared in a Couette device, showed that shearing rearranges the weaker string-like segments and redistributes particles within the floc, leaving a denser floc with a less pronounced radial variation of local volume fraction. They found a fractal dimensionality of $D = 2.5$ for the flocs sheared at widely different shear rates ($\tau_s = 9 - 60$ N m^{-2}). Recently Gmachowski e.a. (1990) reported similar values for the fractal dimensionality of flocs of polystyrene particles formed by flocculation in a stirred tank. The agitation used in their experiments was, however, gentle and the flow was far from turbulent. To our knowledge the turbulence case has not yet been addressed to. In this thesis, therefore, attention is devoted to the structural aspects of flocs formed in a turbulent flow in chapter 5 and 6.

The break-up criteria as defined in section 2.5.4 presume that the surface yield strength is of the order of the bulk tensile strength of the floc. Sonntag and Russel (1987a) showed that the rupture through action of bulk stresses also occurs near the surface of the flocs, approximately at $r = 0.8$ a$_F$. Since the bulk strength of the floc is related to the solids density at this location of rupture and the surface yield stress to the solids density at the floc surface, it follows from eq.(2-93) that the ratio of both amounts to circa $(0.8)^{n(3-D)}$. Assuming that D and n are both about 2.5 the surface yield stress is not much smaller than the bulk strength of the floc, which confirms the use of the break-up criteria as presented in section 2.5.4.

Strictly speaking, the break-up criteria tell us whether a floc will be disrupted or not at a constant level of applied hydrodynamic stress. However, in a turbulent velocity field where the hydrodynamic stresses are constantly changing in time, an additional condition must be met for a floc to break

whenever the velocity difference across its diameter becomes larger than the critical value. This condition is that the time the relative velocity field stays above the critical break-up value must be of the order of or larger than the characteristic deformation time of the aggregate. Because of the small deformations required to rupture the floc (critical relative extension $e_b \cong 2\delta/a_1$), the turbulent characteristic time is in general always larger than the aggregate deformation time. For example, the characteristic time of deformation for a floc subjected to shear motion is $2e_b / s_{ij}$. The characteristic time of the smallest eddies is equal to $\tau_K = (2/15)^{1/2} / s_{ij}$. The ratio of both is $(15/2)^{1/2} e_b$ where e_b is usually smaller than 5% . It follows that break-up of the aggregate will take place whenever the local velocity difference across the aggregate diameter becomes larger than the characteristic break-up velocity, so the break-up criteria as defined in section 2.5.4. also apply to a turbulent fluctuating velocity field.

2.8. BREAK-UP KINETICS

The critical value of the fluid velocity difference across the aggregate diameter $\Delta u_b(d)$ (or $\Delta v_b(d)$) that will break up the aggregate, is defined by the break-up criterion. For reasons of convenience the notation of the velocity difference $\Delta u(d)$ or $\Delta v(d)$ will now be abbreviated to Δu or Δv. The break-up rate is determined by the frequency at which the statistical field of velocity differences becomes larger than this critical value (Delichatsios 1975). Assuming that the change of the velocity difference in time, that is the acceleration of the velocity difference, can take on all possible statistically values independently of the critical value of the velocity difference, Delichatsios and Probstein (1976) showed that the aggregate break-up frequency f_b is given by:

$$f_b = 2 \ (\Delta u^\cdot) \ P(\Delta u_b) \hspace{3cm} (2\text{-}98)$$

where $\Delta u^\cdot$ = the root mean square acceleration of the velocity difference across floc diameter d.

  $P(\Delta u)$ = value of probability density function for velocity difference Δu

Delichatsios and Probstein (1976) then postulated that $\Delta u^{\cdot}$ may be estimated by:

$$\Delta u^{\cdot} \sim \frac{(\Delta u(d))^2}{d} \tag{2-99}$$

This expression was first introduced by Levich (1962) as an estimate for the acceleration of eddies responsible for velocity changes over a distance d.

In analogy with Saffman and Turner (1956) and with Kuboi et al. (1972) the probability density function is approximated by a Gaussian distribution with spread Δu for the viscous and inertial subrange respectively. Then the value $P(\Delta u_b)$ is given by:

$$P(\Delta u_b) = \frac{\exp(-\Delta u_b^2 / 2\Delta u^2)}{(2\pi)^{1/2} \Delta u} \tag{2-100}$$

It follows from eq.(2-98), (2-99) and (2-100) that

$$f_b = \left(\frac{2}{\pi}\right)^{1/2} \frac{(\Delta u)}{d} \exp(-\Delta u_b^2 / \Delta u^2) \tag{2-101}$$

The term $\Delta u/d$ before the exponential function on the right hand side of eq.(2-101) is equal to the eddy frequency as defined by Levich (1962). For the eddy frequency in the inertial subrange, we obtain from eq.(2-22):

$$\frac{(\Delta u)}{d} = 1.37 \, \varepsilon^{1/3} \, d^{-2/3} \tag{2-102}$$

and from eqs.(2-20) and (2-56) the result which is relevant to break-up in the viscous dissipation subrange:

$$\frac{(\Delta v)}{d} = (2\varepsilon / 15v)^{1/2} \tag{2-103}$$

Eq.(2-101) represents the break-up frequency as a function of aggregate size in a homogeneous isotropic turbulent flow field. If velocity differences that are very much smaller than the rms velocity difference already rupture the floc, the break-up frequency reduces to:

$$f_b = \left(\frac{2}{\pi}\right)^{1/2} \frac{(\Delta u)}{d} \tag{2-104}$$

which resembles the floc disruption frequency as introduced by Thomas (1964).

The break-up rate of aggregates consisting of k primary particles with diameter d_k is given by the disruption frequency multiplied by the number concentration of the aggregates:

$$S_k = f_b(k) \ n_k \qquad (2\text{-}106)$$

2.9. POPULATION BALANCES

Prior to the formulation of the population balances we have to discuss the effect of the occurrence of break-up on the growth process. In addition to diminishing the number concentration of the aggregates, the break-up also slows down the growth process by reducing the time for the aggregates to grow any further. Because the break-up is almost instantaneous (see section 2.7), aggregates will not be formed or can take part in the coagulation process during the time the velocity difference is larger than their corresponding critical value. The fraction of time the relative velocity field attains values smaller than this critical velocity difference Δu_b is:

$$f_t = 2 \ \text{erf}(\ \Delta u_b \ / \ \Delta u \ ) \qquad (2\text{-}107)$$

where erf(y) denotes the error function at some particular value of y', which is defined as:

$$\text{erf}(y) = \frac{1}{\sqrt{(2\pi)}} \int_0^y \exp(- y'^2 / 2) \ dy' \qquad (2\text{-}108)$$

To obtain the actual number of collisions leading to the formation of the aggregates, the values computed with the kinetic expressions presented in section 2.4.3 have to be multiplied by this time fraction f_t.

Aggregation kinetics and break-up kinetics together with the break-up criterion are to be combined in population balances over the various aggregate sizes in order to describe the evolution of the aggregate size distribution in the coagulation process. To model the coagulation in stirred tanks, the assumption of homogeneous turbulence, however, is incorrect, as will become clear from the results presented in the next chapter. The application of the expressions presented in this chapter, should therefore be restricted to local values of the energy dissipation rate in the stirred tanks.

2.10. CONCLUSIONS

In this chapter expressions for coagulation frequencies, break-up criteria and break-up rates have been presented for aggregate sizes ranging from the smallest to the largest eddies in stationary homogeneous isotropic turbulent flow.

In liquid suspensions collisions due to inertia of aggregates entrained in the smallest eddies, i.e. with sizes in the viscous subrange of turbulence, are negligible with respect to collisions induced by the fluid flow. They, however, become more important for the larger aggregate sizes in the inertial and macro subrange of turbulence.

Aggregate break-up is most likely the result of hydrodynamic stresses that arise from the fluid velocity differences across the aggregate. In the viscous subrange, shear forces exerted upon the aggregates are responsible for break-up, whereas in the inertial and macro subrange normal pressure forces acting on the aggregates are the main cause for aggregate break-up.

By using a fractal description of the aggregate structure and assuming that the local cohesive strength depends on the aggregate's porosity, we were able to derive break-up criteria that describe the effect of energy dissipation rate on the upper size limit of aggregates entrained by small or large eddies.

Finally the topic of break-up kinetics in homogeneous turbulence has been addressed to. The break-up rate is first order in aggregate concentration and proportional to the frequency at which the shear or pressure forces become larger than the characteristic break-up value.

CHAPTER III
HYDRODYNAMICS IN STIRRED TANKS

3.1. INTRODUCTION

One of the important flow parameters governing the coagulation process in stirred tanks is the turbulent energy dissipation rate. Measurements of the energy dissipation rate reported in the literature revealed its non-uniformity throughout the tank. There is however some obscurity about the exact values of the energy dissipation rate at the different positions within the vessel. Laufhütte and Mersmann (1985) for example reported differences in energy dissipation rate values in the vicinity of the stirrer of the order of a factor 70. Besides different theoretical equations for the calculation of the energy dissipation rate field the different measuring techniques used to characterize the turbulent flow are responsible for these different values for energy dissipation rate.

The different measuring techniques involved are photography of tracer particles (Cutter 1966, Komasawa et al. 1974), hot wire (Günkel and Weber 1975a) and hot film velocimetry (Liepe et al. 1971, Rao and Brodkey 1972, Okamoto et al. 1981, and Barthole et al. 1982) and Laser Doppler velocimetry (Patterson and Wu 1985, Laufhütte and Mersmann 1985, Costes and Couderc 1988b and Wu et al. 1989).

In the first mentioned measurement technique tracer particles are introduced into the fluid and the particle velocities are measured by photographic recording. If the particles suspended in the fluid are sufficiently small, they follow the fluid flow accurately and hence the fluid velocity is measured. With this technique one is immediately confronted with the difficulties associated with flows of high turbulence intensities, as experienced in stirred tanks. With the very rapid changes in time and place practically instantaneous recordings are necessary. Short exposure times and large depths of field are conflicting requirements, limiting the accuracy of the measurement technique.

With hot wire/film (thermal) velocimetry, a probe is introduced into the turbulent flow and turbulence quantities are measured by the changes of

temperature or of electric current through the wire/film dependent on which of the two quantities is maintained constant. In flows with high turbulence intensities, velocities that are negative with respect to the average velocity can occur and therefore equipment using probes which may block the flow reversals is less appropriate. Moreover, a change of sign of the velocity cannot be detected by thermal velocimetry leading to larger and smaller values of the mean velocity and of the rms velocity fluctuations respectively (Costes et al. 1991). Other disadvantages are the nonlinearity of the velocity response, the inability to measure the individual components of the velocity vectors directly and the ageing of the probes (Hinze 1975e) which changes the values of the calibration parameters.

In Laser Doppler velocimetry the velocity of moving scattering particles is measured optically utilizing the Doppler effect. Laser Doppler velocimetry (LDV) seems to be best suited for measurements in flows with high turbulence intensities. LDV is less elaborate than streak photography and meets the requirement of high resolution power in time. Furthermore, with LDV one component of the velocity vector with its sign is directly measured, the velocity response is linear and above all the flow is not obstructed as with thermal velocimetry.

The data concerning LDV measurements are therefore believed to be the most accurate. Laufhütte and Mersmann (1985) and Wu et al.(1989) carried out measurements in a stirred tank of slightly different configuration as those used in our coagulation experiments. The differences in configuration are likely to result in different flow patterns and consequently in different energy dissipation rate values in the stirred tanks. Their data may therefore not be directly applicable to our situation. A previous paper of Patterson and Wu (1985), which concerned a stirred tank of similar geometry, reported extremely high values of the energy dissipation rate and in the paper of 1989, the authors admitted that these data are in error. Finally, the data of Costes and Couderc (1988b) are not detailed enough for our purposes (see chapter 4). Hence we decided to perform LDV measurements at various positions in the stirred tanks used for the coagulation experiments in order to obtain the necessary data on the form of the energy dissipation rate distribution. To detect whether changes in this distribution occur with increasing vessel size, measurements were conducted in three geometrically identical vessels, 10, 20

and 39 cm in diameter. The effect of vessel size on the distribution of the energy dissipation rate ε has also been investigated by Costes and Couderc (1988b). They did not find any vessel size dependency. It should however be noted that their conclusions are based on measurements within two vessels, 45 and 63 cm in diameter, which cover but a small relative size change.

Prior to the presentation of the results of the LDV measurements, the theoretical background for the determination of the energy dissipation rate, the experimental method, i.e., LDV, and the geometry of the agitated vessels are discussed in sections 3.2, 3.3 and 3.4 respectively. In order to normalize the local energy dissipation rate values, the power input from the impeller was measured by means of a dynamometer. The results of these torque measurements are discussed in section 3.5. The following sections are dedicated to the results of the LDV measurements. The characteristics of the mean flow are treated in section 3.6.1. Section 3.6.2 is devoted to the periodic component of the fluctuating velocity that is observed near the impeller. Section 3.6.3 deals with the turbulent fluctuating velocities throughout the vessel. The length scales of the large-scale eddies and the values of the local energy dissipation rate as a function of vessel size are presented in section 3.6.4 and 3.6.5 respectively. In section 3.7 the experimental data are compared to findings in the literature and finally section 3.8 summarizes the main conclusions and discusses briefly the effect of the energy dissipation rate distribution on the coagulation process in stirred tanks.

3.2. THEORETICAL BACKGROUND FOR DETERMINATION OF ENERGY DISSIPATION RATES

Local energy dissipation rate values were obtained from the "inviscid estimate" (Tennekes and Lumley 1972) as discussed in section 2.4.2:

$$\varepsilon = A \ k^{3/2} / \ L \tag{3-1}$$

In order to take into account the anisotropy of the turbulent flow, k and L are obtained by summation of the contributions in the radial, axial and tangential directions (Patterson and Wu 1985):

$$k = 1/2 \cdot (\ u_{rt}^2 + u_{\vartheta t}^2 + u_{zt}^2) \tag{3-2}$$

where u_{rt}, $u_{\vartheta t}$, u_{zt} = rms turbulent fluctuations of the velocity components in radial, axial and tangential direction.

and, $L = L_r + L_\vartheta + L_z$ $\qquad$ (3-3)

where L_r, L_ϑ and L_z denote the integral length scales in the radial, tangential and axial direction respectively.

The integral length scales are the integrals of the space autocorrelation functions $R_{ii}(r_k)$:

$$L_i = \int_0^\infty \ R_{ii}(r_k) \ dr \tag{3-4}$$

where i denotes the radial, tangential or axial direction and r_k represents the displacement in the direction of the mean flow. In general the determination of the space correlation function of the velocity fluctuations is rather difficult and requires more than one velocimeter. The integral length scale may, however, be related to the integral time scale which can be computed from measurements of one velocimeter, by applying Taylor's hypothesis. This hypothesis allows temporal velocity fluctuations measured at one point in space to be interpreted as convected streamwise spatial fluctuations. The time correlation $\overline{u_i(t) \ u_i(t + \tau)}$ is then identical with the space correlation $\overline{u_i(x) \ u_i(x + r_k)}$ where $r_k = U_c \ \tau$ and U_c is the so-called convection velocity of the turbulence pattern. Taylor (1938) assumed the convection velocity U_c to be equal to the average flow velocity $|\bar{U}|$. Hence it follows that:

$$L_i = |\bar{U}| \; T_i \tag{3-5}$$

where T_i = integral time scale = $\int_0^\infty R_{ii}(\tau) \, dt$

The time autocorrelation function $R_{ii}(\tau)$ is defined as:

$$R_{ii}(\tau) = \frac{\overline{u_i(t) \; u_i(t + \tau)}}{u_i^2} \tag{3-6}$$

where τ denotes the delay or lag time.

An alternative method of evaluating the integral time scale is from the zero frequency intercept of the one dimensional power spectrum $E(f)$ (Mujumdar et al. 1970) which is the Fourier cosine transform of the time autocorrelation function:

$$T_i = \frac{1}{4u_i^2} \lim_{f \to 0} E_{ii}(f) \tag{3-7}$$

where $E_{ii}(f) = 4u_i^2 \int_0^\infty R_{ii}(\tau) \cos(2\pi f \tau) \, d\tau \tag{3-8}$

The mean flow velocity $|\bar{U}|$ is given by the vector summation of the radial $(\bar{U}_r)$, axial $(\bar{U}_\vartheta)$ and tangential $(\bar{U}_z)$ mean velocities:

$$|\bar{U}| = \sqrt{(\bar{U}_r^2 + \bar{U}_\vartheta^2 + \bar{U}_z^2)} \tag{3-9}$$

3.3. LASER DOPPLER VELOCIMETRY

3.3.1. PRINCIPLE OF LASER DOPPLER VELOCIMETRY

In laser Doppler velocimetry the scattering of a particle moving through laser light is recorded and the velocity of the particle is inferred from the change in frequency of the scattered light due to the Doppler effect.

The optical arrangement used in the experiments, employs two Gaussian laser that intersect each other in space (fig. 3.1). This configuration is referred to as the dual beam or differential Doppler system. If a particle penetrates the region of intersection of the two coherent light beams, it will scatter light from each of the two beams. As the particle acts both as a moving receiver and transmitter of light waves, the scattered light waves will have Doppler shifted frequencies v_A and v_B given by the following relations (Durst et al. 1981):

$$v_A = v_L \left[\frac{c - |U|\cos(\vartheta - \varphi)}{c - |U|\cos(\vartheta + \alpha)} \right] \qquad (3\text{-}10)$$

$$v_B = v_L \left[\frac{c - |U|\cos(\vartheta + \varphi)}{c - |U|\cos(\vartheta + \alpha)} \right] \qquad (3\text{-}11)$$

where v_L = the frequency of the light incident on the particle

    c = the velocity of light

    U = particle velocity vector

    φ = half angle between the two laser beams (see fig. 3.1)

    ϑ = angle between velocity vector and bisector of the angle between the two beams (see fig. 3.1)

    α = angle between direction of detector and bisector of the angle between the two beams (see fig. 3.1)
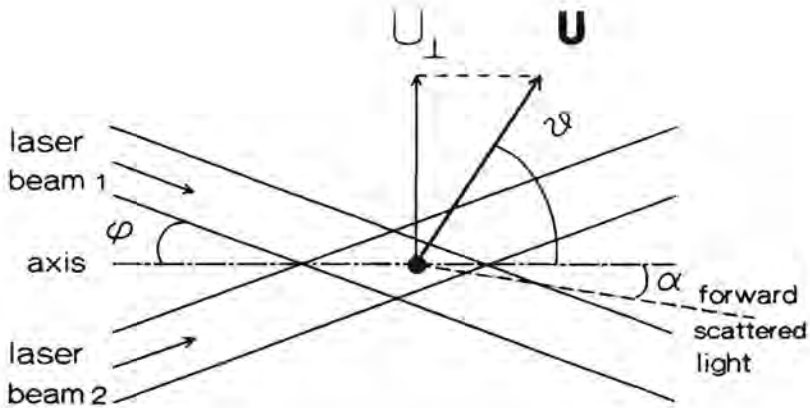
Figure 3.1. Dual beam laser Doppler system with off axis forward scatter detector

The two scattered light waves will interfere at the photodetector and yield a sinusoidal signal which has the frequency given by the frequency difference v_D = v_B - v_A. This frequency difference is, for particle velocities much smaller than the velocity of light:

$$v_D = \frac{2}{\lambda_0} |U| \sin(\vartheta) \sin(\alpha) = \frac{2}{\lambda_0} U_\perp \sin(\alpha) = U_\perp / \Delta x \qquad (3\text{-}12)$$

where λ_0 = wavelength of laser light in air = c / v_L

$\quad$ $U_\perp$ = component of the particle velocity perpendicular to the bisector of the angle between the two beams

$\quad$ Δx = fringe spacing = $\lambda_0 / 2\sin(\varphi)$

For a fluid with refractive index n the same formula can be applied since $\sin(\alpha_{fluid}) = \sin(\alpha)/n$ and $\lambda_{fluid} = \lambda_0/n$.

The term "fringe spacing" stems from the interference fringe model, which was proposed by Rudd (1969) to describe the operation of the laser Doppler velocimeter. The fringe model provides a visualized picture of the Doppler event. If no particle is present in the region in the dual-beam system where the two beams overlap, which is designated as the probe volume (Buchave et al. 1979), the two beams interfere with one another and produce a pattern of plane interference fringes (fig. 3.2). The spacing between these fringes is given by Δx. In the fringe model it is assumed that a particle moves through these interference fringes and scatters light accordingly. The frequency of the resulting signals that are detected from the region in space which is designated as the measuring volume (Buchave et al. 1979), is then equal to the rate $U_\perp$ at which the particle crosses the fringes divided by the fringe spacing Δx, i.e. the Doppler shift as given by eq.(3-12). The measuring volume
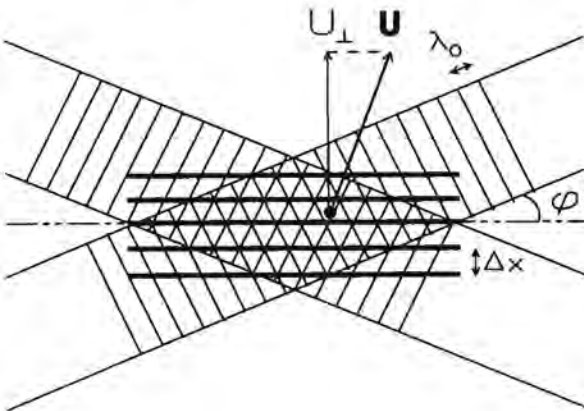
Figure 3.2. Interference fringes in probe volume
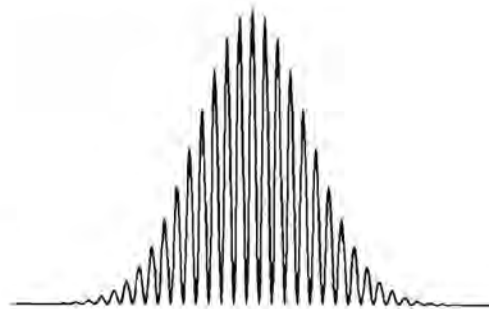
Figure 3.3. Doppler burst

may differ from the probe volume since it depends for instance on the field of view of the photodetector.

The signal burst (Doppler burst) of a single particle which moves through the measuring volume is depicted in fig. 3.3. The Gaussian envelope of the sinusoidal signal results from the Gaussian laser light intensity distribution across the measuring volume. The frequency of the sinusoidal signal is the Doppler frequency and is to be determined by the laser Doppler velocimeter.

For further information concerning the principles of Laser Doppler velocimetry the reader is referred to Durst et al. (1981).

3.3.2. THE LASER DOPPLER VELOCIMETER

The applied DISA 55X modular optical system utilizes a 35 mV He-Ne laser (Spectra-Physics, model 124B) with wavelength λ of 632.8 nm. The laser beam is split into two beams by means of a beam splitter prism. Both beams are focused by a single lens with a focal length of 300 mm. At the focal point of this lens, a fringe pattern consisting of plane fringes of known fringe spacing is created. The length of the probe volume is 1.3 mm and the diameter is .12 mm. The angle between the two beams is adjustable from 4.8 to 14.4°. The forward scattered light from the measuring volume is collected by a lens and focused onto the pinhole section of a photomultiplier. The photomultiplier is connected to the signal processing unit of the laser Doppler velocimeter.

The processor used in the experiments is a one component DISA 55L90a counter, equipped with a Bragg cell and the DISA 55N10 variable electronic frequency shifter.

The Bragg cell superimposes an optical frequency shift v_0 of 40 MHz on one of the incident beams prior to the crossing in the measuring volume. This shifts the whole sinusoidal frequency spectrum of the Doppler burst by v_0, without altering the low frequency spectrum of the Gaussian intensity variation of the burst, the so-called pedestal. The pedestal is subsequently removed electronically by high pass filtering. The frequency shifting also allows the 180 degree ambiguity in the direction of the measured velocity to be resolved. The presence of a frequency difference between the two beams v_0 results in the movement of the fringe pattern with a velocity $U_0 = v_0 \Delta x$. Hence the frequency shift will result in a decrease or increase of the

frequency of the Doppler burst dependent on whether the fringe pattern and the particle are moving in the same or opposite direction respectively. Moreover the frequency shifting enables the determination of zero particle velocities. After elimination of the pedestal the frequency of the Doppler burst is downmixed with the electronic frequency shifter to a frequency of $v_S + v_D$ to enable further processing by the counter. The counter measures the duration Δt_8 of eight signal cycles that are identified by the zero crossings of the Doppler burst and the Doppler burst frequency v_B is calculated from the measured information according to the following formula: $v_B = 8/\Delta t_8$. The burst frequency is also calculated from the first five signal cycles. This frequency is compared to the one calculated from eight signal cycles and if the difference between the two frequencies is smaller than the preset accuracy, the measurement is validated. The downmixing was performed in order to increase the accuracy of the time measurement as the counter has only a finite clock frequency of 500 MHz. Furthermore high frequency noise, caused for instance by stray light from outside the measuring volume reaching the photodetector, can be separated from the Doppler burst frequency by low pass filtering after appropriate downmixing. The Doppler frequency is evaluated from:

$$v_D = v_B - v_S \qquad (3\text{-}13)$$

A personal computer has been interfaced with the digital output of the counter processor. The signals available are the electronic frequency shift v_S, frequency of the Doppler burst v_B and the time between successive measurements.

Mono sized polystyrene spheres of 2.2 or 3.2 µm were used to seed the mixing vessel.

3.3.3. SIGNAL PROCESSING

The counter processor operates on signals generated by single particles passing through the measuring volume and when set to the single burst mode, it produces one velocity measurement per particle. In general, the arrival rate of the measurable particles is dependent on the flow velocity which brings them to the measurement volume. At higher flow velocities, more particles

enter the measurement volume per unit time and simple arithmetic averaging of the particle measurements will result in biased estimates of the time average and root-mean-square (rms) velocity. This is called statistical or velocity bias (McLaughlin and Tiederman, 1973).

The biasing errors are dependent on turbulence intensity I. The turbulence intensity is defined as:

$$I = \frac{(u_{rt}^2 + u_{\vartheta t}^2 + u_{z t}^2)}{(\bar{U}_r^2 + \bar{U}_\vartheta^2 + \bar{U}_z^2)} = \frac{(2k)^{1/2}}{|\bar{U}|} \tag{3-14}$$

Fig. 3.4 and 3.5 show the biasing errors in the mean and rms velocity as a function of the turbulence intensity, as computed for a hypothetical one-dimensional turbulent flow (Kusters et al. 1989). For a one-dimensional turbulent flow the turbulence intensity I is given by u / $\bar{U}$. The one dimensional turbulent flow was approximated by a near-continuous time correlated velocity signal with a Gaussian amplitude distribution computed by an autoregressive algorithm of the first order (Tropea 1987). The generation of the one-component sample set from which the ensemble averages of velocity and fluctuating velocity were computed, was performed using the conveyor belt model described by Tropea (1987), which assumes the scattering particles to be Poisson distributed in space.
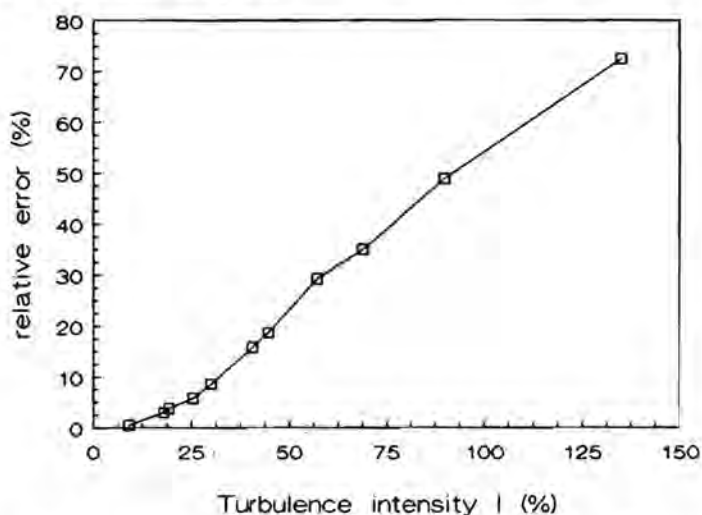
Figure 3.4. Relative biasing error in mean velocity $\bar{U}$ of simulated 1-D turbulent flow.
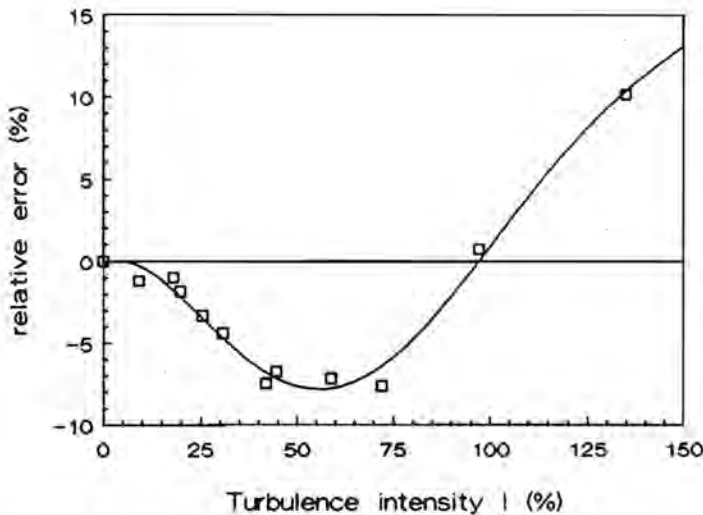
Figure 3.5. Relative biasing error in rms fluctuating velocity u of simulated
1-D turbulent flow.

Buchave et al. (1990) extended these calculations to 3-dimensional Gaussian
turbulence and showed that in that case the biasing errors are less pronounced
but still appreciable at high levels of turbulence intensity.

To obtain reliable values for the local energy dissipation rate, non-biased
time averaged values of mean velocity and especially of the rms fluctuating
velocity (which is raised to the third power in eq. (3–1)) are required.

The velocity bias is corrected for by weighting the individual measurements
with their corresponding interarrival time, i.e. the time between the last and
next measurement (Barnett and Bentley 1979):

$$\bar{U}_{TBD} = \sum_{i=1}^{M} U(i) \, \Delta t(i) \, / \, \sum_{i=1}^{M} \Delta t(i) \tag{3-14}$$

$$u_{TBD}^2 = \sum_{i=1}^{M} (U(i) - \bar{U}_{TBD})^2 \, \Delta t(i) \, / \, \sum_{i=1}^{M} \Delta t(i) \tag{3-15}$$

where $\bar{U}_{TBD}$ = time between data corrected mean velocity

u_{TBD} = time between data corrected rms fluctuating velocity

$U(i)$ = velocity of particle i

$\Delta t(i)$ = time between the arrival times of particle i and i + 1

M = total number of velocity measurements

This correction is, however, only effective at high data rates, i.e. large numbers of measured particles per unit time (Kusters et al. 1989, Buchave et al. 1990). At low data rates several velocity changes occur during the time elapsed between two measurements, and the correlation between measured velocity and detected interarrival time will be weak and the Time Between Data (TBD) correction less effective.

In fig. 3.6 the reciprocal of the interarrival time, i.e. the instantaneous data rate is plotted vs. the radial velocity measured in the impeller stream of a Rushton turbine impeller. As expected, the correlation between instantaneous particle arrival rate and flow velocity is more pronounced at higher mean data rates, making the TBD correction more effective. The mean data rate was increased either by amplifying the photomultiplier output electronically or by increasing the particle concentration in the mixing vessel. In fig. 3.7 the unweighted and weighted estimates of the mean radial velocity are plotted vs. the mean data rates. The difference between the unweighted and weighted estimates levels off for high data rates, indicating that no further correction is obtained by increasing the data rate.
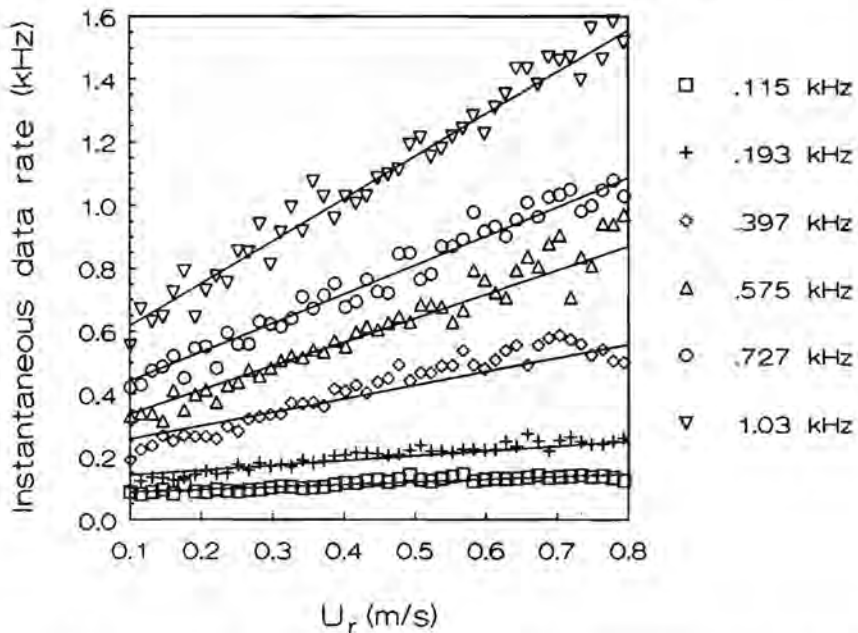
Figure 3.6. Reciprocal of interarrival time versus momentary radial velocity. Parameter: mean data rate. Integral time scale $T_r = 9.63$ ms.

C(particle)   = particle concentration
PM-Voltage   = photomultiplier-voltage
TBD   = time between data corrected, un = unweighted
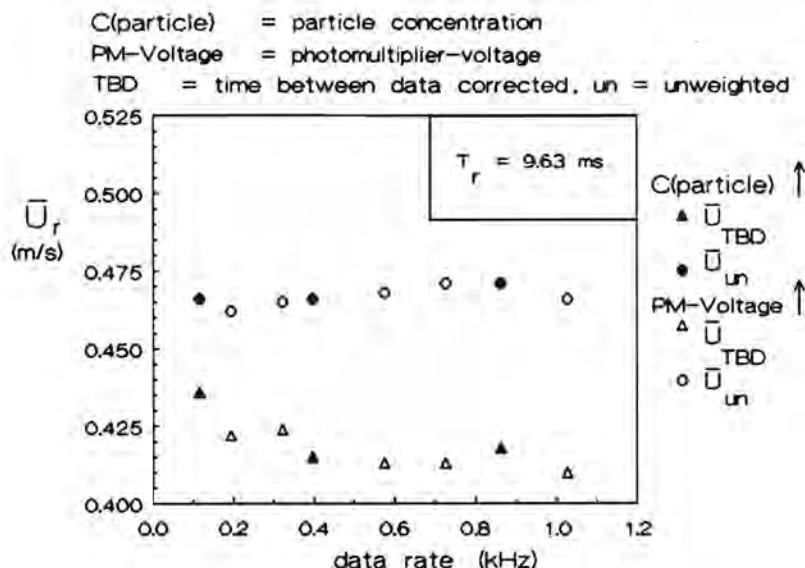
Figure 3.7. Unweighted and weighted estimates of mean radial velocity $\bar{U}_r$ versus validated data rate N. Effect of increasing the data rate by adjustment of particle concentration or photomultiplier voltage.

Velocity bias also prohibits the usage of the Slotting Technique (Mayo 1978) to compute the autocorrelation or power spectrum from which the integral time scale is deduced (Kusters et al. 1989, Edwards and Kolodzy 1986). This is shown in the next section. Time autocorrelation functions or power spectra were computed from a regularly resampled signal, the so-called Sample-Hold signal (Adrian and Yao 1987) because this technique gives unbiased results at high data rates (Tropea 1987).

Summarizing, to obtain reliable values of the time averaged mean and fluctuating velocity and integral time scale, the measurements were performed at high data rates ($N \cdot T_i > 5$, with N denoting data rate and T_i denoting the integral time scale). Next TBD correction was applied to both mean and fluctuating velocity and the autocorrelation function or power spectrum were computed from the Sample-Hold signal.

3.3.4. EFFECT OF VELOCITY BIAS ON CORRELATION FUNCTION COMPUTED WITH SLOTTING TECHNIQUE

The slotting technique, as introduced by Mayo (1978), yields good estimates of the time autocorrelation function from randomly sampled velocity fluctuations. For a brief introduction to the Slotting technique the reader is referred to appendix A. If in the presence of velocity bias no correction is applied to the mean velocity and rms velocity it can be shown theoretically that the second point of the autocovariance function at lag time $\Delta\tau$ where $\Delta\tau$ is much smaller than the integral time scale of the turbulent flow, is larger than the first point at zero lag time. Since the value of the autocorrelation function at lag time $\Delta\tau$ is given by the autocovariance value at this point normalized by the autocovariance value at zero lag time, the second point of the autocorrelation function becomes larger than one: Consider a one dimensional turbulent flow with a Gaussian velocity distribution and a turbulence intensity $I = u / \bar{U} \leq 30\%$, which means no flow reversal. If the arrival rate is taken proportional to the flow velocity, the first point (zero lag time) of the autocovariance function, if it is computed from the eigen (self) products, is given by the unweighted rms velocity which equals $u^2 \cdot (1 - I^2)$. The second point is expected to be equal to $u^2 \cdot (1 + I^4)/(1 + I^2)$. The second point of the measured autocorrelation function is given by the ratio of both autocovariance values, resulting in $(1 + I^4)/(1 - I^4)$, which is slightly larger than 1. At some lag time the data correlate better than with itself at zero lag time, which is certainly physically unrealistic.

When the autocovariance function is computed from the velocity signal from which the TBD corrected mean velocity is subtracted, an even higher peak in the autocorrelation function for small lag times is expected. The value of the peak is given by $(1 + 3I^2)/(1 + I^2)$, as was shown by Kolodzy (1986).

Due to velocity bias, a large velocity fluctuation is more likely to be detected for the small lag times than a small velocity fluctuation, resulting in this anomalous behaviour. Because normalization is done with the mean rms velocity and not by the average corresponding to the data record of the time lag, a peak in the autocorrelation function occurs. Normalization of the autocovariance values by corresponding lag time rms averages indeed leads to disappearance of the peak.

Furthermore it can be shown that for the case of TBD correction the autocorrelation function does not approach zero in the lag time limit, but becomes equal to I^2 even after more appropriate normalization.

This is not the case for the autocorrelation function computed from the uncorrected velocity signal. This autocorrelation function goes to zero but lies beneath the true function and integration will result in slightly smaller integral time scales. Computer simulations (Kusters et al. 1989) showed that this effect is even more pronounced for higher turbulence intensities (> 30%).

Autocorrelation functions were also computed with the Slotting Technique from radial velocity signals measured in the impeller discharge stream of a Rushton turbine impeller. The autocorrelation functions computed with the Slotting Technique were compared with the autocorrelation function obtained from the Sample Hold signal. The Sample Hold signal is created by holding the last measurement value until a new measurement is obtained. From this continuous signal velocity data are sampled periodically with a fixed frequency N_s. From this equidistantly sampled data set autocovariance values
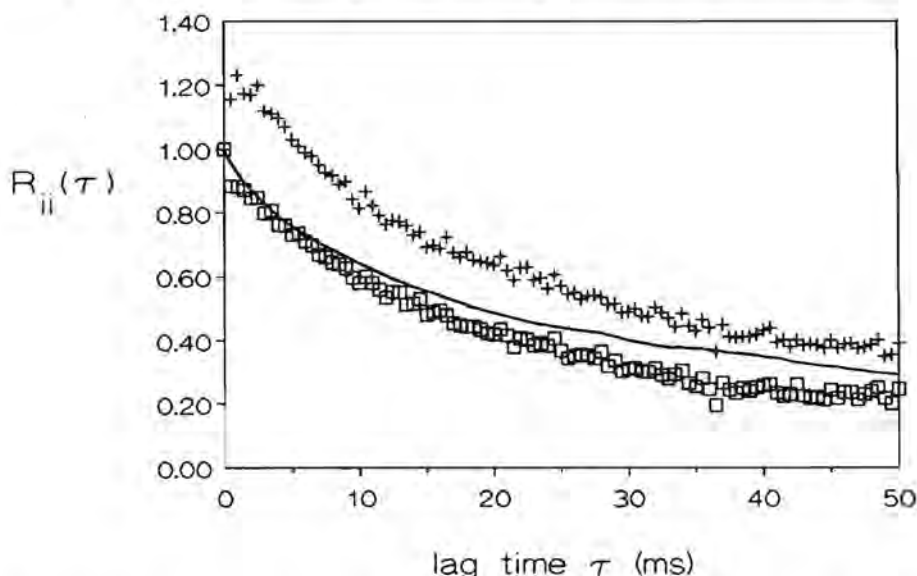
Figure 3.8. Measured autocorrelation functions, computed with the resampling technique (—) from the Sample-Hold signal and with the Slotting technique from the TBD corrected (+) and uncorrected velocity (□) signals, normalized by u_{TBD} and per lag time slot respectively.

for subsequent lag times of k $\Delta\tau$ = k/N$_s$ are readily computed, where k varies from zero to the number corresponding with the largest delay time in consideration. This resampling technique yields unbiased results if the data rate N is large compared to the frequency of the large-scale eddies, i.e. if N • T$_i$ > 5 (Kusters et al. 1989). The autocorrelation functions computed with the Slotting Technique from the uncorrected and TBD corrected radial velocity signal showed similar tendencies as obtained from simulations (fig. 3.8).

It can be concluded that processing of both uncorrected and TBD corrected velocity signals with the Slotting Technique leads to biased autocorrelation functions in the presence of velocity bias.

3.4. MIXING VESSELS

The perspex vessels of similar geometry as those used in the coagulation experiments have a flat bottom, a flat cover, four vertical baffles and a height equal to the tank diameter. The vessels were completely filled with tap water. The stirrer, a standard six bladed Rushton disc turbine impeller, had a diameter of one third of the tank diameter and was located halfway between top and bottom, giving similar flow patterns in top and bottom section. The dimensions of the vessels and impeller are summarized in table 3.1.
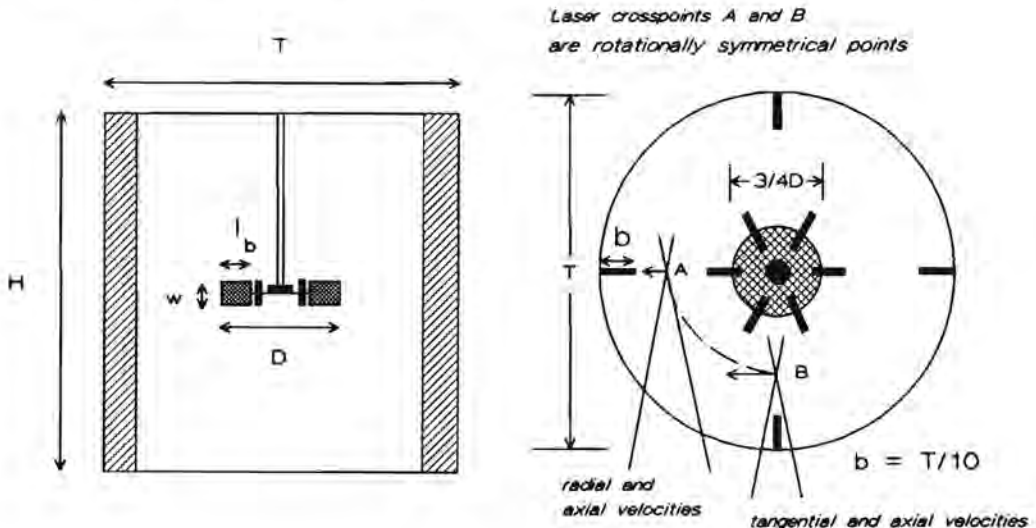
Figure 3.9. Front and top view of basic geometry of the vessels used.
H = T, D = T/3, w = D/5 and l$_b$ = D/4.

The vessels were placed in square transparent glass containers filled also with tap water so that no refraction of the laser light beams from air to water occurs over the curved surface of the container. The tangential and radial velocity component were measured in different but rotationally symmetrical points (fig. 3.9). The axial component was measured in both points and was used to check the validity of rotational symmetry.

Table 3.1. Dimensions of vessels and turbine impellers used

Dimensions in mm.

vessel diameter T	102	200	388
vessel height H	103	200	382
width baffle	10.1	20.0	38.6
thickness baffle	2.15	3.35	3.2
impeller diameter D	33.5	67.0	129.3
blade width w	6.7	13.4	25.7
blade length l_b	8.4	16.7	31.8
blade thickness d_b	0.65	1.1	3.0
disc diameter	24.8	50.2	97.0
disc thickness x	2.15	3.1	6.0
hub diameter	7.8	18.2	34.5
hub height	5.1	11.9	24.8
shaft diameter	5.0	8.1	15.0

3.5. IMPELLER POWER NUMBERS

The power number N_p of the impeller is defined as:

$$N_p = P / \rho N^3 D^5 \qquad\qquad (3\text{-}18)$$

where P = impeller power input

   ρ = fluid density

   N = impeller rotational speed

   D = impeller diameter

The total power input was measured by means of a piezoelectric dynamometer (Kistler, type 9275). Torque measurements were performed with the dynamometer on top of the electric motor that drives the rotating impeller. For the stirrer with a diameter of 6.7 cm measurements were also conducted with the dynamometer placed under the vessel. These measurements resulted in equal power numbers indicating that the friction in the motor was negligible. The power numbers of the stirrers of different size are plotted versus the impeller Reynolds number in fig. 3.10.
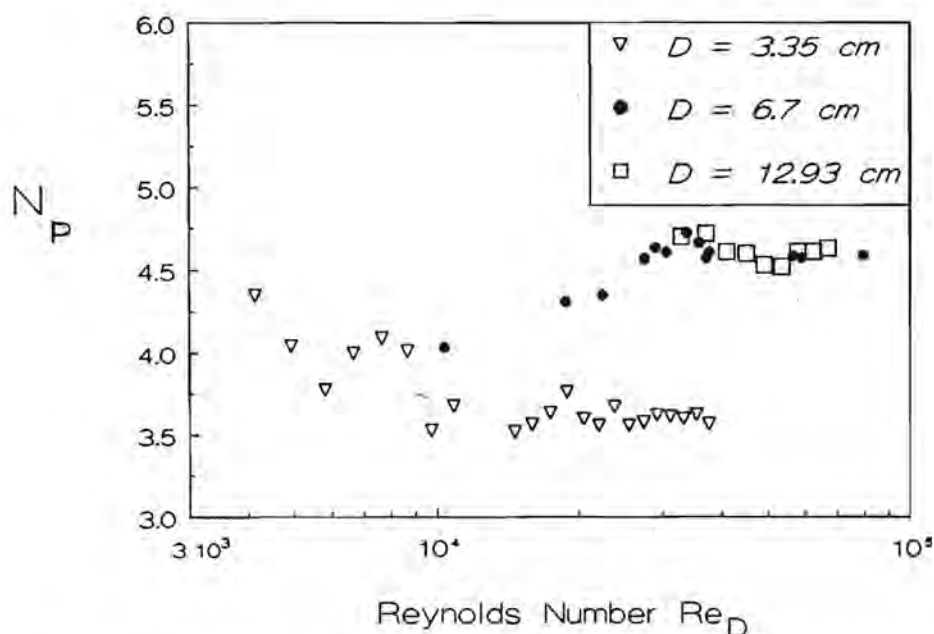
Figure 3.10. Power number N_p for different impeller sizes versus impeller Reynolds number $Re_D = ND^2/\nu$.

The power numbers are almost constant, as expected for closed baffled vessels at large impeller Reynolds numbers Re_D (Bates et al. 1966). The difference between the power numbers for the 3.35 cm and 6.7 cm impeller is caused by improper scaling of the minor dimensions, especially disc thickness x and blade thickness d_b. The ratio of x/D is larger for the 3.35 cm than for the 6.7 cm impeller and according to Nienow and Miles (1971) this would result in a decrease of N_p. Measurements of power numbers with increase of blade thickness revealed that the power number also decreases with the blade thickness according to a power law of $(d_b/D)^{-0.2}$ for d_b/D ranging from .015 to .045. Moreover, the decrease in power number may partly be attributed to a small scale effect, which was observed by Bujalski et al. (1987). This slight increase of power number with scale up can also explain that the 12.93 cm impeller has a power number equal to the one corresponding to the 6.7 cm impeller, although there is a more than proportional increase in blade thickness.

For large Reynolds numbers ($Re_D \geq \sim 10^4$) the power consumption in baffled stirred tanks is almost entirely brought about by turbulent energy dissipation (Laufhütte and Mersmann 1985). Hence for large Re_D the mean turbulent energy dissipation rate in stirred tanks may be estimated by:

$$\bar{\varepsilon} = P/\rho V = N_p \, N^3 \, D^5 / \, V \tag{3-17}$$

where V denotes the volume of the liquid in the tank.

3.6. EXPERIMENTAL RESULTS

The measurements of mean velocities, of the periodic component near the impeller, of the turbulent fluctuating velocities, of the length scales and finally of the energy dissipation rate throughout the vessels will be discussed here. The errors in measured mean, periodic fluctuating and turbulent fluctuating velocities were less than 5%. The errors in the integral length scales and energy dissipation rates amount up to 20%.

Measurements in the upper and lower sections of the tank gave the same results, so the presentation of the results is restricted to one half of the vessel.

The LDV measurements were confined to the baffle plane and the plane intermediate between two baffles. Measurements were performed at rotational speeds of 5 and 7.45 s^{-1} for the 10 cm vessel, at 5 s^{-1} for the 20 cm vessel and at 2 and 6 s^{-1} for 39 cm vessel respectively. The various experimental conditions are summarized in table 3.2.

Table 3.2. Experimental conditions

	N (s^{-1})	
	Middle plane between the baffles	baffle plane
T(cm)	$\vartheta = 45°$	$\vartheta = 0°$
10	5, 7.45	5, 7.45
20	5	5
39	–	2, 6

Most of the results are presented in non-dimensional form. The mean and rms fluctuating velocities are made dimensionless by dividing by the tip speed of the impeller, i.e., πND. The local values of the energy dissipation rate are normalized by the overall power input per unit mass, i.e., $P/\rho V$ which equals the mean turbulent energy dissipation rate at large Reynolds numbers.

3.6.1. MEAN FLOW CHARACTERISTICS

In a baffled tank a turbine impeller develops the well known radial jet. Fig. 3.11 shows the non-dimensional radial velocity profile along the turbine blade for the three impellers of interest. This profile was identical for the baffle plane and the plane intermediate between two baffles. The distances of measurement from the blade tip were 1, 2 and 2 mm for the impeller with a diameter of 3.35, 6.7 and 12.93 cm respectively. The radial profiles for the 6.7 and 12.93 cm impeller nearly coincide, but they are clearly more peaked than the radial velocity profile of the impeller that is 3.35 cm in diameter. The flattening of the radial velocity profile at a height corresponding to the

centerline of the impeller disc (z = 0) is caused by the relatively larger disc thickness of the 3.35 cm impeller.
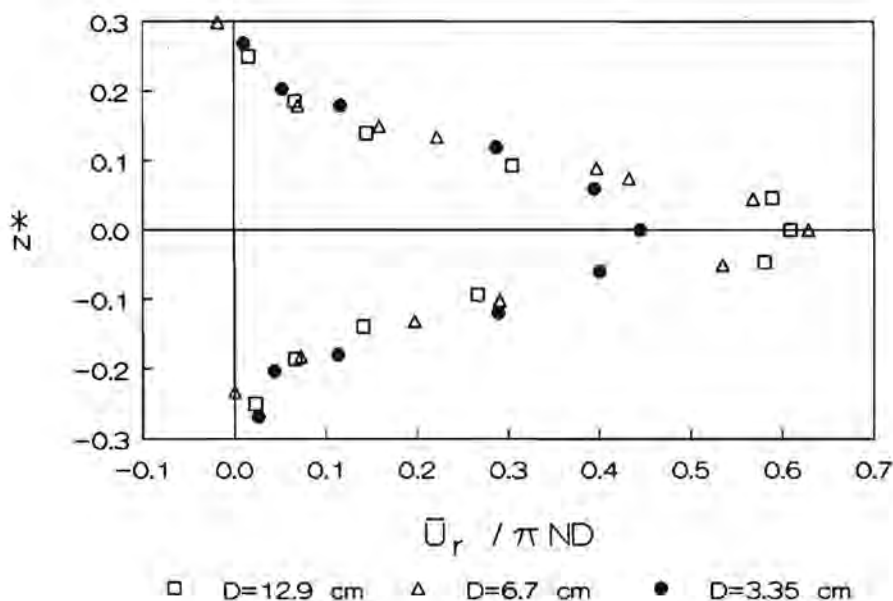
Figure 3.11. Mean radial velocity profiles at impeller tip. The distances of measurement from the blade tip are 1, 2 and 2 mm for the impeller with a diameter of 3.35, 6.7 and 12.93 cm respectively. z^* denotes the dimensionless axial coordinate $2z / D$.

To determine the discharge flow or pumping capacity Q_p of the stirrers, the mean radial velocity profiles were integrated along the width of the stirrer blades. Q_p is given by:

$$Q_p = \pi D \int_{w/2}^{+w/2} \bar{U}_r \, dz \qquad (3\text{-}18)$$

where w = the width of the blade

z = axial coordinate (the z-origin being at the midheight of the liquid, i.e., where the centerline of the impeller disc is located)

and the dimensionless discharge or flow number N_Q is defined by:

$$N_{Q_p} = Q_p / ND^3 \tag{3-19}$$

For several rotational speeds the N_{Q_p} values are summarized for the three stirrers of different size in table 3.3.

Table 3.3. Flow number N_{Q_p}

D(cm)	N (s⁻¹)

D(cm)	1	2	4	5	6	7
3.35	0.60	0.58	0.58	0.59	0.59	0.58
6.7	0.65	0.65	0.67	0.67	0.69	0.69
12.93	0.63	0.65	0.65	0.65	0.64	0.65

From table 3.3 we may conclude that the flow number remains constant with variation of the impeller speed and amounts to circa 0.59, 0.67 and 0.65 for the impeller with a diameter of 3.35, 6.7 and 12.93 cm respectively. The value of pumping capacity of the two larger impellers is smaller than the values reported by Revill (1982) in table 2 of his article. These values are in the range of 0.85 ± 0.1. Most of the data used by Revill to derive these N_{Q_p} values were based on velocity measurements performed with flow obstructive techniques such as hot wire/film anemometers and pitot tubes. As pointed out by Costes et al.(1991), hot wires and pitot tubes cannot detect reversal of flow, i.e. a change of sign in the radial velocity. This results in a larger mean radial velocity than would be obtained with laser Doppler velocimetry. Costes et al.(1991) reported values for flow numbers obtained by hot film and laser Doppler velocimetry that correspond to 0.85 and 0.66 respectively if the impeller flow capacities are calculated by eq.(3-19). The latter value is in close agreement with our measurements.

The value for the pumping capacity of the 3.35 cm impeller is slightly lower due to the larger disc thickness of this impeller with respect to the impellers used by other researchers. A larger disc thickness lowers the power number of the impeller and its corresponding flow number. Apparently it is the mechanical efficiency N_{Q_p} / N_p that remains constant; for the Reynolds numbers larger than 10^4 we found an impeller efficiency of about 15% for all three

impellers.

Fig. 3.12 shows $\bar{U}_r$ at the centerline of the impeller disc as a function of the radial distance from the impeller blade tip for all three impellers. At $r^* = 2.0$ the mean radial velocity of the 3.35 cm impeller is almost completely recovered from the inflexion near the blade tip due to the relatively large disc thickness.
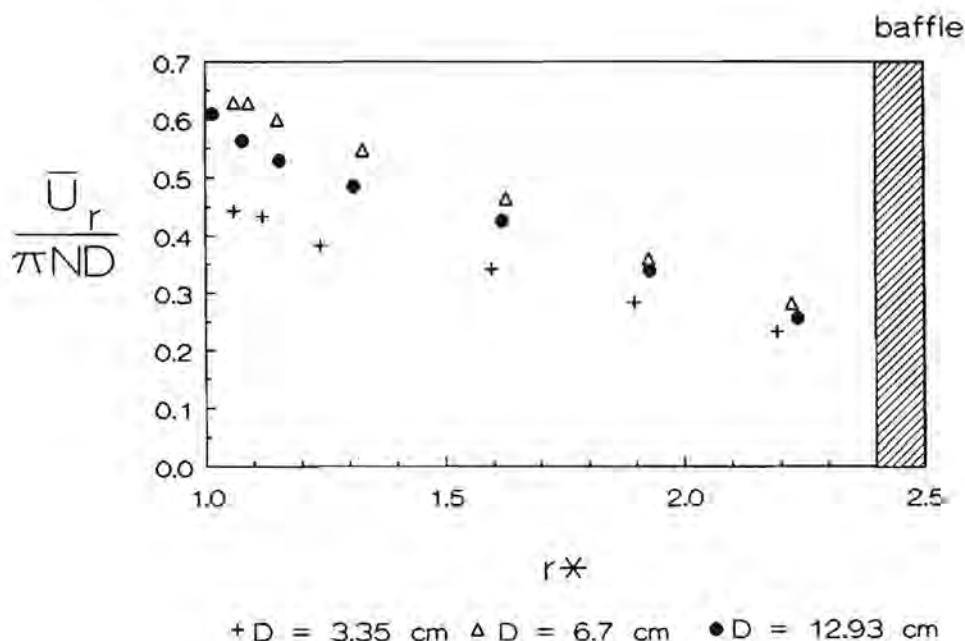
Figure 3.12. Mean radial velocity $\bar{U}_r$, normalized by tip speed, at centerline of impeller disc as a function of dimensionless radial distance r^* from impeller axis ($r^* = 2r / D$).

Fig. 3.13 presents profiles of the resultant of the radial and axial mean velocity components in the plane intermediate between the baffles as determined in the upper part of the 20 cm vessel at a rotational speed of 5 s^{-1}. The high speed jet coming from the impeller broadens and slows down as it progresses. Near the wall the radial component of the fluid velocity decreases rapidly reaching zero at the tank wall with a corresponding increase in the

axial component. The stream circulates in the rest of the tank returning to the impeller region. The centre of the circulation loop is located approximately at the non-dimensional radial coordinate $r_0^* = 2 r_0 / D = 2.4$ and the non-dimensional axial coordinate $z_0^* = 2 z_0 / D = 1.5$. The axial coordinate of the center of the circulation loop was found to be closer to the center line of the impeller stream for the 0.10 cm vessel, namely 1.0 and 1.2 at 5 and 7.45 s^{-1} respectively. No measurements were performed in the plane intermediate between two baffles for the 39 cm vessel. Costes and Couderc (1988a), however, found a value of 1.5 for the dimensionless axial coordinate of the circulation centre in the plane intermediate between two baffles for vessel sizes of 45 and 63 cm. The deviating values we found for the 10 cm vessel are probably due to the turbulent flow pattern being not yet completely developed at the low impeller Reynolds numbers ($< 10^4$) that correspond to the experimental conditions of the 10 cm vessel.
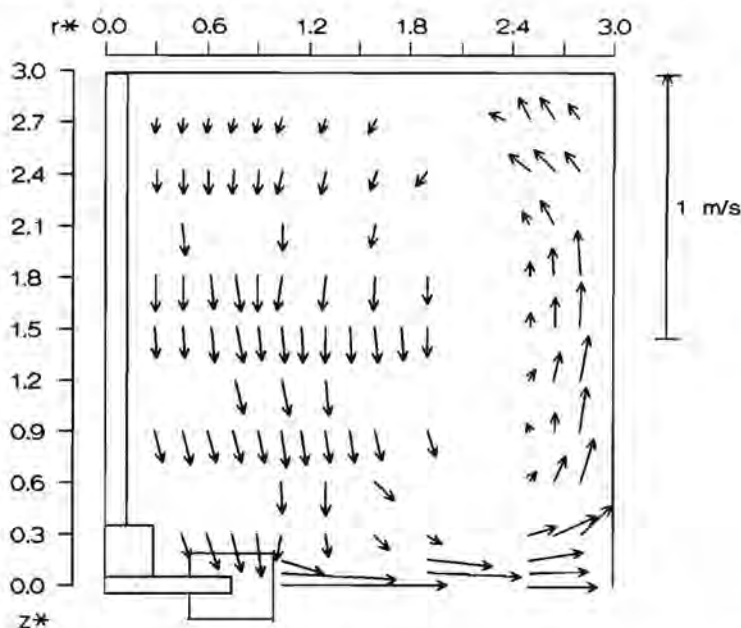
Figure 3.13. Profiles of resultant of the radial and axial mean velocity components in the plane just between the baffles ($\vartheta = 45°$) of the 20 cm vessel at an impeller speed N of 5 s^{-1}.

Laser velocimeter measurements were also carried out in the baffle plane ($\vartheta = 0°$). As an example Fig. 3.14 shows the profiles of the resultant of the radial and axial mean velocity components in the baffle plane, as measured in the 39 cm vessel at a rotational speed of 6 s^{-1}. In agreement of findings of Costes and Couderc (1988a) we observed that the discharge flow is independent of ϑ except for the region close to the baffle. The circulation loops, however, change significantly. The circulation centre was located closer to the centerline of the impeller stream at $z_0^* = 0.8$ and also nearer to the impeller axis at a radial position of $r_0^* = 2$. This location was independent of vessel size.
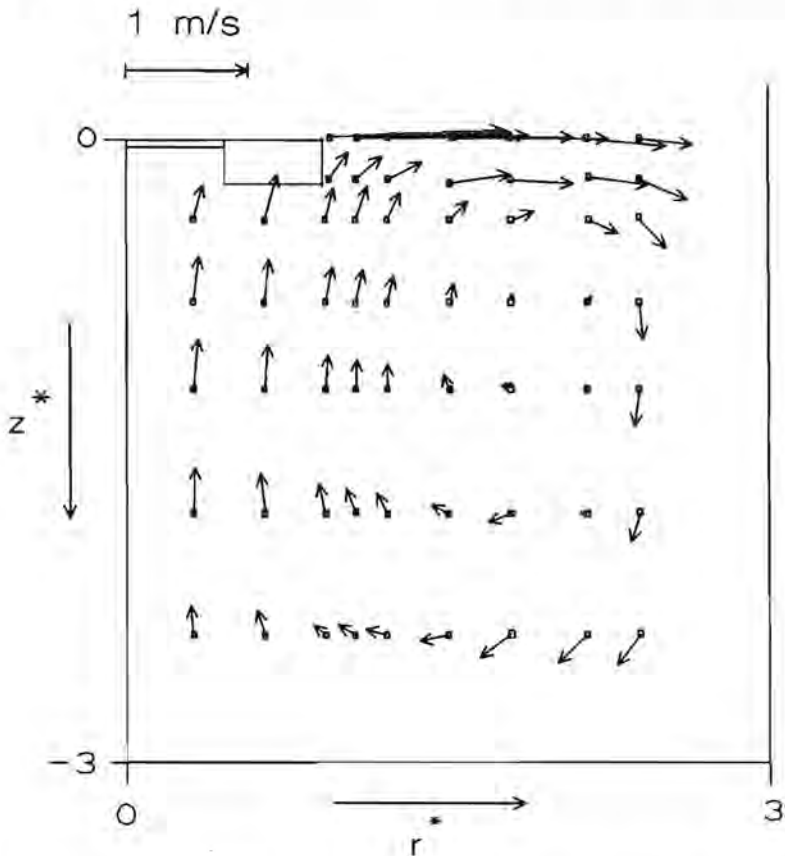
Figure 3.14. Profiles of resultant of the radial and axial mean velocity components in the baffle plane ($\vartheta = 0°$) of the 39 cm vessel at an impeller speed N of 6 s^{-1}.

The circulation flow capacities (Q_c) were determined by integration of the axial mean velocity profile from the impeller axis to the radial coordinate of the circulation centre at the axial position of the circulation centre. This circulation capacity corresponds to the fluid flow which is coming back to the impeller. The circulation flow number N_{Qc} which is defined as $2Q_c / ND^3$, has been tabulated in table 3.4.

Table 3.4. Circulation flow number N_{Qc}

		N_{Qc}	
T(cm)	N(s⁻¹)	$\vartheta = 45°$	$\vartheta = 0°$
10	5	2.2	1.6
	7.45	2.5	1.7
20	5	2.8	1.8
39	2	-	1.9
	6	-	1.8
accuracy		± 0.4	± 0.2

Apart from the case of $N = 5$ s⁻¹ in the 10 cm vessel, the values for the circulation flow numbers do not differ significantly and are approximately equal to 1.8 and 2.7 for the baffle plane and the middle plane respectively. Hence, the ratio of the circulation to the discharge flow number amounts to circa 2.5 and 3.8 for $\vartheta = 0°$ and $\vartheta = 45°$ respectively. In view of the errors involved these values are not any different from the values Costes and Couderc (1988a) presented.

The tangential component proved to be only fairly strong near the turbine impeller. Fig. 3.15 shows the radial and tangential mean velocity on the centerline of the impeller stream in the baffle plane of the 20 cm vessel. The radial and tangential velocities are about equal near the impeller, but the tangential velocity decreases more rapidly than the radial with increasing

distance. These data are in agreement with findings of Cutter (1966), whose results are also presented in fig. 3.15. Compared to the resultant of the radial and axial movements, the tangential component remains less important in the rest of the tank, except for the centres of the circulation loops. In the bulk of the tank its value amounts to approximately 0.05 times the tip speed.
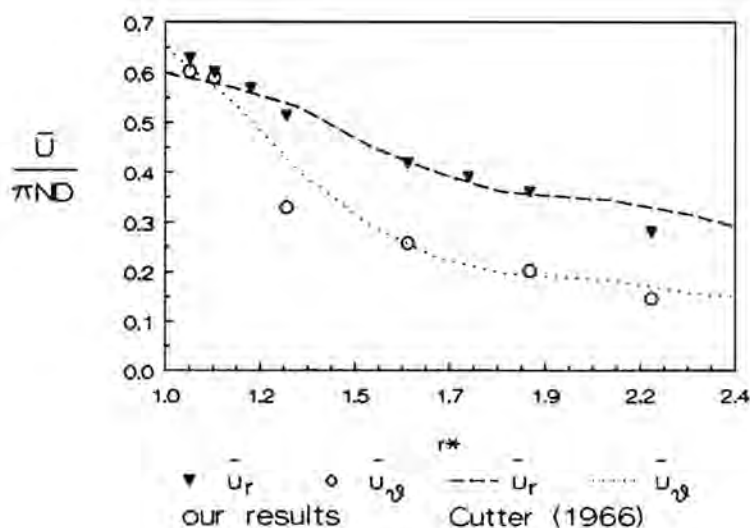
Figure 3.15. Radial and tangential mean velocity at the centerline of the impeller stream in the baffle plane of the 20 cm vessel.

3.6.2. PERIODIC FLUCTUATIONS

The spectra of the 3 fluctuating velocity components in the discharge flow of the turbine impeller show sharp peaks at the frequency of the blades' passage and closer to the impeller also at frequencies of sub- and higher harmonics. Fig. 3.16 shows a representative example of a measured frequency power spectrum near the impeller tip. These peaks reveal the presence of a

strong periodic contribution in the fluctuations, which is caused by the
passing of the trailing vortices coming from behind the turbine blades (Van 't
Riet and Smith 1975). The periodic fluctuating velocity u_p must be separated
from the turbulent part u_t of the fluctuations, because the statements of the
turbulence theory can only be applied to u_t.

It is possible to eliminate the random turbulence in the signal by phase
averaging (Reynolds and Hussain 1972) the velocity signals between successive
leading and trailing blades. With phase averaging the average over an ensemble
of points having the same phase with respect to a reference oscillator (in our
case the rotating blades) is obtained. At first the measurements were
synchronized with the rotation of the impeller to obtain results similar to
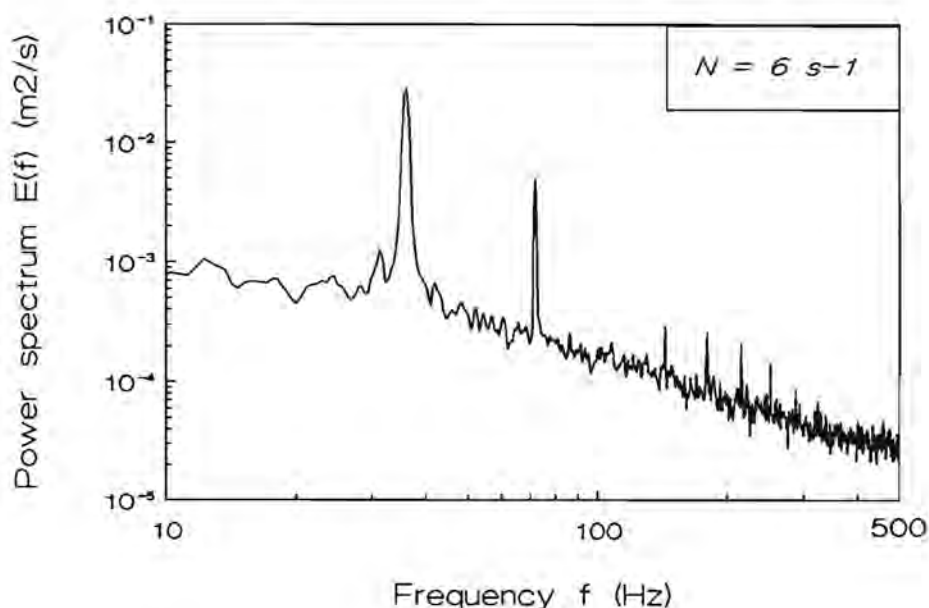
Figure 3.16. Frequency power spectrum $E_{ii}(f)$ near the impeller tip.

those of a rotating probe. This was performed by resampling the sample-hold
signal of the velocimeter with a frequency equal to 40 times the frequency of
the blades' passage. The data rate of the counter was set above 1 kHz in order
to establish at least one measurement per one and a half degree interval of
rotation. After ensemble averaging over the one and a half degree intervals of
rotation only the periodic fluctuation between leading and trailing blade

remains. The ensemble averaging was performed over 125 data points. The number of data points was limited by the finite accuracy with which the rotational speed of the impeller was determined.

Fig. 3.17 shows an example of the velocity vs. time curves constructed in this way. From these periodic velocity signals the so-called peak-to-peak (Van der Molen and van Maanen 1978) and rms values of the periodic velocity fluctuations could be obtained. The peak-to-peak value U_{p-p} denotes the difference between the minimum and maximum periodic fluctuating velocity. The ratio of the rms and peak-to-peak value amounts to circa 3.1 and 3.2 for the radial and axial periodic component respectively. The latter value is in good agreement with the value (3.4) which was deduced from the periodic velocity-time curve (fig. 3) presented by Van der Molen and van Maanen (1978). Subtraction of the periodic signal from the original data set yields the turbulent velocity signal, from which the turbulent rms velocity can be evaluated. The mean squared value of the total fluctuations was also computed from the data set. It was found to be equal to the summation of the mean squared values of the turbulent and periodic velocity fluctuations, indicating that these fluctuations are uncorrelated, i.e.:

$$u_{tot}^2 = u_t^2 + u_p^2 \qquad (3-20)$$
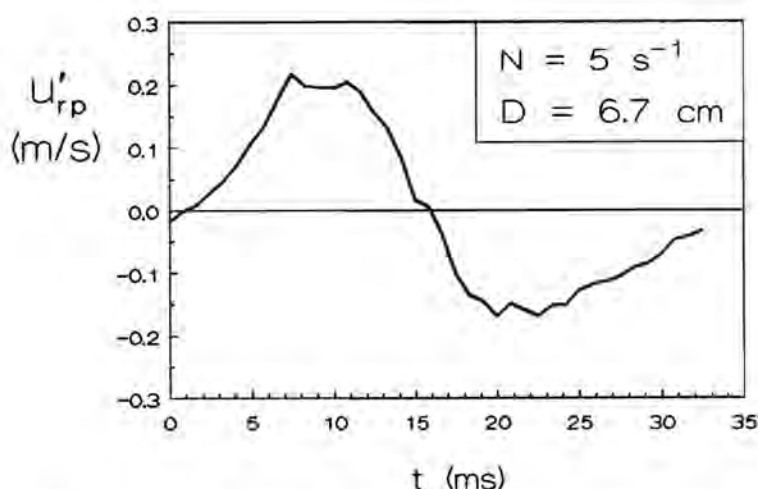
Figure 3.17. Periodic radial fluctuating velocity versus time.

Fig. 3.18 shows the radial periodic component vs. radial separation from the blade tip, for the three stirrers of different size. These values were obtained from one-dimensional power spectra of the radial velocity component. The integral of the one dimensional power spectrum corresponds to the total mean square value of the fluctuating velocity component. Without the periodic fluctuations the power spectrum would be smooth and not reveal any spikes, as shown in fig. 3.16. Because the turbulent and periodic fluctuations are uncorrelated, integration of the power spectrum without the peaks of the periodic component yields the turbulent contribution, whereas the area under the peaks gives the periodic contribution to the total velocity fluctuations. For determining the amplitude of the periodic fluctuations the use of the power spectrum is preferred to the phase averaging technique. The reason is that with the power spectrum the averaging process is not restricted by the finite accuracy with which the impeller speed is known. Furthermore, the
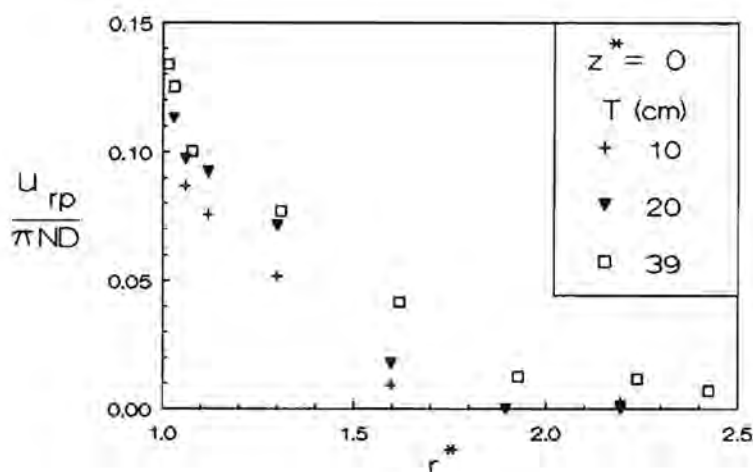
Figure 3.18. rms radial periodic component versus radial coordinate r^*.

passage of the trailing vortices along the measuring volume of the laser velocimeter does not occur continually at exactly the same time intervals. This is caused by errors in the relative positions of the blades and small

deviations of the impeller shaft from the axis of the cylindrical tank during operation. The synchronizing technique, however, can only be tuned to one characteristic frequency, resulting in loss of information about the periodic component due to the small spread in periodic frequency. From the power spectrum the complete area under the peaks is evaluated. A small spread in periodic frequency does not bias the periodic contribution obtained from the power spectrum.

Fig 3.18 shows that the radial periodic component decays very fast with increasing radial distance to the impeller and at $r^* = 2$ almost only pure turbulence remains. The periodic component seems to increase somewhat with scale-up. This was also noticed by Van der Molen and Van Maanen (1978).

In fig. 3.19 the radial periodic component in the $z = 0$ plane for $r^* = 1.03$ is plotted vs. vessel diameter T. Fig. 3.16 also includes data from Van der Molen and van Maanen (1978), Mahouast et al. (1988) and Laufhütte and Mersmann (1985). Van der Molen and van Maanen did not determine u_p but the peak-to-peak value U_{p-p}. We assumed $u_p = U_{r,p-p}/3.4$. From fig. 3.19 it can be concluded that the periodic component increases proportionally with $D^{0.3}$. The scatter in
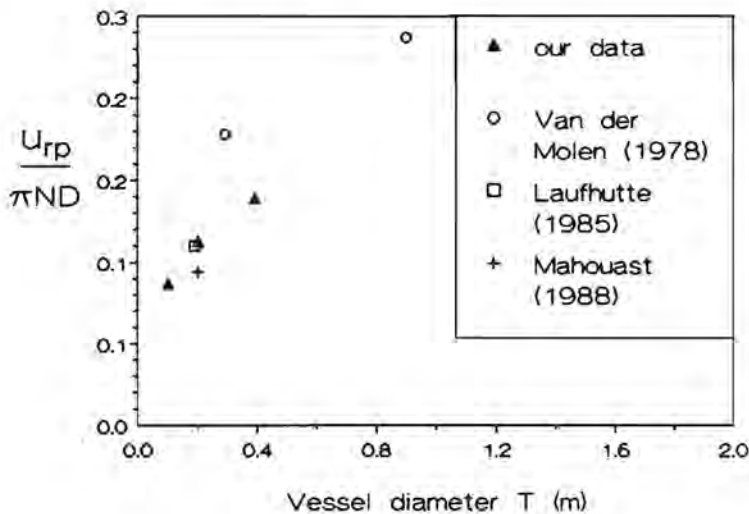
Figure 3.19. rms radial periodic component for $z^* = 0$ and $r^* = 1.03$ versus vessel size T.

the data of fig. 3.19 is probably due to the differences in relative minor
dimensions of the stirrers used by the various researchers. For instance the
blade thickness has a pronounced effect on the amplitude of the periodic
component (Van der Molen and Van Maanen 1978).

Fig. 3.20 shows the variations of the radial and axial periodic velocity
fluctuations over the blade width as observed near the impeller tip for the
20 cm vessel. These plots are consistent with the axial profiles of the
periodic velocity fluctuations (fig. 10) as computed by Placek and Tavlarides
(1985). A minimum respectively maximum is observed halfway between the
impeller disc plane and the blade edge for the radial and axial
periodic component indicating the location of the vortex axis.

In fig. 3.20 also the axial profiles of the radial and axial turbulent rms
velocity are included. Since the periodic fluctuations are not negligible with
respect to these turbulent fluctuations, serious errors would result in the
estimates for the local energy dissipation rate if the periodic component was
not corrected for.
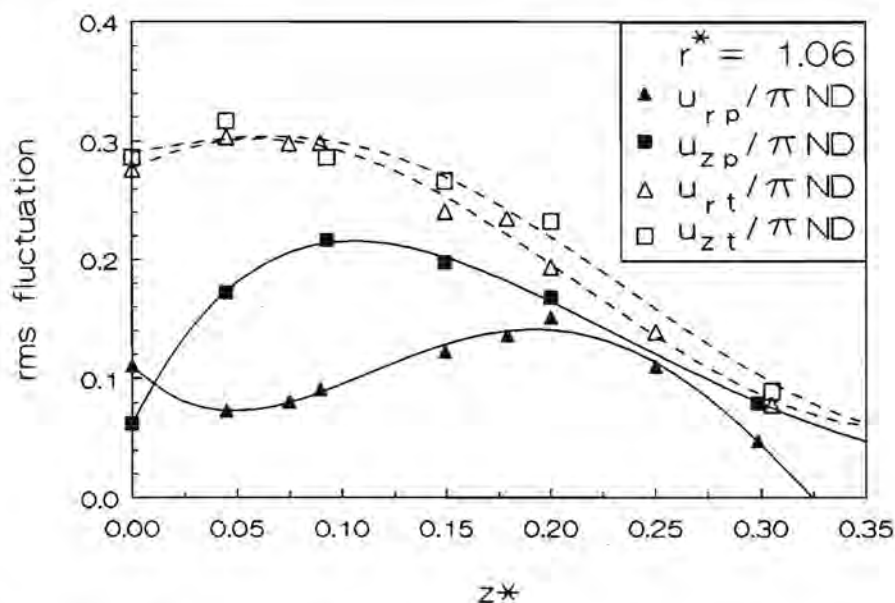
Figure 3.20. Radial and axial rms periodic and turbulent fluctuating
velocities at several axial positions at r^* = 1.06 for the 6.7
cm impeller.

3.6.3. TURBULENT FLUCTUATIONS

Although the periodic and turbulent fluctuations were shown to be uncorrelated this does not mean that the turbulent velocity is uniform over the distance between the impeller blades. By phase averaging the rms turbulent velocity was computed as a function of the angle of rotation $\varphi = \omega t$ ($= 2\pi N t$). Fig. 3.21 shows the variation of the axial rms turbulent velocity near the blade edge of the 6.7 cm impeller. In fig. 3.21 also the periodic axial velocity fluctuation is included. The core of the passing vortex shows up as the steep increase in the periodic velocity curve. The vortex axis is located at circa 20°. The maximum value of the rms velocity fluctuation is also found at this position behind the leading blade. As can be seen from fig. 3.18 the variation of the rms turbulent velocity is stronger near the blade tip. It, however, was found to decrease rapidly with increasing separation distance from the impeller. At $r^* = 1.5$ the rms turbulent velocity is almost uniform over the arc length between the leading and trailing blade.
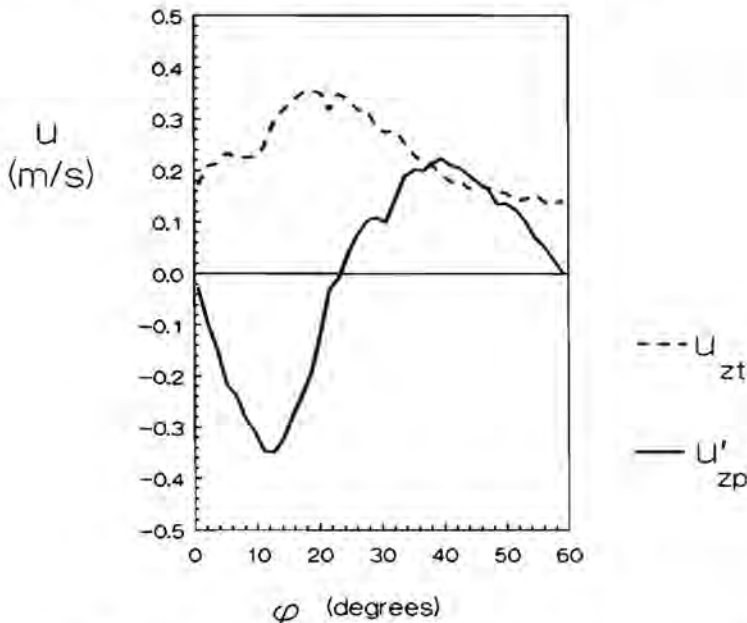
Figure 3.21. Axial rms turbulent velocity u_{zt} and axial periodic velocity u'_{zp} near blade edge of 6.7 cm impeller as a function of the angel of rotation α.

Figure 3.22. Radial rms turbulent velocity u_{rt} profiles in 39 cm vessel.

Figure 3.22 shows curves for the dimensionless radial rms turbulent fluctuating velocity for locations at r^* between 1.3 and 2.24 as measured in the baffle plane of the 39 cm vessel at a rotational speed of 2 s^{-1}. These values were obtained by integration of the power spectrum after cutting off the peaks of the periodic component. The turbulent velocity is about 2 to 5 times larger in the impeller stream than in the bulk of the tank. The spatial variation of turbulent velocity is small in the bulk. Similar results were obtained at a rotational speed of $N = 6$ s^{-1}.

Measurements in the baffle and mid plane of the 10 and 20 cm vessel showed that the turbulent fluctuating velocity field is similar for both planes.

The measurements also indicated that the turbulent velocity field is almost isotropic, i.e., u_{rt} equals $u_{\vartheta t}$ and u_{zt} , except for the region of $z^* \cong \pm 0.2$, where the impeller jet stream merges with the main circulation loop, and in the lower and higher part of the bottom and top section of the circulation loop respectively. As an example fig. 3.23 shows the values of the radial, axial and tangential turbulent velocities in the lower part of the bottom section of the 39 cm vessel, revealing a strong anisotropy.
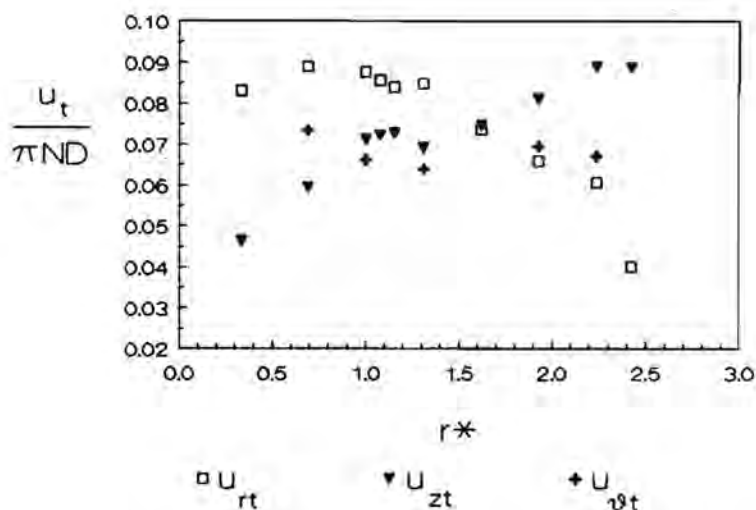
Figure 3.23. Radial, axial and tangential rms turbulent fluctuating velocities at $z^* = 1.86$ in the 39 cm vessel.

In figure 3.24 the radial rms velocity profiles for the 10 and 39 cm vessel at $r^* = 1.06$ are presented in the same plot. The rms velocity fluctuations in the .10 m vessel are larger in the impeller discharge stream zone and smaller in the bulk compared to the 39 cm vessel.
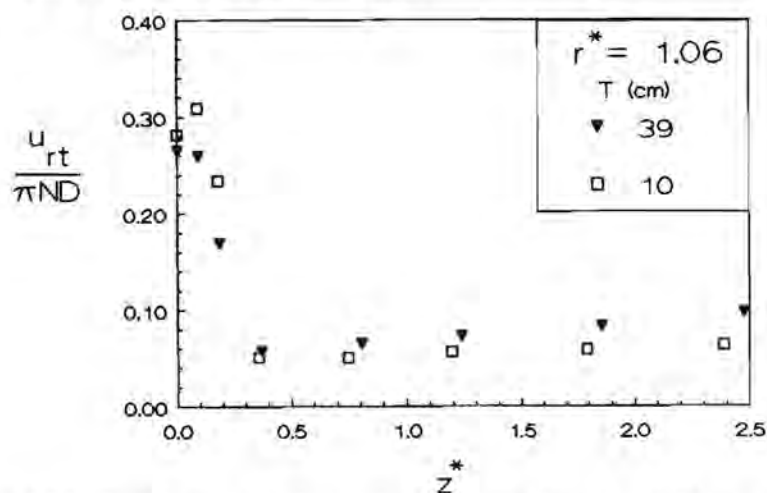
Figure 3.24. Radial rms turbulent velocity profile for 10 and 39 cm vessel.

3.6.4. INTEGRAL LENGTH SCALES

Near the blade tip the integral time scale is difficult to deduce from the autocorrelation function, because of the presence of the periodic component which shows up as a cosine (Mujumdar et al. 1970). The macro time scale was therefore computed from the power spectrum using slightly modified eqs. (3-7) and (3-8):

$$T_i = \frac{1}{4u_{it}^2} \lim_{f \to 0} E_{ii}(f) \qquad\qquad (3\text{-}22)$$

$$\text{where } E_{ii}(f) = 4u_{i,tot}^2 \int_0^\infty R_{ii}(\tau) \cos(2\pi f\tau) \, d\tau \qquad (3\text{-}23)$$

This time scale should provide an estimate of the eddy size unbiased by the large periodic fluctuations produced by the passage of the turbine blades.

The integral length scale L^i in the impeller discharge stream is equal to 0.18D, i.e. approximately the blade width. In the case of isotropic homogeneous turbulence, the determined length scale would correspond to $L = L_f + 2L_g = 2L_f$, where L_f = the longitudinal integral length scale and L_g = the lateral or transverse integral length scale. So our data indicate a longitudinal length scale equal to half the blade width and this outcome is in agreement with findings of other researchers (Cutter 1966 and Mujumdar et al. 1970). Because Cutter and Mujumdar et al. determined $L_r = |\bar{U}| \, T_r$, they observed a moderate variation in the length scale with radial distance, not surprisingly because from the blade tip to the vessel wall, the flow direction changes from tangential-radial to radial and near the wall to radial-axial, so only in the middle region, $T_f = T_r$ and the equality $L_f = L_r$ is justified. Costes and Couderc (1988b) reported a length scale of one fourth of the blade width. They, however, determined $L_r = \bar{U}_r T_r$ which gives smaller values than those obtained by Cutter and Mujumdar et al. because $\bar{U}_r$ is smaller than $|\bar{U}|$.

The integral length scale L^i appears to be roughly equal to the diameter of the trailing vortex, which is approximately 0.14 D (Placek and Tavlarides 1985).

The integral length scale L^b in the bulk is larger than the length scale obtained in the impeller stream. Clearly the information about the shape of the flow inducing impeller has been lost upon interaction of the impeller stream with the baffles and the wall of the tank.

In contrast with the integral length scale in the impeller stream, L^b increases more than proportionally with scale-up. In the 10 cm vessel L^b varies from 2 to circa 3 times L^i, the length scale L^b in the 20 cm vessel exhibits a ratio of 2 to 4 and in the 39 cm vessel even length scales L^b of half or equal to the vessel diameter being 8 to 16 times L^i were observed. If these large length scales are substituted in eq. (3-1) to compute the local energy dissipation rate, the ratio of local and mean energy dissipation rate becomes smaller in the bulk of the 39 cm vessel compared to for instance the 10 cm vessel, despite a higher value of the bulk rms velocity. In fact all values of the normalized energy dissipation rate would be smaller than those obtained in the 10 cm vessel. Adjustment of the constant A in eq. (3-1) would be necessary to assure a correct integral power balance. This constant A however is expected to be independent of scale. Since Taylor's hypothesis does not hold for flows with high turbulence intensities (Fisher and Davies 1964), this might explain the increase of measured length scales in the bulk. In the impeller discharge stream these turbulence intensities $I = (2k)^{1/2}/|\bar{U}|$ amount to about 60% near the impeller tip to 80-90% near the wall. The turbulence intensity increases with distance from the impeller tip as the mean velocity decreases in that direction more rapidly than the rms of the fluctuations. In the bulk average values of 90%, 100% and 110% for the 10, 20 and 39 cm vessel respectively were observed. In the 39 cm vessel even values of I equal to 140-150% were measured. The errors incorporated in usage of Taylor's hypothesis will increase with I and for I > 100% large deviations are to be expected because of flow reversal, resulting in physically unrealistic values of L^b.

For computation of the bulk energy dissipation rate we used the length scales as found in the 10 cm vessel and scaled these values up proportionally with vessel size. In the 10 cm vessel the errors in the measured length scales will be most similar for both bulk and impeller discharge zone, because for this vessel size the turbulence intensity remains almost constant. A constant error throughout the vessel is corrected for by suitable choice of the constant A in eq. (3-1).

A value of L^b as found in the 10 cm vessel is also physically most realistic because it corresponds to the width of the circulation stream near the tank wall. The width of this circulation stream is determined by the baffles that

can be considered as the obstruction responsible for generating the turbulence in the bulk of the tank.

The integral length scale in the bulk flow has also been evaluated by comparing it to the macro length scale which follows from the equality of eq.(3-1) to the following formula for the energy dissipation rate in homogeneous isotropic turbulence (Taylor 1935):

$$\varepsilon = 15 \ v \ \frac{u_t^2}{\lambda_g^2} \tag{3-24}$$

where λ_g denotes the Taylor micro scale or dissipation scale.

Equating eq.(3-24) to (3-1) and assuming isotropy yields for the integral length scale:

$$L = \left(\frac{3}{2}\right)^{3/2} \frac{A \ u_t \ \lambda_g^2}{15 \ v} \tag{3-25}$$

Substitution of the Taylor micro scale λ_g and the turbulent velocity u_t in eq.(3-25) would result in an estimate for the integral length scale. The Taylor micro scale can be obtained from the intercept of the horizontal axis by the parabolic function which describes the transverse autocorrelation function $g(r)$ for small values of the separation distance r. Substitution of the relations $L = c_i \ L_i$ and $\lambda_g = \sqrt{c_i} \ \lambda_i / 2$ that are valid for homogeneous isotropic turbulence, in eq.(3-24) results in the following relationship between L_i and λ_i:

$$L_i = \left(\frac{3}{2}\right)^{3/2} \frac{A \ u_t \ \lambda_i^2}{60 \ v} \tag{3-26}$$

where L_i and λ_i represent the integral and micro length scale in any arbitrary direction and c_i the corresponding geometrical scaling parameter that relates L_i and λ_i to L and λ_g respectively.

The macro length scale obtained from eq.(3-26) can be readily compared to the value calculated by integration of the autocorrelation function $R_{ii}(r_k)$. Eq.(3-26) is easier to apply than eq.(3-25) because it does not require the velocity fluctuations under consideration to be normal to the flow direction.

The determination of the micro scale is a delicate task. The measuring volume of the laser Doppler velocimeter limits the minimum length scale that can be observed reliably. The length of the measuring volume is equal to the length of the probe volume, that is 1.3 mm at its maximum. This length

restricted valid measurements to be made to the bulk flow of the 20 and 39 cm vessel. The computation of $R_{ii}(r_k)$ is discussed in appendix B.

Table 3.5 summarizes some results representative for the measurements conducted in the 20 and 39 cm vessel respectively. In the table the value of the integral length scale inferred from the integral time scale is compared to the macro length scale computed with eq.(3-26) where the proportionality constant A was assumed to be unity (see next section). The values in the 20 cm vessel are in good agreement, but the values for the integral length scale for the 39 cm vessel are too large. This confirms our previous conclusion, that the integral length scale as obtained from the integral time scale measured in the bulk of the 39 cm vessel, should not be used in estimating the local values of the energy dissipation rate.

Table 3.5. Comparison of the macro length scales L_i obtained from the integral time scale (eq.(3-5)) and from the Taylor micro scale (eq.(3-26)).

T	N	z^*	r^*	u_{it}	$|\bar{U}|$	λ_i	L_i eq.(3-5)	eq.(3-26)
cm	s^{-1}			$m\ s^{-1}$	$m\ s^{-1}$	mm	mm	
39	2.0	0.8	1.00	0.0446	0.103	5.7	61.3	23.0
		1.86	1.35	0.0627	0.078	10.2	142.1	48.0
		2.47	1.11	0.0783	0.092	12.7	331.1	83.5
20	5.0	1.49	1.60	0.0686	0.127	3.6	12.7	11.1
		2.39	1.60	0.0617	0.119	5.6	25.3	24.5

3.6.5. ENERGY DISSIPATION RATES

The values of $k^{3/2}/L$ were spatially integrated over the entire tank and multiplied by the density of the fluid to obtain the total power input. With this integration it was assumed that 20% of the energy was dissipated in the impeller itself in analogy with Cutter (1966). Dividing the integrated value by the measured impeller power, the resulting value of the constant A was found to be 1 ± 0.2.

Antonia et al. (1980) evaluated the value of the constant in the inviscid estimate of the energy dissipation rate for a plane jet. They compared the energy dissipation rate deduced from the Taylor micro scale (eq. (3-23)) with the following inviscid estimate:

$$\varepsilon = C \frac{u_0^3}{L_0} \qquad\qquad\qquad (3-27)$$

where u_0 denotes the rms fluctuating velocity in the direction of the mean flow and L_0 denotes the half width of the jet. From their measurements they concluded that $C = 1.02$. Since isotropy in the discharge flow of the impeller prevails and the integral length scale is recognized to be about twice L_0 this result corresponds to a value of 1.11 for the constant A, which is not significantly different from our value.

Near the blade tip the energy dissipation rate is not uniform with respect to the angle of rotation. This follows directly from the rms turbulent velocity fluctuations not being constant over the perimeter of the impeller. Fig. 3.25 shows the variation with the angle of rotation of the energy dissipation rate $<\varepsilon>$ computed from the phase averaged values for the turbulent velocity fluctuations (see section 3.6.3). The location of the maximum value of $<\varepsilon>$ corresponds well with that of the trailing vortex axis. The mean $\overline{<\varepsilon>}$
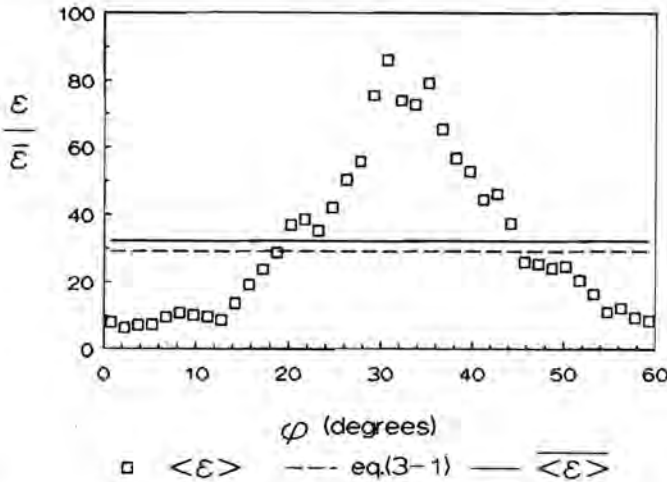
Figure 3.25. Energy dissipation rate $<\varepsilon>$ computed from the phase averaged values for the rms turbulent velocity fluctuations as a function of angle of rotation φ.

over the angle of rotation proved to be only slightly higher than the estimate obtained by substituting the time averaged turbulent kinetic energy in eq.(3-1). The maximum energy dissipation rate occurring near the blade tip cannot be obtained by time averaging. For the 20 cm vessel the time averaged maximum relative energy dissipation rate ε was found to be 37 whereas phase averaging revealed a maximum value of approximately 80.

In fig. 3.26 the time averaged energy dissipation rate profiles at $r^* = 1.06$ are plotted for the three different vessel sizes. A decrease of $\varepsilon/\overline{\varepsilon}$ in the impeller discharge zone near the impeller blade tip and necessary increase of $\varepsilon/\overline{\varepsilon}$ in the bulk zone with vessel size is observed. The maximum values of $\varepsilon/\overline{\varepsilon}$ near the blade tip are 45, 37 and 28 respectively for an increasing vessel size of 10, 20 and 39 cm. The corresponding average normalized energy dissipations in the bulk amount to circa 0.07, 0.11 and 0.15.
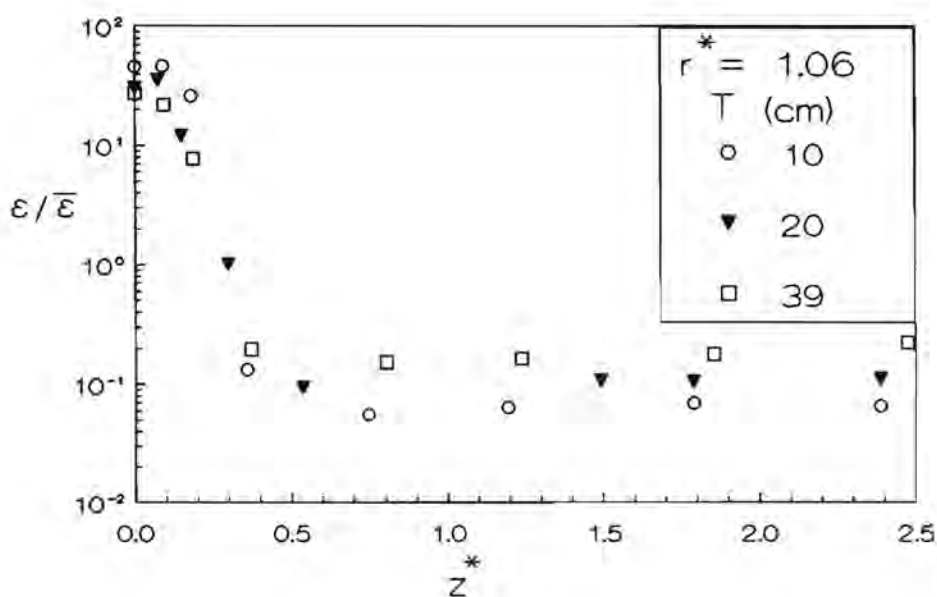
Figure 3.26. ε / $\overline{\varepsilon}$ values for different vessel sizes at several axial locations

In fig. 3.27, 3.28 and 3.29 the lines of equal $\varepsilon/\bar{\varepsilon}$ are plotted for the 10, 20 and 39 cm vessel respectively. For all of these vessels, the turbulence in the turbine impeller discharge stream remains at a fairly constant level except for the immediate vicinity of the impeller. The energy dissipation levels differ, however, considerably throughout the recirculation flow region of the stirred tanks. The minimum levels of energy dissipation rate were found to amount to 0.05, 0.08 and 0.11 for the 10, 20 and 39 cm vessel respectively. The ratio of the maximum to the minimum turbulent energy dissipation rate decreases from 900 for the 10 cm vessel to 250 for the 39 cm vessel.

Such a decrease in the ratio of energy dissipation rate in impeller discharge and bulk zone seems to be induced by a change of the trajectory of the trailing vortices with scale-up. These trailing vortices are mainly responsible for the generation of the turbulent kinetic energy (Placek and Tavlarides 1985). As has been noted by Popiolek et. al. (1987), with increasing impeller size the trajectory of the trailing vortices is directed in a more radial direction. If the propagation velocity of the trailing vortices remains proportional to the tip speed with scale-up, the energy
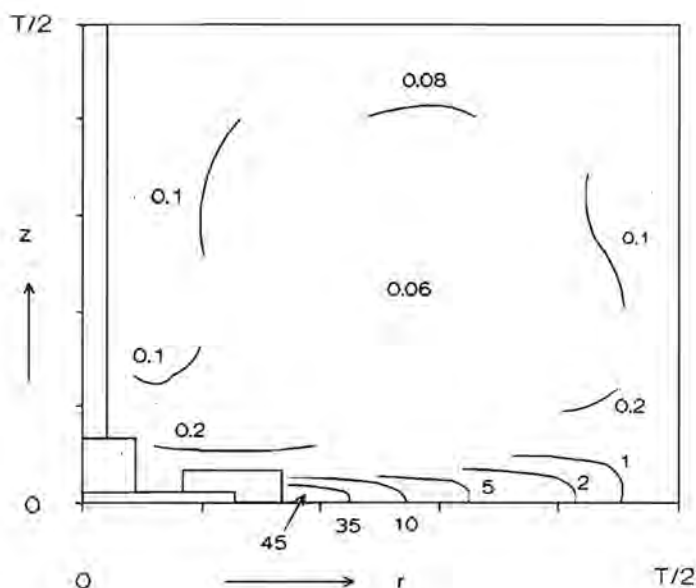
Figure 3.27. $\varepsilon / \bar{\varepsilon}$ isoenergetic lines in 10 cm vessel.
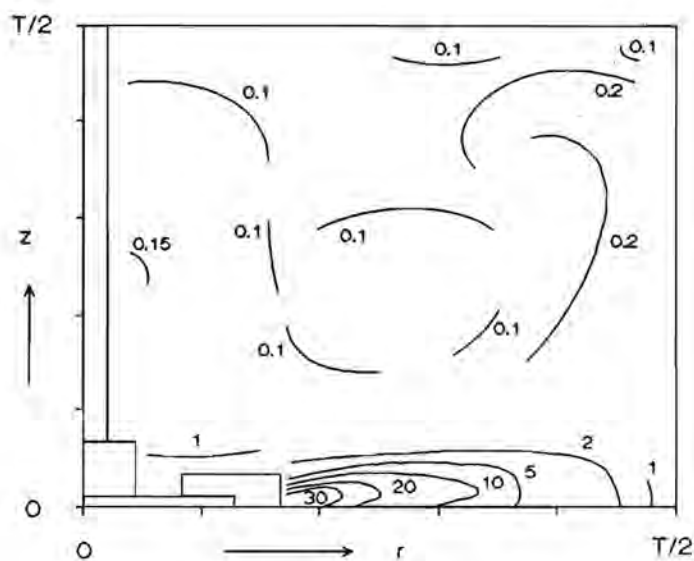
Figure 3.28. $\varepsilon / \bar{\varepsilon}$ isoenergetic lines in 20 cm vessel.
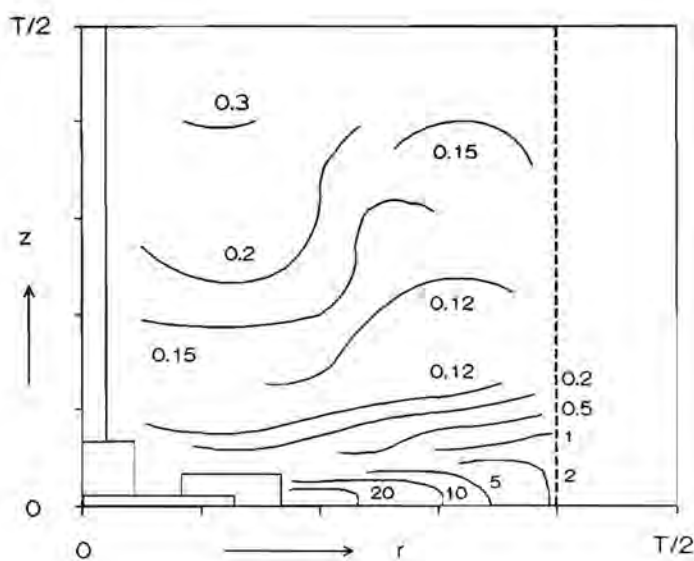
Figure 3.29. $\varepsilon / \bar{\varepsilon}$ isoenergetic lines in 39 cm vessel.

transfer of the trailing vortices to the turbulent eddies is projected towards larger distances from the impeller, resulting in smaller values of ε near the blade tip and larger values of ε in the bulk zone with increasing vessel size (for the same $\bar{\varepsilon}$). Furthermore the change of the trajectory of the trailing vortices with vessel size results in an increasing periodic component in the impeller discharge zone with vessel size. This increase was already observed by Van der Molen and van Maanen (1978) and has also been verified by our own experiments.

3.7. DISCUSSION

The results presented in the previous section are compared to the findings of Costes and Couderc (1988b) and of Laufhütte and Mersmann (1985).

Costes and Couderc determined the values of the local energy dissipation rate from eq.(3-24) which involves the determination of the Taylor micro scale. They reported values for the micro scale of approximately 3 mm near the blade tip of the impeller being almost independent of impeller speed N (table 1 from their article). The micro scale should however exhibit a power law dependency of $N^{-1/2}$ (Günkel and Weber 1975b). It seems likely that their results are influenced by the spatial resolution of the measuring volume of the laser Doppler velocimeter. As the length of the probe volume of the laser Doppler velocimeter Costes and Couderc used, amounted to 3.8 mm (Costes 1986), their measurements are expected to be only accurate up to a similar length scale. Their conclusions about the energy dissipation rate throughout the vessel should therefore be considered with care.

Nevertheless, the rms values of the turbulent velocity fluctuations Costes and Couderc (1988a) presented in Part I of their study, are quite similar to those we measured in the 39 cm vessel except for the immediate vicinity of the impeller. Near the blade tip the velocity fluctuations are larger, probably because no corrections were made by Costes and Couderc for the periodic component. Starting from the "inviscid estimate" for the energy dissipation rate and substituting the appropriate integral length scales in impeller stream and bulk flow, the fluctuating velocity field yields an energy dissipation rate distribution similar to the one as depicted in fig. 3-29 for

the 39 cm vessel except near the impeller tip.

Laufhütte and Mersmann (1985) conducted measurements of the radial fluctuating velocities in the baffle plane of a stirred tank, 19 cm in diameter and similar in geometry except for the position of the impeller and for the absence of the cover at the top of the tank. The impeller was located at one-third of the liquid height from the tank bottom instead of halfway between top and bottom. The different location of the impeller and the absence of the cover will certainly affect the bulk flow. The impeller discharge stream, however, is expected not to be influenced too greatly, validating the comparison of the turbulent characteristics of the impeller discharge streams for the 19 cm and 20 cm vessel respectively.

Laufhütte and Mersmann computed the energy dissipation rate distribution from the radial turbulent velocity field using the following inviscid estimate:

$$\varepsilon = C_1 \frac{u_{rt}^3}{D} \tag{3-28}$$

This equation implies isotropy and a constant length scale throughout the vessel. Laufhütte and Mersmann concluded from their measurements that the constant C_1 equals 6.5.

Their method of subtraction of the periodic component however is incorrect: they computed u_{rt} with use of the following equation: $u_{rt} = u_{r,tot} - u_{rp}$. With use of eq.(3-20) it follows that the maximum $\varepsilon/\bar{\varepsilon}$ value is not 15 as reported, but 25. The correct value of the constant C_1 should be circa 6.2. Assuming that $u_{rt} = u_{\vartheta t} = u_{zt}$ and substituting $L = D / 5$, eq. (3-1) can be rewritten as:

$$\varepsilon = C_2 * u_{rt}^3 / D = 9.2 * u_{rt}^3 / D \tag{3-29}$$

The ratio of maximum energy dissipation rate in the 20 cm vessel to their value should be equal to the ratio of the constants C_2 and C_1:

$$C_2 / C_1 = 9.2 / 6.2 \cong 37 / 25 \cong 1.5.$$

The difference in reported values of the local energy dissipation rates is solely attributed to the assumption of a constant length scale throughout the vessel, that has not been used in the present study. Clearly the assumption of a constant length scale results in an underestimation of the ratio of energy dissipation rates in bulk and impeller discharge zone.

Summarizing, the rms turbulent velocity fluctuations presented in section 3.6.5 are consistent with the findings in the literature. Discrepancies between the reported values of the local energy dissipation rates stem from different theoretical considerations with respect to the calculation of ε.

3.8. CONCLUSIONS

Detailed information about the flow generated by a Rushton turbine impeller in geometrically similar cylindrical baffled tanks, 10, 20 and 39 cm in diameter has been obtained.

When normalized to the tip speed, the mean velocity profiles are approximately independent of the size of the mixing unit and of the rotational speed of the turbine impeller. The impeller pumping capacity and the circulation flow rate in the bulk were determined and the ratio of these two flow rates amounts to circa 2.5 and 3.8 for the baffle plane and the plane intermediate between two baffles respectively.

In the immediate vicinity of the impeller tip there is a distinct periodic contribution to the total velocity fluctuations arising from the trailing vortices coming from the impeller blades. This periodic component increases somewhat with scale-up. As a first approximation one may assume a proportionality with $D^{0.3}$.

The turbulent fluctuating velocity field is also dependent on scale. Near the impeller tip the turbulent velocity when normalized to impeller tip speed, decreases with increasing vessel size whereas the opposite is true for the bulk flow in the tank. The random turbulence is almost isotropic.

The integral length scale in the impeller discharge stream is approximately equal to the blade width. In the bulk of the tank the integral length scale increases to circa 2.5 times this value.

Since the distribution of the energy dissipation rate is governed by the turbulent velocity field, its variation with vessel size is accordingly. The ratio of the maximum and minimum energy dissipation near the blade tip of the turbine impeller and in the bulk of the vessel respectively, decreases with scale-up. It ranges from 900 for the 10 cm vessel size to 250 for the 39 cm vessel size.

The energy dissipation rate field is far from uniform even for the 39 cm vessel, invalidating the assumption of homogeneous turbulence in the stirred tank. The approach of using the mean energy dissipation rate for calculating the coagulation rate in a stirred tank is therefore rather doubtful. Aggregates that are formed in the bulk of the stirred vessel can be unstable in the much more vigorous jet stream coming from the impeller. Aggregate growth and breakup become spatially separated processes and the breakup frequency is not related to a certain eddy frequency as in homogeneous turbulence, but is determined by the exchange rate between the regions of high and low energy dissipation rates. A model that incorporates the heterogeneity of the turbulent flow in stirred tanks is presented in the next chapter.

NUMERICAL PARTICLE TRACKING IN A TURBINE AGITATED VESSEL

4.1. INTRODUCTION

As was shown in the previous chapter, the values of the local energy dissipation rate in a turbine agitated vessel are distributed over a wide range. The spread in the hydrodynamic stress that is responsible for breakup of aggregates in a coagulation process is less pronounced but still appreciable. In order to describe the coagulation process in stirred tanks kinetic modelling with local energy dissipation rates and exchange rates between the various zones of different energy dissipation rate has to be carried out.

Koh et al.(1987) suggested a two-compartment model, in which the stirred tank was divided into an impeller zone and a bulk zone. The impeller flow capacity Q_p was taken as the volumetric exchange rate between the two compartments. The spatial partition was chosen arbitrarily. It is, however, more appropriate to define two compartments for each aggregate size, one in which $\Delta u_1 < \Delta u_b$ and one in which $\Delta u_2 \geq \Delta u_b$. Δu_1 and Δu_2 denote the rms turbulent velocity differences across the aggregate diameter in compartment 1 and 2 respectively and Δu_b is defined as the critical velocity difference that will just break up the aggregate. The flow rate between the compartments and the corresponding residence times in both compartments can be computed by "numerical particle tracking", a method based on the simulation of the movement of the aggregate in the turbulently agitated vessel. Since the particle is assumed to follow the fluid flow accurately, the program is restricted to aggregates smaller than the Kolmogorov micro scale. As the exchange rate between the two compartments is mainly governed by the mean flow, the residence times computed for particles larger than the Kolmogorov micro scale are not expected to be much different, unless their movement is largely influenced by gravity.

For aggregates smaller than the Kolmogorov microscale, the important parameters in the compartment model are the strain rate s, the hydrodynamic shear stress τ_s acting on the aggregates and the residence times of the aggregates in the zones of different strain rate and shear stress.

Eq.(2-50) for the collision rate J^0_{ij} may be rewritten as:

$$J^0_{ij} = 2\pi (a_i + a_j)^3 \, s \, n_i \, n_j \tag{4-1}$$

where $s = \overline{|s'_{ii}|} = \overline{|\Delta u'(R)|} / R$ with R = collision radius = $a_i + a_j$
(see section 2.4.3).

Eq.(4-1) shows that the coagulation rate is controlled by the strain rate s. This strain rate is given by the following equation:

$$s = \left(\frac{2}{\pi}\right)^{1/2} \left[\frac{\Delta u(R)}{R}\right]_{R < \eta} = \left(\frac{2\,\varepsilon}{15\,\pi\,\nu}\right)^{1/2} \tag{4-2}$$

The shear stress τ_s determines the local maximum size of the aggregates in the viscous subrange of turbulence. The shear stress is given by eq.(2-58) in section 2.5.2:

$$\tau_s = \mu \left(\frac{2\,\varepsilon}{15\,\nu}\right)^{1/2} \tag{4-3}$$

The maximum aggregate size is related to its critical shear stress τ_{sb} through the relation:

$$d \sim (\tau_{sb} / S_0)^{\dfrac{1}{n(D - 3)}} \tag{4-4}$$

(section 2.7.1)

For each aggregate size d the vessel can be divided into two compartments one with $\tau_s \geq \tau_{sb}$ and one with $\tau_s < \tau_{sb}$.

The residence time in the zones of low shear stress represents the time during which the aggregates are able to grow beyond sizes which correspond to the zones of high shear stress. Because coagulation of larger aggregates is only possible in the zones of low enough shear stress (eq. 4-4), where these large aggregates are not disrupted, their overall coagulation rate is reduced relative to the coagulation rate of the smaller aggregates which still can grow in a large part of the vessel. If f_t denotes the fraction of time the aggregates spend in the low shear zones and f_s represents the ratio of the

strain rate the aggregates encounter in the low shear zones and the average strain rate the aggregates encounter throughout the vessel, the coagulation rate is reduced with a size dependent factor:

$$f_r = f_t \cdot f_s \tag{4-5}$$

The actual coagulation rate for the aggregates is given by a multiplication of the reduction factor and the coagulation rate for the situation that coagulation would be possible throughout the whole vessel.

The residence times and strain rates in zones of different shear stress required to calculate the reduction factor f_r , are obtained from the particle tracking simulation.

With the particle tracking it is also possible to compute the breakup frequencies for the various aggregate sizes. For this purpose the simulation program keeps up a record of the number of times the aggregates cross the zones with high shear stresses. If disruption is assumed to occur almost instantaneously when the aggregates enter the high shear zones, the breakup frequency f_b is given by the average number of crossings per unit time.

The tracking program requires knowledge of the average and root mean square (rms) fluctuating velocities and integral length scale of the turbulent eddies in every point of the vessel. Therefore, interpolation between the data points measured by laser Doppler velocimetry was performed with mathematical models based on mass and momentum balances and on experimental correlations, which describe the flow pattern and shear field in the stirred vessel. This static fluid flow model is presented in the next section. In section 4.3 it is combined with the concepts of turbulent dynamics in order to predict the turbulent time correlated fluctuating velocity field as experienced by a wandering particle in the agitated vessel. Tracking of the movement of the dispersed phase particle throughout the vessel yields values for the reduction factor and breakup frequency as a function of aggregate size. The results of the particle tracking are discussed in section 4.4. Finally section 4.5 summarizes the main conclusions of this chapter.

4.2 MODEL FOR STATIC FLUID FLOW

The static fluid flow model provides estimates of the mean velocities, the rms fluctuating velocities, the integral length scale and the energy dissipation rate in every point of the 20 cm vessel. The interpolation between the measured points was facilitated by analytic functions for the various parameters fitted to the experimental data. In the following sections the analytic expressions which have been used are discussed.

Mean velocity field

The model proposed here to describe the mean flow patterns in a fully baffled turbine agitated vessel is two dimensional. From the data of Reed et al. (1977), the influence of the baffle upon the mean velocity profiles seems to be mainly confined to a restricted area around the baffle (-5°$\leq \vartheta \leq$ 5°), which suggests that the two-dimensional flow pattern in the 45° plane gives a good first approximation of the turbulent flow in a stirred tank. Furthermore with measurements conducted only in the 0° and 45° plane, the three dimensional experimental picture is far from complete to justify three dimensional modelling.

The top section of the stirred vessel is divided into 6 subregions as shown in fig. 4.1, for which different analytic expressions give a description of the radial velocity profiles. These subregions are:

I & II.   The flow from the impeller

III.   jet stream impinging on vessel wall

IV.   Circulating flow

V.   Axial flow returning back to impeller

VI.   Flow of fluid in the region swept by the revolving impeller

The boundaries between subregions I and III and between II and III are set at the radial coordinate r_0 of the center of the circulation loop for ϑ = 45°. The boundaries between subregions III and IV and between IV and V are set at the axial coordinate z_0 of the circulation center. The dividing line between subregions I and VI corresponds to the impeller tip whereas the boundary between subregions V and VI corresponds to the blade edge. The dividing line between subregions II and V follows from the tangential jet model as will be shown later on.
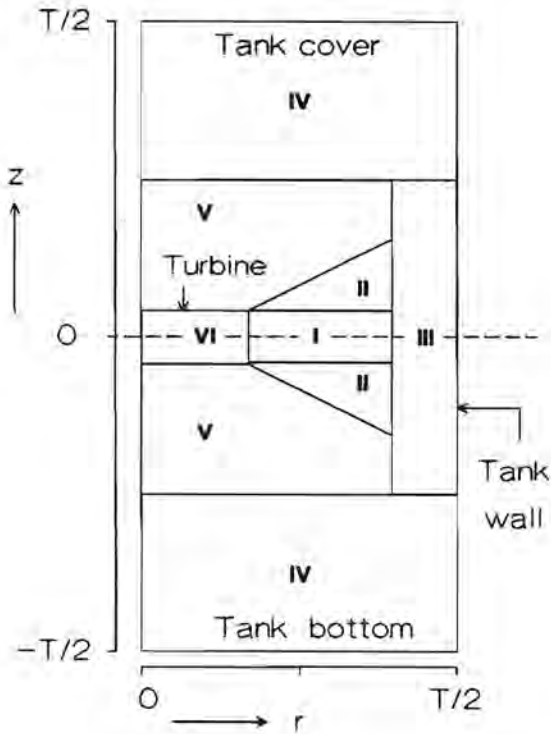
Figure 4.1. Subregions used in the static fluid flow model

The local axial mean velocity gradient is computed from the local radial mean velocity gradient through a mass balance:

$$\frac{\partial(r\bar{U}_r)}{\partial r} + \frac{\partial(r\bar{U}_z)}{\partial z} = 0 \tag{4-6}$$

And:

$$\bar{U}_z(r,z) = 1/r \int_0^z \frac{\partial(r\bar{U}_r(r,z'))}{\delta r} \partial z' \tag{4-7}$$

Eq.(4-6) is based on rotational symmetry, i.e. $\partial(r\bar{U}_\vartheta)/\partial\vartheta = 0$. Outside the impeller stream (region I) this is only approximately true, and therefore only one of the two velocity components (radial or axial) can be made to fit the experimental data. We matched the axial velocity. The analytic expressions for the radial mean velocity profiles obtained from literature were adapted in

order to establish the match between measured and calculated (through eq.(4-6)) axial mean velocities.

The following analytic expressions concern the mean radial velocity in the 6 subregions of the upper part of the tank. The radial velocity in the lower part of the tank can be computed by substituting −z instead of z into these equations:

Region I. The tangential jet stream model as proposed by Desouza and Pike (1972) has been employed to describe the radial mean velocity:

$$\bar{U}_{r,I}(r,z) = \frac{A}{2} \frac{\sigma^{1/2}}{r^{3/2}} (r^2 - a_t^2)^{1/4} \left[1 - \tanh^2 (\frac{\sigma}{2} \frac{z}{r}) \right]$$

$$(4-8)$$

With constant parameters A and a_t the computed tangential jet width was too large near the impeller tip in comparison with the experimental findings. The volumetric flow parameter A and the origin a_t of the tangential jet have been made to vary with the axial coordinate z in order to yield a better fit to the experimental values of the radial mean velocity in the impeller stream. The introduced axial functions for the parameters A and a_t are:

$$A = N D^2 N_p^{1/2} (0.3355 - 15.91 z)$$ $$(4-9)$$
$$a_t = .0223 + 1.918 z$$ $$(4-10)$$

Eq.(4-10) marks the dividing line between section II and V.

The jet width parameter σ was obtained from the empirical correlation proposed by Platzer and Noll (1988):

$$\sigma = 19 \exp(- 0.108 N_p)$$ $$(4-11)$$

Region II. The tangential jet model for this region was modified in order to fit the experimental data to:

$$\bar{U}_{r,II}(r,z) = \frac{A}{2} \frac{\sigma^{1/2}}{r^{3/2}} (r^2 - a_t^2)^{1/4} \left[1 - \tanh^2 (\frac{\sigma w}{r}) \right]$$

$$(4-12)$$

with $A = N D^2 N_p^{1/2} (.3355 - 15.91 w / 2)$
w = blade width

Region III. The basis of the analytic expression for the radial velocity in the region near the wall is the separation of the radial flow dependency into a radial $G(r)$ and axial function $F(z)$ (Platzer and Noll 1988), i.e.:

$$\bar{U}_{r,III}(r,z) = F(z)\ G(r) \tag{4-13}$$

On reaching the tank wall the radial velocity decreases rapidly to zero. The flow near the wall is similar to stagnation flow, for which the radial function $G(r)$ of the radial mean velocity can be described by (Platzer and Noll 1988):

$$G(r) = \frac{r}{4}\left[\left(\frac{2\ r}{T}\right)^4 - 1\right] \tag{4-14}$$

with T = tank diameter

Because of continuity, the mean radial velocity $\bar{U}_{r,III}$ should equal $\bar{U}_{r,I}$ and $\bar{U}_{r,II}$ at the boundary between subregion III and the subregions I and II respectively. It follows that:

$$F(z) = \bar{U}_{r,I}(r_0,z)\ /\ G(r_0) \tag{4-15}$$

$$F(z) = \bar{U}_{r,II}(r_0,z)\ /\ G(r_0) \tag{4-16}$$

where r_0 is the radial coordinate of the circulation centre which denotes the position of the boundary between subregion III and the subregions I and II.

Region IV. As in region III the radial flow dependency is separated into a radial and axial function. For the axial function $F(z)$ we used the equation as proposed by Platzer and Noll (1988):

$$F(z) = \left(1 - \frac{2\ z}{T}\right)^{m-1}\left[\frac{2\ z}{T}(1+m) - 1\right] \tag{4-17}$$

with $m = \dfrac{2\ z_0}{T} - 1$

z_0 = the axial coordinate of the circulation centre

The radial function $G(r)$ results directly from the mass balance between the outward and inward radial flux in each radial plane:

$$G(r) = \int_0^{z_0} \bar{U}_r\ \partial z\ /\ \int_{z_0}^{T/2} F(z)\ \partial z \tag{4-18}$$

Region V. The radial mean velocity $\bar{U}_{r,V}$ in this region is set to zero.

Region VI. This is the region swept by the impeller. No experimental data are available for this region. The radial velocity was assumed to vary linearly with the distance from the impeller axis:

$$\bar{U}_{r,VI} = 2\ U_{r,I}(\ D/2,\ z)\ \frac{r}{D} \tag{4-19}$$

The calculated axial velocities are in close agreement with the experimental data except for the region just above the impeller as shown in fig. 4.2. The differences in the measured and calculated axial velocities presented in fig. 4.2 are due to the somewhat simple models which are used to describe the flow in region V and VI.
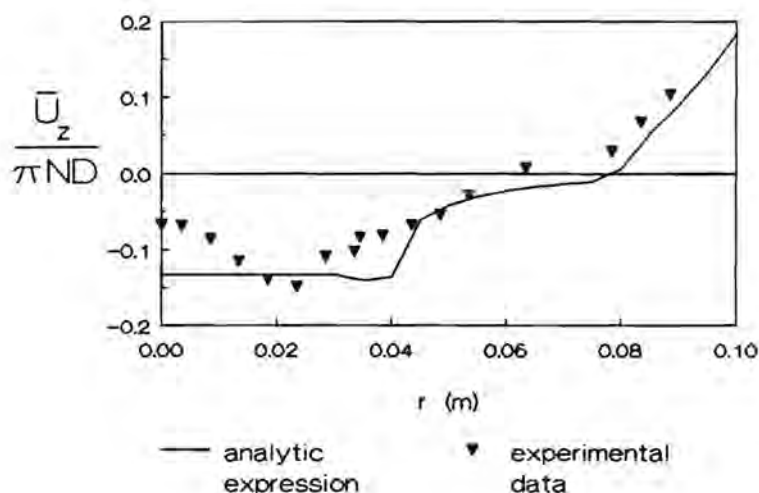
Figure 4.2. Comparison of measured and calculated mean axial velocities just above the impeller in the 20 cm vessel ($z^* = 0.3$).

Fluctuating velocity field

The local rms fluctuating velocity is obtained by multiplying the average flow velocity $|\bar{U}|$ with the turbulent intensity I. The turbulent intensity is defined as:

$$I = \left(\frac{u_{r\iota}^2 + u_{\vartheta\iota}^2 + u_{z\iota}^2}{\bar{U}_r^2 + \bar{U}_\vartheta^2 + \bar{U}_z^2} \right)^{1/2} = (2\,k)^{1/2} / |\bar{U}| \tag{4-20}$$

In addition to radial and axial mean velocities, estimates of the tangential mean velocity are required for computation of the average flow velocity. In the subregions I, II and III the following expression for the tangential mean velocity was applied:

$$\bar{U}_\vartheta = \frac{a_\iota}{(r^2 - a_\iota^2)^{0.5}} \, \bar{U}_r \tag{4-21}$$

which results from the tangential jet model (Desouza and Pike 1972).

If eq.(4-21) yields smaller values for the tangential velocity than the tangential velocity experimentally found in the bulk of the tank, i.e. approximately 0.05 times the tip impeller speed (= πND), the tangential mean velocity is set equal to the latter value. The tangential velocity is also set equal to 0.05 πND in the other subregions of the tank.

Empirical analytic expressions to describe the variation of the turbulent intensity with the radial and axial coordinate were determined from the experimental data and implemented in the static fluid flow model for interpolation between the experimental data.

Isotropy is assumed, i.e. the rms fluctuating velocity is assumed to be equal in all three directions of space:

$$u_r = u_\vartheta = u_z = I \cdot |\bar{U}| \tag{4-22}$$

Local integral length scale

The integral length scale is set equal to the blade width in regions I, II, III and VI, and equal to 2.5 times the blade width in the other regions. See section 3.6.4.

Energy dissipation rate distribution

The local energy dissipation rate is calculated using the inviscid estimate given by eq.(3-1) with A equal to 1. The integration of the computed values of energy dissipation rate over the entire tank equalled the measured total power input within 10%.

4.3. TURBULENT DYNAMIC FLOW

In the previous section, a model producing time averaged quantities like the mean velocity profile was developed. Extended with the concepts of turbulent dynamics the instantaneous turbulent velocity field as experienced by a moving particle can be calculated. The turbulent dynamics are therefore essential in predicting the movement of the particle which is being tracked throughout the vessel.

It is assumed that the moving particle follows the fluid flow accurately. The particle movement is started at randomly generated coordinates in the vessel. At this point the average and rms velocities, local integral length scale and energy dissipation rate are calculated. The instantaneous fluctuating velocity is randomly generated, with the absolute value set equal to the rms velocity. Summation of average and instantaneous fluctuating velocities give the instantaneous velocities in this point. Next the particle is moved by these instantaneous velocities in the corresponding two-dimensional flow direction during a certain time step $\Delta\tau$ much smaller than the Lagrangian integral time scale. The Lagrangian time scale is related to the local integral length scale by:

$$T_L = \frac{0.2\,L}{\sqrt{(2\,/\,3\,k\,)}} \tag{4-23}$$

This expression is equivalent to eq. (2-45) presented in section 2.4.3.

In the next points the same procedure is repeated except for the instantaneous fluctuating velocities which are now made time correlated. This is done by using an auto-regressive algorithm of the first order (Tropea 1987) which returns each fluctuating velocity component time correlated with its previous value by:

$$u_i'(k) = R_L(\Delta\tau)\,u_i'(k-1) + c_i'(k)\,\sqrt{(\,1 - R_L^2(\Delta\tau))} \tag{4-24}$$

where $u_i'(k)$ is sample k of fluctuating velocity component i, $R_L(\Delta\tau)$ is the value of the corresponding Lagrangian autocorrelation function at delay time $\tau = \Delta\tau$ and $c_i'(k)$ is the k-th normally distributed random contribution. Each new velocity sample is thus generated from a combination of the previous one and the present value of the random contribution. The values of $c_i'(k)$ have a mean value of zero and are mutually uncorrelated. Their rms value is equal to the rms value of the velocity fluctuations $u_i'(k)$. The Lagrangian

autocorrelation function is an exponential time correlation:

$R_L(\tau) = \exp(- \tau / T_L)$.

Eq. (4-22) is valid in a homogeneous field, i.e. equal rms velocity in space. In order to incorporate the inhomogeneity of the turbulent field the instantaneous values of $u_i'(k-1)$ are continually multiplied by the ratio of the rms values of $u_i'(k)$ and $u_i'(k-1)$.

Eq.(4-22) yields a Gaussian velocity distribution. The assumption of the velocity being Gaussian distributed is only approximately true for the impeller stream, where the probability density function is clearly positively skewed. This skewness, however, results from the periodic velocity fluctuations which in the present simulation have been neglected.

The application of eq.(4-22) to all three fluctuating velocity components also implies that they are uncorrelated. As the flow field proved to be almost isotropic this seems to be a reasonable assumption.

Precautions have been taken in order to avoid that the particle sticks to the wall or the impeller.

With the static and dynamic fluid flow models combined, we are able to simulate the movement of the aggregates within the vessel. The aim of the particle tracking is to compute estimates for the reduction factor f_r and breakup frequency f_b as a function of the aggregate size. Each aggregate size is related to a critical breakup energy dissipation rate ε_b by eq.(4-2) and (4-3). The vessel is divided into zones of energy dissipation lower and higher than this critical value. During the particle's track the residence time in zones of different energy dissipation rate is recorded, resulting in a residence time distribution as a function of the energy dissipation rate. Integration of this residence time distribution for $\varepsilon < \varepsilon_b$ yields the fraction of time f_t the aggregates spend in the low shear zones. Next the reduction factor f_r is computed by eq. (4.4) from this fraction of time f_t and the ratio f_s between the local strain rate in these zones and the overall time averaged strain rate $\bar{s}_T$. The residence time weighted strain rate $\bar{s}_T$ is calculated by:

$$\bar{s}_T = \sum_{k=1}^{M} s_k / M \qquad (4-25)$$

where s_k is the strain rate in time step k of the particle's track. The strain rate encountered by the aggregates in the low shear zones was calculated by applying eq. (4-23) to the time steps in the zones with $\varepsilon < \varepsilon_b$.

The breakup frequency f_b is computed from the number of times the aggregates enter the zones with $\varepsilon \geq \varepsilon_b$ from zones with $\varepsilon < \varepsilon_b$, divided by the total duration of the particle's track. In the particle tracking program the particle's track is truncated at a hundred crossings of the ε_b boundary and the total time elapsed during the particle's track is computed. The size dependency of the reduction factor f_r and breakup frequency f_b was determined by performing the particle tracking for various values of ε_b.

4.4. RESULTS OF PARTICLE TRACKING CALCULATIONS

To test the particle tracking program the fluctuating velocities were first set to zero. In that case the particle follows the streamlines as shown in fig. 4.3. This figure is obtained by starting the particle's track at $z^* = 1.5$ and successive radial distances of 10, 20, ..., 70 mm from the impeller axis. The streamlines are not completely closed. The displacement of the end point relative to the starting point is dependent on the size of the time step $\Delta\tau$
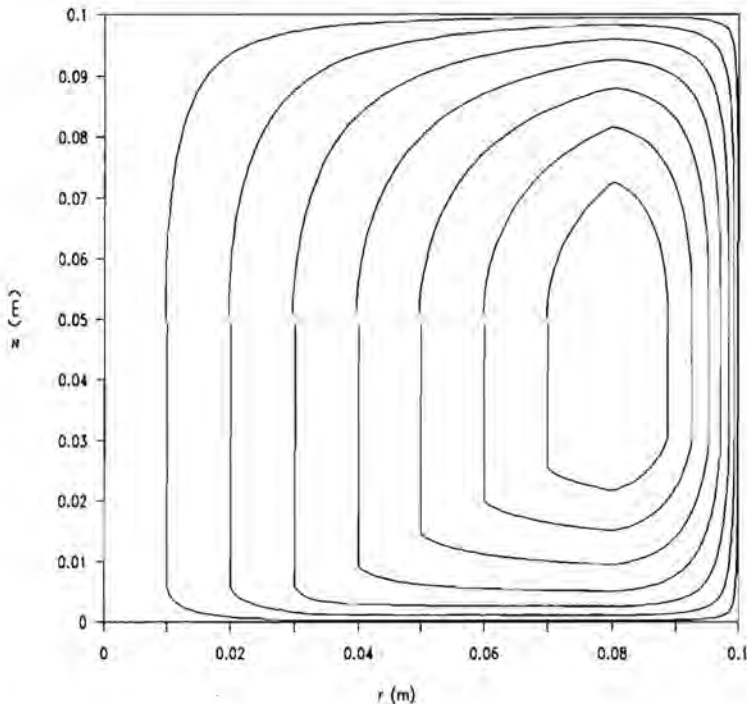
Figure 4.3. Streamlines in upper section of the 20 cm vessel.

which has been applied in the simulation and the size of the grid elements, which were used to solve eq.(4-6) numerically. The time step used to compute fig. 4.3 was $0.05 \cdot T_L$ and the grid was 250 by 400 (radial by axial coordinates). With fluctuations imposed upon the mean path, the particle is able to leave the streamlines. Plotting multiple circulations results in fig. 4.4.
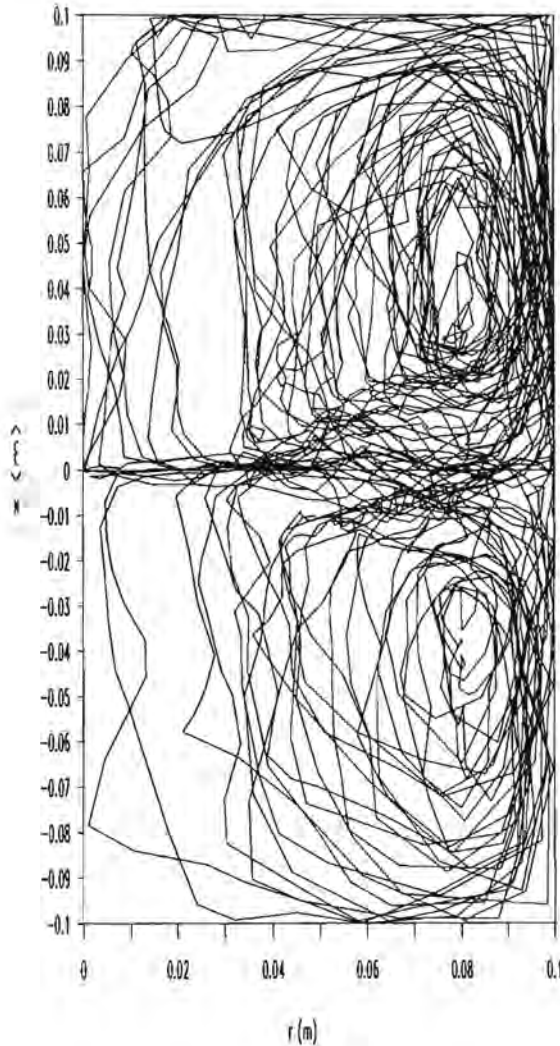
Figure 4.4. The particle's track in the 20 cm vessel.

The residence time distribution of the particle in zones of different energy dissipation rate is shown in fig. 4.5. The residence time distribution does not deviate much from the volumetric distribution of the energy dissipation rate, which is also presented in fig. 4.5, suggesting an equal flow rate through the various zones of different energy dissipation rate. The residence time averaged strain rate $\bar{s}_T$ is therefore almost equal to the volumetric averaged strain rate $\bar{s}_V$: $\bar{s}_V / \bar{s}_T = .98$. The residence time weighted strain rate does however differ much from the strain rate $s_{\bar{\varepsilon}}$ calculated from the mean energy dissipation rate $\bar{\varepsilon}$, which is often substituted erroneously (Koh et al. 1984) in the orthokinetic collision equation to compute the collision frequencies for the initial stages of the coagulation process. The ratio of these strain rates $\bar{s}_T / s_{\bar{\varepsilon}}$ is 0.68.
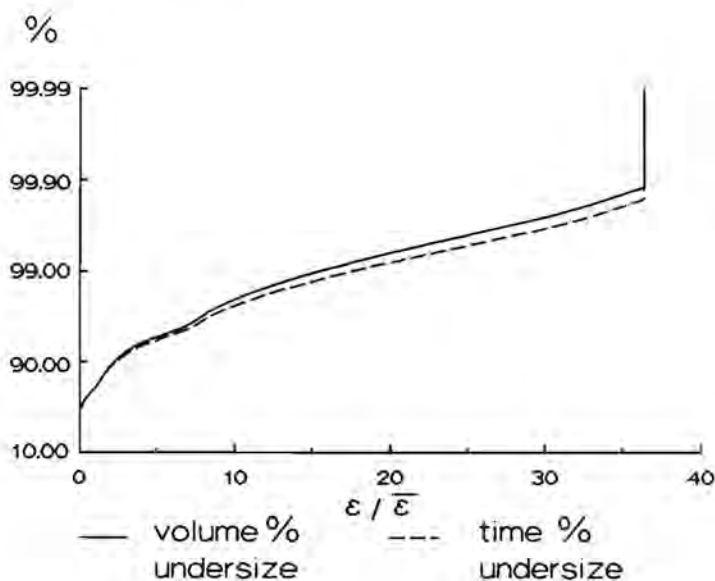
Figure 4.5. Cumulative residence time distribution of the moving particle in the zones of different energy dissipation rate versus the cumulative volume distribution of the energy dissipation rate in the stirred vessel.

In fig. 4.6 the residence times and strain rates in the zones with $\varepsilon < \varepsilon_b$ are plotted versus ε_b. The resulting values for the reduction factor f_r of the coagulation rate are presented in fig. 4.7.
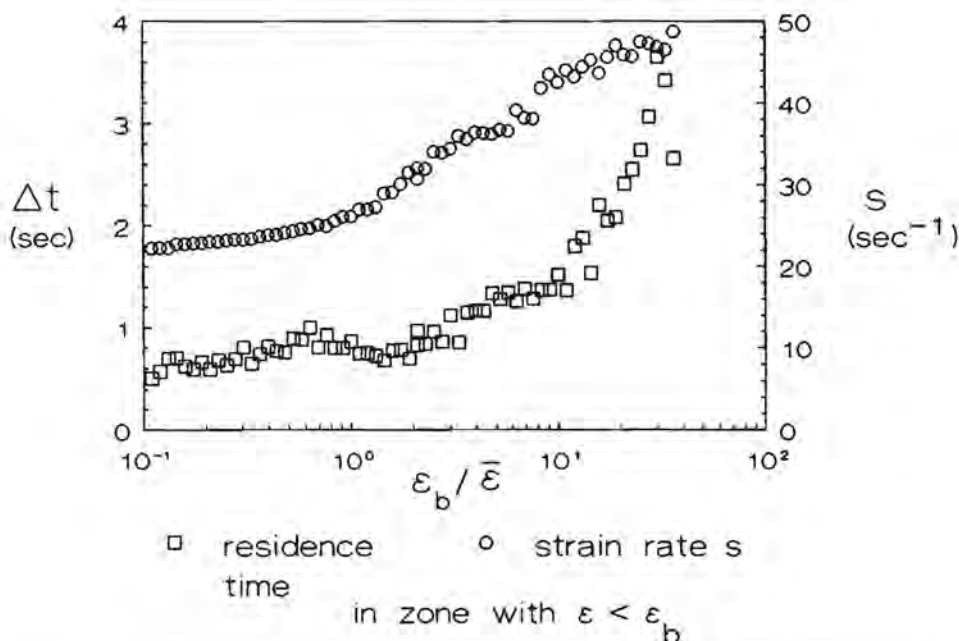
Figure 4.6. Residence times and strain rates in the zones with $\varepsilon < \varepsilon_b$ versus ε_b.

The breakup frequency f_b is shown also in fig. 4.7 as a function of ε_b. This breakup frequency corresponds to an impeller rotating speed N of 5 s^{-1} in the 20 cm vessel. A non-dimensional breakup frequency can be defined by dividing f_b by N. For aggregates with values of critical energy dissipation rate $\varepsilon_b / \bar{\varepsilon}$ < 1, the dimensionless breakup frequency $f_b^* = f_b / N$ amounts to circa 0.2. This value is somewhat larger than the reciprocal of the bulk circulation time probably due to back mixing. The dimensionless bulk circulation time is defined as:

$$T_c^* = NT_c = NV / Q_c = \pi (T/D)^3 N_{Qc} / 4 \qquad (4\text{-}26)$$

With $N_{Qc} = 2.9$ the reciprocal of the dimensionless bulk circulation time amounts to: $(T_c^*)^{-1} = (NT_c)^{-1} = 0.13$
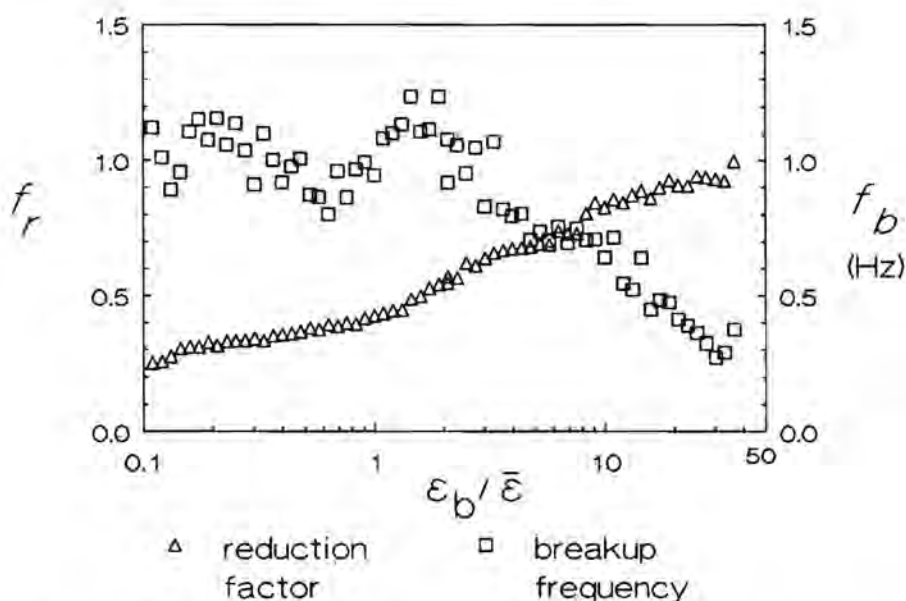
Figure 4.7. Reduction factor f_r and breakup frequency f_b as a function of critical breakup value ε_b of the energy dissipation rate.

The dimensionless breakup frequency is about 0.06 for aggregates that are to be exposed to the maximum (time averaged) energy dissipation rate ε_{max} in the vessel in order to rupture. This value is expected to be of the order of reciprocal of the dimensionless impeller stream renewal time which is defined as:

$$T_R^* = NT_R = NV / Q_P = \pi \, (T/D)^3 \, N_{QP} / 4 \qquad (4\text{-}27)$$

With $N_{QP} = 0.67$, $(T_R^*)^{-1}$ amounts to 0.032, which is smaller than the dimensionless breakup frequency corresponding to the maximum energy dissipation rate ε_{max} in the vessel. This is to be expected as Q_P denotes the radial flow capacity near the impeller tip. The region of ε_{max} is located at some distance from the impeller tip where the radial flow has increased. Furthermore there is also a substantial axial flow entering the region of ε_{max} giving rise to an additional increase of f_b^* with respect to $(T_R^*)^{-1}$.

As ε_b is related to aggregate size by eq.(4-2) and (4-3) fig. 4.8 gives in fact the values of the reduction factor and breakup frequency as a function of aggregate size. If $f_r(k)$ and $f_b(k)$ represent the reduction factor and breakup

frequency respectively of the aggregates of size class k, i.e., aggregates consisting of k primary particles, the frequency of collisions $J^*_{i,k-i}$ resulting in the formation of these aggregates and the corresponding breakup rate S^*_k are given by:

$$J^*_{i,k-i} = f_r(k) \, J_{i,k-i} \tag{4-28}$$

$$S^*_k = f_b(k) \, n_k \tag{4-29}$$

where $J_{i,k-i}$ denotes the collision frequency between aggregates consisting of i and k-i primary particles if the formation of aggregates of size class k would be possible throughout the whole vessel volume. For aggregates smaller than the Kolmogorov micro scale $J_{i,k-i}$ is given by eq.(4-1) with s replaced by $\bar{s}_T$ and multiplied with the collision efficiency $\alpha_{i,k-i}$:

$$J_{i,k-i} = \alpha_{i,k-i} \, 2\pi \, (a_i + a_{k-i})^3 \, \bar{s}_T \, n_i \, n_{k-i} \tag{4-30}$$

where $\alpha_{i,k-i}$ = efficiency of collisions between aggregates consisting of i and
                     k-i primary particles.

  a_i = radius of aggregate made of i primary particles.

  n_i = number concentration of aggregates made of i primary
                     particles.

Eq. (4-29) is equivalent to eq.(2-106) in section 2.8 except for the breakup frequency now being related to the exchange rate between the zones of $\varepsilon < \varepsilon_b$ and of $\varepsilon \geq \varepsilon_b$ and not to a certain eddy frequency.

The total change of the number concentration of aggregates in size class k in the bulk of the stirred tank is given by the following population balance:

$$\frac{dn_k}{dt} = 1/2 \sum_{i=1}^{k-1} J^*_{i,k-i} - \sum_{i=1}^{max} J^*_{ik} + \sum_{i=k}^{max} \beta_{ki} S^*_i - S^*_k \tag{4-31}$$

where β_{ki} denotes the number of fragments of size class k resulting from the breakup of aggregates of i primary particles.

The first term on the right hand side of eq.(4-31) represents the gain of class k from collisions between aggregates of smaller size. The second term denotes the loss from class k by collisions of k-sized aggregates with aggregates of any other size. The third term results from fragments that fall into the size class k from breakup of larger aggregates. Lastly the fourth term is the rate of disappearance of aggregates of size class k by breakup.

The population balances over the various aggregate sizes have to be solved simultaneously in order to describe the evolution of the aggregate size distribution in the batch coagulation process in the stirred tank. To yield an accurate description additional information is required about the size of the aggregates as a function of the number of primary particles they contain, about the number and size of the fragments produced upon rupture of the flocs and about the collision efficiencies α_{ij}. These subjects are treated in the next two chapters of this thesis.

4.5. CONCLUSIONS

The residence time distribution over the various energy dissipation rate zones is almost equal to the volumetric distribution of the energy dissipation rate. For aggregates smaller than the Kolmogorov micro scale either volumetric or residence time weighted strain rate can be used to compute the initial coagulation rate. This effective mean strain rate for coagulation is, however, not the same as the mean value obtained from power input per unit mass, which is commonly inserted in the collision frequency equation.

The reduced coagulation rate and the breakup frequency are essential parameters in modelling the evolution of the aggregate size distribution in the heterogeneous shear field of the stirred tank. With the numerical particle tracking quantitative values of these parameters were obtained for the various aggregate sizes. The present calculations were restricted to the 20 cm vessel. They can however be readily extended to the 10 and 39 cm vessel by adjusting the empirical correlations that have been used to describe the distribution of the turbulence intensity throughout the stirred vessel.

CHAPTER V
AGGREGATION KINETICS IN STIRRED TANKS

5.1. INTRODUCTION

In this chapter the experimental study of aggregate growth by batch coagulation in stirred tanks is presented. The study is confined to aggregation in the viscous subrange of turbulence, i.e., to formation of aggregates smaller than the Kolmogorov micro scale.

The setup of the coagulation experiments is discussed in section 5.2. Section 5.3 deals with the technique used to characterize the size and porosity of the aggregates.

In section 5.4.1 the initial stage of the coagulation process where primary particles form doublets, is discussed. It was shown in the previous chapter that the residence time weighted strain rate should be used to compute the collision frequencies for the initial stages of the coagulation process rather than the strain rate calculated from the average turbulent energy dissipation rate per unit mass in the stirred tank. Starting from this principle, collision efficiencies as presented in the literature are replotted versus this residence time weighted strain rate. Next they are compared to the collision efficiencies that are calculated theoretically for spherical particles in simple shear flow, in order to verify whether the application of these theoretical values to the turbulent shear case is validated.

In section 5.4.2 the kinetics of the following stages of the aggregation process are discussed. De Boer et. al. showed that the first stage of the coagulation process was followed by an accelerated growth that is inconsistent with theoretical predictions that assume a uniform porosity within the aggregates. The porosity is however shown to increase with aggregate size. Since the aggregates are porous, their surface is penetrated by the fluid flow, giving rise to enhanced collision efficiencies. In section 5.4.3. values for the collision efficiencies for encounters between porous aggregates are estimated. Predictions about the course of the aggregation process that follow from the application of these enhanced collision efficiencies in the

description of the coagulation process are compared to experimental data in section 5.4.4. Finally section 5.4.5. discusses the dependency of the coagulation rate on stirrer speed, salt and solids concentration.

5.2. SETUP OF BATCH COAGULATION EXPERIMENTS

Aqueous suspensions of mono sized spherical polystyrene particles with a characteristic size of about 1 μm were used for studying coagulation. Sodium chloride was used to induce coagulation.

The polystyrene particles were prepared by polymerization without the addition of emulsifying agent in order to get stabilization by chemically bound charged surface groups and not by additional adsorption of (charged) surfactants which would make a description of the electrostatic repulsive forces rather complex.

The polymerization was based on the methods as described by De Boer (1987) and Eshuis et. al. (1991). With the method proposed by De Boer (1987) there was mostly a low overall yield to solid polymer, because of considerable amounts of oligomers that were formed. Furthermore there was a low reproducibility with respect to average particle size which varied from 0.3 to circa 1.0 μm. The relative spread in particle size ranged from 20 to 30%. With the method proposed by Eshuis et. al. (1991) the average particle size could be better controlled in the range from 0.5 to 1.2 μm and a larger monodispersity was obtained. The relative spread in particle size was within 10%. Also the yield to solid polymer improved considerably because of the absence of oligomer formation. The solid content of the produced latex amounted to circa 10% by volume.

The residual reactants and product impurities, both inorganic and organic were removed by a microfiltration device (pore size 0.2 μm) to produce a clean model colloid. The size of the primary particles was determined by scanning electron microscopy (SEM). The solids concentration of the final polystyrene latex was determined by evaporation of the fluid.

The main reason for selecting polystyrene latex was the specific density of polystyrene (~ 1050 kgm^{-3}) being almost equal to the density of the sodium

chloride solution. The density of the sodium chloride solution varies from 1020 to 1120 kgm^{-3} for the NaCl concentration range of 0.5 to 3 mol l^{-1}. Sedimentation of solids could thus be avoided, even in quiescent flows. With the spherical shape the spatial orientation of contacting primary particles is not decisive for the strength and structure of the aggregate. At a reproducible size of about 1 μm orthokinetic coagulation predominates Brownian coagulation (Levich 1962). Furthermore the primary particle size is far less than the Kolmogorov micro scale η corresponding to the experimental conditions in the stirred tanks. Hence the expression for the orthokinetic collision frequency as derived for the viscous subrange of turbulence (section 2.4.3.) may be used in the description of the aggregation kinetics.

The results of the coagulation experiments performed at equal process conditions were different for the various polystyrene latices. This is apart from the different sizes due to the low reproducibility of the surface properties of the latices, giving rise to different binding forces between the primary particles within the flocs.

The concentration of sodium chloride was chosen well above the critical coagulation concentration to ensure complete destabilization of the suspension. Above the critical coagulation concentration the electrostatic double layer is compressed to such an extent that the net interaction energy is always attractive, independent of separation between the colliding particles. The coagulation is "rapid" relative to "slow" coagulation in the presence of weak interparticle repulsions.

The coagulation experiments were carried out in stirred tanks of similar geometry as depicted in fig. 3.9. The tank was first completely filled with the sodium chloride solution. Next the electric motor that drives the impeller was started and the proper amount of the polystyrene latex was injected into the electrolyte solution to obtain the desired solids concentration. The polystyrene latex was concentrated by vacuum evaporation to limit the volume that had to be injected. Prior to addition ultrasonics were applied to the concentrated latex to breakup any doublets that might have been formed during the evaporation process. A siphon vessel was used for level control in order to avoid flooding upon addition of the latex and also to ensure that no bubbles were introduced into the stirred tank upon withdrawal of samples from the contents of the tank. The siphon vessel was filled with a sodium chloride solution of equal concentration as in the stirred tank. Samples were withdrawn

from the bulk of the tank. This was done gently with a pipet of large orifice and internal diameter, 5 and 8 mm respectively, in order to avoid breakage of formed aggregates by sampling. Characteristic shear rates during sampling were of the order of 10 s^{-1}.

The coagulation experiments were duplicated. The relative variation in the volume mean diameter of the aggregates (for definition see section 5.3.2) was mostly less than 10%.

5.3. PARTICLE CHARACTERIZATION

5.3.1. SELECTION OF SIZING TECHNIQUE

The evolution of the aggregate size distribution was measured by taking samples which were analyzed with laser diffraction spectrometry. An extensive evaluation of the various sizing techniques presented by De Boer (1987) showed that laser diffraction spectrometry is to be preferred to other techniques for studying coagulation mainly because it is non destructive for the aggregates and makes fast measurements of the aggregate size distribution possible.

Other particle sizing techniques that have been studied are sieving, the electric sensing zone technique (also referred to as the Coulter method), sedimentation and optical microscopy. With sieving and to a lesser extent the electric sensing zone technique larger aggregates are being ruptured. With the electrical sensing zone technique the breakup is most likely to occur upon passage of the aggregate through the measuring aperture, so this does not always introduce large sizing errors. The electrical sensing zone, however, measures only the particulate matter within the floc and does not provide an estimate of the actual size that can be substantially different due to porosity. Hence it is not suitable for studying the kinetics in the later stages of coagulation where information about the collision radii is essential.

Sedimentation techniques for sizing aggregates are difficult to apply because of the small density difference between the aggregates and the suspending medium. Furthermore microscopic techniques are much more time consuming than laser diffraction spectrometry and are only used in the present study to determine the shape of the aggregates.

5.3.2. PRINCIPLE OF LASER DIFFRACTION SPECTROMETRY

With laser diffraction spectrometry the forward scattering from a parallel beam of monochromatic light by particles larger than the wavelength of light is measured as a function of scattering angle ϑ. The scatter pattern is then translated into a particle size distribution.

For particles with a diameter d larger than the wavelength of the light λ the scattering in the forward direction arises mainly from refraction of rays of light through the particle and diffraction of rays of light passing along the particle. The refraction depends on the form, size and the composition of the particle, i.e., for a spherical homogeneous particle on the refractive index m of the particle relative to that of the suspending medium. The diffraction is only dependent on the shape and size of the particle, not upon the particle composition.

As an example the angular intensity distribution for a 10 μm polystyrene sphere (refractive index n_p = 1.6) in water (refractive index n_s = 1.33) is
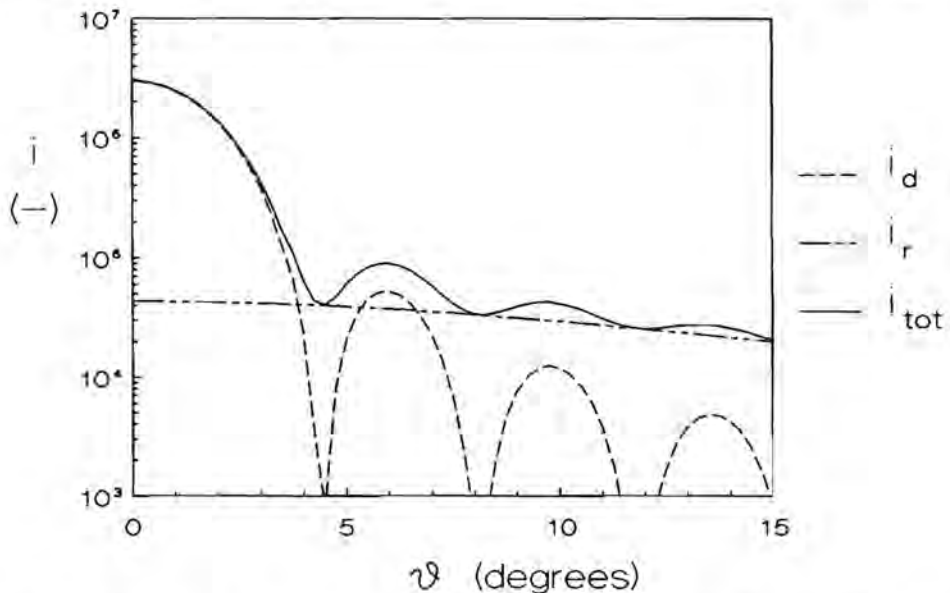
Figure 5.1. Small angle scattering by a polystyrene sphere of 10 μm in water of monochromatic light with wavelength λ_0 = 0.6328 μm. i_d, i_r and i_{tot} are intensity functions for diffraction, refraction and total scattering respectively.

depicted in fig. 5.1. The scattering by refraction is distributed over a wide range of angles and is moderate. The diffraction pattern is narrow and very intense close to the forward direction.

Laser diffraction spectrometry is based on the measurement of the first diffraction ring. Since the diffraction is only dependent on shape and size of the particles, the results of the sizing technique are almost independent of the composition of the particles. For spherical homogeneous particles this implies independency of refractive index ratio m (= n_p / n_s).

The measurement of scattering patterns was carried out by means of a Malvern 2600 particle sizer. The optical arrangement is shown schematically in figure 5.2.
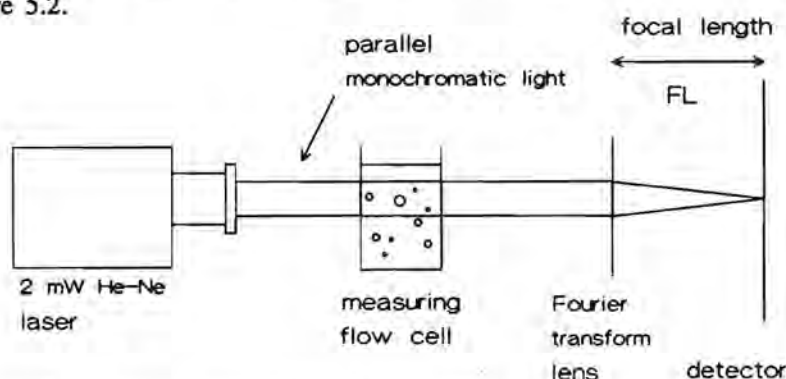
Figure 5.2. Optical arrangement of laser diffraction instrument.

Particles are allowed to move across a parallel laser beam with a diameter of 9 millimeters. The scattered light is focused by a Fourier Transform lens onto 30 semicircular photosensitive rings placed at predetermined radii in the detector plane. The annular rings are approximately log-spaced (Hirleman 1987) and the dimensions of the detector are listed by Dodge (1984) and Hirleman et al.(1984). The particle sizer is equipped with 6 exchangeable lenses, with corresponding size ranges as shown in table 5.1. By proper choice of the lens the resolution in particle size range can be optimized for the particular system of interest. Larger particles diffract light through smaller angles and to differentiate between the larger particle sizes a lens with a larger focal length is required to unravel the scattering at these smaller angles. The size classes the laser diffraction apparatus uses, are defined by the detector

dimensions and focal length through the relation (Swithenbank et al. 1977 and Hirleman et al. 1984):

$$D_i = \frac{\lambda_0}{\pi \cdot \sin(\arctan (r_i / FL))} \cdot 1.357 \qquad (5\text{-}3)$$

where λ_0 = wavelength of He-Ne light in vacuum = 0.6328 μm

r_i = radial distance of detector element i from centre of the detector

D_i = particle size representing the i-th size class

FL = focal length of Fourier Transform lens

Table 5.1. Size classes of Malvern 2600 particle sizer for various focusing lenses.

No. of size class	Focal length of lens (mm)					
	63	100	300	600	800	1000
1	118.20	187.62	562.86	1125.72	1500.96	1876.20
2	54.96	87.24	261.71	523.43	697.90	872.38
3	33.66	53.43	160.29	320.57	427.43	534.29
4	23.70	37.62	112.86	225.71	300.95	376.19
5	17.70	28.10	84.29	168.57	224.76	280.95
6	13.56	21.52	64.57	129.14	172.19	215.24
7	10.56	16.76	50.29	100.57	134.10	167.62
8	8.16	12.95	38.86	77.71	103.62	129.52
9	6.36	10.10	30.29	60.57	80.76	100.95
10	4.98	7.90	23.71	47.43	63.24	79.05
11	3.90	6.19	18.57	37.14	49.52	61.90
12	3.06	4.86	14.57	29.14	38.86	48.57
13	2.40	3.81	11.43	22.86	30.48	38.10
14	1.92	3.05	9.14	18.29	24.38	30.48
15	1.50	2.38	7.14	14.29	19.05	23.81
16	1.20	1.90	5.71	11.43	15.24	19.05

If successive detector elements are united into pairs, 15 size classes are available for each lens. A 16th size class comprises all particle sizes smaller than the lower limit of the 15th size class.

Each detector ring effectively measures the energy of the scattered light at a particular angle to the incident beam. The particle size distribution is then inferred through a modified Chahine iterative algorithm which attempts to match the measured and calculated energy distributions over the detector

rings. This mathematical procedure has been published elsewhere (Kusters et. al. (1991)). The fitting procedure is a model-independent technique, i.e. it does not constrain the volume distribution to follow some common analytic expression, like the two parameter Rosin-Rammler or log-normal distribution function. The fitting error which is optimized, is defined as the logarithm of the sum of the squared differences between the measured and calculated light energy patterns.

The deconvolution problem can be written as a set of linear equations, expressed in matrix notation as:

$$Q = A^{-1} \cdot E \qquad (5-4)$$

where E = light energy vector

$\quad Q$ = particle size volume distribution vector

$\quad A$ = scattering matrix

The total light energy measured on a detector ring is developed from contributions of all particle sizes present. Only the amount of contribution varies with particle size. This information is stored in the scattering matrix A. The scattering matrix has 15 rows (15 detector element pairs) and 16 columns (16 size classes). Matrix coefficient A_{ij} represents the light energy on the adjacent detector elements 2i-1 and 2i, scattered by size class j and normalized on a volume basis:

$$A_{ij} = E_{ij} / D_j^3 \qquad (5-5)$$

where E_{ij} = light energy scattered by size class j on the detector
elements 2i-1 and 2i

The scattered light E_{ij} is computed for homogeneous spherical particles. Hence, the scattering matrix is dependent upon two parameters:

a) Choice of focusing lens. This fixes the particle size range and particle size classes.

b) Refractive index ratio m of the scattering particles. The scattering by refraction is dependent on the choice of the refractive index ratio. The Malvern 2600 particle sizer* utilizes just one standard matrix for each lens, that corresponds to a refractive index ratio of ~ 1.2 (Kusters et al. 1991).

* *Later versions of the 2600 particle sizers have been equipped with two scatter matrices per lens: one based on Fraunhofer diffraction and the other one based on anomalous diffraction for the case of m ≅ 1.2.*

Errors in the size analysis resulting when systems of different values of m are deconvoluted with this fixed value of 1.2 were published earlier (Kusters et. al. (1991). The errors involved result from the less or enhanced scattering by refraction of large particles onto the detector rings corresponding to the smaller sizes (see eq. (5-3)) for m > 1.2 or m < 1.2 respectively. The less or extra light from refraction by the large particles is interpreted as a decrease or increase respectively of diffraction by the small particles resulting in a corresponding under- or overestimation of the volume fractions of these particles. The deviations in the deconvoluted size distribution at the small particle sizes, however, hardly influences the estimate of the volume mean diameter, which is defined as:

$$VMD = D43 = \frac{\Sigma \ N_i \ D_i^4}{\Sigma \ N_i \ D_i^3} = \Sigma \ Q_i \ D_i \qquad (5\text{-}6)$$

where N_i = number concentration of particles of size class i
Q_i = volume fraction of particles of size class i

The estimate of the Sauter mean diameter SMD is more strongly affected by the inappropriate scattering matrix choice because its value is largely determined by the tail of the volume distribution. The SMD is defined as:

$$SMD = D32 = \frac{\Sigma \ N_i \ D_i^3}{\Sigma \ N_i \ D_i^2} = \frac{1}{\Sigma \ Q_i \ / \ D_i} \qquad (5\text{-}7)$$

For the 63 mm lens the systematic errors in VMD and SMD are limited to 10 and 15% respectively for the refractive index ratio ranging from 1.07 to circa 1.3. For the larger lenses the application of the Malvern scattering matrix can be extended to particle systems with m larger than 1.3 and somewhat less than 1.07 without loss of accuracy.

The inversion technique is based on scattering from single particles. To avoid multiple scattering effects (Gorni 1986) that arise from light rays being diffracted by more than one particle, the samples were diluted with the corresponding sodium chloride solution. The obscuration (also referred to as extinction) of the undiffracted laser beam was adjusted to values corresponding to particle concentrations where multiple scattering is

negligible.

The obscuration OB is defined as:

$$OB = 1 - TR = 1 - I_l / I_0 \qquad (5\text{-}8)$$

where TR = transmittance of incident laser beam

I_l = intensity of undiffracted laser beam leaving measuring cell with path length l.

I_0 = intensity of laser beam incident on measuring cell

The intensity I_0 of the incident laser beam is measured prior to addition of the particles to the liquid in the measuring cell (Malvern, type PS14). Background scattering by contaminants in the sodium chloride solution is also recorded. The intensity of the laser beam is detected by a photodiode behind a small hole in the middle of the detector, where undiffracted light is focused. This photodiode is also used to align the detector to the optical axis of the particle sizer.

Gently mixing of sample and sodium chloride solution was performed with a magnetic stirrer at the bottom of the measuring cell. The path length of the light passing through this cell is 14.3 mm. The scattering pattern is obtained after subtraction of the background scattering from the raw signal.

5.3.3. SCATTERING BY LARGE AGGREGATES

The interpretation of scattering patterns is based on the assumption that particles are spherical and homogeneous, which is not true for aggregates. From microscopic observations it could however be concluded that the deviation from the spherical shape is not great. The aggregates show most resemblance to prolate spheroids. The aspect ratio of the agglomerates was normally less than 1.5 except for the initial stages of coagulation.

The inhomogeneous composition of the aggregates only affects the refraction part of the forward scattering and is therefore less important. Latimer (1985) suggested to use the volume averaged value of the refractive index of the component particles and the interstices as an estimate of the "refractive index" of the aggregates in order to take into account the inhomogeneity of the aggregates. The refraction from aggregates however shows a different angular dependency than the refraction from a "refractive index equivalent"

sphere of the same overall size. The light rays falling upon the aggregate are scattered by the primary particles within the floc structure. Since the diameter of the primary particles is about equal to the lower size limit of the Laser Diffraction apparatus, their scattering is more directed to angles beyond the detection angle of the photodetector. This effect is enhanced by the multiple scattering of the light rays within the floc. The refraction by aggregates is expected to be intermediate between the refraction by a polystyrene sphere and the refraction by the "refractive index equivalent" sphere suggested by Latimer.

The software installed in the Malvern 2600 instrument is based on a relative refractive index of the particles of 1.2, which is the value for polystyrene spheres in water. The volume averaged "refractive index ratio" of aggregates is less than 1.2. This implies that aggregates give rise to more scattering on the outer detector rings than solid polystyrene particles of the same overall size. For a aggregate of 10 μm consisting of 1 μm primary particles and with a fractal dimensionality (definition see eq.(2-86)) of $D = 2.5$, the porosity amounts to circa 70%. The volume averaged "relative refractive index" amounts to 1.06. This refractive index corresponds to the lower limit of application of the Malvern scattering matrix as discussed in the previous section. Since the refraction by aggregates will be less than the refraction by particles with relative refractive index equal to 1.06, only a slight overestimation of the volume fractions of the smaller particle sizes is expected when processing the scattering by these aggregates with the Malvern matrix. Failing the knowledge of the precise magnitude of this refraction, no correction has been applied to this minor systematic error.

5.3.4. DETERMINATION OF SOLIDS VOLUME FRACTION WITHIN AGGREGATES

The average solids volume fraction $\overline{\varphi}$ within the aggregates of a sample is given by the ratio of the primary particle volume concentration C_p and the volume concentration of the flocs C_F in the sample. The floc volume concentration C_F is determined by the sum of individual particle and interstitial volumes.

The concentration C_p of the sample in the measuring cell is obtained by dividing the primary particle concentration in the stirred tank with the dilution factor that has been applied to avoid multiple scattering effects in the sizing analysis. The volume concentration of the aggregates C_F is obtained from a combination of the obscuration and scattering pattern measurements that are performed by laser diffraction spectrometry. The obscuration is given by eq.(5-7). The transmittance is related to the turbidity of the sample through the following formula:

$$TR = \exp(-\tau_e\, l) \tag{5-9}$$

where τ_e = turbidity of suspension

l = path length of laser light in sample cell

The turbidity of the suspension is dependent on the particle concentration:

$$\tau_e = \Sigma\, N_i\, A_i\, Q_{ext,i} \tag{5-10}$$

where A_i = projected cross section of particle of size class i

$Q_{ext,i}$ = the extinction efficiency of size class i

For particles larger than the wavelength of light, the extinction efficiency $Q_{ext,i}$ is equal to 2 (Van de Hulst 1957). Since the aggregates are almost spherical their number concentration and cross sectional area can be approximated by respectively:

$$N_i = 6\, C_F\, Q_i\, /\, \pi D_i^3 \tag{5-11}$$

and, $A_i = \pi D_i^2\, /\, 4$ \hfill (5-12)

Substituting these relation in eq.(5-10) yields:

$$\tau_e = 3\, C_F\, \Sigma\, Q_i\, /\, D_i \tag{5-13}$$

Combining eq.(5-10), (5-9), (5-8) and (5-7) yields for the volume concentration of the flocs:

$$C_F = -\, D32\, \ln(\, 1 - OB)\, /\, (3\, l) \tag{5-14}$$

where D32 is obtained from the measurement of the scattering pattern of the flocs.

Hence with the laser diffraction instrument the porosity, i.e., $1 - \overline{\varphi} = 1 - C_p/C_F$, can be determined if the solids concentration C_p of the sample is known. With these measurements the variation of porosity with aggregate size can be recorded during the coagulation process.

5.4. INITIAL STAGES OF COAGULATION

In this section the initial stages of coagulation are studied, where aggregate breakup is absent.

For aggregates that are not disrupted in any part of the tank by the action of turbulent hydrodynamic stresses, the coagulation rate is given by eq.(4-30):

$$J_{ij} = 2\pi \; \alpha_{ij} \; (\; a_i + a_j \;)^3 \; \bar{s}_T \; n_i \; n_j \tag{5-15}$$

where $\bar{s}_T$ denotes the residence time weighted strain rate, which has been shown in the previous chapter to be equal to $0.68 \; s_{\bar{\varepsilon}}$. Here $s_{\bar{\varepsilon}}$ represents the strain rate calculated from the mean turbulent dissipation rate per unit mass $\bar{\varepsilon}$ in the stirred tank:

$$s_{\bar{\varepsilon}} = \sqrt{(\; 2 \; \bar{\varepsilon} \; / \; 15 \; \pi \; \nu \;)} \tag{5-16}$$

Substituting $0.68 \; s_{\bar{\varepsilon}}$ for $\bar{s}_T$ in eq.(5-15) yields:

$$J_{ij} = 0.88 \; \alpha_{ij} \; (\; a_i + a_j \;)^3 \; \Big(\frac{\bar{\varepsilon}}{\nu} \Big)^{1/2} \; n_i \; n_j \tag{5-17}$$

If $i = j$, the effective collision frequency reduces to:

$$J_{ii} = \frac{1}{2} \; 0.88 \; \alpha_{ii} \; d_i^3 \; \Big(\frac{\bar{\varepsilon}}{\nu} \Big)^{1/2} \; n_i^2 \tag{5-18}$$

where the factor $\frac{1}{2}$ ensures that each collision of two equal size particles is counted only once.

5.4.1. DOUBLET FORMATION

The first stage of coagulation is the formation of doublets from collisions between primary particles. The primary particles are spherical, impermeable and smaller than the Kolmogorov micro scale. As pointed out in section 2.4.4., for such particles the collision efficiency in turbulent flow is expected to approach the value as derived for particle encounters in simple shear flow. In fig. 5.3 values for the initial collision efficiency α_{11} as obtained by Higashitani et al. (1983) and De Boer et al. (1989a) are compared with predictions by the simple shear flow theory. The collision efficiency is plotted versus the parameter $N_s = 6\pi \; \mu \; d_1^3 \; \gamma / \; A_{1(2)}$ where the Hamaker constant $A_{1(2)}$ for polystyrene particles was set equal to $3.5 \cdot 10^{-21}$ J (Visser 1972).

The shear rate γ which has to be substituted into the parameter N_s is obtained by comparing the Von Smoluchowski equation for the initial collision frequency in simple shear flow:

$$J_{11}^S = \frac{2}{3} d_1^3 \gamma \bar{n}_1^2 \tag{5-19}$$

to the equation that describes the initial collision frequency in the viscous subrange of turbulence (see also eq.(4-30)):

$$J_{11}^0 = \pi d_1^3 \bar{s}_T n_1^2 \tag{5-20}$$

From equating eq.(5-19) to eq.(5-20) it follows that:

$$\gamma = 3\pi \bar{s}_T / 2 \tag{5-20}$$

De Boer et al. (1989a) performed their experiments in a stirred tank of similar configuration as used in our experiments, so the residence time weighted strain rate $\bar{s}_T = 0.68 \, s_{\bar{\varepsilon}}$ and $\gamma = 0.66 \, (\bar{\varepsilon}/v)^{1/2}$. Higashitani et al. (1983) conducted their experiments in a stirred tank agitated by a 8-flat blade paddle with its diameter equal to half the tank diameter. For such an impeller-tank diameter ratio Koh et al.(1984) showed that the volume average strain rate $\bar{s}_V$ equals 0.86 times $s_{\bar{\varepsilon}}$. Assuming that the equality between the residence time weighted and volume average strain rate also exists for this stirred tank configuration, the data of Higashitani (1983) were plotted versus $\gamma = 0.83 \, (\bar{\varepsilon}/v)^{1/2}$. The theoretical values for the collision efficiency for encounters between equally sized particles in simple shear flow are obtained from the values of the stability ratio as a function of N_s presented by Feke and Schowalter (1983). The stability ratio is the reciprocal of the collision efficiency.

The agreement between the replotted experimental data and theoretical values is quite reasonable. This implies that the collision efficiency for primary particles smaller than the Kolmogorov micro scale may indeed be calculated from particle interception trajectories in simple shear flow provided the correct equivalent shear rate γ is used.
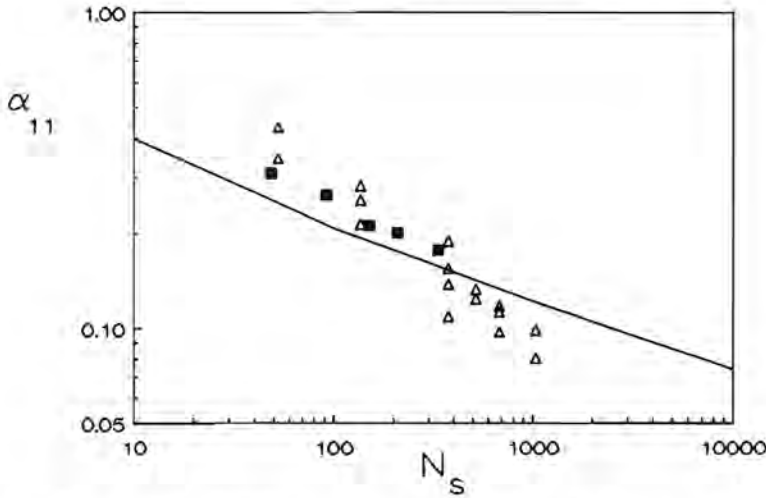
Δ   De Boer et al. (1989): polystyrene particles of diameter $d_1 = 0.74$ μm. Process conditions: $C_p = 7.66 \cdot 10^{-6}$ m^3/ m^3, $c_{NaCl} = 0.48$ mol l^{-1}. Tank geometry: $T = 0.19$ m, $D/T = 0.33$, Rushton turbine disc impeller.

■   Higashitani (1983): polystyrene particles of diameter $d_1 = 0.85$ μm. Process conditions: $c_{NaCl} = 1$ mol l^{-1}. Tank geometry: $T = 0.14$ m, $D/T = 0.5$, Flat blade paddle.

—   Feke and Showalter (1983), α_{11} in simple shear flow

Figure 5.3. Values for the initial collision efficiency α_{11} versus the parameter $N_S = 6\pi\mu \ d_1^3 \ \gamma \ / \ A_{1(2)}$ where $A_{1(2)} = 3.5 \cdot 10^{-21}$ J and $\mu = 10^{-3}$ kgm^{-1}s^{-1}.

5.4.2. LATER STAGES OF COAGULATION

The evolution of the volume mean diameter (VMD) during coagulation in a stirred tank is shown in fig. 5.4. De Boer et al. (1989b) discerned four different stages in the course of the coagulation process. The first stage (I), that is the formation of doublets was treated in the previous section. This stage is followed by an exponential type of growth designated as stage II. The coagulation rate diminishes during stage III of the process because of aggregate breakup and finally a steady state is reached (IV). Stages III and IV are discussed in the next chapter. This section deals with stage II of the coagulation process.
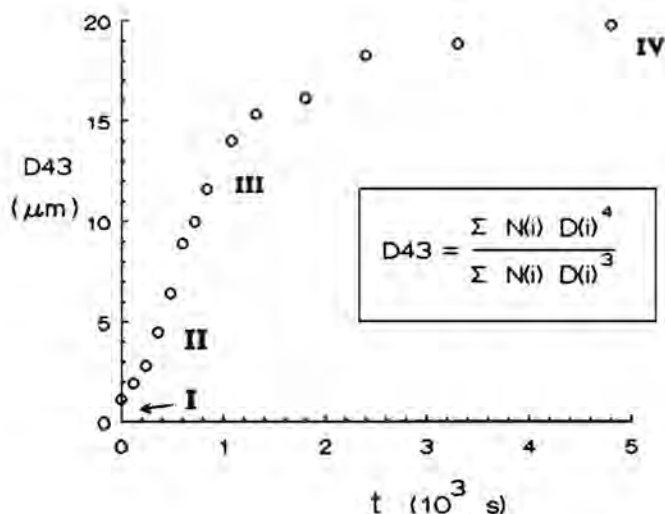
Figure 5.4. Evolution of the volume mean diameter D43 during batch coagulation in a stirred tank. Process conditions: $N = 6$ s^{-1}, $C_p = 3 \cdot 10^{-3}$ m^3/m^3, $c_{NaCl} = 0.48$ M, $T = 0.2$ m. Polystyrene latex produced by method of De Boer (1987), $d_1 = 0.48$ μm.

The accelerated growth as observed in stage II of the coagulation process is in disagreement with computations of coagulation assuming a uniform porosity within the flocs. With a constant collision efficiency a linear increase of the volume mean diameter with time is predicted (De Boer et al. 1989b).

Measurements with the laser diffraction instrument (see section 5.3.4.) showed that porosity increases significantly with aggregate size. Fig. 5.5 is a representative example of the variation of the average density $\bar{\varphi}$ within the flocs as a function of the VMD. The plot shows that $\bar{\varphi}$ decreases with increase of aggregate size according to a power law. Hence it seems plausible that the dependency of the solids density φ on aggregate size can be described with eq.(2-89):

$$\varphi = c \, (d_F / d_1)^D \qquad\qquad (5\text{-}21)$$

where d_F = floc diameter

d_1 = diameter of primary particle

D = fractal dimensionality

As is obvious from fig. 5.5, the fractal law is already applicable for aggregate sizes not much larger than the primary particle size. This is in agreement with findings of Gmachowski et al. (1990).

The average density $\overline{\varphi}$ is related to φ through the aggregate size distribution:

$$\overline{\varphi} = \Sigma \; Q_i \; \varphi_i = c \; \Sigma \; Q_i \; (D_i \, / \, d_i)^{D-3} \qquad (5\text{-}22)$$

where Q_i = volume fraction of aggregate size class i of Malvern particle sizer

D_i = characteristic size of size class i

φ_i = solids density corresponding to size D_i

The various laser diffraction measurements during the course of the coagulation process result in a set of equations of type (5-22). With a least squares fit estimates for c and D were obtained. Characteristic values for c and D were 0.8 and 2.4 respectively.
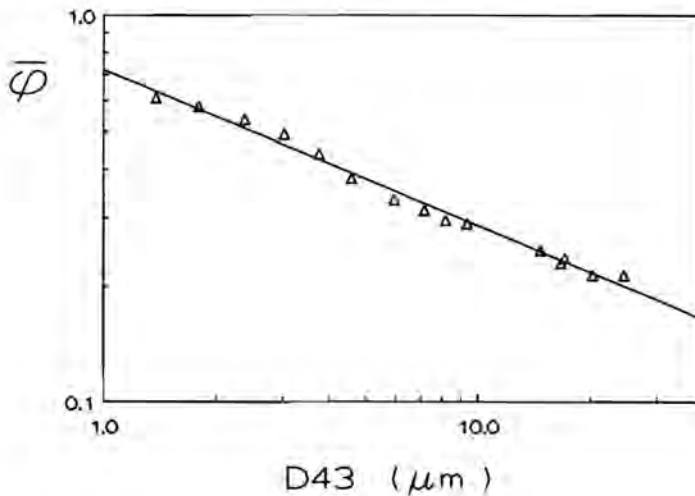
Figure 5.5. Variation of average density $\overline{\varphi}$ within the flocs as a function of volume mean diameter D43. Polystyrene particles produced by method of De Boer (1987) with diameter d_1 = 0.56 μm. Process conditions: N = 2 s^{-1}, C_p = 8·10^{-6} m^3/ m^3, c_{NaCl} = 0.48 M, T = 0.2 m.

Fig. 5.6 shows the calculated influence of the fractal dimensionality on the evolution of the VMD. The evolution of VMD was computed for different values of the fractal dimensionality by solving the population balances over the

various aggregate sizes given by eq.(4-31) without the occurrence of breakup. The values for the collision efficiencies were arbitrarily set equal to unity. For $D = 3$, the aggregate size increases linearly with time. For values of D less than 3 an accelerated increase in the volume mean diameter is observed, similar as in the experiments.
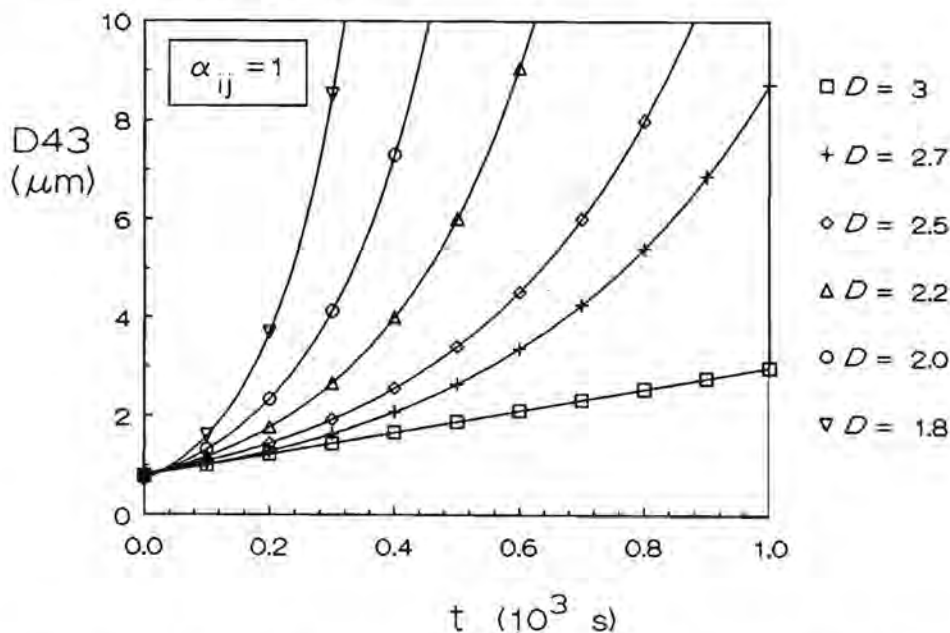
Figure 5.6. Calculated evolution of D43 for various values of the fractal dimensionality D when breakup is excluded and $\alpha_{11} = 1$, $d_1 = 1$ μm, $C_p = 10^{-5}$ m^3/ m^3 and $s_T = 35.9$ s^{-1}.

The porosity within the aggregates can be as large as 0.8. The fluid flow will then penetrate the surface of these porous flocs and enhances the collision efficiency with respect to impermeable solid particles of equal volume. In the next section approximate values for the collision efficiency of porous flocs are estimated.

5.4.3. COLLISION EFFICIENCIES FOR POROUS FLOCS

This section is concerned with the derivation of the collision efficiencies for encounters between porous aggregates.

In section 5.4.1 it was shown that the collision efficiency for primary particles smaller than the Kolmogorov micro scale may be obtained from trajectory analysis in simple shear flow. This analogy is assumed to hold for the aggregates also.

The collision efficiency of solid spheres depends on the ratio N_s of the hydrodynamic repulsive and attractive Van der Waals forces and on the ratio of the two radii λ. If the solid particles would be non-attractive, no collisions would occur due to hydrodynamic interaction and the collision efficiency would be zero. For porous aggregates collisions may still occur due to fluid flow through the flocs. The ratio of the collision frequency caused by penetration of fluid flow within the floc and the collision frequency that follows from the Smoluchowski equation is designated as the capture efficiency of the flocs. The capture efficiency is solely dependent on the permeability of the flocs and λ.

From the rigorous hydrodynamic analysis of Adler (1981a) capture efficiencies can be derived for collisions in simple shear flow between a large uniformly porous floc with radius a_i and a much smaller solid particle with radius a_j where $\lambda = a_j/a_i \leq 0.1$. Similar computations as performed by Adler for $\lambda \leq 0.1$, have not yet been carried out for collisions between more equally sized porous particles ($\lambda \to 1$). In this section an approximate method is presented to derive the capture efficiencies for porous flocs. This method is first tested by comparing its results to the rigorous results obtained from Adler (1981a) for $\lambda \leq 0.1$. Subsequently the capture efficiencies for encounters between porous flocs of more equal size are estimated by this method.

In the trajectory analysis of Adler (1981a) the largest particle is taken as the reference particle whose center is at the origin of the collision sphere. The radius of the collision sphere is the sum of the two radii a_i and a_j of the colliding particles. The relative trajectories of the centers of the "colliding" particles can be either open or closed whether attractive forces

are present or not. With an open trajectory the approaching particle is removed again after the "collision" from the reference particle. With a closed trajectory the particle will finally collapse onto the surface of the reference particle in the presence of attractive forces. A separation surface can be defined as the surface which separates these two kinds of trajectories.

With encounters between porous flocs the trajectories run through the collision sphere and the flocs are assumed to stick together when they make contact. As the flocs become less permeable, the separation surface between open and closed trajectories moves to the surface of the collision sphere resulting in a decreasing capture efficiency. If the separation surface is located outside the collision sphere the capture efficiency is equal to zero. Then the collisions between the porous flocs are no longer induced by the fluid flow penetration. The porous flocs may be considered as impermeable. The collision efficiency of impermeable flocs results from the Van der Waals attraction between the two nearest primary particles (see section 2.4.4.). Note that this attraction is different from the attraction between solid particles. The collision efficiencies of impermeable flocs are considered later in this section.

Values of the capture cross section σ_c due to penetration of fluid flow within the floc for $\lambda \leq 0.1$ were presented by Adler (1981a) as a function of the dimensionless floc size ξ which is defined as:

$$\xi = a_i / \sqrt{k_p} \tag{5-23}$$

where a_i = radius of floc consisting of i primary particles

   k_p = floc permeability

The permeability k_p is defined by Darcy's law which describes the pressure drop through a porous media and has the dimension $[m^2]$.

Values of the capture efficiency due to open trajectories inside the aggregate as a function of ξ follow directly from the capture cross section σ_c (Arp and Mason 1976):

$$\alpha_{ij} = \left[\frac{\sigma_c}{\pi (a_i + a_j)^2} \right]^{3/2} = \left[\frac{\sigma_c}{\pi a_i^2 (1 + \lambda)^2} \right]^{3/2} \tag{5-24}$$

In fig. 5.7 α_{ij} is plotted versus ξ. At $\xi > 10.89$ the separation surface between open and closed trajectories is located outside the porous sphere and the capture efficiency is equal to zero.
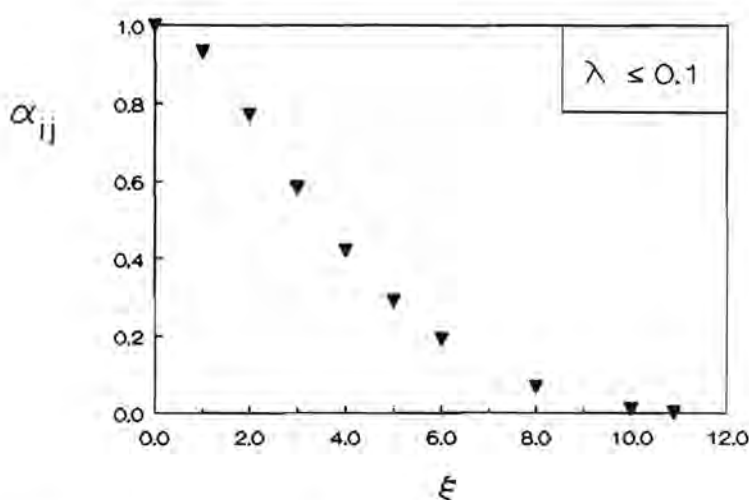
Figure 5.7. Values for capture efficiency α_{ij} versus dimensionless floc size ξ for particle radii ratio $\lambda \leq 0.1$.

In order to relate the capture efficiency to the actual aggregate size we have to know the permeability of the aggregate (see eq.5-23). We estimated the permeability of a floc with solids density φ by:

$$k_p = \frac{3 - \frac{9}{2} \varphi^{1/3} + \frac{9}{2} \varphi^{5/3} - 3 \varphi^2}{18 \varphi (3 + 2 \varphi^{5/3})} d_1^2 \tag{5-25}$$

(Happel 1959)

which reduces to the following equation when $\varphi \to 0$:

$$k_p = \frac{d_1^2}{18 \varphi} \tag{5-26}$$

These expressions are derived for uniform random assemblies of noncontacting spheres. The structure of the flocs is nonuniform, and is expected to display on the average the following variation of solids density with radial distance r from the center of mass:

$$\varphi(r) = c \frac{D}{3} \left(\frac{r}{a_1} \right)^{D - 3} \tag{5-27}$$

From this equation it follows that at small values of the radial distance from the center of the floc the density drops off very rapidly, but at larger

values it decreases more gradually. Hence for large flocs the required
uniformity to apply the expressions (5-25) and (5-26) will not to be a serious
drawback, since the solids density of the fractal floc is quite homogeneous in
the outer layers of the floc.

The requirement of no contact between the particles is not met in the floc
since primary particles are bound to one or more neighbours. These short range
interactions are accommodated through a shielding coefficient $C(k_c) < 1$ which
depends on the coordination number k_c of the primary particles within the floc
(Sonntag and Russel 1987). Then the permeability for $\varphi \to 0$ is given by:

$$k_p = \frac{d_1^2}{18 \; \varphi \; C_{avg}} \qquad\qquad (5-28)$$

where C_{avg} is an average shielding coefficient of the floc, i.e. $C_{avg} = \Sigma$
$f(k_c) \, C(k_c)$ with $f(k_c)$ the fraction of particles with coordination number k_c.
The coordination number of the primary particles in the porous floc is
somewhere between 1 and 2 (Sonntag and Russel 1986). Since $C(1) = 0.724$ and
$C(2) = 0.221$ a value of 0.5 for C_{avg} seems to be a good estimate for all
aggregate sizes except for the doublets where C_{avg} is equal to $C(1) = 0.724$.

Assuming that the shielding coefficient may also be applied to eq.(5-25)
values of the dimensionless floc radius ξ may be computed if we can assume a
relation between floc density and size such as eq.(5-21). This fractal law
(5-21) may be applied to aggregates consisting of more than three primary
particles but it is not applicable to doublets (see section (2.6.2). For the
doublets we assumed $\varphi = 0.8$ in analogy with Treweek and Morgan (1977). Fig.
5.8 shows the dimensionless floc size ξ as a function of aggregate size for
two different values of the fractal dimensionality D. The relation between
dimensionless floc size and actual floc radius makes it possible to couple the
capture efficiencies presented in fig. 5.9 directly to the aggregate sizes.

For encounters between aggregates of similar size ($\lambda \to 1$) the capture
efficiencies are expected to be larger and also to hold for a wider range of
aggregate sizes because the trajectories are more forced inside the collision
sphere. That the trajectories are dependent on λ is clearly demonstrated by
the study on the hydrodynamic interaction of unequal solid non-attractive
spheres in simple shear flow by Adler (1981c). The particles were found to
approach each other closer when $\lambda \to 1$. When λ is small compared to 1, the
smaller sphere follows the streamlines around the larger one. The
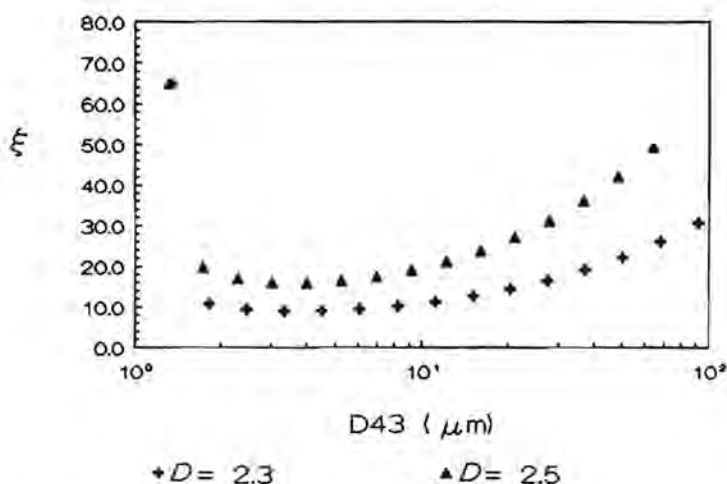
Figure 5.8. Dimensionless floc size ξ as a function of aggregate size a_i for two different values of the fractal dimensionality D. Primary particle size $d_1 = 1$ μm. Constant c in eq.(5-21) is set to unity.

dimensionless minimum distance $H^*_{min} = H_{min}/a_i$ of approach between the large sphere with radius a_i and the small particle amounts to 0.156. This is considerably larger than the value $4.2 \ 10^{-5}$ which was obtained for equally sized particles. It was shown by Adler that for $\lambda > 0.2$ the particles approach each other already much closer than for $\lambda \leq 0.1$.

This information about the minimum distance of approach is useful in an approximate method which is introduced here to derive the capture efficiency for encounters between porous flocs. This approximate method is designated as the shell-core model. In the shell-core model the porous floc is assumed to consist of an impermeable core and a complete permeable shell. In fig. 5.9 two impermeable cores with corresponding permeable shells approaching each other in simple shear flow are depicted. For $\lambda = 1$ and $\lambda \leq 0.1$ the radius of the core R_{Ci} of the largest floc is obtained from the minimum center-to-center distance r_{min} of the impermeable cores minus the minimum distance of approach H_{min} between the surfaces of the cores, i.e., for $\lambda = 1$:

$$R_{Ci} = R_{Cj} = (r_{min} - H_{min}) / 2 = (r^*_{min} a_i - H'_{min} R_{Ci}) / 2 \qquad (5-29a)$$

and for $\lambda \leq 0.1$:

$$R_{Ci} \cong r_{min} - H_{min} = r^{\bullet}_{min} a_i - H'_{min} R_{Ci} \tag{5-29b}$$

where ($^{\bullet}$) denotes normalization by the floc radius a_i and (') normalization by the radius of the impermeable core.

For $\lambda = 1$ it follows that

$$R^{\bullet}_{Ci} = \frac{R_{Ci}}{a_i} = \frac{r^{\bullet}_{min}}{(2 + H'_{min})} \tag{5-30a}$$

whereas for $\lambda \leq 0.1$ the core radius of the largest floc is given by:

$$R^{\bullet}_{Ci} \cong \frac{R_{Ci}}{a_i} = \frac{r^{\bullet}_{min}}{(1 + H'_{min})} \tag{5-30b}$$

The capture efficiency is obtained from trajectories of the two approaching impermeable spherical cores. For this we make use of the data concerning the trajectories with encounters between two solid non-attractive particles presented by Adler (1981b). Adler (1981b) computed "capture cross sections" for the relative trajectories of two non-attractive solid particles penetrating spheres of radii ρ_m larger than the sum of the radii of the two solid particles, i.e. $\rho_m > (R_{Ci} + R_{Cj})$. Values of the dimensionless capture cross sections (σ_c / R^2_{Ci}) were presented as a function of ρ_m / R_{Ci} (Fig. 3a). The analysis of Adler may be interpreted as an evaluation of the capture cross
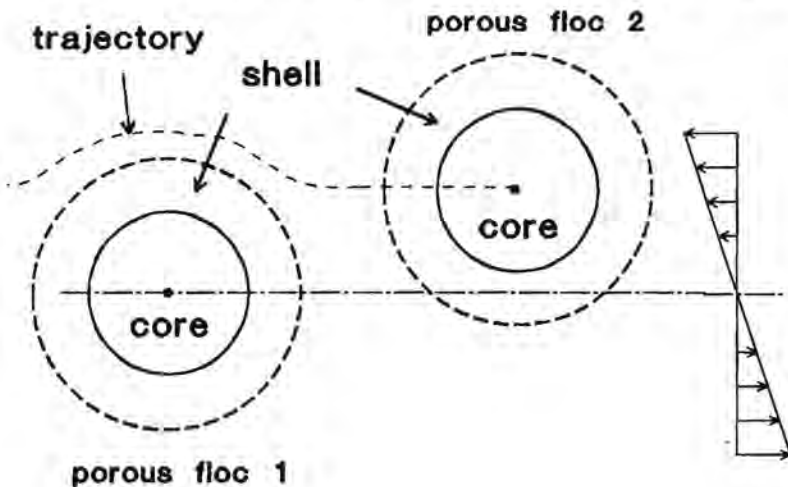
Figure 5.9. Shell core model

section of a porous floc with overall size a_i and core size R_{Ci} as a function of $(a_i + a_j) / R_{Ci}$, i.e., as a function of $2a_i / R_{Ci}$ ($= 2 (R_{Ci}^*)^{-1}$) for $\lambda = 1$ and of $\sim a_i/ R_{Ci}$ ($= (R_{Ci}^*)^{-1}$) for $\lambda \leq 0.1$. Starting from the shell-core model the capture efficiency of the porous floc may be evaluated from:

$$\alpha_{ij} = \left[\frac{1}{\pi} \right]^{3/2} \left[\frac{\sigma_c}{R_{Ci}^2} \right]^{3/2} \frac{R_{Ci}^3}{\rho_m^3} \tag{5-31}$$

So from the values of (σ_c / R_{Ci}^2) versus ρ_m / R_{Ci} as presented by Adler (1981b) values for the capture efficiency of a porous floc as a function of dimensionless core size R_{Ci}^* can be deduced for $\lambda \leq 0.1$ and $\lambda = 1$.

To compare the values for the capture efficiency obtained by the shell-core model with those calculated rigorously from Adler (1981a) for $\lambda \leq 0.1$ the dimensionless core radius R_{Ci}^* has to be related to the dimensionless floc size ξ. Adler (1981a) presented values of minimum center-to-center distance r_{min}^* as a function of ξ for $\lambda \leq 0.1$. These values were substituted into eq.(5-30b) to yield R_{Ci}^* as a function of ξ. The dimensionless H_{min}' was set equal to 0.156. In table 5.2 values of dimensionless floc size ξ and of corresponding core size R_{Ci}^* are presented.

Table 5.2. Values of ξ and corresponding core size R_{Ci}^*

ξ	R_{Ci}^*	ξ	R_{Ci}^*
1	0.175	8	0.802
2	0.336	10	0.850
3	0.474	15	0.909
4	0.581	40	0.971
5	0.662	70	0.984
6	0.722	∞	1

Fig. 5.10 shows the comparison between the values for the capture efficiency obtained from Adler (1981a) and the values calculated by the shell-core model. The agreement is quite satisfactory. Hence the visualization of the porous

floc as an impermeable core with completely permeable shell seems to be justified. This representation is expected to perform even better for the fractal floc than for a uniformly porous sphere because the fractal structure resembles the picture of an impermeable core and completely permeable shell more closely.
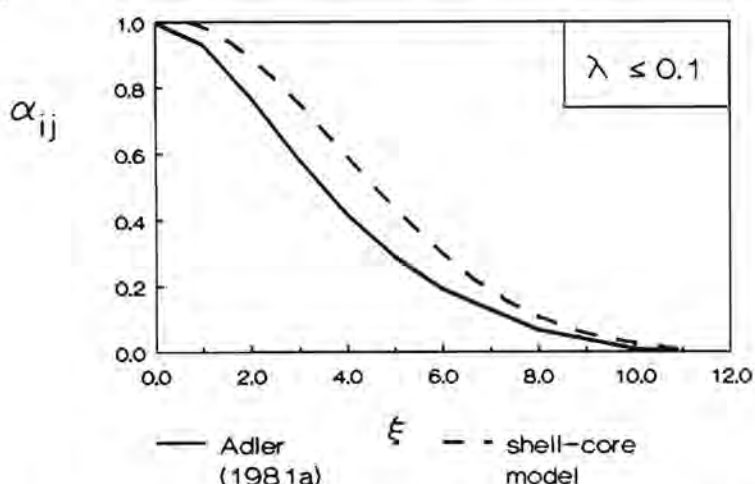
Figure 5.10. Comparison between values for the capture efficiency α_{ij} obtained from Adler (1981a) and the values obtained from the shell-core model for $\lambda \leq 0.1$.

Next starting from the shell-core model, values for the capture efficiency of encounters between equally sized aggregates were computed with use of eq.(5-31) from capture cross sections for non-attractive equally sized solid spheres as presented by Arp and Mason (1976) and by Adler (1981b). Fig. 5.11 shows α_{ij} for both $\lambda \leq 0.1$ and $\lambda = 1$ as a function of ξ. As expected the capture efficiency for encounters between equally sized porous flocs is larger than for encounters where $\lambda \leq 0.1$. Furthermore the capture efficiency does not drop to zero at $\xi = 10.89$ but remains almost constant for $40 < \xi < 100$.

The capture efficiencies for values of $\lambda > 0.2$ are expected to approximate the values calculated for $\lambda = 1$, since the trajectories of the impermeable cores are relatively not much different from those with encounters between equally sized particles (Adler 1981c). The region $0.1 \leq \lambda < 0.2$ is the transition range where the capture efficiency is intermediate between the values corresponding to $\lambda \leq 0.1$ and $\lambda = 1$ respectively.
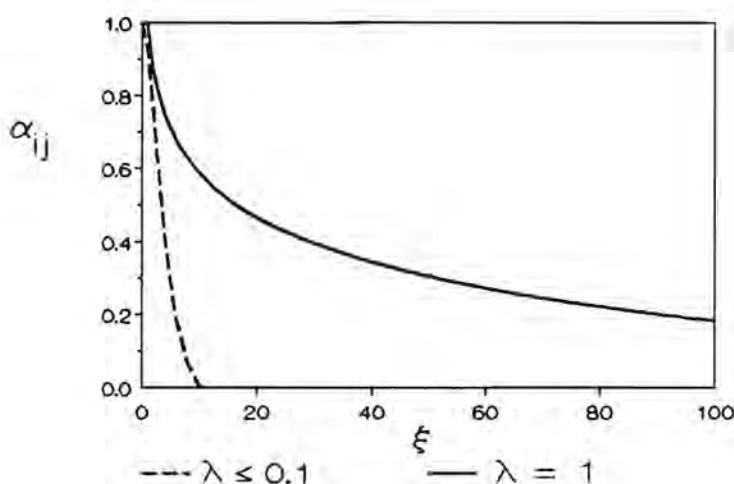
Figure 5.11. Values for capture efficiency α_{ij} for both $\lambda \leq 0.1$ and $\lambda = 1$ as a function of the dimensionless floc size ξ.

Fig. 5.12 shows the calculated capture efficiency α_{ij} for porous flocs derived from the shell-core model and the collision efficiency for solid spheres of equal cross section as a function of floc size. The flocs consist of primary particles of 1 μm and are assumed to have a fractal structure with D equal to 2.5. The collision efficiency computed for solid spheres decreases very rapidly with increase of size, whereas the capture efficiency for porous flocs remains almost constant. Since with a smaller fractal dimensionality the flocs are more porous at a comparable aggregate size, the capture efficiency for porous flocs increases with a decreasing fractal dimensionality.

In fig. 5.12 also the collision efficiencies α_{ij} for porous impermeable flocs are included. These values are the collision efficiencies of solid spheres that correspond to values of the parameter N_S^F that is given by:

$$N_S^F = \frac{6\pi \; \mu \, d_i^4 \; \gamma^{\cdot}}{2 \; A_{1(2)} \; a_i} \tag{5-32}$$
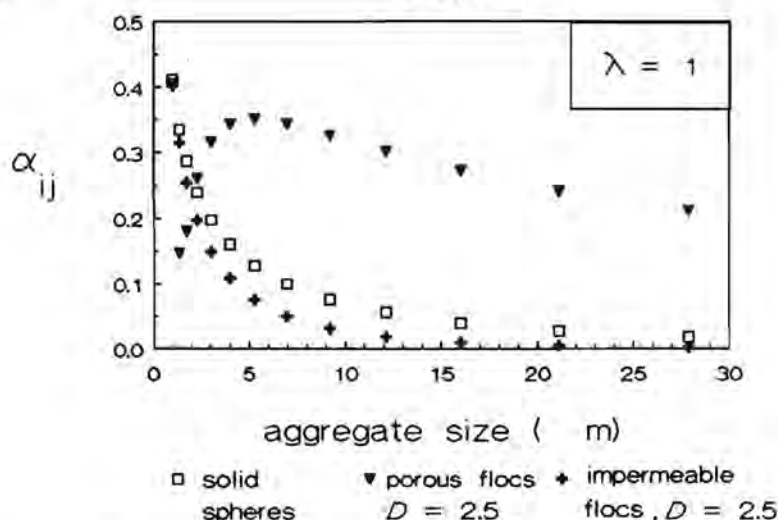
Figure 5.12. Values for the collision efficiency α_{ij} for porous flocs, for solid spheres of equal cross section and for porous impermeable flocs as a function of particle size d_i.

These modified values for the parameter N_S result from the attractive force being different between porous flocs than between solid particles. The Van der Waals attraction between porous flocs is given by eq.(2-73):

$$F_{11} = \frac{A_{1(2)}\ a_1}{12\ H^2} \tag{5-33}$$

whereas the attractive force between solid particles is:

$$F_{ij} = \frac{A_{1(2)}\ (a_i + a_j)\ \lambda}{6\ H^2\ (1 + \lambda)^2} \tag{5-34}$$

The parameter N_S represents the ratio of hydrodynamic repulsive shear forces to attractive Van der Waals forces. Hence the attractive force in the denominator of the parameter N_S has to be modified for porous aggregates with respect to solid particles. This means that the parameter N_S for the solid particles has to be multiplied by the ratio of eq. (5-34) and eq. (5-33):

$$N_S^F = N_S\ \frac{2\lambda\ (a_i + a_j)}{a_i\ (1 + \lambda)^2} = \frac{6\pi\ \mu\ (a_i + a_j)^3\ \gamma'}{A_{1(2)}} \cdot \frac{2\lambda\ (a_i + a_j)}{a_i\ (1 + \lambda)^2} \tag{5-35}$$

Eq. (5-35) reduces to eq.(5-32) when $a_i = a_j$ and $\lambda = 1$.

Since the shell-core model does not take into account the Van der Waals attraction between the flocs, the collision efficiencies computed for impermeable flocs were used whenever these values turn out to be equal or larger than the capture efficiencies calculated with the shell-core model. For $\lambda = 1$ it can be seen from fig. 5.12 that this is only the case for the initial stages of coagulation. For encounters between flocs with size ratios λ smaller than 0.1 this is also true for values of the dimensionless size ξ of the largest floc larger than ξ_c (= 10.89) where the capture efficiency obtained from the shell-core model is equal to zero.
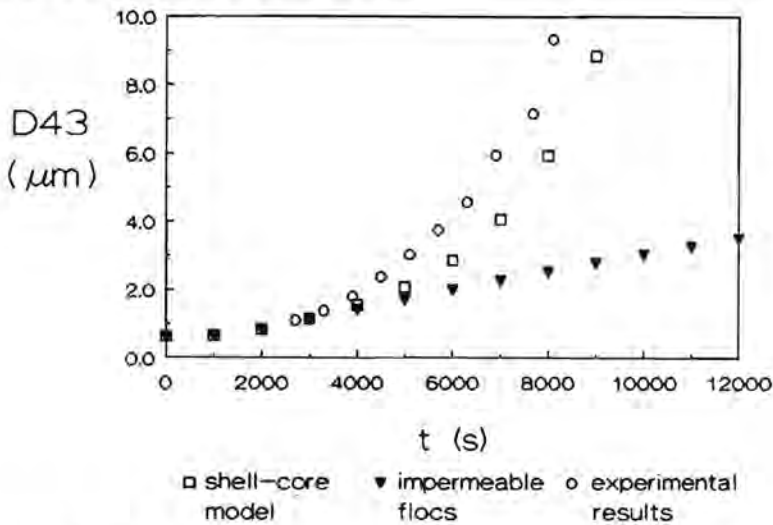
Figure 5.13. Evolution of D43 as determined experimentally and also as obtained by solving the population balances over the various aggregate sizes with the appropriate values for the collision efficiency α_{ij} and with values for α_{ij} for impermeable flocs. Polystyrene particles produced by method of De Boer (1987) with diameter d_1 = 0.56 μm. Process conditions: $N = 2$ s^{-1}, $C_p = 8 \cdot 10^{-6}$ m^3/ m^3, c_{NaCl} = 0.48 M, T = 0.2 m.

In fig. 5.13 the evolution of the volume average aggregate size in stage I and II of the coagulation process is shown as determined experimentally and computed by solving the population balances with the appropriate values for the collision efficiency for the various aggregate sizes. In fig. 5.13 also

the aggregate growth is depicted that follows from the computations where the porous aggregates are assumed to be impermeable. Clearly this assumption underestimates the aggregate growth and should not be used for predictions about the coagulation process. The agreement between the experimental results and data computed with the capture efficiencies from the shell-core model is quite good, consolidating the use of these capture efficiencies in modelling the aggregation process.

5.5. DEPENDENCY OF COAGULATION RATE
ON PROCESS VARIABLES

An increase in coagulation rate is directly expressed in a proportionally enhanced growth of the aggregates. The dependency of the coagulation rate on the various process variables was determined from plots of the volume mean diameter versus time.

In order to determine unambiguously the dependency of the coagulation rate on the process conditions, the later stages of coagulation that are affected by aggregate breakup had to be excluded from the analysis. These later stages could be discriminated by adding a steric stabilizing agent (poly vinyl alcohol) to the suspension after the steady state was reached. Poly vinyl alcohol adsorbs onto the surface of the primary particles and precludes coagulation and recombination of aggregate fragments due to steric hindrance. Hence only breakup remains (De Boer 1987). The evolution of the aggregate size distribution upon addition of poly vinyl alcohol is shown in fig. 5.14. From such plots the aggregate size at which breakup becomes significant was determined. The size evolution prior to this aggregate size was used in the analysis to determine the dependency of the coagulation rate on the various process variables.

The coagulation rate is strongly dependent on the fractal dimensionality the aggregates attain as was shown in section 5.4.2. The fractal dimensionality was therefore determined as a function of the process variables in order to verify whether changes in coagulation rates are to be attributed to different values of D. The fractal dimensionality proved to be independent of impeller speed and of concentration of solids and destabilizer. It was however found to

be slightly different for the various polystyrene latices that were used in the course of the aggregation experiments. This dependency of fractal dimensionality on the polystyrene latex used is discussed in the next chapter.

In the following sections the dependency of the coagulation rate on impeller speed, on solids concentration and on concentration of destabilizer is subsequently discussed.
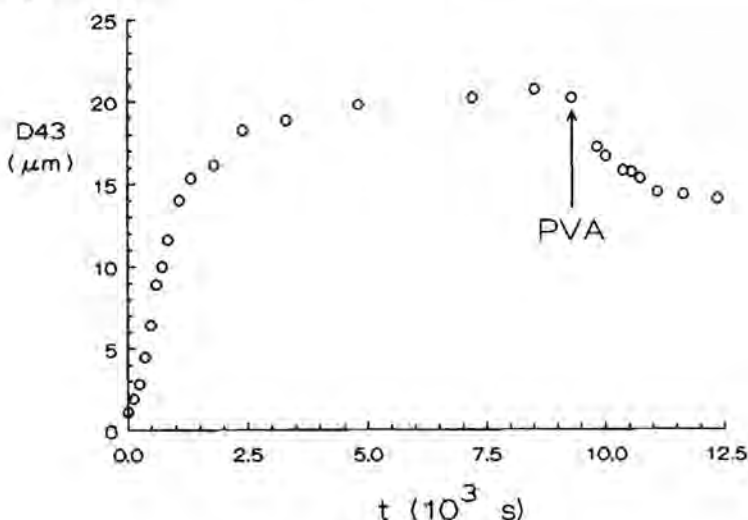
Figure 5.14. Addition of polyvinyl alcohol at steady state. Process conditions: $N = 6$ s^{-1}, $C_p = 3 \cdot 10^{-3}$ m^3/ m^3, $c_{NaCl} = 0.48$ M, $T = 0.2$ m. Polystyrene latex produced by method of De Boer (1987), $d_1 = 0.48$ μm.

5.5.1. EFFECT OF IMPELLER SPEED

The impeller speed N affects the mean energy dissipation rate in the stirred tank:

$$\bar{\varepsilon} = N_p \, \rho \, N^3 \, D^5 / \, V \qquad (5\text{-}36)$$

The residence time weighted strain rate $\bar{s}_T$ which controls the coagulation rate is proportional to the square root of the mean energy dissipation rate $\bar{\varepsilon}$. It follows from eq.(5-36) that $\bar{s}_T$ is proportional to $N^{3/2}$.

Fig. 5-15 shows the results from coagulation experiments carried out at different impeller speeds in the 20 cm vessel. The solids concentration was $6 \cdot 10^{-5}$. The stirrer speeds were 2, 4, 6 and 8 (s^{-1}). Corresponding residence time weighted strain rates were 12, 34, 63 and 97 (s^{-1}).

At increasing impeller speed the coagulation rate is enhanced and the final aggregate size is observed to decrease. The variation of final aggregate size with impeller speed is discussed in the next chapter.

The initial parts of the growth curves where breakup is absent were found to overlap each other approximately when plotted versus $N^{1.3} \cdot t$. The power law coefficient is less than 1.5 because the collision efficiencies in the initial stages of coagulation decrease with the impeller speed according to $N^{-0.4}$ as can be deduced from the dependency of α_{11} on strain rate as depicted in fig. 5.3. This results in an initial power law dependency of the coagulation rate on impeller speed equal to $N^{1.1}$. Since the collision between the larger porous flocs are brought about by the penetration of fluid flow within the flocs, the collision efficiencies of the larger porous flocs are expected to be independent of stirrer speed. Their capture efficiencies increase proportional to the strain rate $\bar{s}_T$, that is proportional to $N^{1.5}$. The power law dependency determined experimentally is intermediate between $N^{1.1}$ and $N^{1.5}$.

Simulation of the coagulation process at equal impeller speeds revealed a power law coefficient of 1.4 for the growth rate, not much different from the experimental result.

5.5.2. EFFECT OF SOLIDS CONCENTRATION

In fig. 5.16 results are shown from experiments in which the solids concentration C_p was varied. It is observed that coagulation proceeds faster at increasing values of C_p. The initial parts of the growth curves where breakup is absent were found to overlap each other approximately when plotted versus $C_p \cdot t$. Hence the evolution of the aggregate size (growth rate) is first order with respect to C_p in agreement with the binary collision assumption.
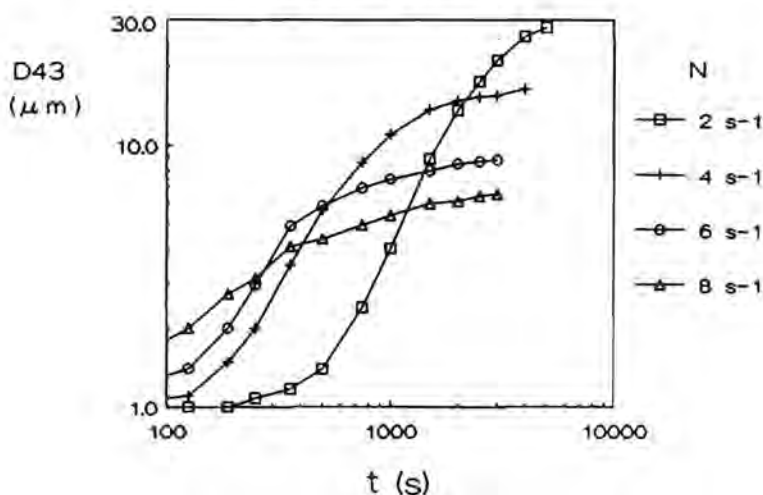
Figure 5.15. Course of coagulation for various impeller speeds at $C_p = 6 \cdot 10^{-5}$ m^3/ m^3, $c_{NaCl} = 0.48$ M, T = 0.2 m. Polystyrene particles with $d_1 = 0.8$ μm produced by polymerization method as proposed by De Boer (1987).
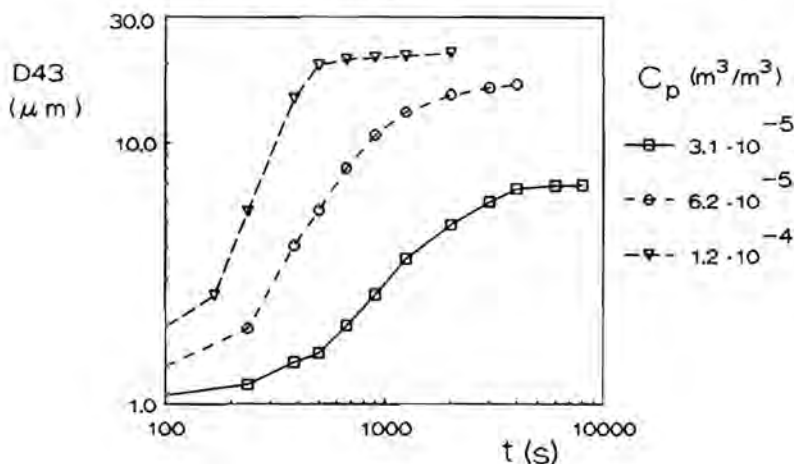
Figure 5.16. Variation of solids concentration C_p. Polystyrene particles with $d_1 = 0.8$ μm prepared with polymerization method of De Boer (1987). N = 4 s^{-1}, $c_{NaCl} = 0.4$ M, T = 0.2 m.

De Boer et al. (1989) reported a proportionality of the growth rate with $C_p^{1.72}$. This large exponent resulted however from an analysis that also included parts of growth curves that were clearly affected by breakup.

The fact that aggregates grow larger at increasing values of C_p is discussed in the next chapter.

5.5.3. EFFECT OF SALT CONCENTRATION

Fig. 5-17 shows the aggregate growth as a function of the concentration of the destabilizer (NaCl) for a specific polystyrene latex. At a salt concentration of 0.5 M the growth rate is significantly smaller than for the larger concentrations. This is caused by an increase of the collision efficiency for the initial stages of coagulation with electrolyte concentration. Increasing the salt concentration merely reduces the electrostatic repulsion to a larger extent and maximizes the attractive force between the colliding particles. Increase of the attractive force with respect to the repulsive hydrodynamic force enhances the orthokinetic collision efficiency and consequently the coagulation rate.
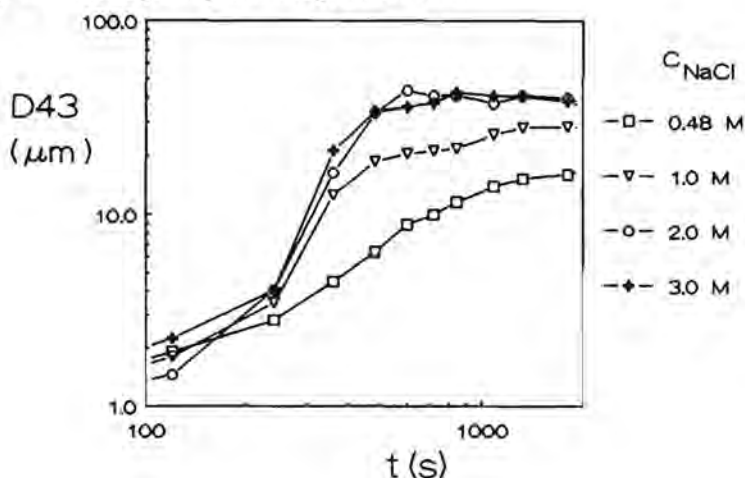
Figure 5.17. Variation of salt concentration c_{NaCl}. Polystyrene particles with $d_i = 0.48$ μm prepared with polymerization method of De Boer (1987). $N = 6$ s^{-1}, $C_p = 2.9 \cdot 10^{-5}$ m^3/ m^3, $T = 0.2$ m.

The increase in attractive force is also clearly demonstrated by the increase of the final aggregate size with salt concentration. The influence of the salt concentration on the final aggregate size is discussed in the next chapter.

Since the values of the initial collision efficiencies derived in previous sections correspond to the case where the electrostatic repulsion is negligible to the Van der Waals attraction, differences between theoretical predictions and experimental data concerning the course of the batch coagulation process may occur when the electrostatic repulsion is still appreciable. For most latices however the variation of the coagulation rate with the salt concentration was found to be less pronounced than for the particular case depicted in fig. 5-17. No serious errors are therefore introduced with the assumption of the electrostatic repulsion being negligible to the Van der Waals attraction between the primary particles.

5.6. CONCLUSIONS

The collision efficiency of encounters between primary particles smaller than the Kolmogorov micro scale may be approximated by the theoretical values derived from trajectory analysis in simple shear flow provided the correct equivalent simple shear rate is used.

The accelerated growth of the aggregates in the stages following the doublet formation of primary particles is to be attributed to the fractal structure of the formed aggregates. In a fractal structure less primary particles are required to build up an aggregate of a certain size than in a uniform closed packed structure. Due to the large porosities the aggregates attain, the fluid flow is able to penetrate the aggregates, resulting in enhanced collision efficiencies. Values for these collision efficiencies between porous flocs have been estimated. The application of these values in the description of the aggregate growth yielded results in agreement with experimental findings.

The dependency of the coagulation rate on solids concentration and on impeller speed was found to be in agreement with the orthokinetic turbulent binary collision mechanism for aggregates smaller than the Kolmogorov micro scale. The variation of the coagulation rate with concentration of destabilizer results from the dependency of the collision efficiencies for the initial stages of coagulation on the attractive force between the primary particles.

CHAPTER VI
MAXIMUM AGGREGATE SIZE
IN STIRRED TANKS

6.1. INTRODUCTION

The steady state in coagulation processes is the result of a dynamic equilibrium between growth and disruption of the flocs, at least for particles like polystyrene with a relatively low value of the Hamaker constant (Thomas 1964, De Boer 1987). The balance between aggregation and floc rupture determines the steady state distribution of floc sizes. The steady state results from the reversibility of the relatively weak Van der Waals bonds between the primary particles within the flocs. The reversibility of the coagulation process is also demonstrated by the independency of the steady state aggregate size distribution on the initial conditions of the batch experiments as will be shown in section 6.2. The non-existence of multiple steady state size distributions also implies the independency of the fractal structure of the flocs upon the process conditions, which was experimentally verified.

Modelling the batch coagulation process is simplified by this independency of both floc structure and binding forces between the primary particles of the process conditions. In section 6.3 a simulation model for batch coagulation in the 20 cm vessel for particles smaller than the Kolmogorov micro scale is presented. The coagulation model is based on the population balances as formulated in chapter 4. The maximum aggregate size as a function of impeller speed, of concentration of solids and destabilizer as predicted by the model is compared to the experimental findings in consecutive sections 6.3, 6.4 and 6.5. Finally the maximum aggregate sizes as formed in the stirred tanks of different sizes is discussed.

6.2. STEADY STATE REVERSIBILITY

In the previous chapter it was shown that after an exponential type of growth the coagulation rate diminishes and finally a steady state is reached. The existence of a dynamic equilibrium was clearly demonstrated by the addition of poly vinyl alcohol to the suspension after the steady state was reached. Poly vinyl alcohol inhibits coagulation and recombination of possible aggregate fragments due to steric hindrance (See also section 5.5). If in the steady state coagulation and consequently breakup would be absent, addition of poly vinyl alcohol should not have any effect on the system. However, addition of the steric agent resulted in a decrease of the volume mean diameter, as was shown in fig. 5.15. Obviously, a dynamic equilibrium exists between growth and disruption of aggregates.
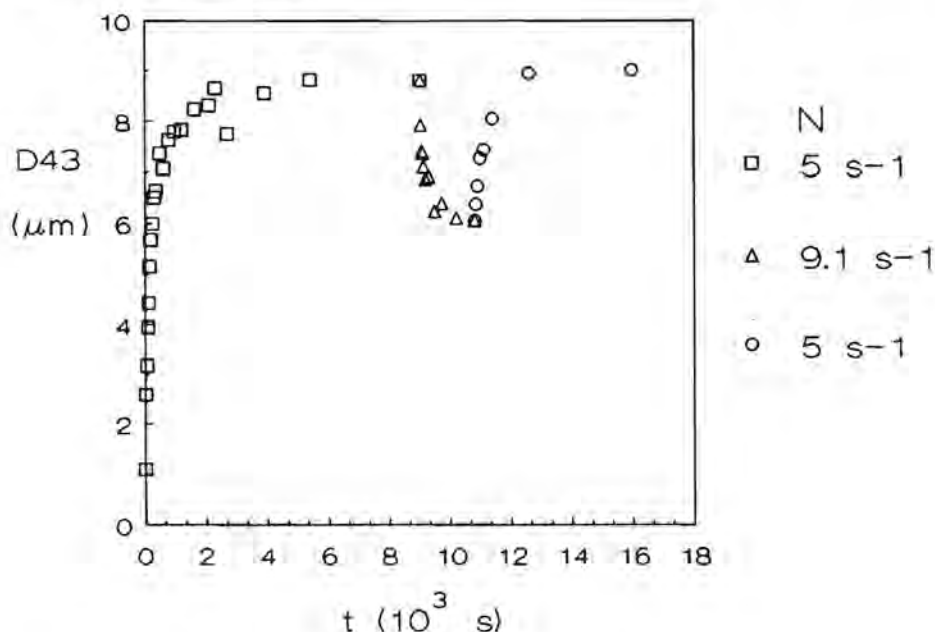
Figure 6.1. Change of impeller rotational speed N at successive steady states. Polystyrene particles produced by method of Eshuis et al. (1991) with $d_1 = 1.1$ μm. Experimental conditions: $T = 0.2$ m, $C_p = 3 \cdot 10^{-4}$ m^3/m^3 and $c_{NaCl} = 1$ M.

The existence of this dynamic equilibrium is also demonstrated by fig. 6.1. In the experiment depicted in fig. 6.1 the stirrer speed was changed from 5 to 9 s^{-1} after the steady state had been reached and later reduced again to 5 s^{-1}. If the final aggregate size was solely determined by aggregate breakup, the aggregate size would remain at the level obtained with the stirrer speed set at 9 s^{-1}. However, the aggregates started to grow again after the stirrer speed had reduced again to 5 s^{-1}. Moreover, total recovery of the previous aggregate size was established implying that the binding forces between the primary particles are unaffected by the continuous breaking and re-establishment of the bonds as would be expected with Van der Waals attraction between the primary particles.
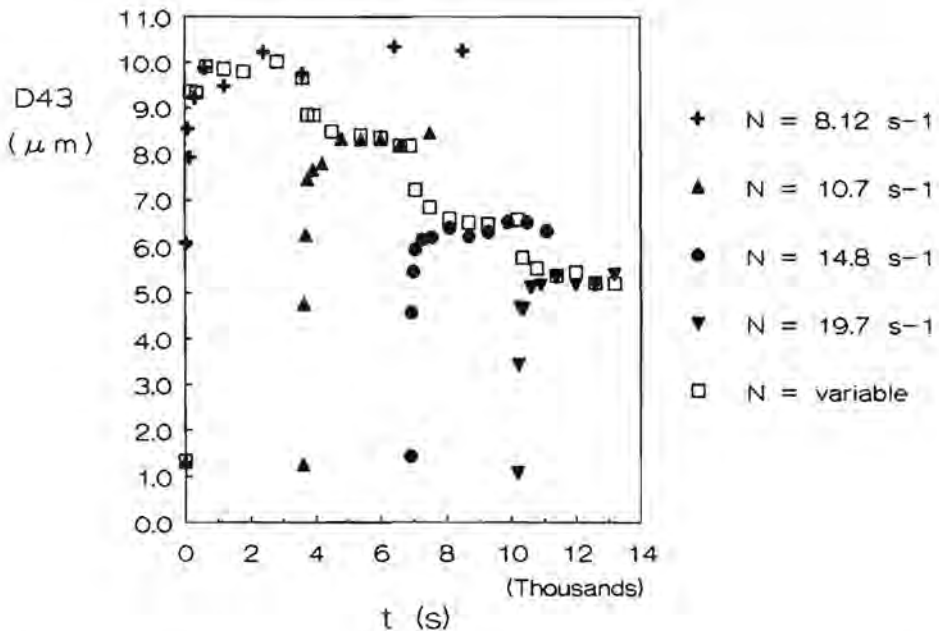
Figure 6.2. Effect of changing impeller speed at successive steady states. Polystyrene particles prepared by method of Eshuis et al. (1991) with d_i = 1.1 μm. Experimental conditions: T = 0.2 m, C_p = $1.7 \cdot 10^{-3}$ m^3/m^3 and c_{NaCl} = 0.48 M.

The re-establishment of the same steady state also indicates that the steady state particle size distribution (PSD) is independent of the initial PSD the final aggregates emerge from. Experiments were conducted to test the independency of the steady state PSD on the initial PSD and consequently on the initial conditions of the aggregation process. In the first experiment the coagulation was started at $N = 8.1$ s^{-1}. Subsequently when the steady state was reached, the impeller speed was raised to 10.7, 14.2, and 19.7 s^{-1}. Batch experiments were also carried out starting with these impeller speeds. The size evolution in these experiments is depicted in fig. 6.2 together with the results of the batch experiments where the impeller speed was varied. Evidently the final aggregate size corresponding to a certain impeller speed is independent on the shear history of the destabilized suspension.

This feature also implies that the fractal dimensionality is independent of applied shear stress. Because if shearing at $N = 9$ s^{-1} as applied in the experiment depicted in fig. 6.1, would lead to structural reorganization of the flocs, it is most unlikely that reaggregation at $N = 5$ s^{-1} would result in a similar steady state aggregate size distribution as obtained before. The independency of the fractal dimensionality on the process conditions was experimentally verified. An explanation for this independency may be that the initial turbulent collision mechanism is responsible for the fractal dimensionality of the flocs and not the shear induced restructuring (see also the discussion in section 6.7).

Fig. 6.3 shows a second experiment where after the steady state was reached an equal amount of polystyrene latex was added to the suspension to double the concentration of solids. In fig. 6.4 also the evolution of the volume mean diameter of the aggregates is shown where the initial concentration of solids was set to this double concentration of solids. The final aggregate size seems to be independent on the way the primary particles were introduced into the stirred vessel, e.g. all at once, or in parts at successive stages. This feature is useful when the variation of the solids concentration is pursued even up to values where the characteristic coagulation time becomes equal or larger than the macromixing time in the vessel. The incomplete mixing at the beginning of the coagulation process will certainly affect the initial coagulation process, but will not be decisive for the final aggregate size distribution.
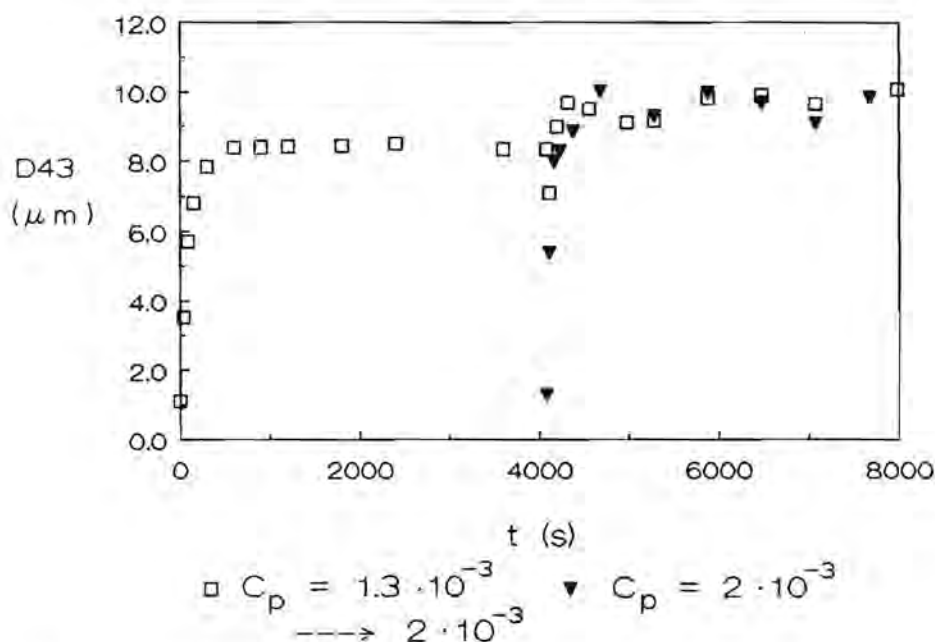
Figure 6.3. Effect of doubling solids concentration after steady state has been reached. Polystyrene particles produced by method of Eshuis et al.(1991) with $d_1 = 1.1$ μm. Experimental conditions: $T = 0.2$ m, $C_p = 1.7 \ 10^{-3}$ m³/m³ and $c_{NaCl} = 0.48$ M.

6.3. COAGULATION MODEL

Based upon the particle tracking results as presented in section 4.4, a simulation program was developed for describing the dynamic behaviour of the particulate system in the 20 cm vessel. The simulation program solves the population balances given by eq.(4-31):

$$\frac{dn_k}{dt} = 1/2 \sum_{i=1}^{k-1} J_{i,k-i}^* - \sum_{i=1}^{max} J_{ik}^* + \sum_{i=k}^{max} \beta_{ki} S_i^* - S_k^* \qquad (6-1)$$

where n_k = number concentration of aggregates consisting of k primary particles,

$$J_{i,k-i}^* = f_r(k) \ \alpha_{i,k-i} \ 2\pi \ (a_i + a_j)^3 \ \bar{s}_T \ n_i \ n_{k-i} \text{ and,}$$

$$S_k^* = f_b(k) \ n_k$$

The increasing porosity with aggregate size is taken into account with use of the fractal law, i.e. eq.(2-87):

$$a_k = (k / c)^{1/D} a_1 \tag{6-2}$$

For reasons of convenience the constant c was set equal to unity in the simulation program.

The initial collision efficiency α_{11} was estimated by its corresponding value in simple shear flow. See section 5.4.1. The collision efficiencies for the porous flocs are computed as explained in section 5.4.2.

The values for the reduction factor f_r and of the breakup frequency f_b are depicted as a function of critical energy dissipation rate ε_b in fig. 4.6. These values can be related to aggregate sizes with use of the breakup criterion given by eq.(2-96):

$$d_k = (\tau_{sb} / S_0)^{\frac{1}{n(D-3)}} = [(\rho \mu \varepsilon_b)^{1/2} / S_0]^{\frac{1}{n(D-3)}} \tag{6-3}$$

where $d_k = 2 a_k$ and S_0 is a fitting parameter.

In the coagulation process aggregates can be formed with sizes that are related by breakup criterion (6-3) to energy dissipation rate values ε_b equal or less than the minimum energy dissipation rate ε_{min} in the bulk flow of the tank. The breakup frequency f_b for these large aggregates is given by the frequency at which the shear stress in the bulk of the tank exceeds the critical yield stress. This breakup frequency follows from section 2.8 if we assume the turbulent flow in the bulk of the tank to be homogeneous and isotropic. For flocs smaller than the Kolmogorov micro scale the frequency for breakup in the bulk of the tank is given by:

$$f_b = (\frac{2}{\pi})^{1/2} \left(\frac{2\varepsilon_{min}}{15 \, v}\right)^{1/2} \left[\exp(-\varepsilon_b / 2\varepsilon_{min}) \right] \tag{6-7}$$

where ε_b = critical energy dissipation rate value at which the aggregates rupture defined by eq.(6-3)

The reduction factor f_r for these large aggregates is given by the ratio f_s of the strain rate $s(\varepsilon_{min})$ in the bulk zone to the residence time weighted strain rate, times the fraction of time f_t the shear stress in the bulk zone

is less than the critical yield shear stress τ_{sb}. This latter time fraction is given by eq.(2-107) which may be rewritten for aggregates smaller than the Kolmogorov micro scale as:

$$f_t = 2 \text{ erf}(\ (\varepsilon_b / \varepsilon_{min})^{1/2}) \qquad (6-8)$$

The strain rate ratio f_s is given by:

$$f_s = s(\varepsilon_{min}) / \bar{s}_T = (0.68)^{-1} (\varepsilon_{min} / \bar{\varepsilon})^{1/2} \qquad (6-9)$$

Combining eqs.(6-9) and (6-8) yields:

$$f_r = f_s f_t = 2.94 \ (\varepsilon_{min} / \bar{\varepsilon})^{1/2} \text{ erf}(\ (\varepsilon_b / \varepsilon_{min})^{1/2}) \qquad (6-10)$$

The coefficients β_{ki} represent the number of fragments of size a_k that result from breakup of aggregates larger than a_k. In order to evaluate the values of β_{ki} we have to know the size distribution of fragments formed upon breakup of aggregates of size a_i where $i > k$. The following sections are devoted to this topic.

With respect to the breakup process the flow in the viscous subrange of turbulence may be approximated by simple shear flow. This is plausible because it is the shear stress in the turbulent flow that causes aggregates smaller than the Kolmogorov micro scale to break up. Hence relevant information for the turbulent case may be obtained from studies of breakup in simple shear flow. With usage of this simple shear flow concept the sizes of the breakup fragments are predicted in the following sections. These predictions are then compared to experimental findings to test the validity of the assumption of simple shear flow.

Sonntag and Russel (1987) derived theoretically that for an isolated fractal floc subjected to simple shear flow the radial location of rupture $\overset{\bullet}{r}_{rupt}$ relative to the floc radius is nearly independent of floc size with a value of circa 0.8. For a Poisson's ratio $v_p \sim 1/4$ and $n(D - 3) < -1.5$, this rupture occurs mostly in the shear plane independent of applied shear stress. The floc is expected to break up in a way as depicted in fig. 6.4. Considering the heterogeneous structure of the parent floc it is not unlikely that only two breakup fragments are formed. The size of the smallest fragment is smaller than the part with which the parent floc size is reduced because of release of

interstitial water upon breakage. To compute the actual sizes of the breakup fragments, we assume that the small fragment and remaining parent floc both reattain a spherical form. Furthermore the self similarity of the fractal flocs is used: both the fragment and the remaining parent floc should obey the fractal scaling law , i.e, eq.(6-2). Hence the size of the fragment follows from the number of primary particles within the part that is separated from the parent floc. This number of primary particles i_{b1} is given by:

$$i_{b1} = \frac{3}{4\pi \, a_1^3} \int_{a_1}^{a_F} \int_0^{\vartheta_0} \int_0^{2\pi} \varphi(r) \, r^2 \sin\vartheta \; dr \, d\vartheta \, d\alpha \qquad (6\text{-}4)$$

where $r' = r_{rupt} \, \cos^{-1}\vartheta$

$$\varphi(r) = c \, D/3 \, (r \, / \, a_1)^{D-3} \text{ with } c \cong 1.$$

For the meaning of ϑ_0 see fig. 6.4.
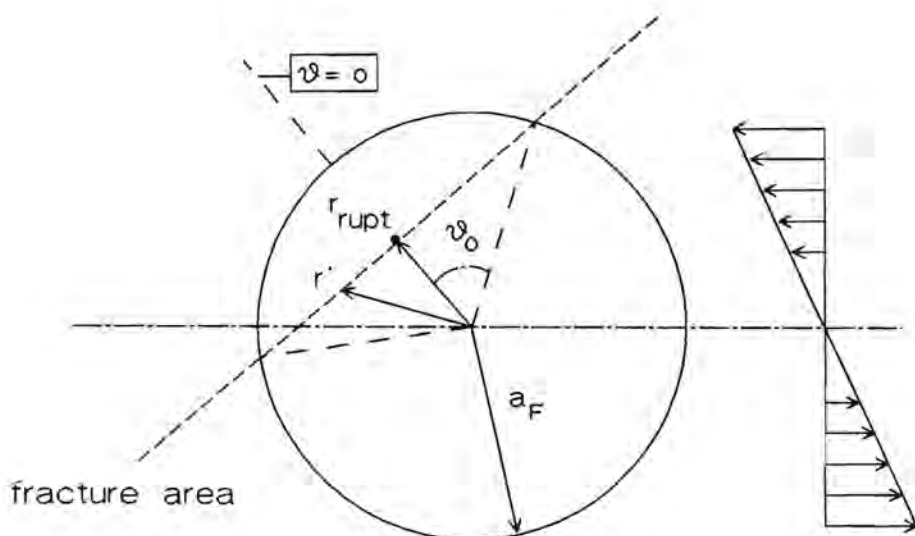
Figure 6.4. Breakup of parent floc in two uneven fragments. Location of rupture is indicated by black dot.

The radius of the breakup fragment a_{b1} is given by $(i_{b1} \, / \, c)^{1/D} \, a_1$. The radius of the remaining parent floc a_{b2} can be deduced from the conservation of

primary particles:

$$\varphi_F \frac{4\pi \, a_F^3}{3} = \varphi_{b1} \frac{4\pi \, a_{b1}^3}{3} + \varphi_{b2} \frac{4\pi \, a_{b2}^3}{3} \tag{6-5}$$

where φ_F, φ_{b1} and φ_{b2} denote the average volume fractions of solids within the parent floc and the smaller and larger breakup fragments respectively. Since φ_i is given by $C \, (a_i / a_1)^{D-3}$, eq.(6-5) may be rewritten as:

$$a_{b2} = (\, a_F^D - a_{b1}^D \,)^{1/D} \tag{6-6}$$

For $D = 2.5$ and $r_{rupt}^* = 0.8$, the radius of the breakup fragment amounts to $0.225 \, a_F$ whereas the remaining parent floc attains a radius of $0.99 \, a_F$. The amount of water released upon breakage of the parent floc is equal to $(1- 0.99^3 - 0.225^3) \, 4\pi \, a_F^3 / 3$, that is 1.83% of the volume of the parent floc.

De Boer (1987) showed that aggregates produce mainly fragments with sizes of about one-third of their diameter. Similar fragment sizes were observed in our studies of the breakup process. This is clearly demonstrated by fig. 6.5 where the evolution of the aggregate size distribution is shown for a particular breakup experiment. The particle size distribution (PSD) that corresponds to time $t = 0$ is the steady state PSD prior to addition of the steric agent poly vinyl alcohol to the suspension. The poly vinyl alcohol precludes any reaggregation of formed fragments and allows in this way for the breakup process to be studied. The PSD at $t = 360$ s is measured immediately after addition of the poly vinyl alcohol solution. The PSD is measured at $t = 6480$ s at the end of the breakup experiment. No further breakup is observed. Fig. 6.5 shows that the breakup process produces a bimodal PSD. Apparently the large flocs of about 20 µm produce fragments of circa 5 µm in size. So we may conclude that fragments of about one fourth of the size of the parent flocs are formed.

The sizes of the breakup fragments observed experimentally are only slightly larger than predicted theoretically from the simple shear flow model. A breakup event is therefore assumed to proceed generally as discussed above. The calculated sizes of the two fragments that are formed upon breakup of the parent floc are fixed by choice of the relative position of rupture r_{rupt}^* which could be varied in the simulation program. Simulation results showed that the steady state volume average aggregate size (VMD) was not much affected by the choice of r_{rupt}^* provided it was less than 0.9. The parameter r_{rupt}^* however had a pronounced effect on the spread of the PSD and
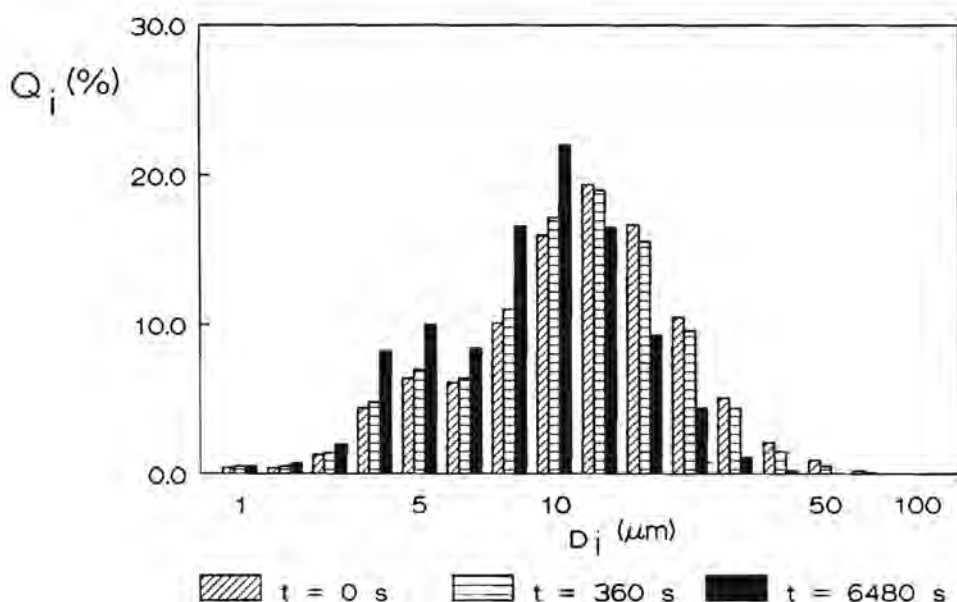
Figure 6.5. Evolution of aggregate size distribution after addition of poly
vinyl alcohol to suspension. Polystyrene particles produced by
method of De Boer (1987) with $d_1 = 0.56$ μm. Experimental
conditions: $T = 0.2$ m, $C_p = 3 \cdot 10^{-5}$ m^3/m^3, $N = 6$ s^{-1} and
$c_{NaCl} = 0.48$ μm.

consequently on the Sauter mean diameter (SMD) of the aggregates. By adjusting
$r^{\bullet}_{rupt}$ the computed PSD could be made to approach the steady state aggregate
size distribution as observed experimentally.

Since the aggregates are assumed to split into two uneven parts, the two
breakup distribution coefficients β_{ki} that correspond to these fragment sizes
are set to unity whereas the other coefficients are set to zero.

6.4. DISCRETIZATION OF COAGULATION MODEL

If the computations are for instance to be extended to aggregates of 20 μm, circa 1800 population balances have to be solved simultaneously, if $D = 2.5$ and the primary particle size is 1 μm. This results in a computational load far greater than is desirable.

To ease and speed up the numerical computation, the entire aggregate size domain is divided into size intervals and discretized rate equations for each size interval are derived. The number of equations that have to be solved simultaneously is then limited to the number of size intervals. Gelbard et al. (1980) presented a rigorous method of discretizing the population balance equations. We used a simpler but approximate method (Batterham et al. 1981) to generate discrete equations to replace the continuous population balances. Discretized rate equations were obtained for sizes in geometric progression such that the characteristic solids volume v^S doubles after each size interval, that is $v_i^S / v_{i-1}^S = 2$. The counter k in the continuous population balance, eq.(6-1), is replaced by 2^j in the discrete size distribution. The counter represents the number of primary particles within the representative floc of the size interval. The characteristic floc diameter $D(2^j)$ of size class 2^j is given by:

$$D(2^j) = [\ 2^{j/D}\ ]\ 2\ a_1 \qquad (6\text{-}8)$$

Size class 2^j has a lower boundary at $V_B^S(2^{j-1}) = 1/2\ [\ v^S(2^{j-1}) + v^S(2^j)\ ] = 3 \cdot v^S(2^j)/4$ and a upper boundary at $V_B^S(2^j) = 1/2\ [\ v^S(2^j) + v^S(2^{j+1})\ ] = 3 \cdot v^S(2^j)/2$. The diameters corresponding to these boundary solids volumes are:

$$D_B(2^{j-1}) = (\ \tfrac{3}{4} 2^j\ )^{1/D}\ 2\ a_1 \qquad (6\text{-}9)$$

$$D_B(2^j) = (\ \tfrac{3}{2} 2^j\ )^{1/D}\ 2\ a_1 \qquad (6\text{-}10)$$

Some aggregation events produce particles at solids volumes which are not permissible in the geometric series of 2. For example, particle of solids volume $1v_1$ and $4v_1$ form a single particle of solids volume $5v_1$. This is handled by adding these "in between" sizes to the size interval that is nearest in the series, for example a $5v_1$ particle is added to the $4v_1$ size class. To conserve the primary particles within the flocs, the number of particles formed or removed is changed accordingly. For example, an aggregation event between one $4v_1$ and one $1v_1$ particle produces 5/4 of an $4v_1$

particle.

It is convenient to distribute the boundary size evenly between adjoining classes in the series. For example one $3v_1$ particle is for one half added to the $2v_1$ size class and for the other half to the $4v_1$ size class. This results in an increase of the number of particles within the size classes by 1/2 $(3v_1/2v_1)$ and 1/2 $(3v_1/4v_1)$ respectively.

The population balance equation for aggregates in the size interval with characteristic solids volume $v_j^S = 2^j\, v_1$ where v_1 denotes the volume of the primary particles is given by:

$$\frac{d\,N(2^j)}{dt} = \underbrace{\frac{3}{8}\,J^*(2^{j-2},\ 2^{j-1})}_{\text{I}} + \underbrace{\frac{3}{4}J^*(2^{j-1},\ 2^j\ )}_{\text{II}} + \underbrace{J^*(2^{j-1},\ 2^{j-1})}_{\text{III}}$$

$$+\underbrace{\sum_{m=0}^{j-2}\left[\frac{2^j+2^m}{2^j}\right]\,J^*(2^j,2^m)}_{\text{IV}} - \underbrace{\sum_{m=0}^{max-1}J^*(2^j,2^m)}_{\text{V}} - \underbrace{J^*(2^j,2^j)}_{\text{VI}}$$

$$-\underbrace{S^*(2^j)}_{\text{VII}} + \underbrace{\sum_{i=j}^{max}\ \sum_{m=0}^{j-2}\left[\frac{2^j+2^m}{2^j}\right]\,\beta(2^j+2^m,2^i)\,S^*(2^i)}_{\text{VIII}}$$

$$+\underbrace{\sum_{i=j}^{max}\beta(2^j,\ 2^i)\,S^*(2^i)}_{\text{IX}} + \underbrace{\sum_{i=j}^{max}\frac{3}{8}\,\beta(\tfrac{3}{4}\cdot 2^j,\ 2^i)\,S^*(2^i)}_{\text{X}}$$

$$+\underbrace{\sum_{i=j}^{max}\frac{3}{4}\,\beta(\tfrac{3}{2}\cdot 2^j,\ 2^i)\,S^*(2^i)}_{\text{XI}} \qquad\qquad (6\text{-}7)$$

where $N(2^j)$ = the number concentration of particles with solids volume $v^S(2^j) = 2^j\,v_1$

$J^*(2^i,2^m) = f_r(2^j)\ \alpha(2^i,2^m)\ [\,D(2^i)+D(2^m)\,]^3\ N(2^i)\ N(2^m)\,\pi\,\bar{s}_T\,/4$ where solids volume $(2^i+2^m)\cdot v_1$ is within size class 2^j, and $D(2^i)$ and $D(2^m)$ represent the diameters of size class 2^i and 2^m respectively.

$S^*(2^j)$ $= f_b(2^j)\ N(2^j)$

$\beta(2^m,2^i)$ = number of fragments of size 2^m produced upon breakup of aggregate of size 2^i.

Equation (6-7) is based on the conservation of primary particles. The equation describes the rate of change of the number of aggregates of size class 2^j. Terms I and II of eq.(6-7) are for aggregation events producing boundary-sized particles. Term III in the equation is for aggregation events in the previous size class producing particles of the characteristic floc size 2^j. The fourth term is for events which produce aggregates within the same size class by aggregation with a small particle below the 2^{j-2} size class. The fifth and sixth terms are for growth out of the size interval by aggregation with any other particle. The seventh term represents the breakup out of the interval. The eighth and ninth terms are for production of breakup fragments falling within size class 2^j and the last two terms are for breakup events that produce boundary sized particles.

The maximum number of size classes required is obtained from eq.(6-3) by substituting the value of the shear stress in the bulk zone of the stirred tank. The resulting aggregate size corresponds to a certain size class that is near the maximum aggregate size feasible in the system. If this size class is represented by 2^i, computations were performed taking size classes into account up to 2^{i+10}. Normally the number of size classes used did not exceed 40. This covers a size range of 10^4 and is more than satisfactory for the present application.

The discretized population balances were solved by using the Fortran NAG library routine D02EBF which is based on Gear's method (Gear 1967). A check for solids volume balance was made at every output. The error was always less than 0.1%.

Note that in the eq.(6-7) collisions between equally sized particles are doubly counted. Except for the disappearance of primary particles the double counting was not corrected for, because solving the uncorrected discretized population balances gave results most resembling to those obtained by solving the continuous population balances.

To compare the computed size distribution with the size distributions measured with the laser diffraction instrument, the number concentration $N(2^j)$ had to be converted into a volume concentration $Q(2^j)$ of size class 2^j. The volume concentration $Q(2^j)$ comprises both the primary particle volumes and interstitial water within the flocs of size class 2^j. In the following section

a relation is derived that links the number concentration $N(2^j)$ directly to $Q(2^j)$.

The solids volume concentration within size class 2^j is given by:

$$Q^S(2^j) = N(2^j) \, 2^j \, v_1 \tag{6-11}$$

This solids volume concentration is assumed to be evenly distributed over the various floc sizes (of m primary particles) within size class 2^j:

$$q^S(m) = Q^S(2^j) / l(2^j) \tag{6-12}$$

where $l(2^j)$ represents the number of floc sizes that are feasible within size class 2^j when originating from the geometrical series of 2 (See table 6.1).

Table 6.1. Floc sizes within size class 2^j. The floc sizes arise from collisions between the characteristic sizes of the various size classes 2^j. The boundary sizes of each size class only belong for one half to the size class.

j	2^j	floc sizes in size class 2^j no. of primary particles in flocs (k)	no. of floc sizes in size class 2^j ($l(2^j)$)
0	1	1	1
1	2	2, 3	1.5
2	4	3, 4, 5, 6	3
3	8	6, 8, 9 ,10, 12	4
4	16	12, 16, 17, 18, 20, 24	5
5	32	24, 32, 33, 34, 36, 40, 48	6
j>2	2^j	$3 \cdot 2^{j-2}$, $3 \cdot 2^{j-1}$ (Boundary sizes), 2^j, $(2^j + 2^m$, where $0 \leq m \leq 2^{j-2})$	j + 1

The number concentration of flocs consisting of k primary particles is given by:

$$n(k) = \delta_B \, q^S(k) / v^S(k) \tag{6-13}$$

where $3 \cdot 2^{j-2} \leq k \leq 3 \cdot 2^{j-1}$ and $\delta_B = 1/2$ if $k = 3 \cdot 2^{j-2}$ or $k = 3 \cdot 2^{j-1}$, $\delta_B = 1$

otherwise. The volume concentration $Q(2^j)$ within size class 2^j results from:

$$Q(2^j) = \Sigma \, n(k) \, v(k) \tag{6-14}$$

where $v(k)$ = volume of floc consisting of k primary particles = $k^{3/D} \, v_1$

Combining (6-13), (6-12) and (6-11) yields:

$$Q(2^j) = N(2^j) \, \frac{2^j \, v_1}{1(2^j)} \sum_{3 \cdot 2^{j-2}}^{3 \cdot 2^{j-1}} \delta_B \, k^{\left(\frac{3-D}{D}\right)} \tag{6-15}$$

where
$$\sum_{3 \cdot 2^{j-2}}^{3 \cdot 2^{j-1}} \delta_B \, k^{\left(\frac{3-D}{D}\right)} = \frac{1}{2} \, (3 \cdot 2^{j-1})^{\left(\frac{3-D}{D}\right)} + \frac{1}{2} \, (3 \cdot 2^{j-2})^{\left(\frac{3-D}{D}\right)}$$
$$+ \sum_{m=0}^{j-2} (2^j + 2^m)^{\left(\frac{3-D}{D}\right)}$$

From eq.(6-15) the volume concentration of aggregates within size class 2^j can be calculated directly from the number concentration $N(2^j)$. These volume concentrations are used to construct similar volume size distributions as are computed with the laser diffraction apparatus. From these volume size distributions the volume mean diameter (VMD) and Sauter mean diameter (SMD) are evaluated through eqs.(5-4) and (5-5).

6.5. MAXIMUM AGGREGATE SIZE AS A FUNCTION OF PROCESS CONDITIONS

In the following sections, the variation of the steady state VMD with impeller speed, solids concentration and concentration of destabilizer are discussed. The experimentally found values for the final aggregate sizes are compared to those obtained from our simulations.

Due to weighting of the larger sizes, the volume mean diameter VMD at steady state indicates, to a good approximation, the maximum floc size in the suspension.

6.5.1. VARIATION OF IMPELLER SPEED

If the impeller speed is increased by a factor of c, then the energy dissipation rate is enhanced by a factor of c^3, and the corresponding strain rates and shear stresses by a factor of $c^{1.5}$.

Fig. 6.6 shows the variation of the steady state VMD with impeller speed as determined in the 10 cm vessel for a particular polystyrene latex. At increasing impeller speed the shear stresses that act upon the aggregates gain in strength. Aggregate disruption is favoured over growth and the maximum aggregate size is shifted towards smaller values.

The simulation results are also shown in fig. 6.6. Although the simulation program was initially developed for the description of the aggregate size evolution in the 20 cm vessel, it could also be applied to the 10 and 39 cm vessels provided the breakup frequency was corrected for the change in vessel size. The best fit with the experimental data was obtained with the constant n from eq.(6-3) equal to approximately 3 and cluster strength S_0 equal to 47.2 N/m^2.

For low solids concentrations the value for the constant n follows directly from plots of the logarithm of the experimental determined values of the VMD versus the logarithm of the impeller speed if we assume that the breakup criterion is directly applicable to the steady state VMD. The slope of the straight line through the data points is then given by $3/(2n(D-3))$ and provides an estimate for the constant n if D is known.
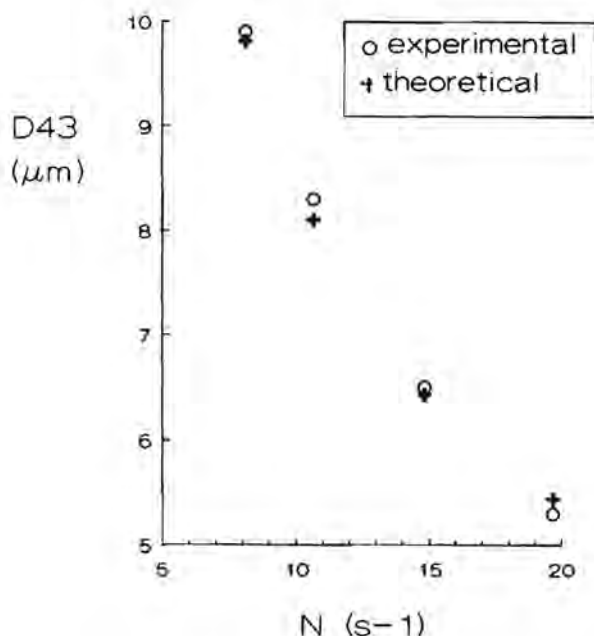
Figure 6.6. Steady state aggregate mean size D43 versus impeller speed N. Polystyrene particles prepared by method of Eshuis et al. (1991) with d_1 = 1.1 μm. Experimental conditions: T = 0.1 m, C_p = 1.7·10^{-3} m^3/m^3 and c_{NaCl} = 0.48 M. Fractal dimensionality D = 2.3 ± 0.05.

In fig. 6.7 the experiments with three different latices are depicted. In the figure the corresponding fractal dimensionalities, which were determined with the laser diffraction apparatus, are indicated. The line corresponding to a fractal dimensionality of 2.6 has clearly a larger slope than the one, with D being equal to 2.3. For the constant n, a value of circa 3 was found independent of polystyrene latex. This value differs only slightly from the value (2.5) found by Sonntag and Russel for polystyrene networks produced by Brownian motion. A possible explanation for the fractal dimensionality being slightly different for the various polystyrene latices used in the coagulation experiments, is discussed in section 6.7.

Figure shows D43 (μm) versus N (s−1) with lines labeled D = 2.5, D = 2.6, D = 2.3, and box: $D43 \sim N^{\frac{3}{2n(D-3)}}$, $n \approx 3$.
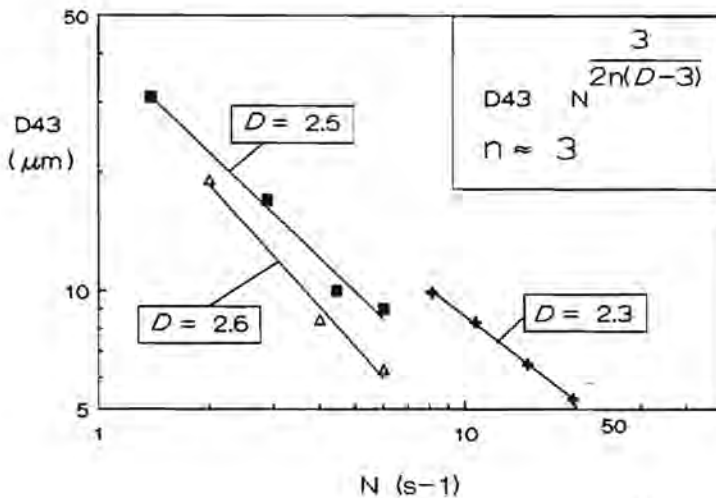
△ Polystyrene particles with $d_1 = 0.56$ μm prepared by method of De Boer. $T = 0.2$ m, $C_p = 8 \cdot 10^{-6}$ m^3/m^3 and $c_{NaCl} = 0.48$ M.

■ Polystyrene particles with $d_1 = 0.88$ μm prepared by method of De Boer. $T = 0.2$ m, $C_p = 7.2 \cdot 10^{-5}$ m^3/m^3 and $c_{NaCl} = 0.48$ M.

+ Polystyrene particles with $d_1 = 1.1$ μm prepared by method of Eshuis et al. (1991). $T = 0.1$ m, $C_p = 1.7 \cdot 10^{-3}$ m^3/m^3 and $c_{NaCl} = 0.48$ M.

Figure 6.7. Steady state aggregate mean size D43 versus impeller speed N for three different latices:

6.5.2. VARIATION OF SOLIDS CONCENTRATION

The concentration of latex was varied at a constant rotational impeller speed of 5 s^{-1} and a constant NaCl concentration of 0.5 M.

In fig. 6.8 the maximum aggregate size is plotted versus the latex volume concentration. As the maximum aggregate size is determined by the dynamic equilibrium of growth and breakup, the maximum aggregate size increases with solids concentration since the coagulation rate is enhanced with respect to the breakup rate. If circulation is strong and coagulation is slow (low solids

concentrations), the aggregates will not be able to grow beyond the maximum size corresponding to the energy dissipation rate in the region of the stirrer and in the impeller discharge stream. On the other hand, if at high latex concentrations coagulation is fast with respect to the circulation, it may be expected that aggregate sizes will be formed which are even disrupted by the low bulk shear stresses.
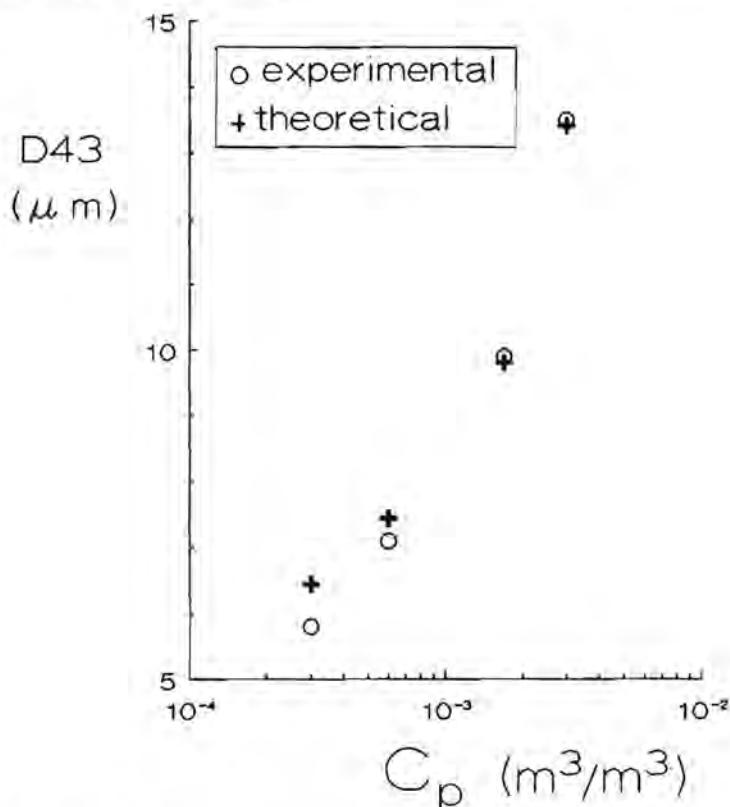
Figure 6.8. Steady state aggregate size D43 versus solids concentration C_p. Polystyrene particles with d_1 = 1.1 μm prepared by method of Eshuis et al. (1991). Experimental conditions: T = 0.1 m, N = 8.1 s^{-1} and c_{NaCl}= 0.48 M.

In fig. 6.8 also the results of the simulation are plotted. In the simulation the values for the constant n and cluster strength S_0 were used that followed from the previous section. Since in the experiments presented in the previous section the same latex was used as in the present experiments the

application of these values for n and S_0 seems to be validated. Our theoretical model correlates the experimental data very well. So we may conclude that the coagulation model is able to predict the variation of the VMD with solids concentration quantitatively.

We were not able to test the performance of the model for higher solids concentrations, since the experiments could not be extended reliably beyond $C_p \cong 5 \cdot 10^{-3}$. At these high solids concentrations, coagulation during sampling becomes significant. Furthermore at these large solids concentrations aggregate sizes are formed which already break up at the relatively small shear stresses that are experienced in the bulk of the tank. These shear stresses are of the same order of magnitude as the shear stresses exerted upon the aggregates during sampling and dilution of the sample. So additional breakup in the sampling and dilution process may occur.

In order to measure the maximum aggregate size accurately sampling and dilution should be avoided. The application of laser scanners like the LAB-TEC 1000 or PAR-TEC 100 of LASENTEC, that should be able to measure particle sizes in-line in undiluted suspensions up to volume concentrations of around 30% is recommended. The application of these techniques for monitoring the coagulation process is however beyond the scope of this thesis.

6.5.3. VARIATION OF DESTABILIZER CONCENTRATION

The variation of floc size with electrolyte concentration can be rationalized by accounting for interparticle forces within the floc. The strength of the cluster matrix S_0 is directly proportional to the binding force between the individual particles the aggregates consist of. If we assume that the potential energy of repulsion between the primary particles is given by eq.(2-4), the binding force F between the primary particles is expressed as:

$$F = \frac{A_{1(2)} \, a_1}{12 \, H_1^2} - \frac{64\pi \, n \, k_B T}{\kappa} \gamma^2 \exp(-\kappa_1 H)$$ (6-15)

(see sections 2.3 and 2.6.1)

where n = number concentration of sodium ions

H_1 = critical separation distance between surfaces of primary particles

γ = tanh($ze\psi_\delta / 4k_B T$)

Eq.(2-4) was chosen for the description of the potential energy of repulsion, because it gives values intermediate between those calculated by eq.(2-3) and (2-5) corresponding to the assumption of interaction at constant potential and at constant charge respectively. These latter expressions are applicable to low values of the Stern plane potential ψ_δ. Substitution of eq.(2-2) for the reciprocal κ of the Debye length and $n = N_{av}\, c_{NaCl}$, where c_{NaCl} denotes the NaCl concentration in mol l^{-1} and the Avogadro constant $N_{av} = 6 \cdot 10^{26}$ kmol^{-1}, in eq.(6-15) yields with the valency z equal to unity:

$$F = \frac{A_{i(2)}\, a_1}{12\, H_1^2}$$

$$- \frac{32\pi\, (2\varepsilon_r \varepsilon_0\, N_{av}\, c_{NaCl})^{1/2} (k_B T)^{3/2}}{e} \gamma^2 \exp\left[-\left(\frac{2e^2\, N_{av}\, c_{NaCl}}{\varepsilon_r \varepsilon_0\, k_B T} \right)^{1/2} H_1 \right]$$

$$(6-16)$$

The second term on the right hand side varies with the salt concentration according to $c_{NaCl}^{1/2} \exp(-c_{NaCl}^{1/2})$. This is a decreasing function with c_{NaCl}. The electrostatic repulsion is reduced with increase of the electrolyte concentration maximizing the attractive force between the primary particles within the floc up to the Van der Waals attraction.

To calculate the magnitude of the residual electrostatic repulsion at salt concentrations above the critical coagulation concentration, an estimate for the potential ψ_δ at the Stern plane is required. This potential ψ_δ may be approximated by the electrokinetic or zeta potential ζ, i.e., the potential at the slipping plane which can be determined by electrophoresis. The slipping plane is defined as the surface at which the relative motion sets in between moving particle plus adsorbed liquid layer and solution in the applied electric field. This surface of shear is well within the double layer, at a location roughly equivalent to the Stern plane.

Electrophoretic measurements were performed with a Malvern Zetasizer up to salt concentrations which were used in the coagulation experiments. Fig. 6.9 shows the results of these measurements for the polystyrene latex used in the coagulation experiments where the salt concentration was varied. The stable suspension at $c_{NaCl} = 10^{-3}$ mol l^{-1} displays a zeta potential of circa 100 mV. With increasing NaCl-concentration the zeta potential decreases down to circa 15 mV at 0.5 mol l^{-1}. Beyond $c_{NaCl} > 0.5$ mol l^{-1} no valid measurements could

be made because of coagulation in the measurement cell. The zeta potential at 0.5 mol l^{-1} is a low enough value to validate the use of eq.(2-4) for description of the potential energy of repulsion between the primary particles within the floc.
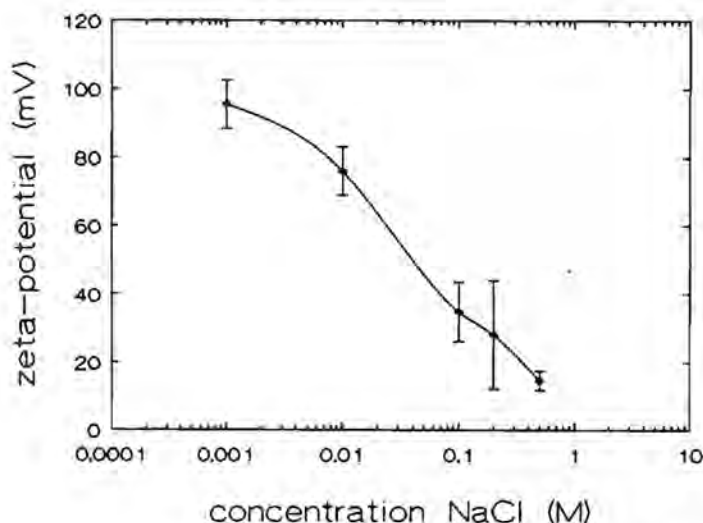
Figure 6.9. Zeta potential of polystyrene particles versus NaCl concentration. Polystyrene particles prepared by method of Eshuis et al. (1991) with $d_1 = 1.1$ µm.

In the coagulation model it is assumed that both the separation distance H_1 and the Stern plane potential ψ_δ stay constant with further increase of the salt concentration beyond $c_{NaCl} = 0.5$ mol l^{-1}. The separation distance H_1 is mainly determined by the short range structural repulsive forces which are expected to be insensitive to the sodium chloride concentration. The independency of the Stern potential on electrolyte concentration for $c_{NaCl} \geq 0.5$ mol l^{-1} could not be experimentally verified for this particular latex, since no valid measurements beyond $c_{NaCl} = 0.5$ mol l^{-1} were possible. Zeta potential measurements with other latices however showed that the zeta potential measured at 1 mol l^{-1} did not differ much from the value obtained at 0.5 mol l^{-1} indicating that the assumption of a constant $\zeta \cong \psi_\delta$ for $c_{NaCl} \geq 0.5$ mol l^{-1} is at least a good first approximation.

The cluster strength S_0 is given by:

$$S_0 = C \, F \, / \, a_1^2 \qquad\qquad\qquad\qquad (6\text{-}17)$$

(See section 2.6.2)

Substitution of eq.(6-16) for the binding force between the primary particles F yields the cluster strength S_0 as a function of electrolyte concentration.

Fig. 6.10 shows the comparison between the VMD-values obtained experimentally and from the simulation with $\psi_\delta = 15$ mV. In the simulation the separation distance H_1 was set equal to 0.7 nm and the constant C from eq.(6-17) amounted to 0.0627 giving a value for S_0 equal to the one obtained from the experiments presented in section 6.5.1 for $c_{NaCl} = 0.5$ M. The agreement between the experimental data and the simulation results is quite satisfactory, considering the assumptions that have been made.
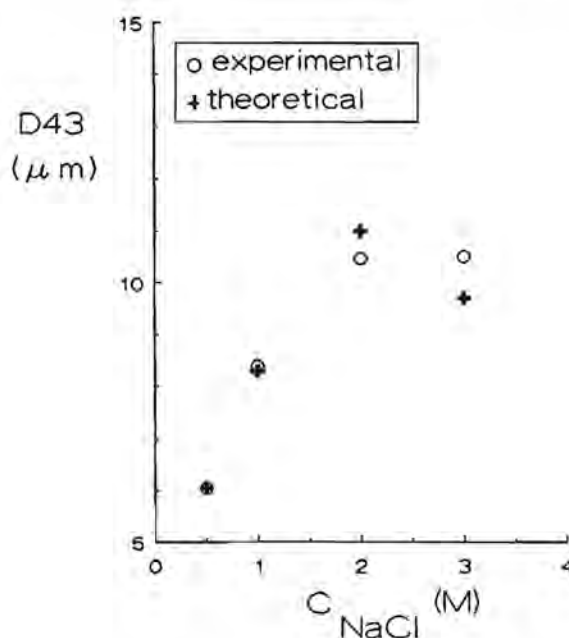
Figure 6.10. Steady state aggregate mean size D43 versus destabilizer concentration. Polystyrene particles with $d_1 = 1.1$ µm prepared by method of Eshuis et al. (1991). Experimental conditions: T = 0.2 m, $C_p = 1.7 \cdot 10^3$ m^3/m^3 and N = 5 s^{-1}.

The decrease of the VMD with the increase of salt concentration from 2 to 3 M is not inconsistent with the present theory. It results from an increase of the turbulent shear stresses that act upon the aggregates due to an increase in dynamic viscosity and density of the suspending medium:

$$\tau_s = \mu \ (2 \ \varepsilon/15 \ v)^{1/2} = (\rho\mu)^{1/2} \ (2 \ \varepsilon/15)^{1/2} \qquad (6\text{-}18)$$

Apparently the increase in shear stress is larger than the increase in the cluster strength S_0 for the change of NaCl concentration from 2 to 3 mol l^{-1}. The increase of dynamic viscosity and density of the suspending medium with salt concentration was also taken into account in the simulation program.

6.6. VARIATION OF VESSEL SIZE

According to De Boer (1987), the course of the batch coagulation process is hardly affected by the scale of operation at equal values of the average rate of energy dissipation. De Boer based his conclusions on results of coagulation experiments conducted at a solids concentration $\Phi = 7.66 \cdot 10^{-6}$ in vessels with internal diameters of 10, 19 and 44 cm and of equal geometry as used in our research. In the present study the coagulation experiments have been extended to somewhat higher solids concentrations to test this hypothesis.

Fig. 6.11 shows the results of coagulation experiments conducted in the 10 and 20 cm vessel at 3 different solids concentrations and 3 different impeller speeds. The impeller speed for the 10 cm vessel was set equal to $(2)^{2/3}$ times the impeller speed in the 20 cm vessel. This procedure corresponds to scale up with a constant mean energy dissipation rate assuming that the power number N_p remains constant with increase of impeller diameter.

The steady state aggregate size in the 20 cm vessel seems to be slightly larger than the one obtained in the 10 cm vessel for all three concentrations. The values of the aggregate sizes in the vessels of different sizes would certainly have been statistically different if the actual power numbers were taken into account with scale up. The power number of the 3.35 cm impeller in the 10 cm vessel is smaller than the power number of the 6.7 cm impeller used in the 20 cm vessel, as was shown in section 3.5. To ensure an energy dissipation rate in the 10 cm vessel equal to the one in the 20 cm vessel, the impeller speed in the 10 cm vessel should be increased additionally with the
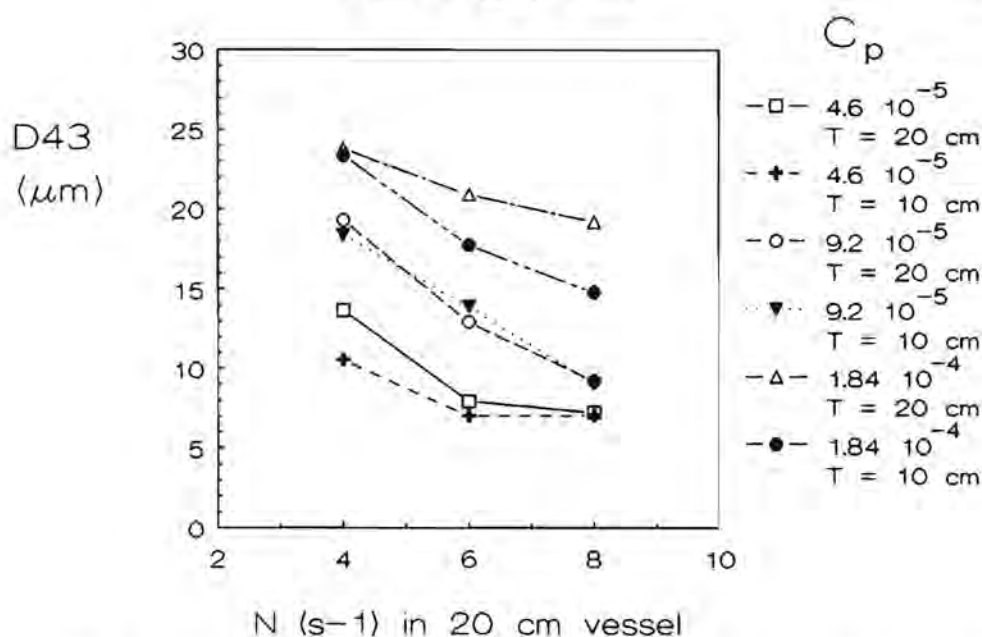
Figure 6.11. Steady state aggregate mean size D43 versus impeller speed for three different solids concentrations and two different vessel sizes. Polystyrene particles prepared by method of De Boer (1987) with $d_i = 0.3$ μm. $c_{NaCl} = 1$ M.

cube root of the ratio of both power numbers. Such an increase in impeller speed will lead to a decrease of the aggregate steady state size in the 10 cm vessel with respect to the one observed in the 20 cm vessel.

Table 6.1 presents values for the steady state aggregate sizes of coagulation experiments conducted with a different polystyrene latex at two solids concentrations in the vessels with internal diameters of 10, 20 and 39 cm. Again the impeller speeds were adjusted with the assumption of a constant power number with scale up. The 10 and 20 cm vessel yield similar values for the steady state aggregate sizes, as expected from the previous experimental results. The steady state VMD at $C_p = 3 \cdot 10^{-4}$ for the 39 cm vessel is also not significantly different from the sizes obtained in the other two sizes, but the VMD at $C_p = 6 \cdot 10^{-4}$ is definitely larger. Since the power numbers of the impellers in the 20 and 39 cm vessels were equal, this is consistent with the previous predicted tendency of the aggregate sizes to increase somewhat with scale up.

Table 6.1. Steady state volume mean diameter D43 with scale-up
        Polystyrene latex produced by method proposed by
        Eshuis et al.(1991). Primary particle size d_1 = 1.0 μm.
        Experimental condition: c_{NaCl} = 0.5 M

D43 in μm.

C_p	T (cm)		
	10	20	39
$3 \cdot 10^{-4}$	7.6 ± 1.0	7.4 ± 1.0	9.4 ± 1.0
$6 \cdot 10^{-4}$	10.0 ± 1.0	9.4 ± 1.0	18.0 ± 2.0

An increase of aggregate size with vessel size is in accord with decreasing breakup frequencies due to an increase of the circulation time with vessel size as experimentally verified by De Boer (1987). The breakup frequency proved to be proportional with the reciprocal of the circulation time. If the power input per unit mass is kept constant with scale up, the breakup frequencies will decrease with the tank size T proportionally to $T^{-2/3}$.

The small increase of steady state aggregate size observed with scale up at the lower solids concentrations could be adequately described by adopting this proportionality of the breakup frequencies with $T^{-2/3}$. Since this change of breakup frequency with scale up results only in minor aggregate size changes, we may conclude that the use of the power input per unit mass as scaling parameter will yield reasonable results up to a solids concentration of $3 \cdot 10^{-3}$.

At larger values of the solids concentration the aggregate size is expected to decrease somewhat with scale up. For large solids concentrations the coagulation rate becomes fast with respect to the circulation times in the stirred tank, and the maximum aggregate size is determined solely by the coagulation and breakup in the bulk of the tank. Since the local energy dissipation rate in this part of the tank was found to increase with vessel size, the aggregate sizes in the bulk of the tank are expected to decrease with scale up. At present this hypothesis could not be tested since the experiments could not be extended to these high solids concentrations for reasons outlined in section 6.5.2.

6.7. DISCUSSION ON FRACTAL DIMENSIONALITY

As mentioned earlier, the fractal dimensionality proved to be slightly different for the various polystyrene latices used in the coagulation experiments. These differences are to be attributed to a variation in the surface chemistry of the primary particles produced by a batch polymerization. This results in variable short range structural repulsive forces between the primary particles. The structural repulsive forces modify the attractive force at small distances of approach (see section 2.6.1). In this way the structural repulsive forces may affect the geometrical configuration of triplets (and quartets) since the final steps in the relative trajectories of primary particles (doublets) with respect to (other) doublets are largely dependent on the attractive force at small distances of approach. The primary doublet acts as an impermeable floc, as shown in section 5.4.3. The open trajectories run through the larger multiplets, so collisions with these multiplets become almost independent of the attractive forces between the particles. Since the triplets and quartets may be considered as the primary growth units of the multilevel structure of the larger multiplets, the configuration of the triplets and quartets - whether compact or more chain-like - may be decisive for the final structure and fractal dimensionality of the larger aggregates. This dependency of fractal dimensionality on the configuration of the primary growth unit is discussed below.

Each level in the multilevel structure of a floc may as a first approximation be considered to result from the combination of two equally sized aggregates. Then the size corresponding to each new level is related to the size of the previous one as follows:

$$d^3(2^j n_{gu}) = 2 d^3(2^{j-1} n_{gu}) / \alpha = 2^j d^3(n_{gu}) / \alpha^j \qquad (6-19)$$

where $d(i)$ denotes the aggregate size consisting of i primary particles, n_{gu} represents the number of primary particles in the primary growth unit and is the volume fraction incorporated in each new level of the floc structure.

At the same time the fractal law (2-86) is valid which may be rewritten as:

$$d^3(2^j n_{gu}) = 2^{3j/D} d^3(n_{gu}) \qquad (6-20)$$

Comparing eq.(6-20) to eq.(6-19) yields:

$$D = 3 \ln(2) / (\ln(2) - \ln(\alpha)) \qquad\qquad (6-21)$$

which relates the fractal dimensionality directly to the volume fraction α incorporated in the successive couples of equally sized but continually smaller aggregates in the multilevel structure of the floc. It is plausible that this volume fraction α is dependent on the "porosity" or configuration within the primary growth unit. This configuration changes with the variation of short range structural repulsive forces with the different polystyrene latices.

6.8. CONCLUSIONS

The steady state aggregate size distribution is shown to be independent of the initial conditions of the batch coagulation experiments.

The fractal dimensionality of the formed flocs proved also to be independent of the process conditions. The fractal dimensionality was however found to be slightly dependent on the polystyrene latex that was used for the coagulation experiments. The values for the fractal dimensionality ranged from 2.3 to 2.6.

With the particle tracking as presented in Chapter 4 based upon a detailed study of the hydrodynamics in the stirred vessel, the influence of the heterogeneous shear field was translated in size dependent coagulation and breakup rates. Based upon these coagulation and breakup rates a coagulation model was developed for predicting quantitatively the maximum aggregate size as a function of impeller speed, solids concentration and salt concentration in a batch coagulation experiment. Apart from coagulation and breakup rates, knowledge about the size of the breakup fragments was required to solve the population balances over the various aggregate sizes. Based upon theoretical considerations and experimental findings, the flocs were assumed to split up into two uneven fragments.

The coagulation model showed that the steady state volume mean aggregate size at low solids concentration varies with impeller speed as follows from the breakup criterion for the viscous subrange of turbulence wherein the relation between critical shear stress and impeller speed is substituted. A value of approximately 3 was found for the constant n in the exponent of the power law that describes the breakup criterion.

The coagulation model proved to predict quantitatively the increase of aggregate size with solids volume fraction up to $3 \cdot 10^{-3}$. The model may be valid for higher values of the solids concentration, but this could not be verified due to experimental limitations.

The increase of aggregate size with concentration of destabilizer could be successfully explained with the coagulation model if the DLVO-theory was incorporated.

The maximum aggregate size was found to increase somewhat with vessel size at equal values of the mean energy dissipation rate. This is in agreement with the decrease of the breakup frequency with scale up. It is expected that for higher solids concentrations this may be different.

CHAPTER VII
EPILOGUE

7.1. INTRODUCTION

The chapters 1 to V have been concerned with the different aspects of aggregation of small particles in agitated vessels. In chapter VI these different aspects were tied together to yield an overall description of the aggregation process in a batch coagulation experiment. In section 7.2 the different aspects incorporated in this coagulation model are summarized. In section 7.3 suggestions for future areas of research are presented.

7.2. CONCLUSIONS

It has been shown theoretically that collisions due to the inertia of the aggregates entrained by the smallest eddies in the turbulent flow, are negligible to those brought about by spatial velocity differences in the fluid. The coagulation model therefore only uses the orthokinetic expression for the collision frequency of particles smaller than the Kolmogorov micro scale.

The expression for the orthokinetic coagulation rate has to be corrected for hydrodynamic and interparticle interactions during encounters between aggregates. The value of the collision efficiency for the doublet formation of the primary particles follows from trajectory analysis in simple shear flow provided the simple shear rate is made to correspond to the residence time weighted turbulent strain rate. This residence strain rate is smaller than the strain rate that is obtained from the mean energy dissipation rate in the stirred tank and which is commonly used to compute the initial coagulation rate.

The collision efficiencies for encounters between the aggregates cannot be approximated by values corresponding to collisions between solid particles, because the aggregates are not closely packed but rather porous. This porosity within the aggregates results in penetration of the surface of the flocs by

the fluid flow, giving rise to enhanced collision efficiencies. Values for the collision efficiencies between porous flocs may be estimated by a model which pictures a porous floc as consisting of an impermeable core and a completely permeable shell. With this shell-core model the trajectory analysis for encounters between solid particles can be applied to the impermeable cores of the porous flocs. Application of the collision efficiencies computed from the shell-core model in the description of the aggregate growth yielded results in agreement with experimental findings.

The porosity within the aggregates was shown experimentally to increase with aggregate size. The laser diffraction instrument proved to be highly suited for these porosity measurements since it is capable of measuring both (average) aggregate size and volume concentration of the flocs at the same time. With the solids concentration of the sample the average porosity within the aggregates could be determined during the growth process. The variation of porosity or solids density with aggregate size could be described adequately by a fractal law, which assigns a fractal dimensionality to the flocs. The increase of porosity with aggregate size together with the enhanced collision efficiencies for porous flocs, give rise to an accelerated growth after the initial stages of coagulation in agreement with experimental findings.

Coagulation experiments showed an increase of the growth rate with solids concentration and with impeller speed in agreement with theoretical predictions. The growth rate increased slightly with increasing destabilizer concentration. This increase may be attributed to a further reduction of the remaining electrostatic repulsive forces between the primary particles with increasing salt concentration, resulting in enhanced collision efficiencies for the initial stages of coagulation.

When the aggregates grow larger, the flocs become weaker because of an increase of porosity with aggregate size. Finally the floc strength becomes too small to withstand the hydrodynamic shear stresses acting upon the flocs, resulting in floc rupture.

Laser Doppler velocimetry measurements performed in stirred vessels identical to those used for the coagulation experiments, showed that the turbulent shear field is far from uniform. The largest shear stresses are experienced near the impeller blade tip, the smallest in the bulk of the tank. Because of the heterogeneity of the shear field, aggregates that are formed in

the quiescent bulk of the tank can be disrupted in the vigorous jet stream coming from the impeller. With the occurrence of breakup in a certain part of the tank, coagulation of larger aggregates is restricted to the zones of low enough shear stress. Hence, the coagulation is reduced relative to the situation where coagulation would be possible throughout the whole vessel volume. The reduction factor with which the orthokinetic coagulation rate needs to be corrected in the presence of breakup, could be computed by the particle tracking simulation program. With the particle tracking also breakup frequencies for the various aggregate sizes were computed.

The particle tracking simulation performs the actual linking of the heterogeneous shear field to the aggregation process in the stirred tank. This is done by formulating size dependent reduction factors and breakup frequencies. The particle tracking requires detailed information about the hydrodynamics in the stirred tank which has been determined by laser Doppler velocimetry.

The coagulation model is based upon independence of both floc structure (fractal dimensionality) and of interparticle forces within the flocs on the applied process conditions. This independency has been verified experimentally. The floc structure was found to be slightly different for the various polystyrene latices used in the coagulation experiments. An explanation for this phenomenon may be that the initial turbulent collision mechanism is responsible for the fractal dimensionality of the flocs, and not shear induced restructuring. The fractal dimensionality of the flocs varied from 2.3 to 2.6.

The final aggregate size in the bulk of the stirred tank is the result of a dynamic equilibrium between growth in the zones of low shear stress and breakup of the aggregates in the zones of high shear stress. A coagulation model was developed for predicting this final aggregate size as a function of impeller speed, solids concentration and salt concentration in a batch coagulation experiment. This coagulation model was tested by comparing its predictions to aggregate sizes as found experimentally for the various process conditions. Good agreement was obtained between experimental and simulation results if the constant n in the breakup criterion was set equal to 3. The increase of aggregate size with solids volume fraction could quantitatively predicted up to $3 \cdot 10^{-3}$. The model may be valid for higher values of solids

concentration, but this could not be verified due to experimental limitations. The increase of aggregate size with concentration of destabilizer (above the critical coagulation concentration) could be rationalized by accounting for interparticle forces within the floc through the DLVO theory.

The final aggregate size was hardly affected by the scale of operation at equal values of power input per unit mass for solids concentrations up to 3 10^{-3}. A small increase with scale up results from a decrease in breakup frequency and probably also from an increase of coagulation rate in the bulk of the tank with increasing vessel size. The increase of coagulation rate is expected since laser Doppler measurements showed that the local energy dissipation rate in the bulk of the tank increases somewhat with vessel size. The laser Doppler measurements also showed that the energy dissipation rate at the impeller blade tip decreases with scale-up. These changes in the energy dissipation rate distribution with vessel size are however presumably too small to affect the coagulation process significantly.

7.3. FUTURE AREAS OF RESEARCH

Additional experimental work could be useful in supporting the coagulation model developed in this thesis, even though reasonable experimental support has been included. It is recommended that experiments are set up to test the application of the model to higher solids concentrations which are of practical importance. It would be interesting to investigate the upper limit of the binary collision assumption. Usually this assumption is assumed to hold up to a volume solids concentration of 10% (Brakalov 1987). Experiments beyond this volume concentration may yield different results because three body encounters are no longer negligible but also for other reasons. Local gel formation and turbulence damping (Delichatsios and Probstein 1976) are for example events which need to be considered as possible causes of disagreement between simulation and experimental results.

Special attention should be devoted to the mechanism that controls the floc structure. If the underlying principle which determines the fractal dimensionality of the flocs has been recognized, it may be possible to predict both floc size and floc structure.

It would be intriguing to see whether changes in the surface chemistry of the primary particles affect the fractal dimensionality of the flocs, as argued in section 6.7. Coagulation experiments are recommended at destabilizer concentrations below the critical coagulation concentration, where the aggregation becomes more 'reaction-limited' (Meakin 1988). With Brownian coagulation such a reduction of destabilizer concentration results in an increase of the fractal dimensionality. It would be interesting to sort out whether the fractal dimensionality in the case of turbulent coagulation can also be controlled by simple adjustment of the destabilizer concentration.

The coagulation model can be easily adapted to include continuous processing of coagulation in a stirred tank. For this purpose an inlet term has to be included in the population balance for the primary particle size and an outlet term in the population balance for each aggregate size. In this way the stirred tank is treated as an ideal mixer, which is a reasonable assumption considering the reversibility of the aggregation process. At present experiments are undertaken in our laboratory to test this hypothesis.

To extend the model to describe precipitation processes a research program should be developed including systems with increasing degree of complexity. Coagulation of primary particles with different particulate properties should be studied. If the particles are spherical, input variables, like the Hamaker constant and the critical breakup distance H_1, need to be adjusted in order to make the model predict the aggregate sizes properly. If the particles are nonspherical, presumably the computation of the collision efficiency for the encounters between the primary particles needs also to be altered, since both mutual Van der Waals attraction (Van den Tempel 1961) and hydrodynamic interaction between the two approaching primary particles (Stein et al. 1986) will change. Experiments could be performed in which crystal growth is included in the process. This addition certainly complicates the modelling since with the crystalline bridges being formed between the primary particles within the flocs, irreversibility is introduced. When the physical Van der Waals bonds between the primary particles in the aggregates are replaced by crystalline bridges, much larger shear stresses are needed to disrupt the flocs. One way of dealing with this matter is to introduce a sticking

probability (David et al. 1991) which describes the probability of the formation of crystalline bridges before shear stresses occur which would normally rupture the floc. Finally, the particle generation (nucleation) process should also be studied and taken into account in order to model the complete precipitation process.

Another area that needs research involves the variation of the dimensions of the stirred tank. It would be interesting to pursue the laser Doppler measurements to larger vessel sizes in order to determine whether the energy dissipation rate distribution still changes with further scale-up. The tendency to a more homogeneous energy dissipation rate distribution with scale-up could be important for processes that are determined by the maximum energy dissipation rate in the system. An example of such a process is flocculation, where aggregation results from polymer bridges. In flocculation processes the rupture of flocs and recombination of floc fragments are not reversible (Tomi and Bagster 1978), due to the polymer chains that are broken up, tending to occupy available adsorption sites on the same particle. This results in a deficiency of adsorption sites and also the remaining extension of the macromolecules is not sufficient to bridge the distance maintained by electrostatic repulsion to other particles. Hence only floc degradation remains after an initial process of floc formation. The final aggregate size is determined solely by breakup of the flocs. The maximum energy dissipation rate in the stirred tank therefore plays an important part in determining this final aggregate size.

The geometry of the stirred vessel can be changed to examine its effect upon the aggregation process. Different impeller-vessel ratios or different types of impellers can be used to change the hydrodynamics in the stirred vessel.

Finally the concept of particle tracking can also be used to link the heterogeneous turbulent flow field in a stirred tank to the aggregation of particles larger than the Kolmogorov micro scale. For this purpose however first the expressions for the coagulation and breakup rates together with the breakup criterion for the inertial and macro subrange need to be tested experimentally. With these large particles the particle tracking may need to be adapted to include possible sedimentation of solids.

APPENDIX A
SLOTTING TECHNIQUE TO COMPUTE
AUTOCORRELATION FUNCTION

The Slotting technique computes the autocorrelation function from randomly occurring measurements. The problem of calculating the autocorrelation function from velocity samples separated by random time differences, is solved by calculating a discretized autocorrelation function. For this purpose the time lag axis is divided into M equidistant slots of width $\Delta\tau$. If the time difference between two samples, from which the average velocity is previously subtracted, falls within the k-th slot, their cross product is added to $SUM(k\Delta\tau)$. The number of crossproducts, which fall within the k-th slot, are registered in $H(k\Delta\tau)$. The value of the autocovariance function $B_{ii}(k\Delta\tau)$ at the midpoint of each slot can now be estimated from:

$$B_{ii}(k\Delta\tau) = SUM(k\Delta\tau) / H(k\Delta\tau), \quad k = 1, 2,..., M \qquad (A-1)$$

where $SUM(k\Delta\tau)$ is the sum of all cross products of $u'(t_i)$ and $u'(t_j)$, separated by lag times in the range $(k-1/2)\cdot\Delta\tau < |t_i - t_j| \leq (k+1/2)\cdot\Delta\tau$ and $H(k\Delta\tau)$ is the total number of cross products falling within the k-th slot. All autocovariance estimates $B_{ii}(k\Delta\tau)$ are scaled by $B_{ii}(0)$ to yield the autocorrelation function coefficients $R_{ii}(k\Delta\tau)$. $B_{ii}(0)$ is determined by ensemble averaging all self products, and is nothing but the mean square value u^2 of the fluctuating velocities.

APPENDIX B
COMPUTATION OF AUTOCORRELATION FUNCTION $R_{ii}(r_k)$
FOR DETERMINATION OF
MICRO LENGTH SCALE λ_i

The space correlation $R_{ii}(r_k)$ is computed from the time correlation $R_{ii}(\tau)$ using Taylor's hypothesis. Hence, $\lambda_i = |\bar{U}| \; \Theta_i$ where the Taylor micro time scale Θ_i is obtained from the intercept of the parabola that matches $R_{ii}(\tau)$ at the origin, i.e., $R_{ii}(\tau) = 1 - \tau^2/\Theta^2$ for small values of lag time τ. The microscale λ_i is thought to be less affected by application of Taylor's hypothesis to large turbulence intensities because it is inferred from well correlated regions of the velocity signals which only seldom contain a flow reversal. Corrections that have been proposed by Heskestad (1965) and Lumley (1965) to eliminate the errors in the microscale which are introduced by virtue of the use of Taylor's hypothesis are not applied in analogy with Antonia et al. (1980). The assumptions underlying the derivation of these corrections are not met in our flow system.

Secondly, the time correlation function had to be computed by the Slotting technique. For a brief introduction to the Slotting technique the reader is referred to appendix A. In contrast with periodic sampling, the Slotting technique is unaffected by noise in the data points except for the zero lag time (Absil et al. 1990) and is not limited by Niquist's criterion to a maximum frequency and minimum lag time corresponding to twice the data rate of the counter (Adrian and Yao 1987). It is, however, as we discussed in section 3.2.4, in error in the presence of velocity bias. The occurrence of velocity bias was monitored and only measurements which did not indicate any statistical errors were used to compute the autocorrelation functions.

Fig. B.1 is an example of the autocorrelation functions obtained with the Slotting technique for small lag times. The autocorrelation function falls off from zero to the first lag time $\Delta\tau$ due to noise in the mean square of the fluctuating velocity, i.e., the autocovariance value at zero lag time with which all autocovariance values have been scaled. The autocovariance values at lag times larger than zero are computed by averaging cross products which eliminates uncorrelated noise-contributions. Consequently, scaling all

autocovariance values with the mean square fluctuating velocity leads to a reduction of the values of the autocorrelation function for lag times larger than zero. The dotted line represents the parabolic function that matches the autocorrelation function at small lag times. Extrapolation of the parabola to the vertical axis provides a means of estimating the noise present in the mean squared velocity fluctuations. The noise in u^2 was found not to exceed 10%. The intercept with the horizontal axis gives the Taylor micro time scale that is converted into the micro length scale by multiplication with the flow velocity $|\bar{U}|$.
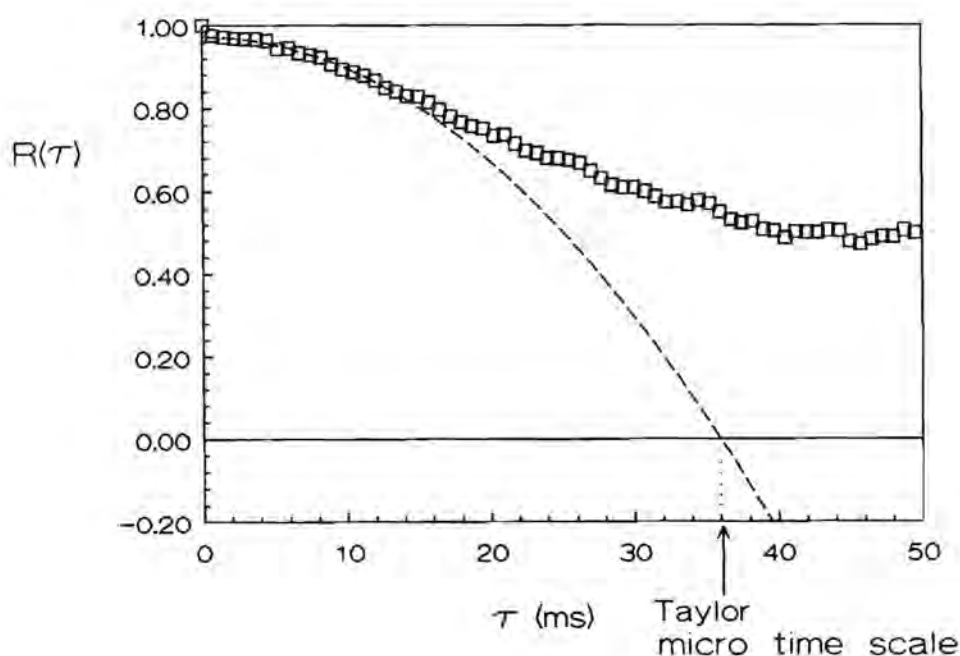
Figure B.1. Autocorrelation function for small lag times τ computed with the Slotting technique.

REFERENCES

Abrahamson, J. 1975, 'Collision Rates of Small Particles in a Vigorously Turbulent Fluid', Chem. Eng. Sci. 30, 1371-1379

Absil, L.H.J., Steenbergen, W. and Passchier, D.M. 1990, 'Time and spatial correlation measurements in the turbulent wake of a circular cylinder using LDA', Appl. Sci. Res. 47, 247-272

Adler, P.M. 1981a, 'Streamlines in and around Porous Particles', J. Coll. Int. Sci. 81, 531-535

Adler, P.M. 1981b, 'Heterocoagulation in Shear Flow', J. Coll. Int. Sci. 83, 106-115

Adler, P.M., 1981c, 'Interaction of Unequal Spheres, I. Hydrodynamic Interaction: Colloidal Forces', J. Coll. Int. Sci. 84, 461-474

Adrian, R.J. and Yao, C.S. 1987, 'Power Spectra of Fluid Velocities measured by Laser Doppler Velocimetry', Exp. in Fluids 5, 17-28

Antonia, R.A., Satyaprakash, B.R. and Hussain, A.K.M.F. 1980, 'Measurement of Dissipation Rate and Some Other Characteristics of Turbulent Plane and Circular Jets', Phys. Fluids 23, 695-700

Arp, P.A. and Mason, S.G. 1976, 'Orthokinetic Collisions of Hard Spheres in Simple Shear Flow', Can. J. Chem. 54, 3769-3774

Barthole, J.P., Maisonneuve, J., Gence, J.N., David, R., Mathieu, J. and Villermaux, J. 1982, 'Measurement of Mass Transfer Rates, Velocity and Concentration Fluctuations in an Industrial Stirred Tank', Chem. Eng. Fund. 1, 17-26

Bates, R.L., Fondy, P.L. and Corpstein, R. R. 1963, 'An Examination of Some Geometric Parameters of Impeller Power', Ind. Eng. Chem. Proc. Des. Dev. 2, 311-314

Batterham, R.J., Hall, J.S. and Barton, G. 1981, 'Pelletizing Kinetics and Simulation of Full Scale Balling Circuits', Proceedings of 3rd Int. Symp. on Agglomeration, Nürnberg, West-Germany, A136-A150

De Boer, G.B.J. 1987, 'Coagulation in Stirred Tanks', Ph.D. Thesis, Eindhoven University of Technology

De Boer, G.B.J., Hoedemakers G.F.M. and Thoenes, D. 1989a, 'Coagulation in Turbulent Flow Part I', Chem. Eng. Res. Des. 67, 301-307

De Boer, G.B.J., De Weerd, C. and Thoenes, D. 1989b, 'Coagulation in Turbulent Flow Part II', Chem. Eng. Res. Des. 67, 308-315.

Barnett, D.O. and Bentley, H.T. 1979, 'Statistical Bias of Individual Realization Laser Velocimeters', Proceedings of 2nd Int. Workshop Laser Velocimetry (Edited by Thompson, H.D. and Stevenson, W.H.), 428-444

Brakalov, L.B. 1987, 'A Connection between the Orthokinetic Coagulation Capture Efficiency of Aggregates and their Maximum Size', Chem. Eng. Sci. 42, 2373-2383

Buchave, P., George, W.K. and Lumley, J.L. 1979, 'The Measurement of Turbulence with the Laser Doppler Anemometer', Ann. Rev. Fluid Mech. 11, 443-503

Buchhave, P., Benzon, H.v. and Rasmussen, C.N. 1990, 'LDA Bias: Comparison of Measurement Errors from Simulated and Measured Data, Proceedings of 5th Int. Symp. Appl. Laser Techn. Fluid Mech., paper 29.3

Bujalski, W., Nienow, A.W., Chatwin, S. and Cooke, M. 1987, 'The Dependency on Scale of Power Numbers of Rushton Disc Turbines', Chem. Eng. Sci. 42, 317-326

Buscall, R. 1982, 'The Elastic Properties of Structured Dispersions: Simple Centrifuge Method of Examination', Coll. Surf. 5, 269-283

Camp, T.R. and Stein, P.C. 1943, 'Velocity gradients and Internal Work in Fluid Motion', J. Boston Soc. Civ. Eng. 30, 219-237

Costes, J. 1986, 'Structure des Ecoulements Generes par une Turbine de Rushton dans une Cuve Chicanee', Ph.D. Thesis, INP, Toulouse

Costes, J. and Couderc, J.P. 1988a, 'Study by Laser Doppler Anemometry of the Turbulent Flow Induced by a Rushton Turbine in a Stirred Tank: Influence of the Size of the Units-I. Mean Flow and Turbulence', J. Chem. Eng. Sci. 43, 2751-2764

Costes, J. and Couderc, J.P. 1988b, 'Study by Laser Doppler Anemometry of the Turbulent Flow induced by a Rushton Turbine in a Stirred Tank: Influence of the Size of the Units-II. Spectral Analysis and Scales of Turbulence', Chem. Eng. Sci. 43, 2765-2772

Costes, J., Alran, C. and Couderc, J.P. 1991, 'Characteristics of the Discharge Flow from a Rushton Turbine. Measurements by Thermal and Laser-Doppler Anemometry', Int. Chem. Eng. 31, 55-65

Cutter, L.A., 1966, 'Flow and Turbulence in a Stirred Tank', AIChE J. 12, 35-45

David, R, Marchal, P., Klein, J. and Villermaux, J. 1991, 'Crystallization and Precipitation Engineering-III. A Discrete Formulation of the Agglomeration Rate of Crystals in a Crystallization Process, Chem. Eng. Sci. 46, 205-213

Delichatsios, M.A., Probstein, R.F. 1975, 'Coagulation in turbulent flows: Theory and Experiment', J. Coll. Int. Sci. 51, 394-405

Delichatsios, M.A. 1975, 'Model for the Breakup Rate of Spherical Drops in Isotropic Turbulent Flows', Phys. of Fluids 18, 622-623

Delichatsios, M.A. and Probstein, R.F. 1976, 'The Effect of Coalescence on the Average Drop Size in Liquid-Liquid Dispersions', Ind. Eng. Chem., Fundam. 15, 134-138

Desouza, A. and Pike, R.W. 1972, 'Fluid Dynamics and Flow patterns in Stirred Tanks with a Turbine Impeller', Can. J. Chem. Eng. 50, 15-23

Dodge, L.G. 1984, 'Calibration of the Malvern particle sizer', Appl. Opt. 23, 2415-2419

Durst, F., Melling, A. and Whitelaw, J.H. 1981, 'Principles and Practice of Laser-Doppler Anemometry', Academic Press, London

Edwards, R.V. 1989, 'Report of the Special Panel on Statistical Particle Bias Problems in Laser Anemometry', J. Fluids Eng. 109, 89-93

Edwards, R.V. and Kolodzy, P.J. 1986, 'Computation of the Autocorrelation Function of Velocity Fluctuations using a Laser Anemometer in Sparsely Seeded Flows', Proceedings 3rd Int. Symp. Appl. Laser Techn. Fluid Mech., 103-112

Eshuis, A., Leendertse, H.J. and Thoenes, D. 1991, 'Surfactants-Free Emulsion Polymerization of Styrene using Crosslinked Seed Particles', to be published in Coll. Polymer Sci. 269

Feke, D.L. and Schowalter, W.R. 1983, 'The Effect of Brownian Diffusion on Shear-induced Coagulation of Colloidal Dispersions', J. Fluid Mech. 133, 17-35

Firth, B.A. and Hunter, R.J. 1976a, 'Flow Properties of Coagulated Colloidal Suspensions I. Energy Dissipation in the Flow Units', J. Coll. Int. Sci. 57, 248-256

Firth, B.A. and Hunter, R.J. 1976b 'Flow Properties of Coagulated Colloidal Suspensions III. The Elastic Floc Model', J. Coll. Int. Sci. 57, 266-275

Fisher, M.J. and Davies, P.O.A.L. 1964, 'Correlation Measurements in a Non-Frozen Pattern of Turbulence, J. Fluid Mech. 18, 97-115

François, R.J. and Van Haute, A.A. 1985, 'Structure of Hydroxide Flocs', Water Res. 19, 1249-1254

Frens, G. and Overbeek, J.Th.G. 1972, 'Repeptization and the Theory of Electrocratic Colloids', J. Coll. Int. Sci. 38, 376-387

Gear, C.W. 1967, 'The Numerical Integration of Ordinary Differential Equations', Math. Computation 21, 146-156

Gelbard, F., Tambour, Y. and Seinfeld, J.H. 1980, 'Sectional Representations for Simulating Aerosols Dynamics', J. Coll. Int. Sci. 76, 541-556

Glasgow, L.A. and Luecke, R.H. 1980, 'Mechanisms of Deaggregation for Clay-Polymer Flocs in Turbulent Systems', Ind. Eng. Chem. Fundam. 19, 148-156

Gmachowski, L., Iwata, M., Adachi, T. and Murase, T., 1990, 'Analysis of Floc Structure Based on The Extended Brinkman Model', J. Chem. Eng. Japan 23, 543-549

Gorni, H. 1986, 'Multiple Scattering Correction in The Measurement of Particle Size and Number Density by The Diffraction Method, Appl. Opt. 25, 3552 -3558

Günkel, A.A. and Weber, M.E., 1975a, 'Flow Phenomena in Stirred Tanks, Part I. The Impeller Stream', AIChE J. 21, 931-939

Günkel, A.A. and Weber, M.E., 1975b, 'Flow Phenomena in Stirred Tanks, Part II. The Bulk of the Tank', AIChE J. 21, 939-949

Happel, J. 1958, 'Viscous Flow in Multiparticle Systems: Slow Motion of Fluids Relative to Bed of Spherical Particles', AIChE J. 4, 197-201

Heller, W. and Peters, J. 1970, 'Mechanical and Surface Coagulation', J. Coll. Int. Sci. 32, 592-585

Heskestad, G. 1965,'A Generalized Taylor Hypothesis with Application For High Reynolds Number Turbulent Shear Flows, Trans. A.S.M.E., J. Appl. Mech. 87, 735-739

Hinze, J.O., 1975a, 'Turbulence', McGraw-Hill, London, 398
         1975b, 'Turbulence', McGraw-Hill, London, 394
         1975c, 'Turbulence', McGraw-Hill, London, 426
         1975d, 'Turbulence', McGraw-Hill, London, 185
         1975e, 'Turbulence', McGraw-Hill, London, 141

Higashitani, K., Ogawa, R. and Hosokawa, G. 1982, 'Kinetic Theory of Shear Coagulation for Particles in a Viscous Fluid', J. Chem. Eng. Japan 15, 299-304

Higashitani, K., Yamauchi, K., Matsuno, Y. and Hosokawa, G. 1983, 'Turbulent Coagulation of Particles Dispersed in a Viscous Fluid', J. Chem. Eng. Japan 16, 299-304

Hirleman, E.D., Oechsle, V., Chigier, N.A. 1984, 'Response Characteristics of Laser Diffraction Particle Size Analyzers: Optical Sample Volume Extent and Lens Effect', Opt. Eng. 23, 610-619

Hirleman, E.D. 1987, 'Optimal Scaling of the Inverse Fraunhofer Diffraction Particle Sizing Problem: the Linear System Produced by Quadrature', Part. Charact. 4, 128-133

Hjelmfelt, A.T. and Mockros, L.F. 1966, 'Motion of Discrete Particles in a Turbulent Fluid', Appl. Sci. Res. 16, 149-161

Van de Hulst, H.C. 1957, 'Light Scattering by Small Particles', John Wiley & Sons Inc., New York

Koh, P.T.L., Andrews, J.R.G., Uhlherr, P.H.T. 1984, 'Flocculation in Stirred Tanks', Chem. Eng. Sci. 39, 975-985

Koh, P.T.L., Andrews, J.R.G. and Uhlherr, P.H.T. 1987, 'Modelling Shear-Flocculation by Population Balances', Chem. Eng. Sci. 42, 353-362

Kolmogorov, A.N. 1941, 'The Local Structure of Turbulence in Incompressible Viscous Fluid for Very Large Reynolds Numbers', C. R. Acad. Sci. U.R.S.S. 30, 301

Kolodzy, P.J. 1986, 'A Statistical Study of Counter Processed Laser Fringe Anemometer Signals', Ph. D. Thesis, Case Western Reserve University

Komasawa, I., Kuboi, R. and Otake, T., 1974, 'Fluid and Particle Motion in Turbulent Dispersion - I. Measurement of Turbulence of Liquid by Continual Pursuit of Tracer Particle Motion', Chem. Eng. Sci. 29, 641-650

Kuboi, R., Komasawa, I. and Otake, T. 1972, 'Collision and Coalescence of Dispersed Drops in Turbulent Liquid Flow', J. Chem. Eng. Japan 5, 423-424

Kuboi, R., Komasawa, I., Otake, T. and Iwasa, M 1974, 'Fluid and Particle Motion in Turbulent Dispersion III Particle-liquid Hydrodynamics and Mass-transfer in Turbulent Dispersion', Chem. Eng. Sci. 29, 659-668

Kusters, K.A, Van Strien, C.J.G., Wijers, J.G. and Thoenes, D. 1990, 'Effect of Velocity Bias on Integral Time Scale', Proceedings of 3rd International Conf. on Laser Anemometry - Advances and Applications (Edited by Turner, J.T.), BHRA/Springer Verlag, 557-566

Kusters, K.A., Wijers, J.G. and Thoenes, D. 1991, 'Particle Sizing by Laser Diffraction Spectrometry in the Anomalous Regime', to be published in Applied Optics.

Latimer, P. 1985, 'Experimental Tests of a Theoretical Method for Predicting Light Scattering by Aggregates', Appl. Opt. 24, 3231-3239

Laufhütte, H.D. and Mersmann, A.B. 1985, 'Dissipation of Power in Stirred Vessels', in Proceedings of the 5th European Conf. on Mixing, BHRA Fluid Engineering, Wurzburg, West Germany, 331-340

Levins, D.M., and Glastonbury, J.R. 1972, 'Particle-Liquid Hydrodynamics and Mass Transfer in a Stirred Vessel Part I - Particle-Liquid Motion', Trans. IChemE 50, 32-41

Levich, V.G. 1962, 'Physicochemical Hydrodynamics', Prentice-Hall Inc., New York

Liepe, F., Möckel, H-O. and Winkler, H., 1971, 'Untersuchungen über Homogenisieren und über Turbulenz in Rührmaschinen', Chem. Techn. 23, 231-237

Liepe, L. 1988, 'Verfahrenstechnische Berechnungsmethoden Teil 4: Stoffvereinigen in Fluiden Phasen - Ausrüstungen und ihre Berechnung', VDH Verlagsgesellschaft mbH, Weinheim, 20

Lumley, J.L. 1965, 'Interpretation of Time Spectra Measured in High-intensity Shear Flows', Phys. Fluids 8, 1056-1062

Lyklema, J. 1968, 'Principles of the Stability of Lyophobic Colloidal Dispersions in Non-Aqueous Media', Adv. Col. Int. Sci. 2., 65-114

Mahouast, M., David, R. and Cognet, G. 1988, 'Periodic Phenomena Generated in the Discharge Flow by a Rushton Turbine in a CSTR and Investigation of the Reynolds Stresses', Proceedings 6th European Conf. on Mixing, 23-28

Mayo, Jr., W.T. 1978, 'Spectrum Measurements with Laser Velocimeters', Proceedings of the Dynamic Flow Conf., 851-868

McLaughlin, D.K. and Tiederman, W.G. 1973, 'Bias Correction for Individual Realization Laser Anemometry Measurements in Turbulent Flows', Phys. Fluids 16, 2082-2088

Meakin, P. 1988, 'Fractal Aggregates', Adv. Coll. Int. Sci. 28, 249-331

Van der Molen, K. and Van Maanen, H.R.E. 1978, 'Laser Doppler Measurements of the Turbulent Flow in Stirred Vessels to Establish Scaling Rules', Chem. Eng. Sci. 33, 1161-1168

Mujumdar, A.R., Huang, B., Wolf, D., Weber, M.E. and Douglas, W.J.M. 1970, 'Turbulence Parameters in a Stirred Tank', Can. J. Chem. Eng. 48, 475-483

Nienow, A.W. and Miles, D. 1971, 'Impeller Power Numbers in Closed Vessels', Ind. Eng. Chem. Proc. Des. Dev. 10, 41-43

Obuchov, A.M. and Jaglom, A.M. 1958, 'Die Mikrostruktur einer Turbulenter Strömung. In: Goering, H., 'Sammelblad zur Statistische Theorie der Turbulenz', Berlin, 97-125

Okamoto, Y., Nishikawa, M. and Hashimoto, K., 1981, 'Energy Dissipation Rate Distribution in Mixing Vessels and its Effect on Liquid-Liquid Dispersion and Solid-Liquid Mass Transfer', Int. Chem. Eng. 21, 88-94

Overbeek, J.Th.G. 1977, 'Recent Developments in the Understanding of Colloid Stability', J. Coll. Int. Sci. 58, 408-422

Parker, D.S., Warren, J.K. and Jenkins, D. 1972, 'Floc Breakup in Turbulent Flocculation Processes', J. Sanitary Eng. Div. 98, Proceedings of the American Soc. Civ. Eng., 79-99

Patterson, G.K. and Wu, H. 1985, 'Distribution of Turbulence Energy Dissipation Rates in Mixers', in Proceedings of the 5th European Conf. on Mixing, BHRA Fluid Engineering, Wurzburg, West Germany, 355-364

Placek, J. and Tavlarides, L.L. 1985, 'Turbulent Flow in Stirred Tanks Part I: Turbulent Flow in the Turbine Impeller Region', AIChE J. 31, 1113-1120

Platzer, B. and Noll, G. 1988, 'Modelling of the Local Distributions of Velocity Components and Turbulence Parameters in Agitated Vessels - Method and Results', J. Chem. Eng. Process. 23, 13-31

Popiolek, Z, Whitelaw, J.H. and Yianneskis, M. 1984, 'Unsteady Flow over Disc Turbine Blades', Proc. 2nd Int. Symp. Appl. Laser Anemometry Fluid Mech., 17.1

Rao, M.A. and Brodkey, R.S. 1972, 'Continuous Flow Stirred Tank Turbulence Parameters in the Impeller Stream', Chem. Eng. Sci. 27, 137-156

Reed, X.B., Princz, M. and Hartland, S. 1977, 'Laser Doppler Measurements of Turbulence in a Standard Stirred Tank', Proceedings of 2nd European Conf. on Mixing, paper B1

Revill, B.K. 1982, 'Pumping Capacity of Disc Turbine Agitators - A Literature Review', Proceedings of 4th European Conf. on Mixing, 11-24

Reynolds, W.C. and Hussain, A.K.M.F. 1972, 'The Mechanics of an Organized Wave in Turbulent Shear Flow. Part 3. Theoretical Models and Comparisons with Experiments', J. Fluid Mech. 54, 263-288

Van 't Riet, K. and Smith, J.M. 1975, 'The Trailing Vortex System Produced by Rushton Turbine Agitators, Chem. Eng. Sci. 30, 1093-1105

Rotta, J.C. 1972, 'Turbulente Strömungen', B.G. Teubner, Stuttgart, 96

Rudd, M.J. 1969, 'A New Theoretical Model for the Laser Dopplermeter', J. Phys. E: Sci. Instrum. 2, 55

Rumpf, H. 1962, 'The Strength of Granules and Agglomerates', in Agglomeration (Edited by W.A. Knepper), Wiley, New York, 379-418

Saffman, P.G., Turner, J.S. 1956, 'On the Collision of Drops in Turbulent Clouds', J. Fluid. Mech. 1, 16-30

Schwartzberg, H.G. and Treybal, R.E. 1968, 'Fluid and Particle Motion in Turbulent Stirred Tanks', I&EC Fundamentals 7, 6-12

Von Smoluchowski, M. 1917, 'Versuch einer Mathematischen Theorie der Koagulationskinetik Kolloider Lösungen, Z. Phys. Chem. 92, 156

Sonntag, R.C. and Russel, W.B. 1986, 'Structure and Breakup of Flocs Subjected to Fluid Stresses I. Shear Experiments', J. Coll. Int. Sci. 113, 399-413

Sonntag, R.C. and Russel W.B. 1987a, 'Structure and Breakup of Flocs Subjected to Fluid Stresses II. Theory', J. Coll. Int. Sci. 115, 378-389

Sonntag, R.C. and Russel, W.B. 1987b, 'Elastic Properties of Flocculated Networks', J. Coll. Int. Sci. 116, 485-489

Stein, H, Logtenberg, E.H., Van Diemen, A.J.G. and Peters, P.J. 1986, 'Coagulation of Suspensions in Shear Fields of Different Characters', Coll. Surf. 18, 223-240

Swithenbank, J., Beer, J.M., Taylor, D.S., Abbot, D. and McCreath, G.C. 1976, 'A Laser Diagnostic Technique for the Measurement of Droplet and Particle Size Distribution", Paper 76-69, AIAA 14th Aerospace Science Meeting, 421-447

Taylor, G.I. 1935, 'Statistical Theory of Turbulence Parts I-IV', Proc. Roy. Soc. A151, 421

Tchen, C. 1947, 'Mean Value and Correlation Problems Connected with the Motion of Small Particles Suspended in a Turbulent Fluid', Ph.D. Thesis, Delft University of Technology

Van den Tempel, M. 1961, 'Mechanical Properties of Plastic-Disperse Systems at Very Small Deformations', J. Coll. Sci. 16, 284-296

Tennekes, H. and Lumley, J.L. 1972, 'A first Course in Turbulence', MIT Press, London, 1989

Thomas, D.G. 1964, 'Turbulent Disruption of Flocs in Small Particle Size Suspensions', AIChE J. 10, 517-523

Tomi, D.T. and Bagster, D.F. 1978, 'The Behaviour of Aggregates in Stirred Vessels', Part I-Theoretical Consideration on the Effects of Agitation, Trans IChemE 56, 1-8

Townsend, A.A. 1947, 'The Measurement of Double and Triple Correlation Derivatives in Isotropic Turbulence', Proc. Camb. Phil. Soc. 43, 560-570

Treweek, G.P. and Morgan, J.J. 1977, 'Size Distributions of Flocculated Particles: Application of Electronic Particle Counters', Env. Sci. Techn. 11, 707-714

Tropea, C. 1987, 'Turbulence-induced Spectral Bias in Laser Anemometry', AIAA J. 25, 306-309

Tropea, C. and Struthers, D. 1987, 'Microprocessor Based On-line Measurement System for LDA', Proceedings Int. Spec. Meeting on "The Use of Computers in Laser Velocimetry" (Edited by Pfeifer, H.J. and Jaeggy, B.), paper 29

Visser, J. 1972, 'On Hamaker Constants: A Comparison between Hamaker Constants and Lifshitz-Van der Waals Constants', Adv. Coll. Int. Sci. 3, 331-363

Wiese, G.R. and Healy, T.W. 1970, 'Effect of Particle Size on Colloidal Stability', Trans. Faraday Soc. 66, 490-499

Verwey, E.J.W. and Overbeek, J.Th.G. 1948, 'Theory of the Stability of Lyophobic Colloids', Elsevier, Amsterdam

Williams, J.J.E. and Crane, R.I. 1983, 'Particle Collision Rate in Turbulent Flow', Int. J. Multiphase Flow 9, 421-435

Wu, H., Patterson, G.K., and van Doorn, M. 1989, 'Distribution of Turbulence Energy Dissipation Rates in a Rushton Turbine Stirred Mixer', Exp. in Fluids 8, 153-160

NOMENCLATURE

Note: This list contains those symbols that are frequently used in this thesis. The symbols that appear only once or twice are defined in the text itself.

a	particle radius	(m)
a_i	radius of floc consisting of i primary particles	(m)
a_F	floc radius	(m)
a_1	radius of primary particle	(m)
A	constant in eq.(3-1), which provides an "inviscid estimate" for the energy dissipation rate	(-)
$A_{1(2)}$	Hamaker constant	(J)
b	$3\rho / (2\rho_p + \rho)$	(-)
c_{NaCl}	NaCl concentration	(mol l^{-1})
C_P	volume concentration of primary particles	(m^3/m^3)
C_F	volume concentration of flocs	(m^3/m^3)
C_{ij}	correlation coefficient between q_i and q_j	(-)
$\mathbb{C}$	constant in fractal law, eq.(2-87)	(-)
d	particle diameter	(m)
d_b	blade thickness	(m)
d_F	floc diameter	(m)
d_i, d(i)	diameter of floc consisting of i primary particles	(m)
d_1	diameter of primary particle	(m)
D	impeller diameter	(m)
D_i	particle size representing the i-th size class	(m)
D32	Sauter mean diameter (SMD)	(m)
D43	Volume mean diameter (VMD)	(m)
D	fractal dimensionality	(-)
e	electron charge, 1.6 10^{-19}	(C)
e	relative extension	(-)
E	elastic bulk modulus	(N m^{-2})
$E_{ii}(f)$	one dimensional power spectrum	(m^2 s^{-1})
f	frequency of velocity fluctuations	(s^{-1})

$f(r)$	longitudinal velocity correlation function	(-)
$f_b, f_b(k)$	breakup frequency (of aggregates consisting of k primary particles)	(s^{-1})
f_s	ratio of strain rates	(-)
f_t	time fraction	(-)
$f_r, f_r(k)$	reduction factor, $f_s \cdot f_t$ (for frequency of collisions leading to the formation of aggregates consisting of k primary particles)	(-)
F, F_{11}	interaction force between primary particles	(N)
F_{ij}	interaction force between aggregates consisting of i and j primary particles respectively	(N)
$F(z)$	axial variation of radial mean velocity	()
FL	focal length of focusing lens of laser diffraction instrument	(m)
g	gravitational acceleration	$(m^2 s^{-1})$
g	acceleration vector due to gravity	$(m^2 s^{-1})$
$g(r)$	lateral or transverse velocity correlation function	(-)
G	elastic shear modulus	$(N\ m^{-2})$
H	separation distance, $r - (a_i + a_j)$	(m)
H_{min}	minimum H between surfaces of cores in shell core model	(m)
H^*_{min}	H_{min} normalized by core radius R_{Ci}	(m)
H_0	distance of closest approach between primary particles	(m)
H_1	critical breakup separation distance between primary particles	(m)
I	turbulence intensity, $(2k)^{1/2} / |\bar{U}|$	(-)
J_{ij}	collision frequency per unit volume corrected for hydrodynamic interaction, i.e., $\alpha_{ij} J^0_{ij}$	$(m^{-3} s^{-1})$
J^0_{ij}	frequency of collisions per unit volume between aggregates consisting of i and j primary particles respectively	$(m^3\ s^{-1})$
$J^*_{i,k-i}$	$f_r(k) J_{i,k-i}$	$(m^3\ s^{-1})$
k_B	Boltzmann constant, $1.38\ 10^{-23}$	$(J\ K^{-1})$

k_c	average number of links per primary particle in the fracture area that have to be broken in order to rupture the aggregate, i.e. coordination number in uniform packed structure	(-)
k_p	floc permeability	(m^2)
k	turbulent kinetic energy per unit mass	$(m^2\ s^{-2})$
K	compressive modulus	$(N\ m^{-2})$
L	macro length scale	(m)
$L_f,\ L_g$	longitudinal and lateral integral length scale	(m)
L_i	integral length scale for fluctuating velocity component in direction x_i	(m)
L_L	Lagrangian length scale	(m)
L^i	macro length scale in impeller stream of stirred tank	(m)
L^b	macro length scale in bulk flow of stirred tank	(m)
m	refractive index of particles relative to that of the suspending medium, $n_p\ /\ n_s$	(-)
n	constant in power law that describes the dependency of the yield strength S on solids density φ, i.e., eq.(2-92)	(-)
n_p	refractive index of particles	(-)
n_s	refractive index of suspending medium	(-)
$n_i,\ n(i)$	number concentration of aggregates consisting of i primary particles	(m^{-3})
N	impeller rotational speed	(s^{-1})
$N_i,\ N(i)$	number concentration of particles in size class i	(m^{-3})
N_p	power number, $P\ /\ \rho N^3 D^5$	(-)
N_{Qp}	discharge or flow number, $Q_p\ /\ ND^3$	(-)
N_{Qc}	circulation flow number, $2Q_c\ /\ ND^3$	(-)
N_s	ratio of hydrodynamic to Van der Waals forces between solid particles	(-)
N_s^p	ratio of hydrodynamic to Van der Waals forces between porous flocs	(-)

N	validated data rate	(s^{-1})
OB	obscuration of incident laser beam	(-)
q	rms velocity difference between particle and surrounding fluid flow	$(m\ s^{-1})$
q_i	relative velocity vector between particle i and fluid flow	$(m\ s^{-1})$
Q_C	circulation flow	$(m^3\ s^{-1})$
Q_P	impeller discharge flow	$(m^3\ s^{-1})$
Q_i, Q(i)	volume fraction of particles in i-th size class	(m^3/m^3)
Q	particle size volume distribution vector	(m^3/m^3)
p	pressure stress	$(N\ m^{-2})$
P	impeller power input	(W)
$P(\Delta u)$	probability density function for spatial velocity difference Δu	$(m\ s^{-1})$
r	radial coordinate or separation distance between centers of approaching particles	(m)
r^*	dimensionless radial coordinate, 2r / D	(-)
r_0	radial coordinate of center of circulation loop	(m)
r_0^*	dimensionless r_0, i.e., $2r_0$ / D	(-)
r_{min}	minimum center to center separation distance between cores in shell-core model	(m)
r_{min}^*	r_{min} normalized by floc radius a_i	(m)
r_{rupt}	radial coordinate of rupture location	(m)
r_{rupt}^*	r_{rupt} normalized by floc radius a_i	(-)
r	separation vector	(m)
R	collision radius, $a_i + a_j$	
R_{Ci}	radius of impermeable core of porous floc with radius a_i	(m)
R_{Ci}^*	R_{Ci} normalized by floc radius a_i	(-)
$R_L(\tau)$	Lagrangian autocorrelation	(-)
$R_{ij}(r_k)$	two point velocity correlation function	(-)
Re_D	impeller Reynolds number, $N\ D^2$ / v	(-)
Re_L	Reynolds number of large scale eddies, $\Delta u(L)\ L$ / v	(-)
Re_p	particle Reynolds number, $\|U - U_p\|_{rms}\ d$ / v	(-)

s	mean value of absolute strain rate in turbulent flow, i.e., $\overline{|s'_{ii}|}$	(s^{-1})
s_{ii}	rms strain rate in turbulent flow, i.e., $[\ \overline{(\partial u'_i / \partial x_i)^2}\ ]^{1/2}$	(s^{-1})
s_{ij}	rms shear rate in turbulent flow, i.e., $[\ \overline{(\partial u'_i / \partial x_j)^2}\ ]^{1/2}$	(s^{-1})
s'_{ii}	instantaneous strain rate in turbulent flow, i.e, $\partial u'_i / \partial x_i$	(s^{-1})
$\bar{s}_T$	residence time weighted strain rate	(s^{-1})
$\bar{s}_V$	volume averaged strain rate	(s^{-1})
$s_{\bar{\varepsilon}}$	strain rate corresponding to mean energy dissipation rate in stirred tank	(s^{-1})
S_k, S^*_k	breakup rate of aggregate consisting of k primary particles	$(m^{-3}s^{-1})$
S	tensile strength of floc	$(N\ m^{-2})$
S_0	tensile strength near center of floc	$(N\ m^{-2})$
t	time	(s)
Δt	time step in particle tracking simulation	(s)
T	absolute temperature	(K)
T	vessel diameter	(m)
T_i	integral time scale for fluctuating velocity component in the x_i direction, defined by eq.(3-5)	(s)
T_L	Lagrangian time scale	(s)
u	rms fluctuating velocity averaged over the 3 directions in space, as defined by eq.(2-9)	$(m\ s^{-1})$
u'_i	momentary fluctuating velocity component in x_i direction	$(m\ s^{-1})$
u_i	rms fluctuating velocity in x_i direction	$(m\ s^{-1})$
u_p	rms periodic fluctuating velocity	$(m\ s^{-1})$
u_t	rms turbulent fluctuating velocity	$(m\ s^{-1})$
u_{tot}	rms total fluctuating velocity	$(m\ s^{-1})$
u_{ip}, u_{it}	u_p and u_t respectively of velocity component in x_i direction	$(m\ s^{-1})$

u_r, u_z, u_ϑ	radial, axial and tangential rms fluctuating velocities (m s^{-1})	(m s^{-1})
$\Delta u'(r)$	momentary velocity difference over a distance r	(m s^{-1})
$\Delta u(r)$	rms velocity difference over a distance r	(m s^{-1})
Δu_b, Δv_b	critical breakup velocity differences over floc diameter	(m s^{-1})
$\Delta u^{\cdot}$	rms acceleration of velocity difference across floc diameter	(m s^{-1})
U_i	momentary fluid velocity component in x_i direction	(m s^{-1})
$\bar{U}_i$	mean velocity component in x_i direction	(m s^{-1})
$U_{p\text{-}p}$	peak-to-peak value of periodic velocity component	(m s^{-1})
$\bar{U}_r$, $\bar{U}_\vartheta$, $\bar{U}_z$	mean radial, tangential and axial velocities	(m s^{-1})
U	fluid velocity vector	(m s^{-1})
$|\bar{U}|$	amplitude of mean velocity vector	(m s^{-1})
v_K	Kolmogorov microscale of velocity	(m s^{-1})
$\Delta v(r)$	rms lateral velocity difference over a distance r	(m s^{-1})
V	volume of fluid in stirred tank	(m^3)
V_A	Van der Waals potential energy	(J)
V_R	electrostatic repulsion energy	(J)
V_R^σ, V_R^ψ	V_R at constant charge and constant potential	(J)
w_i	rms fluctuating velocity of particle i	(m s^{-1})
w	blade width	(m)
$\Delta w(R)$	rms difference between the velocities of two colliding particles	(m s^{-1})
x	position vector	(m)
z	axial coordinate	(m)
$z^{\cdot}$	dimensionless axial coordinate, 2z / D	(-)
z_0	axial coordinate of center of circulation loop	(m)
$z_0^{\cdot}$	dimensionless z_0, i.e., $2z_0$ / D	(-)
z_i	valency of ion i	(-)

Greek symbols

α	size parameter, i.e., $\pi d / \lambda_0$	(-)
α_{ij}	efficiency of collisions between aggregates consisting of i and j primary particles respectively	(-)
β_{ij}	number of fragments of aggregates consisting of i primary particles arising from breakup of aggregates made of j primary particles	(-)
γ	shear rate in simple shear flow	(s^{-1})
δ	distance from primary particle surface to Stern plane	(m)
ε	energy dissipation rate	$(m^2 \, s^{-3})$
$\bar{\varepsilon}$	mean ε, $P/(\rho \, V)$	$(m^2 \, s^{-3})$
ε_b	critical breakup energy dissipation rate value	$(m^2 \, s^{-3})$
ε_{min}	minimum ε in stirred tank	$(m^2 \, s^{-3})$
ε_r	relative dielectric constant	(-)
ε_0	permittivity of vacuum	$(F \, m^{-1})$
ζ	electrokinetic or zeta potential	(V)
η	Kolmogorov micro length scale	(m)
ψ	scattering angle	(rad)
ϑ	tangential coordinate	$(^\circ)$
κ	reciprocal of Debye length, defined by eq.(2-1)	(m^{-1})
λ_0	wavelength of light in vacuum	(m^{-1})
λ	ratio of particle radii, a_j / a_i, where $a_i \geq a_j$	(-)
λ_g	Taylor micro scale or dissipation scale	(m)
μ	dynamic viscosity of suspending medium	$(kgm^{-1}s^{-1})$
ν	kinematic viscosity of suspending medium	$(m^2 \, s^{-1})$
ν_B	frequency of Doppler burst	(s^{-1})
ν_D	Doppler frequency	(s^{-1})
ν_L	frequency of light	(s^{-1})
ν_P	Poisson's ratio	(-)
ν_S	shift frequency	(s^{-1})
ξ	dimensionless aggregate size, $a_F / \sqrt{k_P}$	(-)

ξ_c	critical value of ξ, where separation surface between open and closed trajectories is located at the surface of the collision sphere	(-)
ρ	fluid density	(kg m^{-3})
ρ_p	particle density	(kg m^{-3})
σ_c	capture cross section	(m^2)
σ_s	surface shearing stress	(N m^{-2})
τ_K	Kolmogorov micro time scale	(s)
τ_{pi}	relaxation time of particle i	(s)
τ_s	shear stress, $\mu\, s_{ij}$	(N m^{-2})
τ_{sb}	critical breakup shear stress	(N m^{-2})
φ	angle of impeller rotation	($^\circ$), (rad)
ψ_0	surface potential	(V)
ψ_δ	potential at Stern plane	(V)
φ	solids density within floc	(m^3/m^3)

Curriculum Vitae

Karl Kusters was born on February the 11th 1964 in Erp, the Netherlands. In 1982 he received his undergraduate degree (Gymnasium β) at the Monseigneur Zwijsen College in Veghel. In the same year he started his graduate study at the Department of Chemical Engineering at the Eindhoven University of Technology. In 1987 he graduated with honors in the Master of Science program. During the period 1987-1991 he had a grant from the Dutch organization for Scientific Research (Nederlandse organisatie voor Wetenschappelijk Onderzoek) to pursue a Ph.D. in Chemical Process Technology at the Eindhoven University of Technology. In 1992 he will be working at the Center for Aerosol Processes at the University of Cincinnati as a postdoctoral fellow.

STELLINGEN

behorende bij het proefschrift van K.A. Kusters

1. De versnelde groei van aggregaten in de beginfase van het coagulatieproces in een geroerde tank is een gevolg van de toename van de porositeit met de aggregaatgrootte.

   Dit proefschrift, hoofdstuk 5.

2. In tegenstelling tot hetgeen Barnett en Bentley opperden, verdwijnt de zogenaamde 'velocity bias' bij laser Doppler snelheidsmetingen niet door een verlaging van de strooideeltjesconcentratie tot een niveau waarbij de tijd tussen opeenvolgende metingen groter wordt dan de integrale tijdschaal van de turbulente stroming.

   Barnett, D.O., Bentley, H.T. 1979, 'Statistical Bias of Individual Realization Laser Velocimeters', Proceedings 2nd Int. Workshop on Laser Velocimetry (Edited by Thompson, H.D. and Stevenson, W.H.), Purdue University, West Lafayette, USA, 428-444

3. Ter eliminatie van 'velocity bias' verdient bij een hoge meetfrequentie weging van Laser Doppler snelheidsmetingen met de overeenkomstige meetintervaltijden de voorkeur boven weging met de overeenkomstige verblijftijden van de strooideeltjes in het meetvolume van de Laser Doppler snelheidsmeter.

   Hoesel, W. and Rodi, W. 1977, 'New Biasing Elimination Method for Laser-Doppler Counter Processing', Rev. Sci. Instrum. 48, 910-919

4. Door verschillende onderzoekers is onvoldoende aandacht geschonken aan het feit dat de eindige afmetingen van het meetvolume een beperking opleggen aan de schaal van de turbulente wervels waarvan de invloed nog betrouwbaar bepaald kan worden.

   Nishikawa, M., Okamoto, Y. and Hashimoto, K. and Nagata, S. 1976, 'Turbulence Energy Spectra in Baffled Mixing Vessels', J. Chem. Eng. Japan 9, 489-494

   Costes, J. and Couderc, J.P. 1988, 'Study by Laser Doppler Anemometry of the Turbulent Flow Induced by a Rushton Turbine in a Stirred Tank: Influence of the Size of the Units-II. Spectral Analysis and Scales of Turbulence', Chem. Eng. Sci. 43, 2765-2772

5. Om onderscheid te kunnen maken tussen het gelpolarisatie-model en het osmotische drukmodel bij ultrafiltratie dienen fluxmetingen onder instationaire condities uitgevoerd te worden.

van Oers, C.W., Vorstman, M.A.G., Muijselaar, W.G.H.M. and Kerkhof, P.J.A.M. 1991, 'Determination of the Presence of a Gel Layer by Instationary Flux Measurement', J. Membrane Sci. (Submitted)

6. Bij precipitatie waarbij één vaste stof gevormd wordt, kunnen locale mengeffecten in een continue geroerde tankreactor volledig worden bepaald door de grootschalige wervelstruktuur van turbulentie. In dat geval dient bij geometrische opschaling zonder verandering van de verblijftijd het toerental constant gehouden te worden.

7. In de opleiding tot scheikundig ingenieur wordt onvoldoende aandacht besteed aan stromingsleer ter beschrijving van de werking van procesapparaten. Voor een training in de stromingsleer dient derhalve in de tweede fase van de universitaire opleiding plaats ingeruimd te worden.

Rietema K. 1981, 'De Fysische Technologie is aan Vernieuwing toe', de Ingenieur 12, 18-19

8. De spelling van een taal is van veel groter belang in verband met de informatieoverdracht via het geschreven woord, dan als weergave van de uitspraak. Bij voorstellen voor spellingshervorming dient daarmee rekening gehouden te worden.

9. Na zinsnedes zoals: "It is obvious that...", "Het zal duidelijk zijn dat...", in wetenschappelijke publicaties komt veelal een onduidelijke gevolgtrekking.